Development of Digital Silicon Photomultipliers Based Detectors for High-Resolution Positron Emission Tomography

Ontwikkeling van detectoren gebaseerd op digitale siliciumfotomultiplicatoren voor positronemissietomografie

Radoslaw Marcinkowski

Promotoren: prof. dr. S. Vandenberghe, prof. dr. R. Van Holen
Proefschrift ingediend tot het behalen van de graad van
Doctor in de ingenieurswetenschappen: biomedische ingenieurstechnieken

UNIVERSITEIT
GENT

Vakgroep Elektronica en Informatiesystemen
Voorzitter: prof. dr. ir. R. Van de Walle
Faculteit Ingenieurswetenschappen en Architectuur
Academiejaar 2016 - 2017

ISBN 978-90-8578-930-7
NUR 954
Wettelijk depot: D/2016/10.500/62

Department of Electronics and Information Systems
Faculty of Engineering and Architecture
Ghent University

MEDISIP
IBiTech - iMinds
Campus Heymans, Block B
De Pintelaan 185
9000 Ghent
Belgium

Promotors:
Prof. dr. Stefaan Vandenberghe
Porf. dr. Roel Van Holen

Board of examiners:
Prof. dr. Kathy Steppe, Ghent University
Prof. dr. José María Benlloch, Institute for Molecular Imaging Technologies, Spain
Dr. Christophe Lerche, Forschungszentrum Jülich, Germany
Prof. dr. Christian Vanhove, Ghent University
Dr. Samuel España, Spanish National Cardiovascular Research Centre, Spain

This work was supported by the 7th Framework Programme for Research (FP7) of the European Union through the SUBLIMA project (Grant Agreement No 241711).

Acknowledgements

When I started my studies at the Warsaw University of Technology I never envisioned that I would find medical engineering as the most fascinating field and I would choose it as my major. Moreover, I never anticipated that I would start a PhD in this field and certainly I did not envision doing PhD in Ghent, Belgium, 1300 km away from my beloved family, friends and town. But here I am, after four years of my PhD writing these words. This is, I guess, one of the life's wonders, to never know what life will bring you next through its twisted paths and coincidences (if there are such things as coincidences at all – of course I am not speaking here about the coincidences in PET; in PET coincidences occur for sure and this PhD is yet another proof of this). One thing is sure; this work would not have been possible without the help and support of others. Therefore, I would like to begin this dissertation by thanking all of them.

First of all I would like to thank my promotors, **prof. dr. Stefaan Vandenberghe** and **prof. dr. Roel Van Holen**.

Stefaan, I would like to thank you for giving me the opportunity to follow my interest in the medical engineering as a researcher at MEDISIP and accepting me to your group even when it meant waiting for me longer than you expected. Thank you for giving me so many opportunities to go to international conferences where I could meet many extraordinary scientists and learn about their work which allowed me to improve myself as a researcher. **Roel**, thank you for giving me fresh ideas and suggestions regarding my research. Thank you for your guidance but also for giving me a freedom in my work. I am also grateful that you always found some time for me each time I unexpectedly appeared in your office. In particular, I would like to thank both you and Stefaan for your help in improving all my written work by providing me with your valuable comments.

Secondly, I would like to thank all my colleagues from MEDISIP with whom I shared joys and anxieties of PhD life, lunch breaks, discussions, conferences, drinks in the kitchen and fun after work.

The first person I would like to thank is **dr. Samuel España Palomares**, who was a post-doc at MEDISIP when I started my work there. You took me under your wings and helped me to take my first steps in the world of scientific research. Thank you for all the things that you taught me, all your explanations, countless discussions, brainstorming and collaboration in the laboratory. Simply, thank you for always having time and guidance for me. You were a true mentor and a friend. I cannot image the start of my PhD without you. You were simply irreplaceable!
Next, I would like to thank **Faruk** with whom I shared the office since the start of my PhD. You were a true friend and a great person, always willing to take a break in your work and help others in their research. Thank you for sharing your codes, scripts and helping with all kind of computer issues, which was a huge time saver. I will never forget our trip around California after the conference in Anaheim.
Lara, thank you for always surprising me with your unique statements and actions. You always raised my spirit with them. Thank you also for being a part of our small non-Flemish PhD researcher support group, especially in the last period of our PhD when we basically formed two members club. Most of all however, thank you for our discussions; I just loved them and never had enough. I will miss them so, so much. I wish you the best lack in whatever you decide to do in the future.
Carmen, thank you for always sharing with me the news about upcoming rock/heavy metal concerts and all sort of other events going on around in Ghent and in the rest of Belgium. Thank you also for always helping me with the Dutch translations whenever a need occurred. Also thank you for being one of the friendliest colleagues in the lab.
Shandra, for being the most optimistic and cheerful person in MEDISIP in my opinion. I always found your cheerfulness contagious, what sometimes was so much needed. **Nathalie**, for her outgoing, adventurous personality full of energy and for your exceptionally colourful outfits. Thank you also for inviting me for MEDISIP Ladies' Nights, though I still cannot figure out why I received this honour as an only male member of MEDISIP. **Karel**, for sharing the lab space with me and always helping me with mechanics related tasks and problems. **Pieter Mollet**, thank you for sharing and explaining to me your PET image reconstruction software and collaboration on the small animal PET scanner. **Pieter van Mierlo**, for always having this charming smile whenever he met me

in the office and for his both working and parting attitudes. **Karen**, thank you for providing always well considered advices regarding PhD.

Ester and **Stijn**, were great office and lunch mates and I am really grateful for their help with Dutch translations. **Willeke**, I am thankful for your effortless switching conversations to English whenever I was close so I could also fully participate in them. **Victoria**, I want to thank for the unforgettable dance on the kitchen's table during my welcome party (yes, together with Lara). **Prof. dr. Christian Vanhove**, **Benedicte** and **Scharon** I am grateful for their expertise and support in the Infinity Lab, especially in terms of animals scanning and for obtaining radio-tracers whenever I needed them for my experiments. **Ewout**, I am very thankful for his vast network and his experience and guidance with writing grant proposals what was especially helpful for me at the end of my PhD. (IWT-IM scholarship here I come!). **Saskia** and **Inge**, always saved me whenever I run into administrative/financial/invoice tasks, for which I never had heart myself. Your work is a tremendous help and time saver for everyone in the group. Many thanks also to my other colleagues with whom I had pleasure to work: **Gregor**, **Bert**, **Vincent**, **Enrico**, **Thibault**, **Kim**, **Jens**, **Hendrik**, **Roma**, **Margo**, **Tiziana**, **Ekaterina**, **Gwennaelle** (and I am sorry if I forgot anyone!).

I would also like to thank the colleagues of Biommeda for contributing to the nice atmosphere at the 5th floor of block B. Especially **prof. dr. Patrick Segers** and **prof. dr. ir Pascal Verdonck** for the IBiTech dinners.

Next, I would like to thank everyone from **Cherry Lab** at the **University of California, Davis**. I want to direct special acknowledgements to **prof. Simon R. Cherry** for making my research stay in his lab possible and giving me the opportunity to work with him and his excellent group. Being a part of your lab for six months was a wonderful experience, which I will never forget. **Sun Il**, I want to thank for taking care of me during my stay at UC Davis, collaboration in the laboratory and countless scientific discussions. I had a great time working with you. **Emilie** and **Julien** for their support in my research and for inviting me to my first Thanksgiving celebration. **Martin**, for always patiently answering all my questions and for saving me when I was lucky enough to be caught in California by downpour so heavy that even the Belgian weather would be impressed. **Eric** and **Junwei**, for sharing with me lab space and helping in my experiments. **Susan** and **Malena** for helping with all sort of administrative tasks and for helping me to find a place to stay in Davis, which was not a simple task. **Greg**, **Andre**,

Nadine, **Justin**, **Edwin** and **Yongfeng** for creating a wonderful work atmosphere in which I always felt invigorated for further scientific work. I would also like to thank **prof. Jinyi Qi**, **prof. Ramsey D. Badawi** and all members of their labs for sharing their work and profound discussions during weekly meetings, which enriched me as a researcher. Thank you all for your warm welcome and all the wonderful times I had with you. I hope that our paths will cross again.

Furthermore, I would also like to thank the entire **Philips Digital Photon Counting** team; let be honest without them and theirs digital silicon photomultipliers this PhD would not be possible. Special thanks to **Ralf Schulze** for his support and explanations regarding dSiPMs and their technicalities. Next, to **York Haemisch** and **Anja Schmitz** for making our collaboration so easy and friendly. Thanks to all members of the SUBLIMA collaboration.

My beloved wife **Kamila** I want to thank for her unceasing support in every aspect of my life and for believing in me even when I am losing faith in myself. You are the best friend and the best companion I could ever wish for. You are the reason for which I want to be a better man with each passing day. Thank you for always being there for me and for the fact that I can speak with you about everything.

Last, but not least I would like to thank my parents and my entire family. **Kochani Rodzice** dziękuję Wam z całego serca za wszystko co od Was otrzymałem. Za Wasze nieustające wsparcie, za inwestowanie w moją edukację i stwarzanie mi jak najlepszych warunków do rozwoju oraz za akceptowanie moich wyborów i pozwalanie mi na obranie własnej ścieżki w życiu. Przede wszystkim jednak dziękuję Wam za Waszą bezgraniczną miłość i za to, że zawsze byliście ze mną. To dzięki Wam jestem tym, kim jestem i osiągnąłem to, co osiągnąłem!

Chciałbym ogromnie podziękować mojej cioci **Miłce** za jej miłość, troskę i wsparcie, którymi mnie obdarza przez całe moje życie.

Dziękuję również rodzinie mojej żony Kamili, **Rodzicom** i szwagierce **Agnieszce**, za ciepłe przyjęcie mnie do rodziny, wiarę we mnie i doping przy pisaniu pracy. **Aga**, dzięki również za wszystkie wspólne wyjazdy, w trakcie których mogłem podładować baterie do dalszej pracy.

Radek
September 2016
Ghent

"All truths are easy to understand once they are discovered; the point is to discover them."

Galileo Galilei

Table of Contents

Table of Contents i

List of Figures vii

List of Tables xv

List of Acronyms xviii

English summary xxv

Nederlandstalige samenvatting xxxi

1 Introduction **1**
- 1.1 Research objectives . . . 1
- 1.2 Thesis outline . . . 2

2 Medical imaging **5**
- 2.1 Introduction . . . 5
- 2.2 Nuclear Medicine . . . 7
- 2.3 Preclinical imaging . . . 8
- 2.4 Positron Emission Tomography . . . 9
  - 2.4.1 Clinical applications . . . 10
  - 2.4.2 PET imaging principles . . . 11
  - 2.4.3 PET image reconstruction . . . 13
    - 2.4.3.1 Analytical methods . . . 13
    - 2.4.3.2 Iterative methods . . . 15
  - 2.4.4 PET image quality . . . 16
    - 2.4.4.1 Spatial resolution . . . 16
    - 2.4.4.2 Sensitivity . . . 18
    - 2.4.4.3 True, random and scatter coincidences . . . 19
  - 2.4.5 Time-of-Flight PET . . . 22

2.4.6 Multi-modality imaging 25
2.5 Small animal PET imaging 27

3 PET detectors 31
3.1 Introduction 31
3.2 Characteristics of PET detector 33
3.2.1 Energy resolution 33
3.2.2 Timing resolution 34
3.2.3 Spatial resolution 35
3.2.4 Sensitivity 35
3.2.5 Count rate performance 36
3.3 Scintillators 38
3.3.1 Introduction 38
3.3.2 Scintillation mechanism 39
3.3.3 Properties of scintillators 40
3.3.3.1 Efficiency 40
3.3.3.2 Photoelectric fraction 41
3.3.3.3 Light yield 42
3.3.3.4 Decay time 43
3.4 Photodetectors 44
3.4.1 Introduction 44
3.4.2 Photomultiplier tubes 45
3.4.3 Avalanche photodiodes 47
3.4.3.1 Geiger mode APDs 49
3.4.4 Silicon photomultiplier 51
3.4.4.1 Architecture and principle of operation . . . 51
3.4.4.2 Noise in SiPM 53
3.4.4.3 The advantages of SiPM 56
3.4.5 Digital silicon photomultiplier 56
3.4.5.1 Introduction 56
3.4.5.2 dSiPM architecture 57
3.4.5.3 Acquisition sequence 58
3.4.5.4 Neighbour Logic 62
3.4.5.5 RTL refresh 63
3.4.5.6 Inhibit memory 64
3.5 Small animal PET detectors 64
3.5.1 Disadvantage of pixelated detectors 65
3.5.2 Monolithic detectors 66
3.5.2.1 Event positioning 66
3.5.2.2 Challenges 67

4 **Optimized light sharing for high-resolution TOF PET detector based on Digital Silicon Photomultiplier** **69**
- 4.1 Introduction 69
- 4.2 Materials and Methods 71
  - 4.2.1 Working principle of DPC arrays 71
  - 4.2.2 Reference detector 74
  - 4.2.3 Pixelated array with a light guide 75
    - 4.2.3.1 Coincidence resolving time, energy resolution and flood map 76
    - 4.2.3.2 Time calibration 76
    - 4.2.3.3 Estimation of event loss due to dark counts 76
  - 4.2.4 Special reflector arrangement without NL 76
- 4.3 Results 78
  - 4.3.1 Reference detector 78
  - 4.3.2 Pixelated array with light guide 78
    - 4.3.2.1 Coincidence time, energy resolution and flood map 78
    - 4.3.2.2 Skew time calibration 79
    - 4.3.2.3 Valid events 80
  - 4.3.3 Special reflector arrangement 82
- 4.4 Discussion 84
- 4.5 Conclusion 85
- 4.6 Acknowledgements 86

5 **Effects of dark counts on digital silicon photomultipliers performance**
87
- 5.1 Introduction 87
  - 5.1.1 Digital Silicon Photomultipliers 87
  - 5.1.2 The influence of dark counts on the dead time and the spectrum of dSiPM 89
- 5.2 Materials and methods 90
- 5.3 Results 93
  - 5.3.1 Quantification of event loss 93
  - 5.3.2 False events caused by the RTL refresh option 94
  - 5.3.3 Verification of the dead time of the dSiPM 96
- 5.4 Discussion 97
- 5.5 Conclusion 99

6 **DigiPET: Sub-millimetre spatial resolution small animal PET**

imaging using thin monolithic scintillators 101
6.1 Introduction 101
6.2 Materials and methods 103
6.2.1 System description 103
6.2.1.1 Description of the PET system 103
6.2.1.2 dSiPM description 104
6.2.2 Acquisition configuration 105
6.2.2.1 System calibration 106
6.2.3 Performance 107
6.2.3.1 Detector performance 107
6.2.3.2 System performance 108
6.3 Imaging 109
6.3.0.1 Phantom imaging 109
6.3.0.2 Rat-brain imaging 109
6.4 Results 110
6.4.1 Detector performance 110
6.4.2 System performance 112
6.4.2.1 Spatial resolution 112
6.4.2.2 Axial sensitivity profile 112
6.4.2.3 Coincidence resolving time 113
6.4.3 Phantom imaging 114
6.4.4 Rat-brain imaging 115
6.5 Discussion 116
6.6 Conclusion 119
6.7 Acknowledgements 120

7 Sub-millimetre DOI detector based on monolithic LYSO and digital SiPM for a dedicated small-animal PET system 121
7.1 Introduction 121
7.2 Materials and methods 123
7.2.1 Detector 123
7.2.1.1 Detector assembly 123
7.2.1.2 dSiPM tile configuration 124
7.2.1.3 Detector's cooling 125
7.2.2 Measurement setup 125
7.2.3 Calibration and data processing 126
7.2.3.1 Events processing and filtering 126
7.2.3.2 Mean maps creation 127
7.2.4 Events positioning 130
7.2.5 Evaluation of detector performance 131

7.3 Results . . . 132
  7.3.1 Energy resolution . . . 132
  7.3.2 Timing resolution . . . 133
  7.3.3 Position estimation . . . 134
    7.3.3.1 Spatial resolution . . . 134
    7.3.3.2 Positioning bias . . . 135
    7.3.3.3 DOI resolution . . . 137
7.4 Discussion . . . 138
7.5 Conclusion . . . 140
7.6 Acknowledgements . . . 141

8 Evaluation of DigiPET2, a dedicated high resolution small animal PET scanner 143
8.1 Introduction . . . 143
8.2 Materials and methods . . . 145
  8.2.1 System description . . . 145
  8.2.2 Data acquisition and processing . . . 146
  8.2.3 Spatial resolution . . . 147
  8.2.4 Sensitivity, scatter and count-rate performance . . . 148
  8.2.5 Imaging studies . . . 148
    8.2.5.1 Phantom studies . . . 148
    8.2.5.2 Animal studies . . . 149
8.3 Results . . . 149
  8.3.1 Spatial resolution . . . 149
  8.3.2 Imaging studies . . . 151
    8.3.2.1 Phantom studies . . . 151
    8.3.2.2 Animal study . . . 153
8.4 Discussion . . . 154
8.5 Conclusion . . . 157
8.6 Acknowledgement . . . 157

9 General conclusions 159
9.1 Summary . . . 159
9.2 Future research possibilities . . . 164
9.3 Final conclusion . . . 165

Bibliography 167

List of Figures

2.1 Images of different medical imaging modalities. Top row from left, an X-ray of a hand, a CT of a chest, an MRI of a head. Bottom row from left, an ultrasound of a foetus, a SPECT image of the brain, a PET image of a brain. 6

2.2 Modern clinical whole-body PET/CT scanner - Siemens Biograph mCT Flow. In front of the scanner there is a patient bed that slides the patient into PET/CT ring during a scan. 9

2.3 Imaging principle of PET: positron emission from unstable nucleus, annihilation of a positron and emission of two back-to-back 511 keV photons and construction of an LOR from the detected 511 keV photon pair. 13

2.4 Acquisition of projections of an object and back-projection of the projections into image space. 14

2.5 Illustration of the parallax error. Without DOI information errors in LOR positioning may occur for gamma photons incident at oblique angles. 18

2.6 Different types of coincidences possible in PET. 20

2.7 Attenuation-corrected (AC) PET image (left) and non-attenuation-corrected (NAC) PET image (right) of a patient's body. In the NAC image, the body interior is blurred and organs are not clearly visible nor distinguishable. In the AC image, the structures of body interior are much clearer. . 22

2.8 The TOF PET principle. The time-of-flight difference Δt is related to the distance $d = c\frac{\Delta t}{2}$ from the centre of the LOR to the annihilation. During reconstruction of the image, the activity is attributed only to those voxels along the LOR that are close to the estimated voxel in which annihilation took place. 24

2.9 Patient with non-Hodgkins lymphoma (140 kg, BMI = 46). Representative transverse, sagittal, and coronal images (not triangulated) for non-TOF reconstruction (top) and the same cross-sectional images for TOF reconstruction (bottom). In each image, the different lesions are seen more clearly in TOF reconstruction than in non-TOF reconstruction. Research originally published in JNM [97]. Reprinted with permission. 25
2.10 Axial (top) and coronal (bottom) images from PET/CT scan. PET images are on the left, CT images in the center, and PET/CT fusion images on the right. PET images show intense uptake in the descending colon corresponding to a soft tissue density that by CT criteria is not distinguishable from fecal contents. Endoscopy and subsequent surgery confirmed that this was an adenocarcinoma of the colon, in this case an incidental finding on a study performed for another indication. Reprinted with permission from Radiology Rounds [140] 27

3.1 Schematic of the classic block detector design. 32
3.2 The energy spectrum of a ^{22}Na source. ΔE marks Full Width at Half Maximum of the 511 keV photopeak. 34
3.3 The behaviour of paralyzable and nonparalyzable detectors. The nonparalyzable detector detects events 1, 2, 4 and 6, while the paralyzable detector detects only events 1, 2 and 4. 37
3.4 The detector count rate for different types of detector models. In ideal detector count rate increases linearly with the event rate. In reality however, count rate of the paralyzable detector will drop to zero, while for nonparalyzable detector the count rate will eventually saturate at very high event rates. 37
3.5 Different types of scintillator crystals. From left, a single LYSO crystal 2×2×20 mm^3; a LYSO array of 24×24 individual LYSO crystals, each 2×2×20 mm^3; a monolithic crystal of LYSO 32×32×5 mm^3 with black reflector on lateral sides and white reflector on top and a monolithic of BGO 32×32×30 mm^3 with unpolished lateral sides. 39
3.6 Energy band structure of an activated crystalline scintillator. 40
3.7 Emission spectrum of LYSO crystal excited by gamma rays. . 43
3.8 Simplified schematic of a PMT and its principle of operation. 46
3.9 Simplified schematic of a MA-PMT. The metal dynodes multiply the electrons with minimal spatial spread. 47

3.10 Schematic of a *p*-side entrance reach-through APD. 48
3.11 G-APD simple passive quenching circuit. 50
3.12 Simplified schematic of SiPM. A SiPM consists of array of thousands of G-APD connected in parallel. 51
3.13 Examples of different SiPM arrays. (left) SensL 12 × 12 array with 3 × 3 mm pixels, (center) FBK 8 × 8 array with 4 × 4 mm pixels, (right) Hamamatsu 4 × 4 array with 3 × 3 mm pixels. 52
3.14 Schematic overview of the dSiPM architecture. The dSiPM consists of 16 independent dies, placed on the tile in a 4 × 4 matrix. Each of these dies is further subdivided into four pixels, arranged in a 2 × 2 matrix. For the DPC-3200-22-44 dSiPM type each pixel consists of 3200 microcells. 58
3.15 Top side (left) and bottom side (right) of the dSiPM tile. Top side is the active area of the dSiPM consisting of G-APDS microcells grouped in pixels. In the centre of the bottom side there is the FPGA, which is responsible for the configuration and synchronization of the individual dies. 59
3.16 Acquisition sequence of the dSiPM die. 60
3.17 Trigger probabilities for the dSiPM die. Trigger scheme 1 is not plotted as a single photon is sufficient to trigger the die. Plot obtained from the PDPC MTEK Manual v0.31. [172] . 60
3.18 Validation logic network of the dSiPM. 61
3.19 Simplified representations of a scintillation light distribution in a monolithic detector for different positions of gamma photon interactions. 67

4.1 Overview of the DPC. The array consists of 4 × 4 dies, each cnsisting of 4 × 4 pixles that further splits into 4 × 4 sub-pixels. 72
4.2 Acquisition sequence for a single die of the DPC. 74
4.3 Schematic of the setup containing a reference detector (right) and an array detector (left). 75
4.4 Schematic representation of the 4 × 4 LYSO crystal array and the special reflector arrangement proposed to focus the scintillation light onto single die of the DPC array. Each crystal has a size of 1.9 × 1.9 × 22 mm^3. Individual crystals are represented by black boxes. Four pixels of a single die of DPC are represented here by four green squares. The dashed area represents white reflector and the remaining inter-crystal area represents an optically transparent foil. 77

4.5 (a) CRT for all the crystals of a 15 × 15 LYSO array obtained using the trigger level 1 option. (b) Histogram of the CRT for all crystals in the array using different trigger levels. . . . 78
4.6 (a) 511 keV photopeak position and (b) energy resolution FWHM across the detector array. 79
4.7 (a) Flood histogram of the array of 15 × 15 LYSO crystals coupled to a DPC array and (b) line profile across the row of crystals inside the box shown in the flood histogram. 80
4.8 Map of electronic time skews the dies in DPC using the one labelled with a 0 as a reference. The values are in units of picoseconds. 80
4.9 Examples of recorded events (a) where all dies were available during photon detection and (b) where one die (marked by the orange box) adjacent to the position of gamma interaction was lost. Colour scale represents number of recorded optical photons in DPC's pixels (8 × 8) 81
4.10 CRT for all crystals in the array with special reflector arrangement. Values obtained for trigger level 1 82
4.11 (a) 511 keV photopeak position and (b) energy resolution FWHM across all crystals of the array with special reflector arrangement. 83
4.12 (a) Flood histogram of the array of 4 × 4 LYSO crystals coupled to a DPC array and (b) line profile across the column of crystals inside the box shown in the flood histogram. . . . 83

5.1 Acquisition sequence of dSiPM sensor. 88
5.2 Illustration how dark counts can lead to the loss of gamma events in dSiPM. 89
5.3 Example of recorded light distribution of 511 keV interaction where all dies of dSiPM array were available (a) and where one die was missing (marked by the orange box) due to undergoing recharge (b). Color scale represents number of recorded optical photons in dSiPM's pixels. 90
5.4 Overview of the measurement setup. 91
5.5 Cumulated dark counts rate (DCR) of a single die at 4°C. Values in the box show cumulated DCR for 100%, 90%, 80% and 70% of active cells. 92
5.6 Spectrum of recorded LED pulse by dSiPM for RTL refresh turned on (blue) and RTL refresh turned off (red). 96

5.7 Fraction of recorded LED events as a function of dark counts trigger rates (blue) with fit of simulated number of recorded events according to non-paralyzable dead time model for different dead time lengths (red). 97

6.1 Schematics (a) and picture (b) of the PET system prototype developed in this study. 104
6.2 Schematics (a) and picture (b) of the PET system prototype developed in this study. 107
6.3 Energy spectrum obtained for some beam positions (a) and map of photopeak positions across one of the detectors (b). A schematic of the dSiPM array is shown to explain the reason of the three dark lines in the map. 110
6.4 Maps of intrinsic spatial resolution in X (a) and Y (b) directions and bias (c) obtained for one of the detectors of the system. The black lines on the bias map show the translation from the true beam positions to the measured one. 111
6.5 Radial (solid), tangential (dashed) and axial (dotted) spatial resolution (FWHM and FWTM) obtained for the DigiPET scanner as a function of the radial position. 112
6.6 Absolute sensitivity profiles along the central axis of the DigiPET scanner for 250-650 keV (solid) and 400-650 keV (dashed) energy windows. 113
6.7 Time difference spectrum obtained with DigiPET scanner for a ^{22}Na point source located at CFOV. 113
6.8 Reconstructed images of the hot-rod phantom acquired using the DigiPET scanner (a) and the LabPET-8^{TM} scanner (b). . 114
6.9 Profiles through a row of 1.0 mm diameter hot rods (blue dashed lines in 6.8) in both images. 115
6.10 Image of the ^{18}F-FDG rat brain study obtained with the MRI (a), the LabPET-8^{TM} scanner (b) and the DigiPET scanner (c). 116
6.11 Sensitivity at CFOV obtained with Monte Carlo simulation for different variation of the DigiPET system in terms of crystal thickness (from 2 to 5 mm), number of detector rings (1 and 2 rings) and energy window (250-650 keV and 400-650 keV). 119

7.1 Schematic overview of the structure of the dSiPM tile. One die is enlarged to present in more detail the structure of the dSiPM die. 124
7.2 An overview of the calibration setup. 126

7.3 An example of the sorted variance values of normalized light fraction recorded by the dSiPM pixels per event. Dashed, vertical lines demarcate the estimated boundaries between defined DOI layers. 129
7.4 An example of normalized mean maps calculated for each DOI layer. 130
7.5 An example of maps of normalized value for a given pixel at each interpolated grid position for different DOI layers. The colour scale range is kept the same for all three displayed maps. 130
7.6 Map of detector energy resolution (a) and 511 keV photopeak position (b) obtained at each calibration position. 133
7.7 Histogram of the CRT values obtained at each calibration position. 133
7.8 Maps of detector's intrinsic spatial resolution in x (a) and y (b) directions. 134
7.9 . Maps of intrinsic spatial resolution in x and y direction calculated for each of pre-defined DOI layer independently (the top layer is the layer furthest away from dSiPM array, the bottom one is the closest one, and the middle one is in between). 135
7.10 An image of positioned grid scan with line profiles through it. Arrows indicate the row and column selected for plotting the line profiles. Roman numbers associate the plotted profiles with the selected through-image lines. 136
7.11 Map of detector's bias magnitude and direction. The colour scale decodes bias magnitude, black arrows show the translation from the true beam position to the measured one. . . 136
7.12 DOI resolution (mean absolute error) of the detector as a function of the DOI. DOI of 0 mm corresponds to the entrance face of the detector (proximal surface from the radiation beam). 137

8.1 Front (left) and side (right) picture of the new DigiPET2 scanner. 145
8.2 Radial (squares), tangential (triangles) and axial (diamonds) spatial resolution FWHM (solid) and FWTM (dashed) obtained for the DigiPET2 scanner as a function of the radial position. 150

8.3 Radial (squares), tangential (triangles) and axial (diamonds) spatial resolution FWHM (solid) and FWTM (dashed) obtained for the DigiPET2 scanner as a function of the radial position for the point source located one-fourth off the center of the axial FOV. 150
8.4 Reconstructed images of the micro-Derenzo phantom acquired with the DigiPET2 scanner. 151
8.5 Profiles through the row of 0.8 mm diameter hot rods along the lines depicted in figure 8.4. 152
8.6 Transverse slice through the uniform region of the micro-Derenzo phantom and the profile through it (dashed line). . . 152
8.7 Comparison of the reconstructed images of the micro-Derenzo phantom acquired with the DigiPET2 scanner (left) and the LabPET-8^{TM} scanner (right). 153
8.8 Transversal (a), coronal (b) and sagittal (c) images of the mouse head obtained with the ^{18}F-NaF. 153
8.9 Transverse images of the mouse head obtained with (a) DigiPET2, (b) X-CUBE and (c) co-registered PET/CT image. 154
8.10 Coronal (a) and sagittal (b) images of the mouse head obtained with the DigiPET2 scanner and co-registered with the CT. 155

List of Tables

2.1 List of positron-emitting isotopes used for PET with their maximum energy, half-life, mean free path and production method. 12

2.2 Positron range in water, FWHM in mm, for different isotopes used for PET imaging [Raylman et al 1992, Bailey 1996]. . . 17

3.1 Properties of several scintillators used in PET. (Data from [207]) 42

3.2 Different trigger schemes of dSiPM. 61

3.3 Validation schemes of the dSiPM die and the simulation results for average and minimum threshold of detected optical photons to successfully validate an event. Values obtained from the PDPC MTEK Manual v0.31. 62

4.1 Simulated spatial resolution (FWHM) for different LYSO pixel sizes 71

4.2 Boolean interconnections of different trigger levels of DPC . 73

4.3 Boolean interconnections of different validation levels of DPC 73

5.1 Percentage of recorded LED events for different validation time (settings used: trigger level 4, validation level 8) 94

5.2 Percentage of recorded LED events for different validation levels (settings used: trigger level 4, validation time 40 ns) . 95

5.3 Percentage of recorded LED events for different trigger levels (settings used: validation level 8, validation time 40 ns) . . . 95

5.4 Percentage of recorded LED events for different RTL & NL configurations (settings used: trigger level 4, validation level 8, validation time 40 ns) 95

5.5 Percentage of recorded LED events for different number of dies needed to record a single event (settings used: trigger level 4, validation level 8, validation time 40 ns) 95

6.1 dSiPM parameter settings used in all the acquisitions performed in this study 106

7.1 Intrinsic spatial resolution for the detector in each DOI layer and entire crystal volume 135

List of acronyms

A

AC	Attenuation Correction
ADC	Analog to Digital Converter
APD	Avalanch PhotoDiode
ASIC	Application Specific Integrated Circuit

B

BGO	Bismuth Germanate

C

CFOV	Central Field Of View
CMOS	Complementary Metal–Oxide–Semiconductor
CRC	Contrast Recovery Coefficient
CRT	Coincidence Resolving Time
CT	Computed Tomography

D

DC	Dark Count
DCR	Dark Count Rate
DOI	Depth of Interaction
DPC	Digital Photon Counter
dSiPM	digital Silicon Photomultiplier

E

EM	Expectation Maximization
EN	Excess Noise
ET	Emission Tomography

F

FBP	Filtered Backprojection
FDG	FlouroDeoxyGlucose
FFT	Fast Fourier Transform
fMRI	functional MRI
FOV	Field Of View
FPGA	Field Programmable Gate Array
FWHM	Full Width at Half Maximum
FWTM	Full Width at Tenth Maximum

G

G-APD	Geiger Avalanch PhotoDiode
GATE	Geant4 Application for Tomographic Emission
GPU	Graphics Processing Unit
GSO	Gadolinium Orthosilicate

H

HMDP	Hydroxymethylene Diphosphonate

I

IQ	Image Quality

K

k-NN	k-Nearest Neighbour

L

LED	Light Emitting Diode
LOR	Line of Response
LSO	Lutetium oxyorthosylicate
LYSO	Lutetium-Yttrium oxyorthosylicate

M

MC	Monte Carlo
ML	Maximum Likelihood
MLEM	Maximum Likelihood Expectation Maximization
MNN	Mean Nearest Neighbour
MPPC	Multi-Pixel Photon Counters
MRI	Magnetic Resonance Imaging
M-TEK	Module Technology Evaluation Kit

N

NAC	Non-Attenuation Correction
NECR	Noise Equivalent Count Rate
NL	Neighbour Logic

O

OSEM	Ordered Subsets Expectation Maximization

P

PCB	Printed Circuit Board
PDE	Photo Detection Efficiency
PET	Positron Emission Tomography
PDPC	Philips Digital Photon Counting
PMT	Photomultiplier Tube
PSPMT	Position Sensitive Photomultiplier Tube
PSF	Point Spread Function

Q

QE	Quantum Efficiency

R

RMSE	Root Mean Squared Error
ROI	Region Of Interest
RTL	Row-Trigger-Lines

S

SiPM	Silicon Photomultiplier
SNR	Signal-to-Noise Ratio
SOM	Self-Organizing Map
SPAD	Single Photon Avalanche Photodiode
SP	Single Pixel
SPECT	Single Photon Emission Computed Tomography
SSPM	Solid-State Photomultiplier
SUV	Standard Uptake Value

T

TEC	Technology Evaluation Kit
TDC	Time-to-Digital-Converter
TOF	Time-Of-Flight

U

US	Ultrasound
UV	Ultraviolet

V

VOI	Volume Of Interest

English summary

Nederlandstalige samenvatting

English summary

The work presented in this dissertation is situated in the field of positron emission tomography (PET) and is focused on the development of new detector designs.

Positron emission tomography is a medical imaging modality and one of the two main techniques in nuclear medicine. It allows for *in vivo* visualization of biological processes in the living body without disturbing them. PET is based on the tracer principle, which states that molecules that contain radioactive isotopes participate in physiological processes of the organism in the same way as molecules without radioactive isotopes. Therefore, radioactive isotopes can be used to label and to track the distributions of specific molecules in the body by detecting the radiation generated by these radioactive isotopes. The radio-tracer is delivered to a patient via an injection. It is then distributed within the body and accumulates in specific regions in the body. PET uses positron emitting isotopes for labelling molecules. The radio-tracer decays by emitting positrons, which travel a short distance after their emission and annihilate with electrons within the body. During the annihilation process, two gamma photons, each with an energy of exactly 511 keV, are emitted 180° apart. These emitted gamma photons are detected in the ring of PET detectors surrounding the patient during the scan. The coincidence electronics register the detected gamma photon pair and define a line of response: a line along which the annihilation occurred and along which the radio-tracer was located. Subsequently, the PET image, i.e., the 3D visualization of the radio-tracer distribution within the body, is reconstructed from the measured lines of response.

A PET scanner is a ring of detectors that detect the emitted gamma photons. The detectors determine the overall performance of the PET scanner and together with the image reconstruction method defines the quality of PET images. Therefore, the detectors are the main component of the system. An overview of PET detectors is presented in chapter 3.

Since the first development of PET in 1950s, the detectors were constructed almost exclusively with pixelated scintillator arrays coupled to photomultiplier tubes (PMTs). However, with the recent progress in the field of photosensors and semiconductors, new types of photosensors suitable for developing PET detectors have become available. The most recent type of these new photosensors are silicon photomultipliers (SiPMs). SiPMs have a number of characteristics that impart them with certain advantages over PMTs in terms of performance and are highly promising for developing new, better PET detectors that outperform those based on PMTs.

In this dissertation, we investigate new PET detectors that were developed using the newest type of SiPMs called the digital SiPM (dSiPM). dSiPM employs early digitalization of the detected signals by integrating CMOS circuitry into the SiPM chip, which results in gain-independent and fully digital readout of measured light signal. The presented PET detectors were developed with a focus on high-resolution PET imaging; thus, their designs place emphasis on high spatial resolution and sufficient sensitivity. In the first part of this dissertation we investigate detectors for clinical PET systems used for whole-body human imaging. These detectors are designed to achieve high spatial resolution and display good timing resolution which allows to introduce time-of-flight capability to the PET system. In the second part we focus on development of PET detectors for preclinical systems intended for imaging of mice and rats. In order to achieve sub-millimetre spatial resolution we investigate detectors based on monolithic scintillator crystals as an alternative to the classical pixelated detectors.

In chapter 4, we developed a high-resolution PET detector based on a dSiPM and LYSO array with a 2 mm pixel pitch intended for a high-resolution whole-body time-of-flight PET scanner. Two different detector designs were developed and evaluated. The first design was a classical detector design and consisted of an array of 15 × 15 LYSO crystal, each with a size of $2 \times 2 \times 22$ mm^3, coupled through the light-guide to a dSiPM photosensor. This detector achieved a good energy resolution of 14.5 % on average, and timing resolution of 376 ps was achieved. However, due to a lack of 1:1 coupling between LYSO crystals and dSiPM pixels combined with the noise caused by dark counts and dSiPM's acquisition sequence, the classical detector design had poor count rate performance.

Therefore, a second optimized detector design was developed and evaluated. The second design consisted of an array of 4 × 4 LYSO crystals, each with a size of $1.9 \times 1.9 \times 22$ mm^3, with a special reflector arrangement between them to ensure that all crystals can be individually resolved. The size of the LYSO crystals was slightly decreased to better fit onto the active area of a single dSiPM die - a group of four pixels. Thus, 1:1 coupling between the dSiPM die and the LYSO array resulted in a remarkable improvement in terms of the detector's count rate in comparison to the first design because a single event did not have to be readout by multiple dies. Moreover, the second detector design achieved an improved timing resolution of 295 ps and an average energy resolution of 11 % due to the lack of light sharing between dies. Thus, the second detector design based on the special reflector arrangement was better because it provided better results than the classic design in terms of count rate performance and both timing and energy resolution.

The main source of noise in SiPMs are dark counts, which are the false signals generated in the SiPM itself due to thermal excitations. This noise is distinctive for semiconductor photodetectors such as the SiPMs and is not present in PMTs. We found that the influence of the dark counts on the detector's count rate performance is an important problem of dSiPMs. Therefore, in chapter 5 we quantified the loss of events for different configurations of the dSiPM and provided guidelines on the optimal configuration for different detector designs and applications. The main focus was on the count rate performance and on scenarios in which multiple dies of dSiPM are required to record a single event.

Currently all PET systems are based on detectors built with pixelated scintillator arrays in which pixels are separated with reflective material. The size of the pixels determines the resolution of the detector. The smaller pixels, the better resolution can be achieved. However, with the decrease of the pixels size the amount of reflective material increases. This results in reduced sensitivity of the detectors. Thus, in pixelated detectors, a trade-off has to be made between detector resolution and sensitivity. This trade-off is especially problematic for small animal PET systems for which both high resolution and high sensitivity is desired. Moreover, the production of finely pixelated scintillation crystals is complex and expensive. Therefore, we used detectors based on monolithic (continuous) scintillator crystals as an alternative for the pixelated detectors. Monolithic detectors offer a number of advantages. Due to the absence of any reflective material within the scintillator, higher sensitivity can be achieved. Monolithic detectors intrinsically provide depth of interaction correction without any additional modifications in the detector design. Finally, monolithic crystals are easier and less expensive to manufacture. The disadvantage of monolithic detectors is the need for estimation of the interaction position of a gamma photon in a monolithic crystal. This is far more complex than in pixelated detectors and therefore, sophisticated positioning algorithms and extra electronics are required to obtain high resolution in the monolithic detectors. Moreover, these algorithms often require time-consuming calibrations.

In chapter 6, we introduced a prototype of a high-resolution dedicated mouse/rat-brain PET imaging system called DigiPET. DigiPET was a proof of concept of using thin monolithic scintillator crystals to obtain PET detectors with sub-millimetre spatial resolution for preclinical imaging. The system consisted of four detectors placed in a square arrangement with a large solid angle coverage around the animal. Thanks to the combination of thin monolithic crystals and the employed position algorithm, the DigiPET system achieved an excellent spatial resolution of 0.7 mm FWHM uniformly throughout the entire FOV. This is substantially better than the spatial resolution of the majority of currently available commercial small animal PET scanners. Furthermore, we performed an ex vivo FDG study of a rat brain that demonstrated the feasibility of imaging real objects with the prototype scanner.

The drawback of the developed DigiPET prototype was its low sensitivity due to the low detection efficiency of the 2 mm thick LYSO crystals. Therefore, to overcome this sensitivity limitation we developed an improved detector design based on a 5 mm thick monolithic LYSO crystal, which is presented in chapter 7. Because of the use of the thicker crystal, the nominal sensitivity of the detector was improved 2.21 times, increasing the coincidence sensitivity by a factor of greater than 4. Simultaneously, to sustain sub-millimetre spatial resolution, a number of modifications were introduced: depth of interaction decoding, a modified detector calibration procedure and a 3D event positioning algorithm. Due to the applied modifications, the new detector achieved an intrinsic spatial resolution of 0.6 mm FWHM compared to the 0.54 mm FWHM intrinsic spatial resolution achieved in the detector with the 2 mm thick LYSO crystal.

Finally, in chapter 8, based on the improved detector design, we developed the second version of our high-resolution small animal PET system. The new DigiPET scanner consisted of seven detector modules arranged in a heptagonal ring. Consequently, a larger field of view (FOV) for easier accommodation of the scanned animal was achieved, and the count rate performance of the scanner was improved due to the increased number of detectors. The second version of the DigiPET scanner achieved an average spatial resolution of $\sim$0.9 mm FWHM. This was worse than the first prototype; however, the second system achieved improved sensitivity. Nevertheless, the second version of the DigiPET scanner still significantly outperformed the majority of current commercial small animal PET systems in terms of spatial resolution. To demonstrate the imaging capabilities of the new scanner, the micro-Derenzo phantom and a bone scan of a mouse head were acquired. In the reconstructed image of the micro-Derenzo phantom, all hot rods with a diameter down to 0.8 mm could be clearly resolved. Furthermore, *in vivo* mouse head imaging demonstrated the feasibility of high-resolution imaging of real objects.

Nederlandstalige samenvatting

Het in deze thesis voorgestelde onderzoek handelt over positronemissietomografie (PET) en focust in het bijzonder op het ontwikkelen van nieuwe PET-detectoren.

Positronemissietomografie is een nucleaire beeldvormingstechniek en een van de twee meest gebruikte technieken in nucleaire geneeskunde. Deze techniek laat toe om in vivo biologische processen in het lichaam in beeld te brengen zonder ze te verstoren. PET baseert zich op het speurstofprincipe. Dit principe zegt dat moleculen, gemerkt met radioactieve isotopen, op dezelfde manier aan fysiologische processen van het organisme deelnemen als niet-gemerkte moleculen. Dit betekent dat radioactieve isotopen kunnen gebruikt worden om moleculen te merken en hun verspreiding in het lichaam te detecteren door de uitgezonden straling op te meten. De radioactieve speurstof wordt via een injectie toegediend aan de patiënt, waarna de speurstof zich verspreidt doorheen het lichaam en zich op specifieke plaatsen zal ophopen. In het geval van PET gebruikt men positronemitters om de moleculen te merken. Deze speurstof zendt positronen uit bij zijn verval. De uitgezonden positronen zullen zich vervolgens over een korte afstand voortbewegen vooraleer ze annihileren met een in het lichaam aanwezige elektron. In het annihilatieproces worden twee gamma-fotonen gegenereerd die elk een energie van exact 511 keV bezitten en in een hoek van ongeveer 180° worden uitgezonden. De gamma-fotonen worden vervolgens gedetecteerd door de PET-detectoren die de patiënt omringen gedurende een scan. De aanwezige coïncidentie-elektronica zal het fotonenpaar registreren en een lijn van respons definiëren. Deze lijn van respons is de lijn waarlangs de annihilatie plaatsnam en waarlangs de speurstof zich dus bevond. Ten slotte wordt het PET-beeld, een 3D visualisatie van de speurstofverdeling in het lichaam, met een analytische of iteratieve methode gereconstrueerd op basis van de opgemeten LOR-data.

Een PET-scanner bestaat uit een ring van detectoren die de uitgezonden gamma-fotonen detecteren. Deze detectoren bepalen de algemene performantie van de PET-scanner en definiëren samen met de reconstructiemethode ook de kwaliteit van de finale PET-beelden. Daarom zijn de detectoren het belangrijkste onderdeel van de PET-scanner. Een overzicht van PET-detectoren wordt voorgesteld in hoofdstuk 3.

Van bij het begin werden de PET-detectoren bijna uitsluitend opgebouwd uit gepixelleerde scintillatiekristallen gekoppeld aan fotomultiplicatie-buizen (PMT's). Dankzij recente ontwikkelingen op het gebied van fotosensoren en halfgeleidertechnologie, kwamen nieuwe types fotosensoren op de markt die gebruikt kunnen worden voor de ontwikkeling van PET-detectoren. De meest recente van deze nieuwe sensoren zijn silicium fotomultiplicatoren (SiPM's). Vergeleken met de klassieke PMT's hebben SiPM's een aantal karakteristieken die enkele voordelen met betrekking tot performantie hebben. Ze zijn dan ook veelbelovend voor de ontwikkeling van nieuwe en betere PET-detectoren in vergelijking met detectoren gebaseerd op PMT's.

In deze thesis stellen we enkele nieuwe PET-detectoren voor die ontwikkeld werden op basis van het nieuwste type SiPM's, namelijk de digitale SiPM (dSiPM). De voorgestelde detectoren werden ontwikkeld met het oog op hoge-resolutie PET. De detectorontwerpen leggen dus de nadruk op een hoge spatiale resolutie en voldoende hoge sensitiviteit. In het eerste deel van deze thesis onderzoeken we detectoren voor klinische PET-systemen, meer bepaald de systemen voor het in beeld brengen van het gehele menselijke lichaam. Deze detectoren zijn ontworpen om een hoge spatiale resolutie te bereiken en tegelijk hebben ze een goede tijdsresolutie. Dit laat toe om *time-of-flight* metingen te introduceren in het PET-systeem. In het tweede deel focussen we op de ontwikkeling van PET-detectoren voor preklinische systemen, bedoeld voor muizen en ratten. Om een sub-millimeter resolutie te bereiken, onderzoeken we detectoren gebaseerd op monolithische scintillatorkristallen als alternatief voor de gepixelleerde detectoren.

In hoofdstuk 4 hebben we een hoge-resolutie PET-detector ontwikkeld op basis van een dSiPM en een gepixelleerde LYSO scintillator bestaande uit pixels met een breedte van 2 mm. Deze detector is bedoeld voor een hoge resolutie, *time-of-flight* PET-scanner die het volledige lichaam in beeld kan brengen. Twee verschillende detectorontwerpen zijn ontwikkeld en geëvalueerd. Het eerste ontwerp is gebaseerd op het klassieke detectorontwerp en bestaat uit een rooster van 15 bij 15 LYSO-kristallen, elk met een grootte van $2{\times}2{\times}22$ mm^3, die met behulp van een lichtgeleider aan een dSiPM sensor gekoppeld zijn. Met deze detector kan een goede gemiddelde energieresolutie van 14.5% bereikt worden en een tijdsresolutie van 376ps. Maar door het ontbreken van een 1 op 1 koppeling tussen de LYSO-kristallen en de dSiPM-pixels, door de aanwezigheid van *dark counts* en door het acquisitie schema van de dSiPM, heeft het klassieke detector ontwerp een slechte performantie wat betreft het telvermogen.

Daarom werd een tweede, geoptimaliseerde detector ontworpen en getest. Dit tweede ontwerp bestaat uit een rooster van 4 bij 4 LYSO-kristallen, die $1.9{\times}1.9{\times}22$ mm^3 groot zijn, en een speciale schikking van de reflectoren tussen de kristallen. Dit moet ervoor zorgen dat alle afzonderlijke kristallen goed onderscheiden kunnen worden. Opdat er een betere aansluiting zou zijn tussen de LYSO-kristallen en de actieve regio van een dSiPM-*die*, werden de LYSO-kristallen iets kleiner gemaakt. Deze een-op-een koppeling tussen de dSiPM-*die* en het LYSO-rooster zorgt ervoor dat het telvermogen sterk verbetert ten opzichte van het eerste ontwerp. Dankzij de afwezigheid van lichtdeling tussen de *dies*, kunnen we met het tweede ontwerp daarboven ook een betere tijdsresolutie van 295ps en een gemiddelde energieresolutie van 11% halen. Dit tweede ontwerp, gebaseerd op een speciale reflectorplaatsing, is dus optimaal, aangezien het betere resultaten oplevert dan het klassieke ontwerp met betrekking tot het telvermogen en zowel de tijdsresolutie als de energieresolutie.

De belangrijkste bron van ruis in een SiPM is de aanwezigheid van *dark counts*. Dit zijn valse signalen die in de SiPM zelf gegenereerd worden ten gevolge van thermische excitaties. Deze ruis is kenmerkend voor halfgeleider detectoren zoals SiPM's en dus niet aanwezig in PMT's. We hebben ondervonden dat de invloed van de *dark counts* op de telvermogen performantie een belangrijk probleem is van de dSiPM's. Daarom hebben we in hoofdstuk 5 gekwantificeerd hoeveel events er verloren gaan bij de verschillende dSiPM configuraties. We hebben ook richtlijnen opgesteld voor de optimale configuratie van verschillende detectorontwerpen en van verschillende toepassingen. De focus lag hierbij op het telvermogen en op toepassingen waarbij meerdere dSiPM-*dies* vereist zijn om een enkel event op te meten.

Alle huidige PET-systemen zijn gebaseerd op detectoren met gepixelleerde scintillator-roosters, waarbij de pixels van elkaar onderscheiden worden met reflecterend materiaal. De grootte van de pixels bepaalt hierbij de resolutie van de detector. Hoe kleiner de pixels, hoe beter de resolutie die bereikt kan worden. Anderzijds, met het verkleinen van de pixels wordt de hoeveelheid reflecterend materiaal groter. Dit resulteert in een verlaagde sensitiviteit van de detectoren. Daarom moet in gepixelleerde detectoren een afweging gemaakt worden tussen resolutie en sensitiviteit. Deze afweging is in het bijzonder problematisch in preklinische PET-systemen waar zowel hoge resolutie als hoge sensitiviteit gewenst zijn. Tevens is de productie van fijn gepixelleerde kristallen complex en duur. Daarom hebben we detectoren gebaseerd op monolithische (continue) scintillatorkristallen voorgesteld als een alternatief voor de gepixelleerde detectoren. Monolithische detectoren bieden een aantal voordelen tegenover de gepixelleerde. Dankzij de afwezigheid van reflecterend materiaal in de scintillator, kan een hogere sensitiviteit bereikt worden. Met monolithische kristallen kan men corrigeren voor de interactiediepte (*depth-of-interaction*) zonder dat bijkomende wijzigingen in het detectorontwerp nodig zijn. Ten slotte zijn monolithische kristallen makkelijker en goedkoper te produceren. Het nadeel van monolithische detectoren is het schatten van de interactiepositie van een gamma foton in het monolithische kristal. Dit is veel complexer dan bij gepixelleerde kristallen en daarom zijn gesofistikeerde positioneringsalgoritmen nodig als men de hoge resolutie wil bereiken met monolithische detectoren. Deze positioneringsalgoritmen hebben ook vaak tijdrovende kalibraties nodig.

In hoofdstuk 6 introduceren we de DigiPET, een prototype PET-scanner die zich toespitst op hoge resolutie hersenbeeldvorming bij muizen en ratten. De DigiPET is een *proof-of-concept* voor het gebruik van dunne, monolithische scintillatiekristallen in PET-detectoren om een sub-millimeter spatiale resolutie te bekomen voor preklinische beeldvorming. Dit systeem bestaat uit vier detectoren geplaatst in een vierkante opstelling om een zo groot mogelijke deel van het dier in beeld te brengen. Dankzij de combinatie van de dunne monolithische kristallen en het gebruikte MLE-positioneringsalgoritme, kan het DigiPET systeem een zeer goede *Full Width at Half Maximum* (FWHM) spatiale resolutie van 0.7 mm doorheen het volledige gezichtsveld bekomen. Dit is aanzienlijk beter dan de spatiale resolutie van huidige, commerciële preklinische PET-scanners. Daarnaast hebben we ook een ex vivo FDG-studie van rattenhersenen uitgevoerd die aantoonde dat het prototype ook geschikt is om realistische objecten in beeld te brengen.

Een nadeel van het ontwikkelde DigiPET prototype is de lage sensitiviteit gelinkt aan het lage stoppend vermogen voor 511 keV fotonen in enn 2 mm dik LYSO-kristal. Om deze beperking op de sensitiviteit op te heffen, hebben we het detectorontwerp verbeterd door gebruik te maken van een 5 mm dik LYSO-kristal. Dit werk wordt voorgesteld in hoofdstuk 7. Dankzij het gebruik van dit dikkere kristal werd de nominale sensitiviteit van de detector met een factor 2.21 verbeterd. Dit verhoogt de coïncidentiesensitiviteit met een factor groter dan 4. Om tegelijkertijd ook de sub-millimeter spatiale resolutie te behouden, werden nog enkele aanpassingen doorgevoerd aan de nieuwe detector, zoals wijzigingen aan de decodering van de interactiediepte, aan het kalibratieproces van de detector en aan het 3D event positioneringsalgoritme. Dankzij de aangebrachte wijzigingen, kan de nieuwe detector een intrinsieke spatiale resolutie van 0.6 mm FWHM bereiken in vergelijking met een 0.54 mm FWHM-resolutie bereikt met de detector met een 2 mm dik LYSO-kristal.

Tot slot hebben we in hoofdstuk 8, gebaseerd op het verbeterde detectorontwerp, een tweede versie van ons hoge-resolutie preklinisch PET-systeem ontwikkeld. De nieuwe DigiPET scanner bestaat uit zeven detectormodules geordend in een heptagonale ring. Dit geeft aanleiding tot een groter gezichtsveld, zodat het te scannen dier eenvoudiger kan gepositioneerd worden, en een hoger telvermogen door het hogere aantal detectoren. Met de tweede versie van de DigiPET kunnen we een gemiddelde spatiale resolutie van 0.9 mm FWHM bereiken. Dit is minder goed dan het eerdere ontwerp, maar het levert wel een verbeterde sensitiviteit. Desondanks presteert het nieuwe DigiPET ontwerp nog steeds significant beter dan huidige commerciële PET-systemen met betrekking tot spatiale resolutie. Om de beeldvormingsmogelijkheden van de nieuwe scanner aan te tonen, werd een micro-Derenzo fantoom gescand en een botscan van een muis uitgevoerd. In het gereconstrueerde beeld van het micro-Derenzo fantoom, konden alle staven met een diameter van 0.8 mm of groter duidelijk onderscheiden worden. De in vivo muisbeelden toonden daarnaast ook aan dat het systeem geschikt is om hoge resolutie beelden van realistische objecten op te nemen.

Chapter 1

Introduction

1.1 Research objectives

The work presented in this dissertation is focused on positron emission tomography (PET), particularly on the design of high-resolution PET detectors and systems.

Until recently, PET detectors were constructed almost exclusively using photomultiplier tubes (PMTs). However, with the recent progress in the field of photosensors and semiconductors, new types of photosensors suitable for PET detectors have become available. The most recent type of these new photosensors is silicon photomultiplier (SiPM). These devices provide high gain, a dynamic range, fast response and excellent timing properties, are insensitive to magnetic fields, operate at moderate bias voltages and are both compact and robust. These traits make them highly promising for developing new, better PET detectors that can surpass the older, PMT-based PET detectors in every aspect.

In fact, looking at the current trends in the research community and the number of works involving SiPM-based PET detectors and systems, the PET field is in a transition phase of switching its technology from mature but old PMTs to novel and highly promising SiPMs. The research community is constantly exploring to what extent it can exploit this new SiPM technology for developing improved PET detectors.

The research presented in this thesis focuses on one of the newest types of SiPMs, the digital SiPM (dSiPM), and the use of this novel photosensor for developing new types of PET detectors meant to provide high spatial resolution and adequate sensitivity suitable for high-resolution PET imaging.

Therefore, there are two primary objectives of this thesis. The first is to characterize the performance of the dSiPM and investigate the best ways for using them in PET detectors. The second is to use this obtained knowledge to develop new, high-performance PET detectors and PET imaging systems that will surpass the currently available PET technology.

1.2 Thesis outline

The research presented in this thesis is organized as follows. Chapter 2 provides an introduction to the PET imaging technique and presents its use in the clinical practice. The principles of PET imaging are discussed, followed by the explanation of the PET image reconstruction process. Subsequently, the effects that cause degradation of PET image quality are described. Next, the concept of Time of Flight PET is introduced and the evolution of PET imaging into multi-modal imaging techniques is discussed. Finally, the use of PET for small animal imaging in preclinical research is discussed together with the challenges of high resolution and high sensitivity in small animal PET imaging.

Chapter 3 presents an introduction to PET detectors. The performance characteristics of such detectors and their components are provided. The emphasis is on different types of photosensors suitable for PET detectors, particularly digital silicon photomultipliers (dSiPM). PET detectors dedicated to small animal imaging and PET detectors based on monolithic scintillator crystals are discussed separately in more detail.

In chapter 4, a high-resolution PET detector based on dSiPM and an LYSO matrix with a 2 mm pixel pitch is presented for a whole-body Time of Flight PET scanner. Two different detector designs are presented and evaluated. The first is based on the classical detector design consisting of a regular LYSO matrix coupled through a light-guide to the dSiPM photosensor. The second is based on the special arrangement of LYSO pixels and pixel reflectors optimized for providing an improved light sharing that allows better detector performance to be achieved. The performances of both detector designs in terms of energy resolution, coincidence resolving time, intrinsic spatial resolution and count rate performance are evaluated and compared.

In chapter 5, based on the findings described in the previous chapter, the influence of dark counts on dSiPM performance is investigated in detail. Emphasis is placed on the count rate capabilities of the dSiPM-based PET detector in the situation where multiple pixels of the dSiPM are needed to record a single gamma photon event. Based on our findings, an optimal configuration of dSiPMs is proposed.

Chapter 6 presents a concept of a dedicated, high-resolution small animal PET scanner based on thin scintillator crystals and dSiPMs. First, the architecture of the prototype scanner, which is called DigiPET, is described. The configuration of detectors and calibration procedure using maximum likelihood estimation (MLE) event positioning are also discussed. Next, the intrinsic performance of the scanner's detectors is evaluated in terms of energy resolution, coincidence resolving time and intrinsic spatial resolution. Finally, the performance of the entire DigiPET system is evaluated in terms of spatial resolution, sensitivity and image quality obtained with both phantom and rat brain imaging studies.

In chapter 7, an improved detector design for the DigiPET scanner is introduced. The aim of the improved detector is to overcome the intrinsic sensitivity limitation of the previous design and simultaneously maintain the sub-millimetre spatial resolution. This is achieved by replacing the 2 mm thick LYSO with 5 mm crystals, improving the calibration procedure together with the mean nearest neighbour (MNN) positioning method. Furthermore, we introduce depth of interaction (DOI) in the detector. In the second part of this chapter, the performance of the improved detector is evaluated, and the results in terms of energy resolution, timing resolution, intrinsic spatial resolution and DOI resolution are presented.

Chapter 8 presents an improved second version of the dedicated high-resolution small animal PET imaging scanner called DigiPET2. The design of the system and the results obtained with this scanner are presented. The new DigiPET2 system is based on the improved detector introduced in the previous chapter, has a larger field of view (FOV) and contains a dedicated cooling system. These features allow the limitation of the previous DigiPET prototype to be overcome. The spatial resolution of the system and the image quality using both phantom and animal studies are evaluated.

Finally, in chapter 9, a general overview of the most important results of the preceding chapters is discussed, conclusions are drawn, and an outlook for further possible research steps is given.

Chapter 2

Medical imaging

2.1 Introduction

Medical imaging refers to a number of techniques that allow for visualization of structures and processes in the human body. Medical imaging is a well-established and powerful tool that is used for diagnosis and follow up of therapy in modern medicine. It is also widely used for research purposes (e.g. for new drug development or for better understanding of the brain).

There are several different techniques (modalities) that are being used in medical imaging. Each of these techniques is based on a different physical principle. X-ray radiography and X-ray computed tomography (CT) are among the medical imaging modalities that are best known to the general public. Other medical imaging modalities commonly used in medical practice are ultrasound (US), magnetic resonance imaging (MRI), single photon emission computed tomography (SPECT) and positron emission tomography (PET). Examples of medical images from different modalities are presented in figure 2.1.

The different medical imaging modalities can be divided into two groups: anatomical imaging (also called structural imaging) and functional imaging. Anatomical imaging enables visualization of the anatomy of the patient's body. Radiography, most CT and MRI techniques and ultrasound belong to the anatomical imaging group. Radiography produces two-dimensional (2D) images of the attenuation of X-rays transmitted through the body. Because bone tissues have significantly higher attenuation than other tissue types, radiography is mostly used to image bone fractures. CT produces images of cross-sections of the body, which are obtained by acquiring transmission images at many different angles. From the series of such images acquired

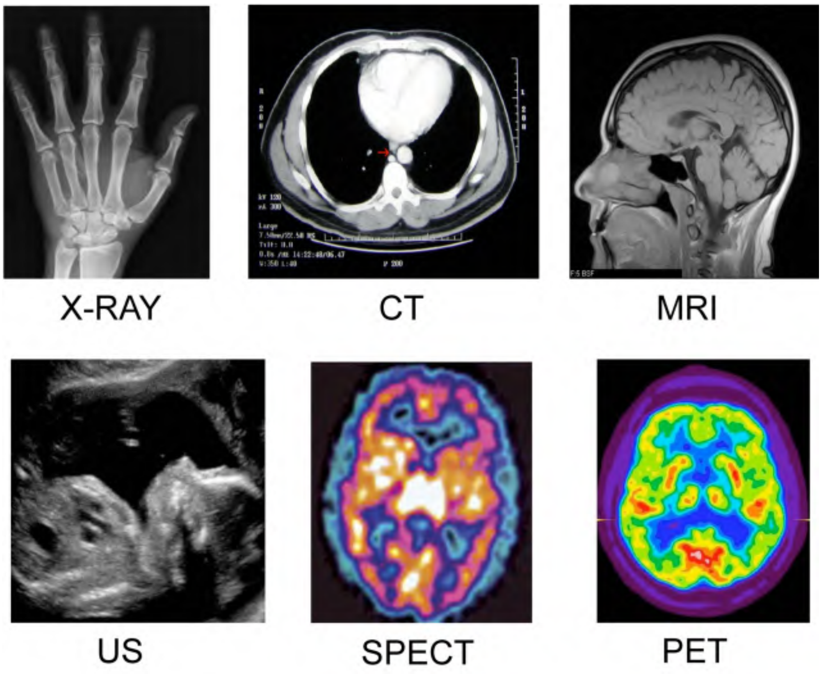

Figure 2.1: Images of different medical imaging modalities. Top row from left, an X-ray of a hand, a CT of a chest, an MRI of a head. Bottom row from left, an ultrasound of a foetus, a SPECT image of the brain, a PET image of a brain.

around a common axis of rotation, three-dimensional (3D) images of patient anatomy can be reconstructed. Such 3D CT images can be acquired within seconds. In both CT and radiography, a trade-off must be made between the radiation dose delivered to a patient and the obtained image quality. In addition, these techniques have relatively low soft tissue contrast compared to MRI. MRI is based on measuring proton spin density and relaxation times, which depend on the distribution of hydrogen molecules and the magnetic susceptibility of tissues. MRI achieves high resolution and high contrast, particularly for soft tissues. The drawbacks of MRI are its low sensitivity to molecular targets and the presence of strong magnetic fields, which prevents imaging patients with objects that are incompatible with magnetic fields such as prostheses and pacemakers. Ultrasound uses high-frequency acoustic pulses, which reflect at the boundaries between different tissues. By measuring the time delay and the intensity of the reflected pulses, an image of tissue interfaces within the body can be reconstructed. Ultrasound imaging is fast and does not deliver radiation to a patient. However, contact between the ultrasound device and the body is required, and interferences from bones need to be addressed. Furthermore, performing a whole-body scan is very difficult. Conversely, functional imaging allows visualization of the functional processes of the patient's body, such as metabolism or blood flow; in other words, it reveals how the patient's body is working. PET and SPECT both belong to functional imaging. Additionally, some techniques in MRI can be used to obtain functional information. In functional MRI (fMRI), haemoglobin can be used as a paramagnetic tracer, which allows, e.g., brain activation to be measured. Other examples of the MRI use for functional imaging are perfusion imaging via arterial spin labelling (ASL) or Diffusion Tensor Imaging (DTI) among others. One of the most important branches of functional imaging is nuclear medicine.

2.2 Nuclear Medicine

Nuclear medicine uses radio-tracers that target a specific function of the body or a specific organ. Visualization of the radio-tracer distribution provides information about a certain function of the body. PET and SPECT are the two main techniques in nuclear medicine.

As the names *positron emission tomography* and *single photon emission computed tomography* suggest, both PET and SPECT imaging are based on two principles: emission (of positrons or photons) and tomography. The word tomography is derived from two ancient Greek words: *tomos* (τόμος), which means 'slice, section', and *grapho* (γράφω), which means 'to write'. Thus, tomography refers to imaging the object's interior through sections or sectioning. Tomographic images are calculated from the measured projections of the object during a process called image reconstruction, which will be described in the next section of this chapter. Positrons (in PET) or gamma photons (in SPECT) are emitted from the radioactive decay of certain unstable isotopes.

PET and SPECT are based on the tracer principle. The tracer principle is based on the fact that molecules consisting of radioactive isotopes participate in physiological processes of the organism in almost the same way as molecules consisting of non-radioactive isotopes. Thus, radioactive isotopes can be used to mark substances and to track their flow and distribution in the body by detecting the radiation generated by these isotopes. Substances labelled with a radioactive compound used for medical imaging are called radio-tracers or radiopharmaceuticals. Multiple radio-tracers, which target different processes of the body's metabolism, have been developed, and research to develop new, target-specific radio-tracers is constantly ongoing. For example, in PET imaging, the fluorine-18 (^{18}F) fluorodeoxyglucose (FDG) [90] is commonly used in oncology to detect cancer. SPECT imaging uses ^{99m}Tc-HMPAO (hexamethylpropylene amine oxime) to perform functional brain imaging by visualizing the cerebral blood flow.

PET and SPECT are also called molecular imaging. They are capable of imaging functional processes of the body at the molecular level, which allows very subtle metabolic changes to be detected. Moreover, both PET and SPECT allow for quantitative measurements. This is of great importance because the early detection of a disease in its initial phase is often critical for a successful treatment and patient survival.

The sensitivity of PET to molecular targets is $\sim 10^2$-10^3 higher than the sensitivity of SPECT due to the absence of a collimator, which is an integral part of SPECT scanners. PET also achieves higher resolution ($\sim$4 mm in current clinical systems) than SPECT (typically $\sim$10 mm in clinical systems). However, PET requires a nearby cyclotron for the production of short-lived positron radio-tracers, whereas SPECT can use different radio-tracers that do not have to be produced on-site.

As functional imaging modalities, PET and SPECT both suffer from a lack of anatomical information. Therefore, there is a trend in clinical practice for multi-modality imaging that combines functional and anatomical medical imaging. PET/CT, SPECT/CT and PET/MR provide images that combine high-resolution anatomical information (CT and MR) with quantitative functional information (PET and SPECT). These fused images translate into better diagnoses. The benefits of such multi-modality approaches have been demonstrated by PET/CT in cancer diagnosis and therapy [20]. The anatomical images of CT and MR are also used to derive the body attenuation coefficient, which can be used to correct for the effect of the attenuation of gamma-rays within the patient's body [102], [98]. In addition, the anatomical information obtained from CT or MR images can be used to improve the quality of PET and SPECT images.

2.3 Preclinical imaging

As previously mentioned, medical imaging techniques are also widely used for research purposes. Over the past two decades, the field of biomedical research has experienced a rapid increase in the use of small animal models, mostly mice and rats, to study diseases, evaluate therapies or study the biodistribution of new drugs [75], [83], [126], [209], [183], [91], [125], [5].

In vivo studies are important because they allow a disease to be studied in its true, natural biological state, including regulatory and feedback mechanisms, such as the immune and circulatory systems. Due to the size of the body and organs associated with the animals used in these studies, dedicated high-resolution imaging systems of the previously described clinical modalities were developed. To distinguish the use of medical imaging for human diagnosis and treatment from the use for research purposes, the former is commonly referred to as clinical imaging and the latter as preclinical imaging.

2.4 Positron Emission Tomography

This dissertation focuses on new detectors for positron emission tomography (PET). An image of a clinical whole-body PET scanner is presented in figure 2.2.

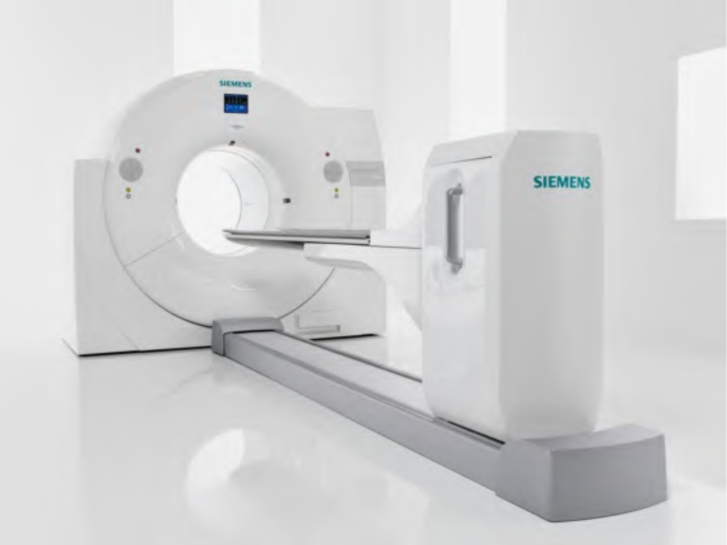

Figure 2.2: Modern clinical whole-body PET/CT scanner - Siemens Biograph mCT Flow. In front of the scanner there is a patient bed that slides the patient into PET/CT ring during a scan.

As mentioned previously, PET is a molecular imaging modality that enables *in vivo* visualization of biological processes of the living body without disturbing such processes. For example, for certain disease types, changes in functional processes occur prior to any anatomical change in the body.

Therefore, PET imaging can detect and diagnose a disease in its early stage when treatment has the highest chance of success. A primary advantage of PET over other medical imaging modalities is its high sensitivity. PET is capable of detecting very small changes in radio-tracer concentrations within the body: it can detect changes in biological processes at the pico-molar level. PET is thus a powerful tool for both clinical and research use because it can detect even a very subtle change.

2.4.1 Clinical applications

Today, PET is a well-established medical imaging modality that is widely used in clinical practice. The most important application of clinical PET imaging is in oncology [103], [51]. The primary objectives of oncologic PET imaging are lesion detection, lesion characterization (differentiating between benign and malignant tumours), staging of malignant lesions, assessment of therapeutic response and detection of recurrent disease. FDG, which allows visualization of glucose metabolism in the body, became widely used for oncologic applications because malignant cells have a higher rate of glucose consumption. However, there is a large number of other radio-tracers that can target different physiological processes. To list just a few such radio-tracers, 3'-deoxy-3'-fluorothymidine (^{18}F-FTL) allows visualization of cell proliferation [80], fluoromisonidazole (^{18}FMISO) allows visualization of cell hypoxia [159], 16α-fluoro-17β-estradiol (FES) targets estrogen receptors that are correlated to 70% of breast cancer types [17], and 21-fluoro-16α-ethyl-norprogesterone (FENP) and 4-fluoropropyl-tanaproget (FPTP) target progesterone receptors [56], [216].

In addition to oncology, PET imaging has also become a useful tool in the diagnosis of cardiovascular diseases. Cardiac PET allows for the assessment of the glucose metabolism and, through dynamic quantitative imaging (series of images showing the temporal uptake of tracer), blood flow of the myocardium. It also allows for the assessment of the risk of developing cardiac disorders, such as coronary artery disease or myocardial viability [103], [99]. For cardiac PET imaging, ^{82}Rb, a potassium analogue, and ^{13}N labelled ammonia radio-tracers are typically used for myocardium perfusion visualization, while ^{18}FDG is used to diagnose coronary artery disease.

Neurology and Neuroscience are another important clinical fields where PET is widely used. Brain activity can be assessed by measuring the amount of oxygen-rich blood flow in various regions of the brain following the administration of ^{15}O-labelled dihydrogen oxide radio-tracer to a patient. However, the ^{15}O isotope has a very short half-life of 2.03 minutes, which requires this isotope to be produced very close to the scanner. ^{18}FDG is commonly used in assessing brain activity because the brain also uses glucose for its metabolism and because more active regions will have a higher demand for glucose and a higher concentration of the radio-tracer within them. Amyloid tracers, such as ^{11}C labelled Pittsburgh compound B (11C-PiB) or ^{18}F labelled FDDNP, allow for visualization of amyloid plaques in the patient's brain. With these amyloid tracers, PET allows for the early diagnosis of Alzheimer's disease (AD) through the detection of the increased concentration of amyloid plaques, which are the main pathological hallmarks of AD [161], [149]. PET also allows for the early diagnosis of Parkinson's disease: ^{18}F-DOPA and ^{18}FDG PET scans enable detection of the loss of dopaminergic neurons in the *substantia nigra* caused by this disease [24]. Another example of the application of PET in neurology is the early detection of Huntington's disease, which can be diagnosed many years before the first neurologic or psychiatric symptoms appear [84], [64]. While ^{18}F-FET (flour ethyl tyrosine) PET is used in neuro-oncology for imaging of Gliomas, which are malignant tumours of the glial tissue of the nervous system. Furthermore, PET offers also a unique *in vivo* tool for Neuroscience to study the bio-distribution of neurotransmitters, neuro-receptors and other metabolites under different conditions.

In addition to these examples, PET is routinely used in many other clinical applications, such as thyroid imaging and therapy [163], [142], kidney imaging [21], [178], bone imaging [121], [86] and lung imaging (e.g., mediastinal disease) [52].

2.4.2 PET imaging principles

PET uses radio-tracers that are labelled with isotopes that undergo β^+ decay. During β^+ decay, a proton p in an unstable nucleus is converted into a neutron n and a positron (β^+) and a neutrino (ν_e) are emitted:

$$p \longrightarrow n + \beta^+ + \nu_e + E_k \tag{2.1}$$

The radioactive isotopes that are currently used for PET imaging are listed in table 2.1.

The radio-tracer is typically delivered to a patient via an intravenous injection. Then, the radio-tracer is distributed within the body over time and accumulates in the targeted tissues. The radio-tracer decays, emitting positrons with a certain kinetic energy (E_k). This yields a continuous spectrum with a maximum that depends on the type of isotope. The emitted

Table 2.1: List of positron-emitting isotopes used for PET with their maximum energy, half-life, mean free path and production method.

Nuclide	E_{max} (MeV)	$t_{1/2}$ (min)	Mean range in water (mm)	Source
^{11}C	0.959	20	1.1	On-site cyclotron
^{13}N	1.197	11	1.5	On-site cyclotron
^{15}O	1.738	2	2.5	On-site cyclotron
^{18}F	0.633	110	0.6	Regional cyclotron
^{68}Ga	1.898	68	2.9	^{68}Ge/Ga generator
^{89}Zr	0.4	4710	1.2	Regional cyclotron
^{82}Rb	3.4	1.25	5.9	^{82}Sr/Rb generator

positrons propagate through the surrounding material and undergo scattering interactions. Through these scattering interactions, the positron loses its kinetic energy and changes its direction of propagation. After the positron has lost sufficient kinetic energy, it annihilates with an electron from the surrounding tissue. The positron range depends on the initial energy; e.g., it is approximately 0.6 millimetres for ^{18}F. During the annihilation process, exactly two photons are simultaneously created, each with an energy of exactly 511 keV. Due to the rule of the conservation of momentum, these two 511 keV photons are emitted almost exactly in opposite directions. This process is illustrated in figure 2.3. The annihilation photons have an energy of exactly 511 keV and are emitted almost exactly 180° apart.

After injection of the radio-tracer and after some time to allow the radio-tracer to be distributed and accumulated in the patient's body, the patient is placed in a PET scanner that consists of multiple rings of radiation detectors that surround the patient. The detectors, which are fundamental components of a PET scanner, are described in detail in chapter 3. The emitted 511 keV photons are then detected by opposing detectors. If two photons of the appropriate energy (511 keV) are detected within a certain amount of time, called the coincidence time window, it is assumed that these two detected photons originate from the same annihilation and that the annihilation occurred somewhere along the line connecting the two detectors. This coincidence detection of the pair of annihilation photons defines a line of response (LOR): a line along which the annihilation occurred and along which the radio-tracer, the source of positrons, was located. The detection of pairs of 511 keV photons and the construction of LORs is illustrated in figure 2.3. After measuring a large number of such LORs, a tomographic PET image can be reconstructed that visualizes the distribution and concentration of radio-tracer within the patient's body.

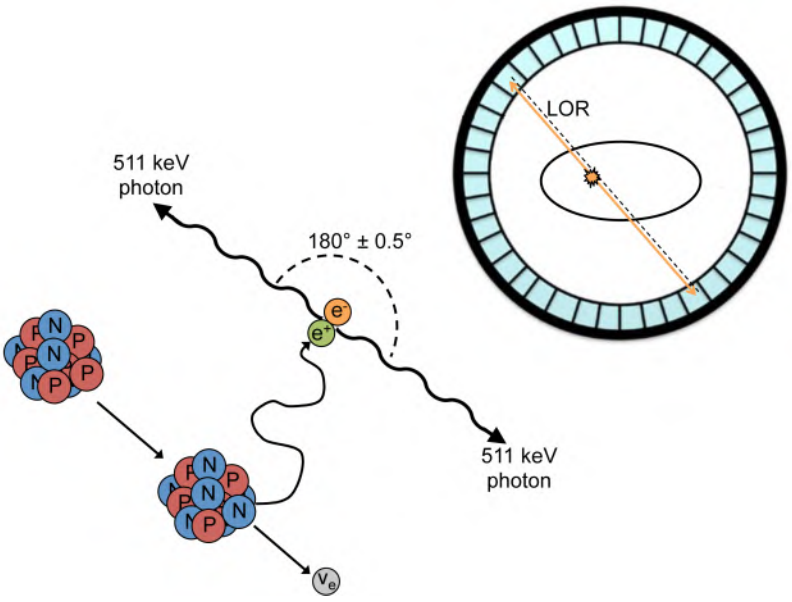

Figure 2.3: Imaging principle of PET: positron emission from unstable nucleus, annihilation of a positron and emission of two back-to-back 511 keV photons and construction of an LOR from the detected 511 keV photon pair.

2.4.3 PET image reconstruction

As mentioned in the previous section, PET images are reconstructed from many (10^6-10^8) LORs measured during a PET scan. Several methods have been developed to reconstruct LORs into a 3D image of the radio-tracer distribution within a patient's body. In general, these image reconstruction algorithms are categorized into two groups: analytical and iterative methods.

2.4.3.1 Analytical methods

Analytical methods are based on the principle that the distribution of the radio-tracer can be estimated from the measured LORs through a process called back-projection. Figure 2.4 illustrates how this process can be performed. Each acquired LOR is associated with a pair of detector coordinates. The activity that is 'seen' by each detector pair corresponds to the integrated activity of the radio-tracer along the LOR. By back-projecting each LOR into an image using the corresponding coordinates, an image of the distribution of the radio-tracer is obtained. In practice, back-projection is performed by placing a constant value into the image voxels along the back-projected LOR. The intensity value for an individual image voxel is obtained by integrating over all LORs that intersect the voxel. However, a simple back-projection does not provide a correct reconstruction. The simple back-projection results in a blurring of the reconstructed image. It can be shown that this blurring is equivalent to a convolution of the image with a point spread function $h(x, y) = (x^2 + y^2)^{-1/2}$. To solve this problem, the filtered back-projection (FBP) method was introduced [101], [213]. FBP is based on the Fourier slice theorem and uses a ramp filter to filter projection data prior to performing back-projection. This removes image blurring and the shape of the filter, and its cut-off frequencies determine the noise level and resolution in the reconstructed image.

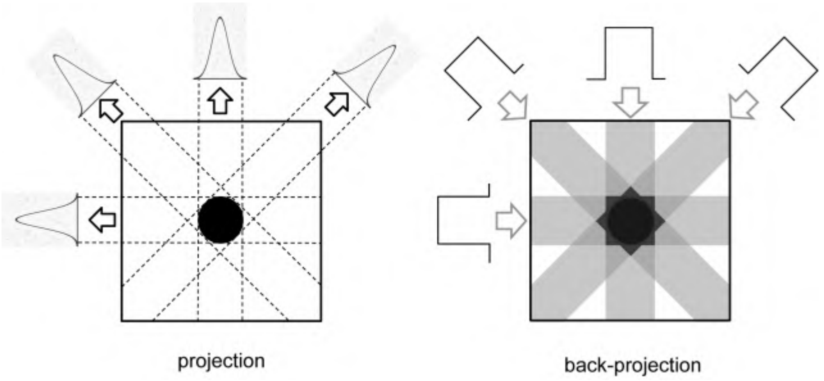

Figure 2.4: Acquisition of projections of an object and back-projection of the projections into image space.

Although the analytical methods are rapid and relatively easy to implement, they are based on a simplified model of photon detection physics. These methods do not account for the real resolution of the detector or various image degradation effects, such as random coincidences, scattering and attenuation of photons within patient's body. Furthermore, back-projection methods require a uniform angular sampling of the projections. These factors lead to a degradation of image quality and amplification of noise in the reconstructed image.

2.4.3.2 Iterative methods

To overcome the limitations of the analytical algorithms, iterative algorithms have been developed [158]. The principle of iterative algorithms is to find the distribution of radio-tracer given the measured data, information about the architecture of the PET system and statistical models related to the data acquisition process. Furthermore, models for the attenuation and scattering of annihilation photons, limited spatial sampling or detector-related effects can be included. Iterative reconstruction begins with an initial estimation of the radio-tracer distribution (typically a uniform image). Then, all projections of this estimated distribution are calculated (by forward-projection) using a model of the data acquisition process. These estimated projections are then compared with the measured ones, and the estimated image of the radio-tracer distribution is updated according to a selected cost function (discrepancies) between the forward-projection and the acquired data. The typical steps are forward projecting the image, comparing the projections with measured data and updating the estimated image. These steps are repeated (iterated) until convergence of the cost function is reached. An example of an iterative algorithm can be maximum likelihood expectation maximization (MLEM) [177],[59].

The combination of a statistical model and knowledge of the data acquisition process leads to improved image quality. However, iterative algorithms are more expensive in terms of computation costs and reconstruction time compared to analytical algorithms. Historically, due to computational power limitations, analytical methods such as FBP were widely used. However, with faster computers, iterative algorithms are currently used for reconstructing PET images. Examples of popular iterative algorithms that are commonly used for PET image reconstruction are ordered subset expectation maximization (OSEM) [88] and maximum a posteriori (MAP-EM) [116]. Continuous efforts are devoted to improving existing algorithms and developing new, better ones.

However, it is important to remember that the image reconstruction is an ill-posed problem. This means that small changes in the measured data can lead to unpredictable changes in the reconstructed image. In practice, it means that due to the presence of statistical noise introduced by the stochastic nature of the photon decay, no exact image reconstruction is possible and some level of noise is always present in the reconstructed image. Therefore, some type of regularization is required to reduce the noise and constrain the reconstructed image to physically acceptable values. The most common type of regularizing image reconstruction is simple smoothing. In the FBP algorithm, this is performed by applying a window function to the ramp filter. The smoothing reduces the noise in reconstructed images but causes the undesirable side effect of increased blurring in the image. In the iterative algorithms, the regularization can be performed using different methods. The iterative algorithms based solely on maximum-likelihood criteria produce images that become unacceptably noisy as the iterations proceed. Therefore, one method for regularization is to stop the iteration before the images become too noisy (long before convergence) [210]. The smoothing approach can also be used for the iterative algorithms. Iterations are continued until convergence, followed by post-smoothing of the image [182]. Alternatively, smooth basis functions can be used [118]. Finally, the maximum-likelihood criterion can be replaced with a penalized-likelihood (or maximum a posteriori) objective function that includes a roughness penalty to encourage image smoothness [106]. Compared to other regularization methods, the penalized-likelihood has two major advantages over the other methods. First, the penalty function improves the conditioning of the reconstruction problem, and thus, certain iterative algorithms converge very quickly. Second, the penalty function can be chosen to control the desired properties of the reconstructed images, such as preserving edges [106] or incorporating anatomical information [70].

2.4.4 PET image quality

The quality of PET images is determined by two factors: spatial resolution and signal-to-noise ratio (SNR). An overview of the effects that determine these two factors is presented in this section.

2.4.4.1 Spatial resolution

The spatial resolution of the image is defined as the size of spatial features in the image that can be distinguished and resolved from each other. The spatial resolution depends on a number of different factors. These factors range from the physical properties of positron emission and radiation detection to the design of PET detectors and scanners. Another factor that influences spatial resolution is the image reconstruction method used.

The resolution of PET images is intrinsically limited by the positron range. As mentioned in the previous section (see 2.4.2), after emission, a positron travels a certain distance in which undergoes scattering and direction changes before it annihilates with an electron. This distance depends on the initial energy of the positron, which in turn depends on the type of isotope and the material in which the positron propagates. The finite distance that the positron travels inherently limits the resolution of PET images. This results in a blurring effect in the reconstructed images. The full width at half maximum (FWHM) of the blurring profile for different isotopes is given in table 2.2.

Table 2.2: Positron range in water, FWHM in mm, for different isotopes used for PET imaging [Raylman et al 1992, Bailey 1996].

Isotope	^{15}O	^{13}N	^{11}C	^{18}F	^{82}Rb	^{68}Ga
FWHM in mm	2.5	1.5	1.1	0.6	5.9	2.9

Another factor that has an influence on spatial resolution is the acollinearity of two annihilation photons. As mentioned in the previous section (see 2.4.2), these two photons are emitted in almost opposite directions. However, when a positron annihilates with an electron, their combined center of mass may still have a residual momentum. Because the momentum is preserved during the annihilation, a slight deviation from the exact 180° angle between the paths of the two annihilation photons may occur. This angular uncertainty results in a blurring in the reconstructed image, which increases with the diameter of the detector ring. The relation between the scanner diameter and blurring in the image can be estimated as $R_{acollinearity} \approx 0.0022 \cdot D_{scanner}$. Thus, for a clinical PET scanner with a ring diameter of 90 cm, the acollinearity causes resolution blurring of approximately 2 mm FWHM.

All of the described effects that have an impact on the spatial resolution of PET images are related to the fundamental radiation physics involved in PET. However, the dominant factor that determines the spatial resolution of PET is the intrinsic resolution of the detectors. The majority of current PET scanners are based on detectors that contain arrays of individual scintillator crystals (see chapter 3). The size of these crystals has a dominant influence on spatial resolution. The measured interaction position is limited only to the information in which crystal the detection occurred and not where exactly in the crystal. Thus the smaller crystals, the more precisely the place of the interaction can be defined.

The uncertainty of exactly at which depth within the individual crystal the annihilation photon was detected causes another resolution-limiting effect, which is called the parallax error. The scintillator crystals used in PET need to be relatively thick to have sufficient stopping power (see chapter 3). When an annihilation photon interacts within an individual crystal of the detector, the PET system assigns a single point of photon interaction to this crystal, which is typically at the center of the crystal. However, for photons that enter the crystals at an oblique angle, such assignment may be incorrect and this results in a mispositioning of the LOR. This in turn results in radial blurring in the reconstructed PET images at off-center positions. The parallax error can be reduced by measuring the depth of interaction (DOI) in a PET detector. The DOI allows for the determination of the depth at which the interaction occurred; thus, the LOR position can be defined more precisely. Reducing the size of the crystal while retaining its thickness results in longer, thinner crystals. This results in the increased effect of the parallax error, because the thinner crystals, the higher probability of photons interacting at other crystals (see figure 2.5). However, the DOI information can partially compensate for this effect and preserve high and uniform spatial resolution.

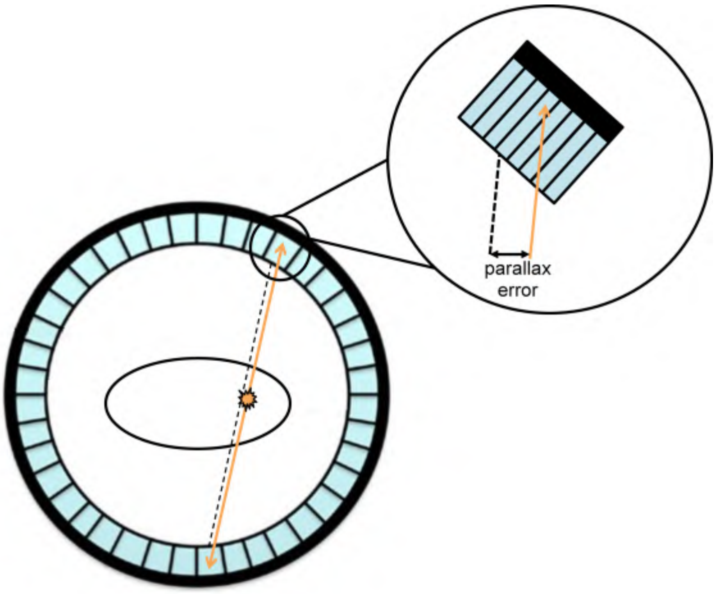

Figure 2.5: Illustration of the parallax error. Without DOI information errors in LOR positioning may occur for gamma photons incident at oblique angles.

2.4.4.2 Sensitivity

PET imaging is inherently influenced by Poisson statistics because it is based on radioactive decay (random process). To reduce the effect of statistical fluctuations on the quality of the reconstructed images, it is important to acquire as many coincidence events (measured LORs) as possible. The more data that are acquired at the same time, the smaller the impact that the statistical fluctuations will have on image quality and the higher the signal-to-noise ratio (SNR) will be. The SNR determines the accuracy of the estimated concentration of the radio-tracer in the voxels of the reconstructed images. A high SNR is particularly important for high-resolution PET, where image voxels are smaller and visualization of low concentrations of radio-tracer with high accuracy is required. However, the use of small voxels requires a large number of events. If the SNR is not sufficiently high, it is impractical to reconstruct the image with smaller voxels. Otherwise, the uncertainty of the radio-tracer distribution in an image would be too high rendering the reconstructed image unfit for diagnostic purposes. Without sufficient number of registered events, larger voxels need to be used. However, larger voxels limit the accuracy with which the concentration of radio-tracer can be represented in the image. Therefore, even when the detector employed in the PET scanner theoretically allows for better spatial resolution, the use of larger voxels for sufficient SNR prevents from reaching it.

The sensitivity of a PET scanner is defined as the ratio of the number of coincidence events detected per second from a particular volume and the true number of radioactive decays per second in the same volume. A high-sensitivity scanner collects more coincidences in a fixed amount of time, thereby improving the SNR and the quality of reconstructed PET images. A high sensitivity of the PET scanner can be achieved by improving the detection efficiency of the detectors (see chapter 3) and/or by increasing the solid angle coverage of the scanner's field of view (FOV).

2.4.4.3 True, random and scatter coincidences

From an SNR perspective, it is always desirable to acquire a large number of coincidences. However, there are different types of coincidences that can be detected in PET scanners. Coincidence events can be divided into three types: true, scatter and random. A true coincidence is when both 511 keV photons emitted from a single positron annihilation process are detected in two opposite detectors of the PET ring without undergoing Compton scatter. When one or both 511 keV photons undergo Compton scatter before being detected in a detector, it is a scattered coincidence. A random coincidence occurs when two photons that originated from two different annihilation processes are detected close enough in time for the PET scanner electronics to recognize them as a coincidence event. This scenario may occur when two annihilation processes occur almost simultaneously and one photon from each annihilation process is detected while the other is not. The three types of coincidence events are illustrated in figure 2.6.

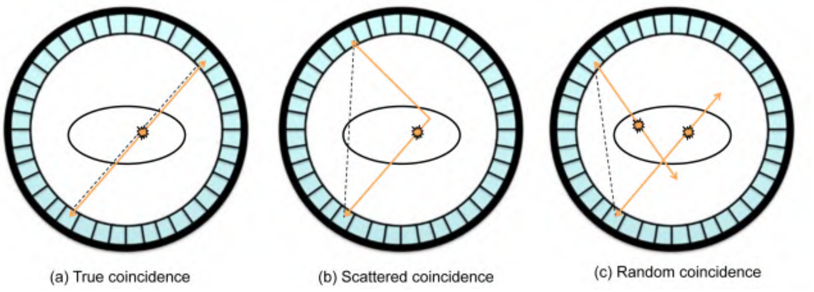
(a) True coincidence (b) Scattered coincidence (c) Random coincidence

Figure 2.6: Different types of coincidences possible in PET.

From the three coincidence types, only true events are useful, and collecting a large number of these events improves the SNR and quality of reconstructed PET images. Scattered and random coincidences are not desired because they lead to the wrong assignment of LORs and result in a reduction of the SNR and degradation of the image quality. In particular, in whole-body 3D PET imaging, the scattered coincidences can become a very large fraction of the detected events, leading to significant reduction in the SNR [42], [10]. A PET scanner should be able to limit the number of detected scattered and random coincidences and correct for them to prevent degradation of PET images. The ability of a PET scanner to distinguish between true, scattered and random events at a certain activity rate is characterized by the noise equivalent count rate (NECR) [12], [108] defined as:

$$NECR = \frac{T^2}{T + S + kR} \tag{2.2}$$

where T, S and R are the true, scattered and random coincidence count rates, respectively. k is a factor that depends on the method used for the correction of random events. The count rates of true, scattered and random coincidences depend on the activity of the delivered radio-tracer, on the subject and on the PET system.

The values of T, S and R are determined by performing a series of measurements of a dedicated phantom filled with a decaying radioactive source (e.g., solution of radio-tracer). Through regular measurements taken while the activity in the phantom decays over several half-lives and analysing the acquired event rates as described in the NEMA NU 2 standard [9], one can derive the values of T, S and R.

NECR is equivalent to the coincidence count rate that would have the same noise properties as the measured true coincidence count rate after correcting for random and scatter coincidences. NECR is a good indicator of image quality since the squared root of the NECR is proportional to the image SNR [188]. A larger NECR indicates a higher ratio of true coincidences to the overall detected coincidences which include randoms and scatters. The NECR typically increases up to a maximum with increasing of activity inside the FOV. Then, the NECR decreases as the random coincidence rate increases quadratically with activity, while the true coincidence rate increases linearly in the absence of dead time losses. This means that above some activity level, the image quality decreases because randoms and scatters start to dominate over true coincidences. Thus, the NECR is useful for determining the maximum useful activity for a particular scanner.

Attenuation

After positron annihilation, the emitted 511 keV photons travel through the patient's tissue before they reach the detectors. During propagation, there is a possibility that the photons will interact with the surrounding tissue. The photons can interact through Compton scattering or through the photoelectric effect. In Compton scattering, the photon loses part of its energy and changes its direction of propagation. In the photoelectric effect, the photon is absorbed. Thus, only a limited fraction of the emitted annihilation photons will reach the detectors. This effect is known as attenuation. Different tissues attenuate photons with different strengths. This attenuation strength is characterized by the attenuation coefficient μ, which depends on the tissue (its electron density) and the energy of the photon that propagates through it. A fraction of the photons that propagate through a homogeneous material of thickness l without interaction is given by:

$$F = e^{-\mu l} \tag{2.3}$$

Equation 2.3 indicates that photons emitted from deeper inside a patient's body have a lower probability of reaching the detectors. This results in a smaller number of detected coincidences from this region of the body. The attenuation effect can be corrected in image reconstruction if information about the attenuation coefficients of the patient's body is provided to the reconstruction algorithm. The attenuation map of the patient's body is typically obtained from a CT scan that accompanies the PET scan (see section 2.4.6) [20], [102], [11]. Examples of PET images of a patient's body reconstructed with and without attenuation correction are shown in figure 2.7. It can be observed that in the image without attenuation correction, the interior of the body is of lower intensity and organs are not as clearly visible as in the image with the correction, where the structures within the body's interior can be clearly distinguished.

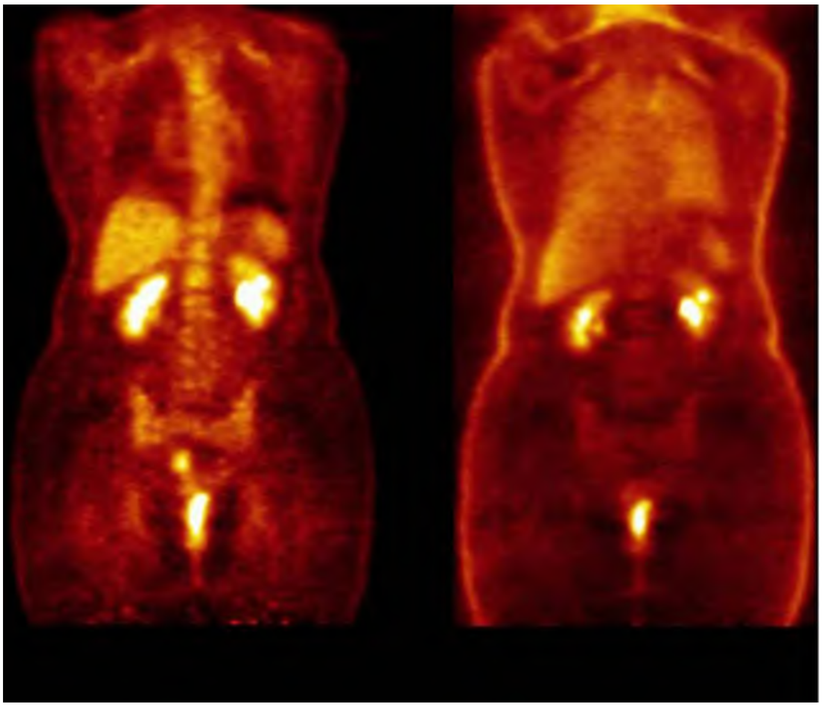

Figure 2.7: Attenuation-corrected (AC) PET image (left) and non-attenuation-corrected (NAC) PET image (right) of a patient's body. In the NAC image, the body interior is blurred and organs are not clearly visible nor distinguishable. In the AC image, the structures of body interior are much clearer.

2.4.5 Time-of-Flight PET

In a conventional PET scanner, the exact location of the annihilation along the LOR is unknown. The only available information is that the annihilation occurred somewhere along the LOR, and all positions along the LOR are assumed equally probable. Time-of-flight (TOF) PET measures the difference in the arrival times of the two 511 keV photons at both detectors to estimate the location along the LOR where the annihilation occurred. This estimation allows for modification of the probability of occurrence of the annihilation process along the LOR and assigns modified weights to voxel values in the reconstructed image. The time difference Δt is directly related to the distance d from the center of the LOR to the position of the positron annihilation:

$$d = c\frac{\Delta t}{2} \tag{2.4}$$

where c is the speed of light. However, to be able to implement the time-of-flight concept in a PET scanner, PET detectors need to measure the arrival times of photons with high precision. The higher the precision, the more accurate is the estimation. The precision with which a detector is able to measure the arrival time of the photon is characterized by the timing resolution $\Delta\tau$. The full width at half maximum (FWHM) is the spatial equivalent of the distribution of time differences Δt:

$$FWHM = c\frac{\Delta\tau}{2} \tag{2.5}$$

The principle of TOF PET is illustrated in figure 2.8.

The concept of TOF PET was recognized as early as the 1960s [8], [25], [30]. Nonetheless, the first TOF PET scanners were developed only during the 1980s [198], [199], [76] [214], [117], [135] thanks to the progress in detector technologies that allowed arrival times to be measured with sufficient accuracy. The first systems achieved timing resolution in the range of 450-750 ps. However, due to the scintillators used (CsF and BaF_2), these systems had poor spatial resolution and poor sensitivity, thereby making the initial TOF PET systems not competitive with non-TOF PET scanners with BGO scintillators. Only with the development of new scintillators in the 1990s (e.g., LSO and LYSO) was a new generation of TOF PET scanners with satisfactory overall performance developed [192], [97]. The first commercially available PET scanner was introduced by Philips in 2006 [189]. Current TOF PET scanners achieve timing resolution between 400 and 600 ps, which allows the annihilation location to be estimated with a precision of approximately 7.5 to 9 cm. With the recent progress in the field of photodetectors and scintillators, detectors with a timing resolution of 200 to 400 ps were reported by different research groups [203], [185], [141], [113], and in

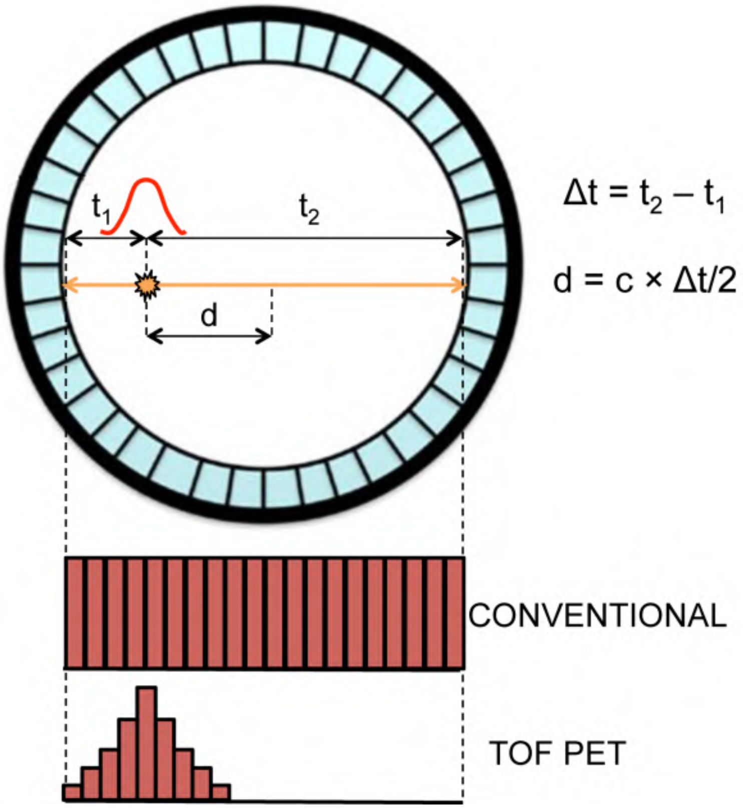

Figure 2.8: The TOF PET principle. The time-of-flight difference Δt is related to the distance $d = c\dfrac{\Delta t}{2}$ from the centre of the LOR to the annihilation. During reconstruction of the image, the activity is attributed only to those voxels along the LOR that are close to the estimated voxel in which annihilation took place.

some cases, an event timing resolution of approximately 100 ps was reported [166]. The TOF effect on the SNR is proportional to the FWHM gain and is larger in larger objects.

A significant improvement in the quality of PET images achieved with the TOF PET, particularly for oncology, was shown in a number of studies [97], [48], [65]. An increase of the effective SNR by a factor of $\sim$2.1 was reported for a TOF PET scanner with a coincidence resolving time (CRT) of 600 ps [189], [93], and the highest gains in image quality were reported for larger patients and for low contrast lesions [65].

An example of the superiority of TOF PET over conventional PET for clinical imaging is shown in figure 2.9, which shows a patient with non-Hodgkin's lymphoma. The small lesions are more visible and easier to distinguish in TOF PET images.

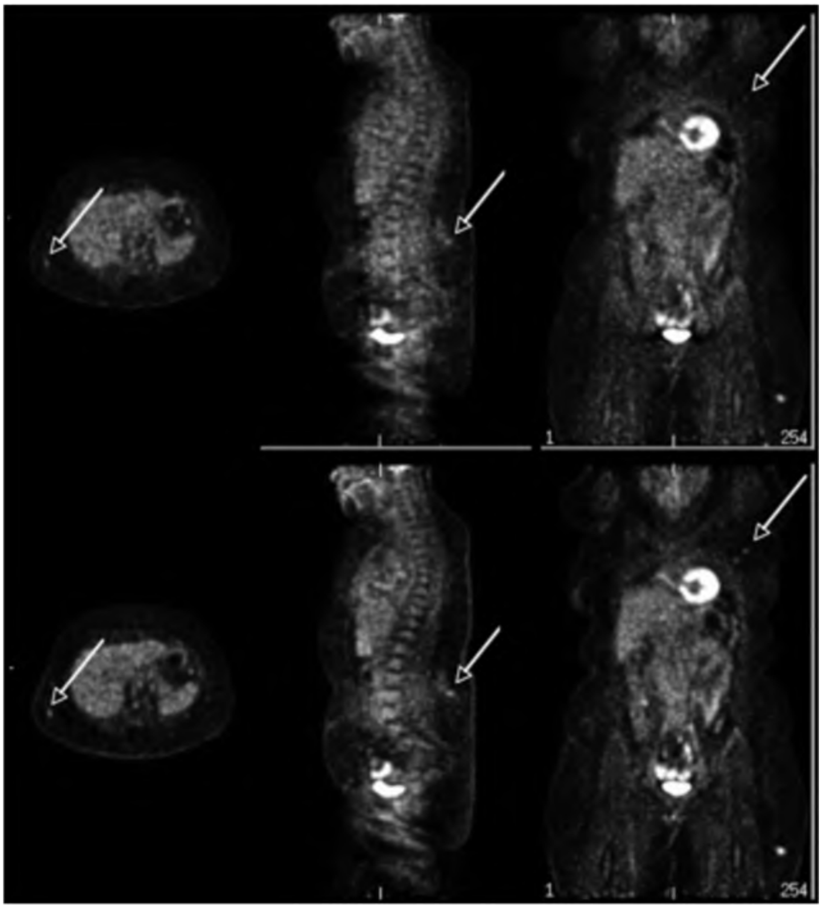

Figure 2.9: Patient with non-Hodgkins lymphoma (140 kg, BMI = 46). Representative transverse, sagittal, and coronal images (not triangulated) for non-TOF reconstruction (top) and the same cross-sectional images for TOF reconstruction (bottom). In each image, the different lesions are seen more clearly in TOF reconstruction than in non-TOF reconstruction. Research originally published in JNM [97]. Reprinted with permission.

2.4.6 Multi-modality imaging

Multi-modality imaging involves combining different imaging modalities to provide improved diagnostic accuracy or to provide new visualization applications. In current clinical practice, anatomical imaging is combined with functional imaging because they complement each other and provide doctors with an overall overview of the patient's body and its functions. Initially, each imaging modality was acquired separately, and then the images were fused together using a dedicated co-registration software. Currently, multi-modal images are acquired with dedicated sequential imaging systems or with fully integrated imaging scanners that allow for almost simultaneous registration.

As a stand-alone imaging modality, PET suffers from a lack of anatomical information. The combination of PET images with the high-resolution anatomical images obtained using CT significantly improved diagnostic accuracy, particularly in oncological applications [15], [20], [168]. Furthermore, CT allows the attenuation coefficient map of the patient's body to be rapidly obtained. The usefulness and benefits of combined PET/CT imaging have been demonstrated; therefore, nearly all clinical PET scanners currently in use are PET/CT combinations, and almost 100 % of PET images are obtained as multi-modal PET/CT images. An example of a PET/CT image and how these two modalities complement each other is shown in figure 2.10. In this case, PET visualized intense uptake in the descending colon, corresponding to a soft tissue density that was not distinguishable from fecal contents by CT criteria. The CT image allows for positioning of the high uptake region in the identified anatomical location within the patient's body, which allowed for targeting of the region during an endoscopy.

MRI has high anatomical resolution, provides unsurpassed soft-tissue contrast [6], [202] and, compared with CT, does not deliver radiation dose to the patient. Furthermore, MRI provides complementary functional imaging capabilities. The lack of an extra radiation dose during the scan is particularly important for paediatric patients [23], [22]. Consequently, there is significant interest in the research community to develop multi-modal PET/MRI systems. An additional benefit of combining PET and MRI is the fact that these systems can be fully integrated into a single system. This allows for truly simultaneous acquisitions, which guarantee that both modality images are acquired in exactly the same arrangement of the patient's body and creates an opportunity for motion correction in PET images [36], [35], [46].

However, combining PET and MRI is not a trivial task [208]. PET detectors need to be compact and able to operate in strong magnetic fields. Furthermore, the two integrated modalities should not influence the performance of each other, which would result in degradation of the image quality. Recent developments have shown that MR-compatible PET detectors can

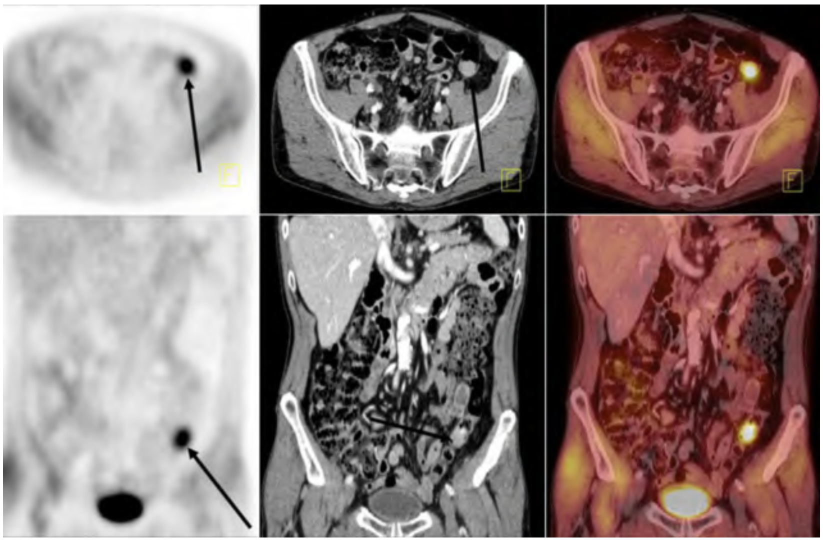

Figure 2.10: Axial (top) and coronal (bottom) images from PET/CT scan. PET images are on the left, CT images in the center, and PET/CT fusion images on the right. PET images show intense uptake in the descending colon corresponding to a soft tissue density that by CT criteria is not distinguishable from fecal contents. Endoscopy and subsequent surgery confirmed that this was an adenocarcinoma of the colon, in this case an incidental finding on a study performed for another indication. Reprinted with permission from Radiology Rounds [140]

be constructed, primarily due to new types of photosensors (see chapter 3) [79], [154], [66], [96], [170]. The first clinical whole-body PET/MRI scanners were introduced to the market by Siemens [58]. Despite these developments, there are still a number of technical issues, such as MR-based attenuation correction, that need to be resolved before the full potential of simultaneous PET/MRI can be achieved.

2.5 Small animal PET imaging

PET is also a commonly used tool in preclinical research for studying the molecular basis of diseases and guiding the development of new drugs and treatments [75], [83], [126], [209], [183], [91], [125], [5]. There are multiple reasons for the use of PET. First, PET allows for the non-invasive visualization and study of the cellular and molecular processes in living organisms. This allows for repeated and longitudinal studies of diseases in their natural biological state, including regulatory and feedback mechanisms, such as the immune and circulatory systems. Second, PET is capable of detecting concentrations of radio-tracers at the picomolar level, which makes PET capable of tracking subtle molecular changes. PET is also a well-established standard in clinical practice, which facilitates the translation of new preclinical discoveries into the clinic. However, PET systems face a number of challenges for their efficient use in preclinical research.

The major challenge is the size of the animals used in preclinical research. Efforts to develop animal models of diseases have concentrated on rodents, particularly mice. The mouse genome is very similar to that of humans and is relatively easy to manipulate. Mice are inexpensive, easy to breed, have a short life span and are small [40], [73], [179]. Consequently, more than 90% of preclinical studies currently use mouse models [129]. For neuroscience and neurosurgery research, rats are commonly used instead of mice because their brains are five times larger.

However, to clearly visualize and accurately quantify the biodistribution of a PET radio-tracer in mice and rats, PET systems with high resolution and high sensitivity are required. The spatial resolution and sensitivity requirements for small animal PET scanners are considerably more demanding than those for clinical systems. This is caused by the size of the organs, the anatomic structures of the rodents and the limited volume and activity of a radio-tracer that can be delivered to the animal without disturbing the biological processes under investigation. The typical adult mouse weighs only $\sim$ 30 g with a body length (nose to base of tail) between 7 and 10 cm. The blood volume of a mouse is only $\sim$ 2.5 ml, which limits the volume of injected radio-tracer to $\sim$ 0.2 ml. To achieve a SNR in small animal images similar to that in human PET images, the number of acquired coincidences should be increased proportionally to the reduction of voxel volume used for the reconstructed images, which can be a factor of a few hundreds. Consequently, the activity concentration per unit body mass of radio-tracer for small animal imaging is considerably higher ($\sim$1000 MBq/kg) than that for human imaging ($\sim$3 MBq/kg).

The last ten to fifteen years of intense research to develop dedicated small animal PET systems resulted in the development of numerous academic prototypes [44], [57], [217], [81], [85] and commercially available scanners [194], [14], [212], [19], [105], [173]. The preclinical PET systems constructed to date achieve spatial resolution in the range of 1-2 mm FWHM and system sensitivity of 1 % to 16 % for an axial detector length of 6-11 cm [77]. However, preclinical PET has not yet reached its full performance potential. A sub-millimetre spatial resolution is desired for small animal PET imaging.

To achieve a similar level of detail in mouse PET images as in human images, a spatial resolution of $\sim$ 0.4 mm is required. Furthermore, the positron range, parallax and DOI have a larger impact than in human scanners. An improvement in terms of spatial resolution also requires an improvement in sensitivity to achieve a sufficient SNR. Increasing the sensitivity of preclinical PET scanners requires improved detector efficiency and solid angle coverage of the scanner's FOV. Therefore, there are still substantial improvements to be made in preclinical PET systems to fully exploit the potential of PET imaging for molecular research.

Chapter 3

PET detectors

3.1 Introduction

The detector is an important component for the overall performance of a PET system, and together with the image reconstruction algorithm, it determines the quality of PET images. PET detectors detect gamma photons and derive the spatial coordinates, the energy and time information (timestamp) of detected events.

Almost all PET scanners are currently based on scintillation detectors. Other detectors design are also being investigated [63], [38], [94]; however, because this thesis investigates scintillation detectors, the discussion will be limited to this type of detectors. The fundamental design and components of a PET block detector are shown in figure 3.1. A PET detector block consists of an array of finely segmented, individual scintillation crystals coupled to the photodetector, which is typically a photomultiplier tube (PMT) (see section 3.4.2).

The scintillation crystals convert the energy deposited by gamma photons through Compton scattering or the photoelectric effect into visible or ultraviolet (UV) light. The amount of light that is produced is proportional to the energy of the gamma photon deposited in the scintillator. The light is then converted by the photodetector into an electric signal, which is proportional to the amount of detected light. Thus, the final electrical output signal of the detector is proportional to the energy of the detected gamma photon. Due to size and cost constraints, individual scintillation crystals are generally not coupled directly to an individual PMT. Rather, a group of crystal elements is coupled to a smaller number of PMTs, as illustrated in figure 3.1. The scintillation crystals are often spread onto the PMTs through the light

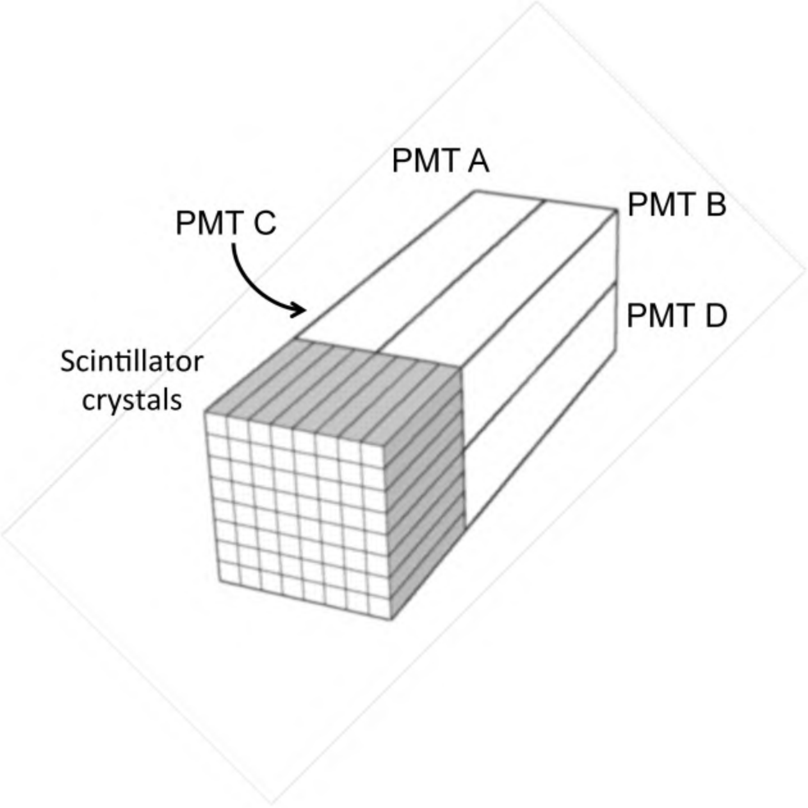

Figure 3.1: Schematic of the classic block detector design.

guide that is placed between the scintillation crystal array and the PMTs. The light guide allows the light produced in an individual crystal of the array to be spread across a larger area and shares the light between PMTs. The coordinates (X and Y) of the gamma photon interaction within the detectors are estimated based on the weighted proportion of light detected in each PMT [7], [78], [47] :

$$X = \frac{(B+D)-(A+C)}{A+B+C+D} \quad Y = \frac{(A+B)-(C+D)}{A+B+C+D} \tag{3.1}$$

where A, B, C and D represent the anode signals of PMTs with the notation as in figure 3.1. This method allows for the identification of individual crystals in the scintillator array; however, the response is not linear across the whole detector surface. This non-linearity is caused by the fact, that the

PMTs responses to the amount of light detected from different crystals in the array are not completely linear across whole detector face. To overcome this issue, look-up tables that correlate the measured position (X and Y) to the individual crystal are experimentally measured. Both scintillation crystals and photodetectors are covered in detail in sections 3.3 and 3.4 of this chapter, respectively.

There are five main parameters that characterize the performance of a PET detector: energy resolution, timing resolution, spatial resolution, detection efficiency and count rate performance. These parameters are described in detail in the following sections of this chapter.

3.2 Characteristics of PET detector

3.2.1 Energy resolution

The energy resolution characterizes the detector's ability to discriminate gamma photons of different energy. A small energy resolution is desired for a PET detector because it allows for efficiently distinguishing photons that underwent Compton scattering. This allows for discriminating between scattered coincidences and true coincidences and for rejecting a large fraction of the former, ensuring a higher SNR in the reconstructed images. The energy spectrum is obtained by plotting the number of measured gamma photons with a given energy as a function of the energy of the gamma photons. The shape of the energy spectrum depends on the energy of the gamma photons and on the properties of the detector materials. An example of the energy spectrum of ^{22}Na measured with a PET detector is shown in figure 3.2. This spectrum consists of a photopeak that corresponds to 511 keV gamma photons and a region of lower energies that corresponds to Compton scattered photons that did not deposit their entire energy in the scintillator.

The energy resolution of a detector is defined as the full width of the photopeak at one half of its maximum amplitude (ΔE) divided by the energy of the photopeak E:

$$E_{res} = \frac{\Delta E}{E} \times 100\% \tag{3.2}$$

Energy resolution is expressed as a percentage. A smaller energy resolution is better; a detector with a smaller energy resolution has a better capability

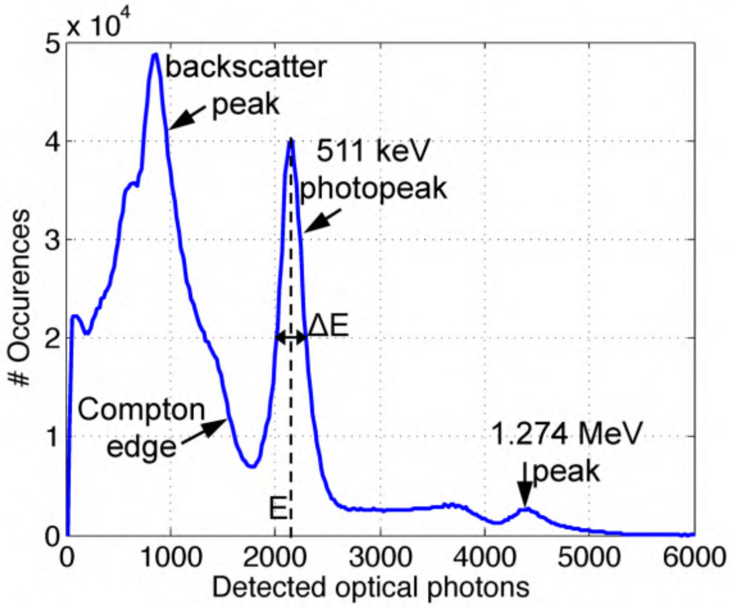

Figure 3.2: The energy spectrum of a ^{22}Na source. ΔE marks Full Width at Half Maximum of the 511 keV photopeak.

of distinguishing between two gamma photons whose energies are close to each other. Because the energy resolution depends on the width of the particular photopeak and on the energy of the gamma photons, the energy of the gamma photons must always be specified when reporting energy resolution. Energy resolution is worse at lower energies because there is a smaller number of photoelectrons, which results in higher statistical fluctuations in the measured signal. For scintillation detectors, energy resolution is primarily defined by the light yield of the scintillator and by the quantum efficiency of the photodetector.

3.2.2 Timing resolution

The timing resolution of a detector describes how precisely the detector can measure the time of gamma photon detection. A good timing resolution enables the use of a narrower timing window, which allows to decrease the number of registered randoms. Furthermore, a good timing resolution allows for the introduction of time-of-flight (TOF) to the PET detector, which improves the SNR via reducing noise propagation during image reconstruction. The better the timing resolution is, the more significant is the improvement in the SNR of the reconstructed image for the TOF PET scanners.

3.2.3 Spatial resolution

The spatial resolution of a detector, which is also often referred to as intrinsic detector resolution, characterizes the ability to resolve spatially separated objects. A higher spatial resolution means that the detector is better at resolving small objects, which results in sharper, less blurred images that more clearly visualize small features.

In PET images, a single point source of radioactivity is not represented as a single pixel in the image but rather as a group of pixels over which the source is blurred. This blurring results from a number of physical factors that are intrinsic for the formation of PET images (see section 2.4.4). When the measured activity distributions of radioactive sources overlap due to the limited spatial resolution, these sources cannot be distinguished from each other. Rather than being represented as separate sources in the reconstructed PET image, they appear as a single, broader, low-contrast source.

In detectors based on arrays of individual scintillation crystals, the size of the crystals limits the spatial resolution of the detector. Thus, a detector achieves better spatial resolution with smaller crystal elements. In detectors based on large, continuous scintillation crystals, the best achievable spatial resolution is determined by the algorithm used for positioning of the detected gamma photons, the amount of the detected light and the sampling in the photodetector. Thus, with smaller crystal elements or finer spatial sampling, the detected gamma photon can be more precisely localized and the spatial resolution will be enhanced.

The intrinsic detector resolution has an impact on the overall spatial resolution of PET systems; the better the intrinsic resolution of the detector, the better the spatial resolution of the entire PET scanner. There are, however, intrinsic limits due to positron physics and system geometric calibration.

3.2.4 Sensitivity

The detector sensitivity (also referred to as efficiency) is defined as the ratio of the number of detected gamma photons and the total number of emitted gamma photons that reach the detector:

$$Sensitivity = \frac{N_{detected}}{N_{emitted}} \tag{3.3}$$

This fraction should be as high as possible to achieve a good signal-to-noise ratio (SNR). The detector sensitivity depends on the effective atomic number Z, density and thickness of the detector material, the packing fraction of the crystal, the energy of gamma photons, and the energy window used.

3.2.5 Count rate performance

The count rate describes how fast the detector can process the incoming gamma photons. In the ideal case, the output count rate of the detector, i.e., the number of detected gamma photons in a fixed unit of time, increases linearly with the rate of gamma photons that are incident on the detector. However, due to the finite time that the detector needs to process the detection of a gamma photon, this is not true. The time needed to process the detection of the gamma photon is called dead time (τ). During the dead time, the detector is incapable of detecting any new gamma photons; thus, all gamma photons that arrive at the detector during the dead time are lost. The detectors are classified depending on their dead time behaviour as paralysable and nonparalysable detectors. In nonparalysable detectors, new gamma photons that interact in the detector during its dead time have no impact on the detector's behaviour. Therefore, after each gamma photon detection, the detector is always *dead* for exactly τ. Conversely, in paralysable detectors, every new gamma photon that interacts in the detector during its dead time prolongs the dead time of the detector by an additional τ. The behaviour of paralysable and nonparalysable detectors is illustrated in figure 3.3.

Consequently, paralysable detectors at higher event rates can spend a considerable amount of time in the dead time state, resulting in a very poor count rate performance. For very high event rates, the count rate of paralysable detectors can drop to zero, whereas for nonparalysable detectors, the count rate will saturate. Thus, nonparalysable detectors can process more gamma photons at high event rates than paralysable detectors. This is illustrated in figure 3.4.

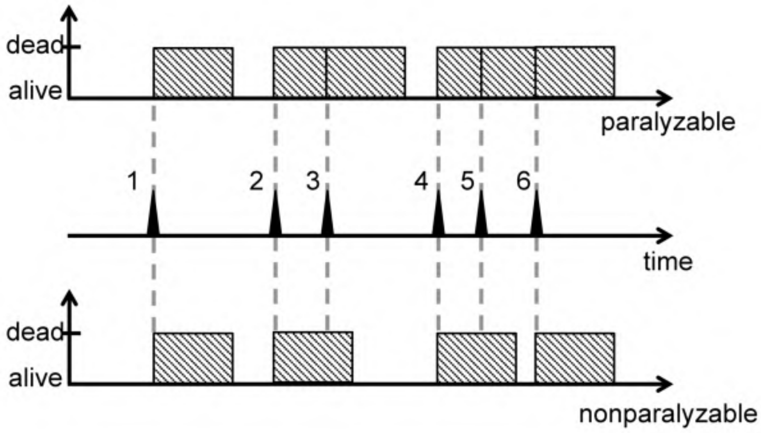
dead
alive
paralyzable
1
2
3
4
5
6
time
dead
alive
nonparalyzable

Figure 3.3: The behaviour of paralyzable and nonparalyzable detectors. The nonparalyzable detector detects events 1, 2, 4 and 6, while the paralyzable detector detects only events 1, 2 and 4.

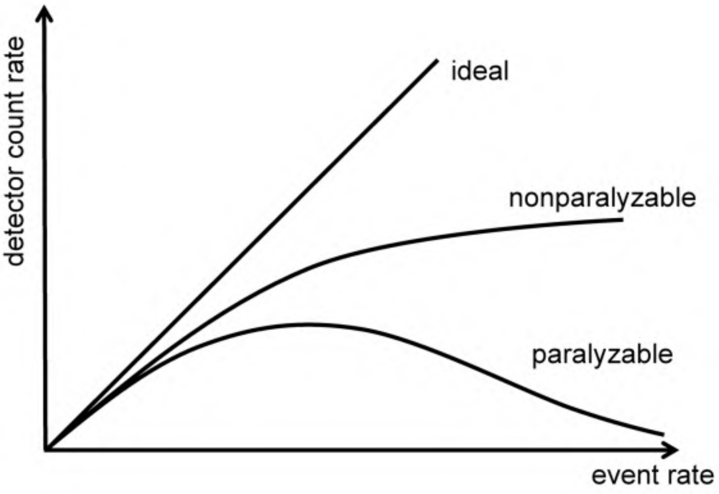

Figure 3.4: The detector count rate for different types of detector models. In ideal detector count rate increases linearly with the event rate. In reality however, count rate of the paralyzable detector will drop to zero, while for nonparalyzable detector the count rate will eventually saturate at very high event rates.

3.3 Scintillators

3.3.1 Introduction

A scintillator is a material that converts the deposited energy into visible or ultraviolet light. The amount of light that the scintillator emits after the interaction is proportional to the energy of the gamma photon. Thus, by measuring the amount of light, i.e., the number of emitted optical photons, the energy of the gamma photon can be determined. There are a number of properties that an ideal scintillator should possess:

- The conversion of gamma photon energy into light should have a high efficiency - the scintillator should emit a large number of optical photons per gamma quantum and should be able to absorb a high fraction of incident gamma photons.
- The conversion should also be linear - the light yield should be proportional to the deposited energy over a wide range.
- The scintillator should be transparent to the wavelength of its own emitted light to avoid re-absorption of optical photons.
- The decay time of the scintillation light should be short such that fast signal pulses can be generated, which is particularly important for applications such as TOF PET.
- The scintillator should be easy to manufacture and process into crystals feasible for detector use and preferably should not be hygroscopic.

No scintillation material meets all these requirements simultaneously, and the choice of the scintillation material that performs best for a particular application is always a compromise between all of the listed properties.

Scintillators, depending on their mechanism of converting the energy of gamma photons into light, can be divided into two classes: organic and inorganic scintillators. Organic scintillators are generally faster than inorganic ones; however, they produce less light and have a low stopping power for gamma photons. Consequently, organic scintillators are preferred for the detection of electrons and neutrons, whereas inorganic scintillators, due to their high atomic number, are the main choice for the detection of gamma photons. Therefore, in the following sections, the emphasis will be on inorganic scintillators, and organic scintillators will not be discussed further in this dissertation.

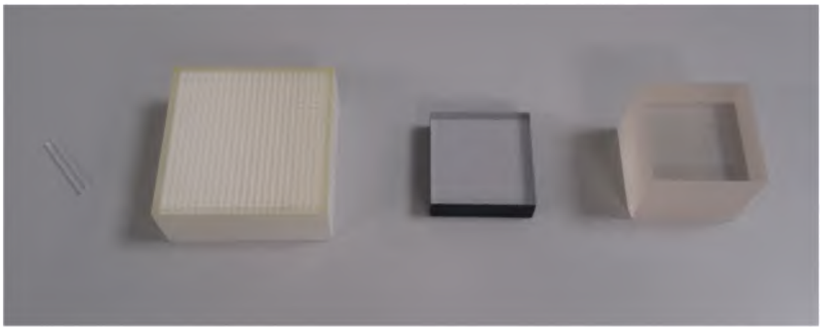

Figure 3.5: Different types of scintillator crystals. From left, a single LYSO crystal 2×2×20 mm^3; a LYSO array of 24×24 individual LYSO crystals, each 2×2×20 mm^3; a monolithic crystal of LYSO 32×32×5 mm^3 with black reflector on lateral sides and white reflector on top and a monolithic of BGO 32×32×30 mm^3 with unpolished lateral sides.

3.3.2 Scintillation mechanism

The scintillation mechanism in inorganic scintillators is based on the band structure found in crystals (see figure 3.6). The band structure determines the discrete ranges of energies that electrons within a scintillator crystal may have (allowed bands) and cannot have (forbidden gap). Allowed bands are the valence band, which contains bound electrons at lattice states, and the conduction band, which contains loose electrons. Between these bands, there is the forbidden gap (also called the band gap) in which electrons can never be present in a pure crystal. An electron from the valence band can be excited by absorbing the energy of a gamma photon that interacted with the scintillator. This leaves a hole in the valence band, and the electron is moved to the conduction band. Such an electron then de-excites, loses its energy and moves back to the valence band. This energy is released as photons [16], i.e., scintillation light. However, in the pure lattice of the scintillator, the return of the electron to the valence band through photon emission is not efficient. Moreover, due to the width of the forbidden gap, the emitted photons would have an energy that is too high to be in range of visible or UV light.

Therefore, impurities are deliberately introduced in scintillator crystals. These impurities in the crystal's lattice create additional energy states within the forbidden gap, which the electron can occupy. Thus, the de-excited electron can move back to the valence band through these introduced energy states. The electron-hole pair created by the interaction of the gamma photon with the scintillator travels through the crystal lattice. The hole drifts to an impurity activator site and ionizes it because the ionization energy of the impurity is smaller than that of pure lattice state. The electron moves through the crystal lattice until it is captured by this ionized impurity activator, where it rapidly de-excites by emitting scintillation light. The activator impurities are chosen such that the emitted scintillation light is in the visible or near-UV range. Thus, the emission spectrum of the scintillator is determined by the modified energy structure in the crystal's lattice.

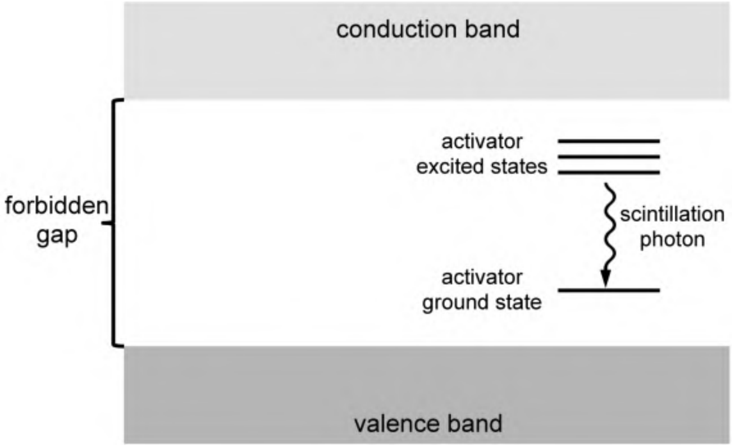

Figure 3.6: Energy band structure of an activated crystalline scintillator.

3.3.3 Properties of scintillators

3.3.3.1 Efficiency

Because the main purpose of a scintillator is to convert a gamma photon into visible light, one of the most important parameters for the scintillator is its efficiency. The efficiency characterizes how well the scintillator material absorbs the incident gamma photons and emits their deposited energy as optical photons. The efficiency of a scintillation crystal is determined by its density, atomic number, and its thickness. The attenuation of a beam of gamma photons in a piece of material is given as:

$$\frac{I(x)}{I(0)} = e^{-\mu x} \tag{3.4}$$

where $I(0)$ and $I(x)$ are the gamma photon flux at material depths of 0 and x, respectively, and μ is the total linear attenuation coefficient that represents the total sum of the attenuation coefficients for the different possible mechanisms of gamma photon interaction with the material. For gamma photons with an energy of 511 keV, the main interaction mechanisms are the photoelectric absorption effect and Compton scattering. Thus,

$$\mu \approx \mu_{pa} + \mu_C \tag{3.5}$$

where μ_{pa} and μ_C are the linear attenuation coefficients for photoelectric absorption and Compton scattering, respectively. μ_{pa} and μ_C depend on the density (ρ) and the atomic number (Z) of the scintillation material. The approximated relation for μ_{pa} and μ_C is:

$$\mu_{pa} \propto \rho Z^{3-4} \tag{3.6}$$

and

$$\mu_C \propto \rho Z^0 \tag{3.7}$$

From equations 3.4 to 3.7, it is evident that a high efficiency is obtained for scintillators with a high density and a high atomic number.

In this place it should be also mentioned that μ_{pa} depends also on the energy of the gamma photons E_γ. No single analytic expression is valid for μ_{pa} over all ranges of E_γ and Z, but a rough approximation is:

$$\mu_{pa} \propto \frac{Z^{4-5}}{E_\gamma^3} \tag{3.8}$$

3.3.3.2 Photoelectric fraction

As mentioned in chapter 2.4.4, the desired mechanism of gamma photon interaction in PET is photoelectric absorption, in which the entire energy of the gamma photon is deposited in the scintillator in a single interaction.

Compton scattering is not desired because it results in lower energy depositions, leading to detections outside the photopeak. Equation 3.6 shows that the fraction of the total number of gamma photons that interact through photoelectric absorption increases as the atomic number of the scintillator increases. The fraction of the photoelectric absorption interactions (P_{pa}) in the scintillation material of thickness x and photoelectric attenuation coefficient μ_{pa} can be estimated as:

$$P_{pa} = \frac{\mu_{pa}}{\mu}(1 - e^{-\mu x}) \tag{3.9}$$

Therefore, scintillators with a high Z are especially desired for PET, where gamma photons have an energy of 511 keV (see equation 3.8). Table 3.1 shows several scintillators used in PET detectors; note that the photoelectric absorption fraction for the BGO scintillator, which has the highest Z, is only 40%.

Table 3.1: Properties of several scintillators used in PET. (Data from [207])

	NaI:Tl	BGO	LSO	LYSO	GSO	LaBr3
Light yield (ph/MeV)	41000	9000	26000	32000	8000	61000
emission wavelength (nm)	365	480	420	420	440	358
decay time (ns)	230	300	40	40	6.7	35
density (g/cm^3)	3.67	7.1	7.4	7.1	6.7	5.3
attenuation length 511 keV (mm)	29.1	10.4	11.4	11.5	14.1	21.3
Z_{eff}	50.8	75.2	66.3	60	59	46.9
Photo-fraction 511 keV (%)	17	40	32	30	25	13
Hygroscopic	yes	no	no	no	no	yes

3.3.3.3 Light yield

Another important property of a scintillator is its light yield, i.e., the number of optical photons that are emitted after the absorption of a gamma photon. A high light yield of the scintillator has a large positive impact on the energy resolution and spatial resolution of the detector. It is also desirable for the number of emitted optical photons to be linearly proportional to the deposited energy of gamma photons over a wide energy range.

The spectrum of the light emitted by the scintillator is continuous; however, each scintillator has its own maximum emission peak, which determines the dominant wavelength of the emitted light. An example of the emission spectrum for the LYSO scintillator is shown in figure 3.7. The maximum emission of the scintillator should match the quantum efficiency (see section 3.4) of the photosensor for optimal detection efficiency of the scintillation detector.

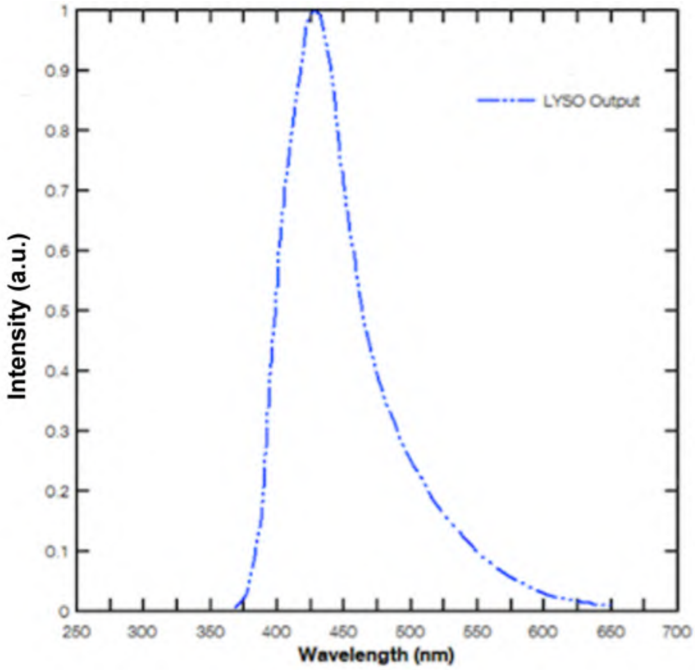

Figure 3.7: Emission spectrum of LYSO crystal excited by gamma rays.

3.3.3.4 Decay time

It is also desired for a scintillator to have short rise and decay times of the emitted optical photons. These times have an impact on the maximum count rate and timing properties of the detector. Fast light pulses are desired because they limit the length of the dead time of the detector and allow the arrival time of gamma photons to be more precisely measured, which improves the timing resolution of the detector. For the majority of scintillators, the time course of the emitted scintillation light can be modelled as:

$$I = I_0 e^{-t/\tau} \tag{3.10}$$

where τ is the decay time of the scintillator. Typically, the rise time of the scintillator is considerably shorter than the decay time; often, when modelling the time course, the rise time is assumed to be infinite.

In addition, from an economic perspective, it is desired that the scintillator should be easy to grow and to process into crystals. Scintillators crystals need to be manufactured in large volumes cost-effectively to make them affordable for use in medical scanners. large volumes to make them affordable for use in medical scanners.

Table 3.1 shows the properties of several scintillators used in PET scanners. Note that none of the listed scintillators have the overall best properties. The first PET scanner employed NaI(Tl) [152], which despite an excellent light yield has a low density and low atomic number. This resulted in limited sensitivity of the scanner for 511 keV gamma photons. Later PET scanners employed BGO crystals [55], which due to a very high density and a high atomic number, ensured high sensitivity for detectors based on them. However, due to the low light yield and relatively long decay time, the BGO-based detectors exhibited rather poor energy and timing resolution. With the recent progress in the field of scintillation materials, lutetium oxyorthosilicate (LSO) and lutetium-yttrium oxyorthosilicate (LYSO) were introduced [139], [151]. Thanks to the combination of high light yield, high atomic number and fast scintillation decay time, LSO and LYSO have become the scintillator of choice for the majority of modern PET scanners.

3.4 Photodetectors

3.4.1 Introduction

In this section, different types of photodetectors that can be used in scintillation detectors are presented.

One of the most important properties of a photodetector is its quantum efficiency (QE). The QE characterizes how efficiently the photodetector converts the optical photons into photoelectrons:

$$QE = \frac{\mathit{Number\ of\ collected\ photoelectrons}}{\mathit{Number\ of\ optical\ photons\ incident\ on\ photosensor}} \tag{3.11}$$

A high QE is desired for a photodetector because the amount of collected photoelectrons has a considerable influence on the detector's energy resolution and spatial resolution. The QE of a photodetector is a function of the wavelength of optical photons. Thus, the maximum QE of a photodetector should match the maximum emission wavelength of the scintillator to achieve high detector sensitivity.

It is also desired that the photodetector possess a high fill factor to ensure effective collection of optical photons across its area. The fill factor is the ratio of the light-sensitive area of the photodetector to the total area of the photodetector:

$$\mathit{Fill\ Factor} = \frac{\mathit{Photodetector\ light\ sensitive\ area}}{\mathit{Photodetector\ total\ area}} \tag{3.12}$$

Due to constraints of technology from which a photodetector is made and the housing that is used, this ratio varies typically between 0.2 and 0.8. For example, in an array of silicon photomultipliers (see section 3.4.4), part of the photodetector's area is occupied by gaps between the array's pixels, wire bondings and finally borders between separate microcells in the silicon structure.

Considering the concept of multi-modality PET-MR imaging systems, the detector's compatibility with magnetic fields becomes an important property. The photodetector should be able to operate without any or with minimal performance degradation in a strong MR field, even up to 9 T. The photodetector should neither cause any distortion to the MRI scanner nor cause degradation of the MRI images.

3.4.2 Photomultiplier tubes

Photomultiplier tubes (PMTs) are the standard type of photodetector and have been the most widely used photodetectors in emission tomography. A schematic of a PMT is shown in figure 3.8. The PMT consists of a vacuum glass housing that contains a photocathode, focusing electrodes, a chain of dynodes and an anode. Optical photons emitted by the scintillator are incident on the photocathode, causing the emission of primary electrons from the photocathode through the photoelectric effect. These primary electrons are focused by the focusing electrodes and are accelerated towards the first dynode by the strong electric field applied between the photocathode and the dynode. Due to the additional kinetic energy obtained by the acceleration in the external electric field, the primary electrons upon striking the first dynode cause the emission of additional electrons (referred to as secondary electrons). These secondary electrons are accelerated by the electric field towards another dynode in the chain, and the process repeats. The geometry of the chain of dynodes is designed such that a cascade occurs with an exponentially increasing number of electrons being produced at each stage. The electrons produced at the final dynode are collected at the anode, where the final signal is produced. The total gain achieved in this way in PMTs is on the order of 10^6-10^7, which provides a good signal for further electronic processing.

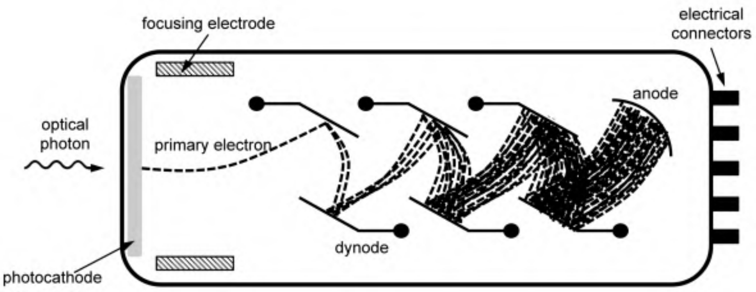

Figure 3.8: Simplified schematic of a PMT and its principle of operation.

Multi-anode PMTs (MA-PMTs) are PMTs that have multiple anodes, and they provide information on the position of the detected scintillation light [3], [4], [150]. An exemplary schematic and image of such MA-PMT, Hamamatsu H8500, is presented in figure 3.9. Because of the structure of the dynodes, the electrons are multiplied with minimal spatial spread and are guided to the anode that is underneath the location of the interaction of the optical photons with the photocathode. Thus, by measuring the signals from multiple anodes, the light spread can be measured. The overall performance of MA-PMTs is comparable to that of conventional PMTs; however, MA-PMTs have a large variation in gain between individual channels of the same device [3].

PMTs are stable in operation and are mature, reliable technology. However, PMTs have some limitations. One of the drawbacks is the limited

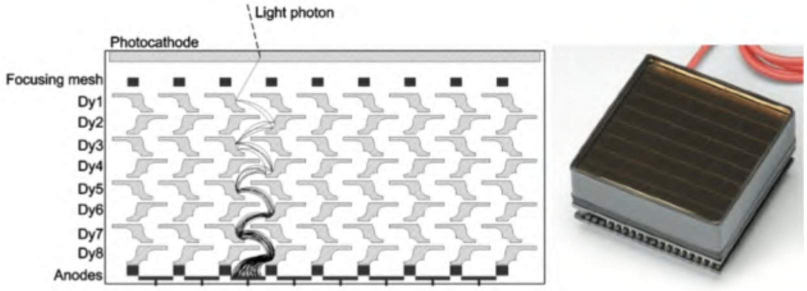

Figure 3.9: Simplified schematic of a MA-PMT. The metal dynodes multiply the electrons with minimal spatial spread.

quantum efficiency (QE), which is typically approximately 25%. PMTs require a high voltage to operate (up to $\sim$ 1000 V) as the electric field between successive dynodes increases. They are fragile due to the glass housing and are bulky, which makes tight packing of PMT-based detector modules in scanners difficult. Finally, PMTs are very sensitive to magnetic fields, which influences the path of propagation of the electrons. Thus, PMTs are unable to work in the strong magnetic fields generated by MRI scanners, which prevents the development of PMT-based MRI-compatible PET detectors.

3.4.3 Avalanche photodiodes

An avalanche photodiode (APD) is a type of semiconductor-based photodetector that uses the photoelectric effect to convert optical photons into electrical signals. An APD operates with a relatively high reverse voltage but below the breakdown voltage. This causes an acceleration of the electrons and holes excited by absorbed optical photons such that they can generate secondary electrons and holes. Thus, an APD provides an internal gain mechanism similar to that in a gas detector.

APDs consist of *pn*-junctions with several layers of differently doped semiconductor materials, most commonly silicon. The doping concentrations are selected such that a region with a very high electric field is created when a reverse bias voltage is applied to the APD. Many different types of APD structures have been developed, each with specific characteristics. However, the most common type of APD is the so-called "reach through" structure. There are two versions of the "reach through" structure. The first is where optical photons enter from the *n*-side of silicon, and the second is where optical photons enter from the *p*-side. The *n*-side type of APD has useful sensitivity in the 450 nm to 1000 nm wavelength range, whereas the *p*-side exhibits high sensitivity to UV – blue light and operates in the range from 200 nm to 800 nm. Thus, for PET scintillator detectors, the *p*-side APD is more useful. The structure of such an APD and its internal electric field is shown in figure 3.10.

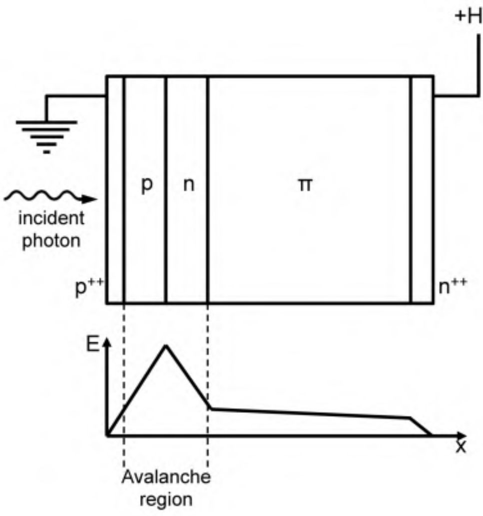

Figure 3.10: Schematic of a *p*-side entrance reach-through APD.

An incident optical photon can ionize the material of the entrance layer and excite the primary electron-hole pair. The applied electric field accelerates the electron towards the anode and the hole towards the cathode. Thus, the electron crosses the high electric field region on its way towards the anode. In this region, the electron acquires sufficient kinetic energy. By collisions with atoms of the silicon lattice, it causes an ionization, which results in the generation of secondary electron-hole pairs. Some of these secondary electron-hole pairs can cause further ionization. In this way, an avalanche multiplication of electrons is created, which results in amplification of a single incident photon. The amplified output of the APDs is proportional to the amount of detected optical photons.

The ionization of any individual electron-hole pair has a certain probability of occurrence; thus, the overall gain from the APD is the statistical average of all ionization events. Therefore, the gain of the APD fluctuates, which is known as *excess noise*. The noise of the APD can be given by the following formula:

$$ES = kM + (2 - \frac{1}{M})(1 - k) \tag{3.13}$$

where k is the ratio of the hole ionization coefficient to the electron ionization coefficient and M is the gain of the APD.

The gain of APDs typically ranges from 10^2 to 10^3 and is sensitive to changes in the bias voltage and the temperature. Thus, APDs require stable bias and temperature for good operation. The gain of APDs is lower than the gain of PMTs, which makes APDs more susceptible to electronic noise. However, APDs have a considerably higher quantum efficiency (QE), typically between 70% and 80% [160], than PMTs, and they are more compact and robust. Furthermore, APDs are insensitive to magnetic fields, which makes them a suitable candidate for MR-compatible PET detectors.

It is important to describe the dark current, which is distinctive for all semiconductor photodetectors. The dark current is caused by thermal, rather than optical, generation of electron-hole pairs within the bulk of the silicon. These thermally generated electron-hole pairs are then multiplied in the gain region and give rise to a dark current from the APD even in the absence of optical photons. Therefore, increasing the gain of the APD by increasing the applied bias voltage also increases the dark current. Consequently, the dark current creates a constant pedestal signal (at a fixed bias voltage and temperature), which limits the minimum amount of light that can be detected. Because the dark current is thermally dependent, it can be reduced by lowering the temperature. The lower the temperature of the semiconductor material of the APD, the lower the probability of the generation of thermal electron-hole pair is, and consequently, the lower the dark current.

3.4.3.1 Geiger mode APDs

As mentioned in the previous section, the gain of an APD depends on the applied bias voltage, which is set below the breakdown voltage. However, the APD can also be operated above the breakdown voltage. In this case, it operates in Geiger mode (G-APDs). In this mode, the avalanche multiplication of the generated electron-hole pair is self-sustaining, and the number of electron-hole pairs increases exponentially with time. This condition is called *avalanche breakdown* of the photodiode. The gain of the G-APD is virtually infinite, and the devices produce a large output signal, even when detecting a single optical photon. Therefore, these devices are also known as single photon avalanche photodiodes (SPAD).

Although the gain of G-APDs is virtually infinite, in reality, it is limited by quenching its output current because otherwise the device would become damaged. The quenching can be performed with a passive quenching circuit or with a more advanced active quenching circuit. A simple passive quenching circuit consists of a single resistor in series with the G-APD, as shown in figure 3.11. When an optical photon is detected, the Geiger discharge is created, and the device generates a large output current. This current causes a voltage increase over quenching resistor, which causes a drop in bias voltage, effectively ending the Geiger avalanche breakdown. When the Geiger avalanche is stopped, the output current is low again and the APD recovers. After the APD fully recovers, it is ready for new detection.

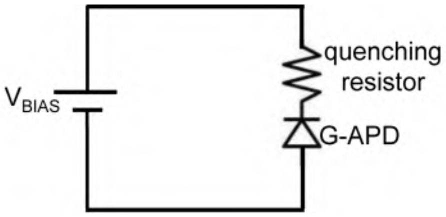

Figure 3.11: G-APD simple passive quenching circuit.

The gain of the G-APD is on the order of 10^5-10^6. As a result of this high gain, they achieve excellent timing response. However, in Geiger mode, the APD's output is not proportional to the number of detected optical photons. In principle, the G-APD becomes a binary digital device, which distinguishes only between the state when no optical photon was detected and the state where at least one optical photon was detected as the device's output signal is the same regardless of the number of detected optical photons.

This mode is not very useful for PET detectors, where the number of photons produced in the scintillator needs to be related to the energy of the detected gamma photons to distinguish and reject events that have undergone Compton scattering. Nevertheless, G-APDs are the basic building component of silicon photomultipliers, which are described in the next section and show great potential for PET.

3.4.4 Silicon photomultiplier

3.4.4.1 Architecture and principle of operation

The silicon photomultiplier (SiPM), also known as multi-pixel photon counters (MPPCs) or solid-state photomultipliers (SSPMs), is a single-photon-sensitive device constructed from many G-APDs on a common silicon substrate. A SiPM consists of a 2D array of thousands of small G-APDs, with sizes ranging from 10 to 100 μm, all connected in parallel to form a single output (see figure 3.12). Each individual G-APD together with its individual quenching circuit is called a cell, microcell or SPAD. Every microcell operates individually and responds independently when the incident optical photons interact in that microcell.

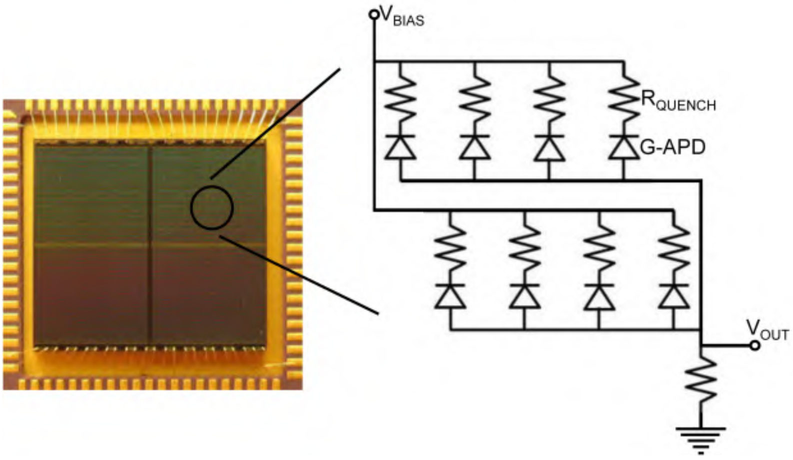

Figure 3.12: Simplified schematic of SiPM. A SiPM consists of array of thousands of G-APD connected in parallel.

At low light levels, the probability that a single microcell is hit by multiple optical photons is low. Therefore, each cell operates as a binary device that can be in one of two possible states: optical photon is detected or not. Because all microcells are connected in parallel, the summed currents from all microcells form an output signal that is proportional to the number of detected optical photons. Consequently, the SiPM preserves the high sensitivity and high gain of a G-APD, and at the same time, it has a dynamic range for detecting light with higher intensities.

Gain

The gain of the SiPM ranges between 10^5 and 10^7, and as in case of G-APDs, it depends on the applied bias voltage and temperature. The gain of the SiPM is sensitive to changes in the bias voltage and the temperature at a given bias voltage. The main reason for the dependency of SiPM's gain on temperature is that the breakdown voltage of the cells varies with temperature.

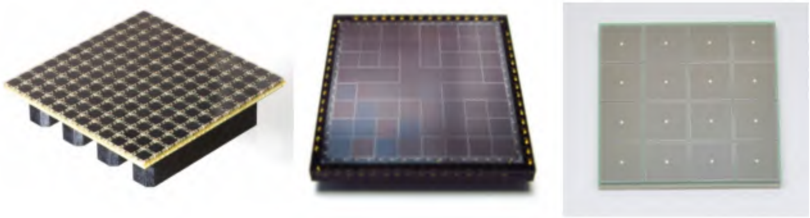

Figure 3.13: Examples of different SiPM arrays. (left) SensL 12 × 12 array with 3 × 3 mm pixels, (center) FBK 8 × 8 array with 4 × 4 mm pixels, (right) Hamamatsu 4 × 4 array with 3 × 3 mm pixels.

Photon detection efficiency

For a given incident light level, the signal produced by a SiPM depends primarily on the gain and the photon detection efficiency (PDE). The PDE of the SiPM is smaller than that of G-APDs. This is primarily caused by the fill factor (FF) of the SiPM, which is the ratio of the active area of microcells to the total area of the SiPM. The microcells are surrounded by dead areas (e.g., wire bonding and optical tranches), which makes the microcell pitch a few microns larger than the size of the microcell itself. The FF is a constant parameter inherent to the geometry of the particular type of SiPM device. Typical fill factors in current SiPM range between 20% and 80% [1], [156], [2]. The PDE of the SiPM also depends on the quantum efficiency (QE) and the probability of Geiger discharge in the microcell (PG). PG typically ranges between 0.5 and 1 [157] and depends on the location where the primary electron-hole pair is created and the electric field shape, and it increases with overvoltage above the breakdown point. The QE strongly depends on temperature and the wavelength of optical photons. For visible light, the QE is typically greater than 80% [162]. The PDE of the SiPM can be given by the following formula:

$$PDE = QE \times PG \times FF \tag{3.14}$$

Saturation

As previously mentioned, the output of a single microcell is the same regardless of the number of optical photons that simultaneously fall on it. Therefore, the SiPM is able to detect the intensity of a photon flux only with a large number of microcells in a small area. If the number of SiPM microcells is not large enough and/or the light flux is too high, then the probability of multiple gamma photons incident on one microcell is no longer negligible. In such a situation, saturation of a SiPM occurs. The response of a SiPM to a flux of optical photons is not linear and can be described by an exponential function:

$$\widehat{N}_{fired} = N_{tot}(1 - exp(-PDE \times \frac{N_{ph}}{N_{tot}})) \tag{3.15}$$

where $\widehat{N}_{fired}$ is the average number of microcells that fired, N_{ph} is the total number of incident optical photons, N_{tot} is the total number of available microcells, and PDE is the photon detection efficiency of the SiPM.

The timing properties of the SiPM depend on the Geiger discharge time and microcell recovery time, which defines the rise time and decay time of the output signal. The Geiger discharge is a fast process resulting in a rise time of typically just a few ns. The decay time is governed by the recovery time, which depends on the type of quenching circuit used. With passive quenching, the decay time is typically approximately 30 ns. Furthermore, the rise time and decay time both also depend on the total capacitance of the SiPM; the larger the capacitance, the longer both times are. Because the capacitance of a SiPM increases with its area, better timing properties are achieved for smaller SiPMs. In general, due to the fast rise time dictated by the rapid process of Geiger discharge, a SiPM achieves excellent timing properties that surpass those of PMTs.

3.4.4.2 Noise in SiPM

The main source of noise in a SiPM is the thermally generated dark count rate (DCR). The DCR is the number of microcells fired per second with no light source. As in the case of an APD, the electron-hole pair can be thermally generated within the sensitive area of a SiPM microcell, which can then trigger the multiplication avalanche. As the microcells work in Geiger mode, this thermally generated electron-hole pair produces the same output as if an optical photon were detected. The dark count rate increases with the area of the SiPM, temperature, and applied bias voltage. Depending on the type of SiPM, the DCR can range from a few MHz/mm^2 at room temperature to a few kHz/mm^2 at -20 °C . Because the outputs of all microcells are summed, the DCR gives rise to a dark current at the SiPM output. At fixed temperature and bias voltage, the DCR and the dark current created can be assumed to be constant. Thus, the dark current forms a pedestal signal at the SiPM output. However, this dark current is small because the probability of thermally fired microcell decreases by approximately an order of magnitude for each microcell already fired at a given moment [62]. Therefore, the probability of having simultaneously large number of thermally fired microcells is very low. Consequently, the dark current pedestal is well below the average signal generated by the interaction of 511 keV gamma photons with a scintillator. Therefore, the dark current at the SiPM output can be neglected by setting the detector's pulse trigger threshold above the dark current pedestal.

This however, has a negative impact on the timing resolution of the detector. The best time resolution in SiPM based detectors is achieved when the timing threshold on the detector's readout electronic is set as low as possible, just over the noise level. The lower the threshold, the earlier gamma photon interaction can be detected. This allows for a more precise timestamp generation and better timing resolution of the detector. High DCR of the SiPM, and thus high dark count current at the SiPM output, prevents the use of low threshold. Otherwise detector would be constantly triggered by the dark counts leading to the high dead time and the low sensitivity of the detector. Therefore DCR has a negative impact on the timing resolution of the SiPM based detectors. This is especially important for applications in which good timing resolution is required such as TOF PET. For such application the DCR should be as low as possible to ensure good timing capabilities.

In addition to the DCR, there are two other phenomena that can give rise to a false signal in a SiPM: optical crosstalk between neighbouring microcells and afterpulsing.

Optical crosstalk is a phenomenon in which an optical photon can be generated within a G-APD microcell operated at the breakdown voltage (3×10^{-5} photons per electron crossing the junction [104], [148]). This optical photon can then move to a neighbouring microcell and trigger a Geiger avalanche similar to an incident scintillation optical photon. Therefore, the optical crosstalk generates an output signal that is indistinguishable from the correct one and can result in two microcells being fired within a SiPM even though only one scintillation photon was detected. Consequently, the optical crosstalk can result in an overestimation of the SiPM's signal if it is not corrected for. The optical crosstalk in SiPM varies from 1% to 50% and depends on both the SiPM structure and applied bias overvoltage [186], [31]. To reduce crosstalk, optical isolation can be applied between microcells. Optical isolation can be achieved by introducing a large pitch between microcells or by creating optical trenches filled with an opaque material between them [157], [92], [136]. However, both of these solutions reduce the fill factor and consequently the PDE of the SiPM.

Afterpulsing is a phenomenon in which a charge carrier is trapped in a metastable trap during a Geiger discharge and then released after a certain amount of time. If this time is longer than the avalanche time, then the released carrier can cause a new avalanche. In this way, the afterpulsing can lead to a situation in which a single microcell is fired twice despite only one scintillation photon being detected. Consequently, afterpulsing affects the performance of photodetector. The metastable traps are created by the impurities in the silicon material. The time after which a charge is released depends on the energy level of the trap in the material band gap. The probability of the afterpulse (P_{ap}) as a function of time can be expressed as:

$$P_{ap}(t) = P_t \times \frac{exp(-t/\tau_t)}{\tau_t} \times P_{atp} \tag{3.16}$$

where P_t is the trap capture probability, τ_t is the trap lifetime, and P_{atp} is the avalanche trigger probability. P_t depends on the density of impurities in the silicon and the flux of carriers during the avalanche, P_{atp} depends on the strength of the electric field in the G-APDs, and τ_t depends on the energy level of the trap in the band gap and the temperature of the silicon lattice. The probability of the afterpulse typically ranges from 0.3% to 10% [186], [71] and generally increases with the applied overvoltage as both P_t and P_{atp} increase linearly with the overvoltage.

3.4.4.3 The advantages of SiPM

Due to the combination of high gain, dynamic range, moderate bias voltage (<100 V), insensitivity to magnetic fields, compactness, robustness, fast response and excellent timing properties, SiPMs are currently being regarded as the best photodetector for replacing PMTs in PET scanners. The excellent timing achieved with SiPMs [100], [111], [147], [137] makes them a promising candidate for TOF PET detectors. Moreover, their insensitivity to magnetic fields makes them a good choice for PET/MRI applications. SiPMs are currently available in a wide variety of sizes and designs from several commercial manufacturers (Hamamatsu, SensL, RMD, FBK-AdvanSiD, Zecotek Photonics Inc., and STMicroelectronics, to list a few). Considering their properties, SiPMs combine the advantages of PMTs and APDs. In fact, examining the current trends in the research community and the number of studies involving SiPM-based PET detectors and systems, the PET field is in a transition phase of switching its technology from well-established but old PMTs to novel and highly promising SiPMs. The SiPM is however, not yet a fully mature technology. Despite the progress that has been made over the past few years with designs, performance improvements, and larger-area sensors, work to further improve SiPMs and push the technology limits is constantly ongoing. The research community is also constantly exploring to what extent it can exploit this new promising technology for developing PET applications.

3.4.5 Digital silicon photomultiplier

3.4.5.1 Introduction

The digital silicon photomultiplier (dSiPM) was introduced by Philips Digital Photon Counting (PDPC) in 2009 [74]. This device fully exploits the binary nature of SiPM microcells. On the contrary to the typical analog SiPM, which sums currents from individual G-APDs into a single analog output, the dSiPM integrates each microcell with CMOS logic circuits. This results in an early digitization of the generated signal from each microcell and fully digital readout of the number of fired microcells. As a result, a gain-independent, noise free photon counting is achieved. The device uses an active quenching circuit, which allows microcells to be quenched in a controlled manner. Besides the digitization of each microcell response, the integrated CMOS electronics also provides a digital timestamp. This timestamp marks the arrival time of optical photons and a number of configurable options that control the acquisition flow of the dSiPM such as triggering conditions, integration time length or validation threshold (see following sections for details). Thus, the dSiPM ingrates a significant amount of electronic readout that is necessary for the analog SiPMs to process their output signals.

This approach results in a complete new detector architecture. With traditional analog types of photosensors such as PMTs, APDs or SiPMs, there was a need to post-process the analog output signals. In general, this post-processing required additional electronic circuits involving amplification, filtering and digitization. Due to the number of analog outputs and the need for high uniformity of each processing channel, a dedicated application specific integrated circuit (ASIC) were typically used to develop these analog post-processing electronics. With the dSiPM this problem is overcome as the device itself has a digital output. The main challenge for the dSiPM is the digital bandwidth which needs to be sufficient to transmit without loss, large amounts of data to the digital processing boards and image reconstruction computers.

3.4.5.2 dSiPM architecture

The Philips dSiPM tile consists of 16 independent sub-sensors called dies. The dies are placed on the tile in a 4 × 4 matrix. Each of these dies is further subdivided into four pixels, arranged in a 2 × 2 matrix (see figure 3.14). Each pixel consists of 3200 microcells for the DPC-3200-22-44 dSiPM type. The discharged microcells are summed up on a pixel basis to produce the photon count value. Each microcell can detect only one optical photon per acquisition sequence, thus the number of microcells per pixel defines the maximum photon count value. For the validation process, which will be described later, of the registered events each pixel is separated into four sub-pixels of 800 microcells. These sub-pixels are further divided into 25 row-trigger-lines (RTL) and contain a validation network, which is used to reduce the amount of false counts originating e.g. from dark-counts. For timestamp generation each die has a time-to-digital-converter (TDC), which generate a single timestamp per die for the registered photon detection events. The exact moment and condition under which a timestamp is generated, is determined by the configured trigger level. Per recorded event a die generates four photon count values, one per pixel, and one timestamp.

On the back of the dSiPM tile a FPGA is located, which is responsible for the configuration and synchronization of the individual dies as well as for the post-processing of measured data. In addition, the dSiPM consists of a flash memory chip, which stores calibration data and the inhibit maps that allow to disable individual microcells of dSiPM dies. This allows to identify

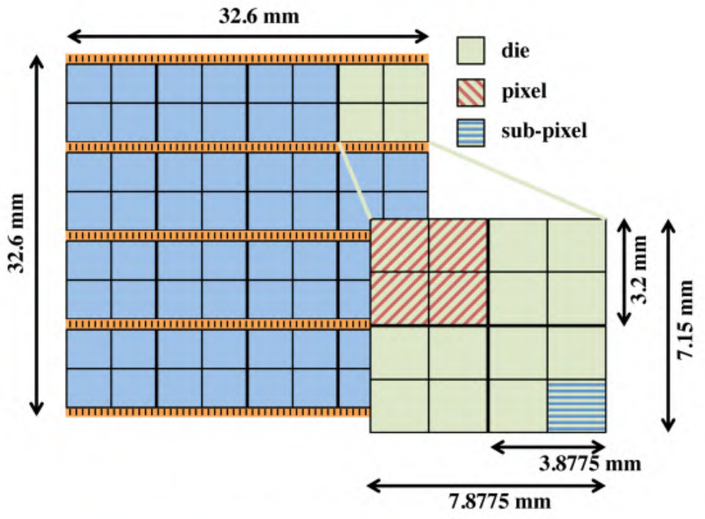

Figure 3.14: Schematic overview of the dSiPM architecture. The dSiPM consists of 16 independent dies, placed on the tile in a 4 × 4 matrix. Each of these dies is further subdivided into four pixels, arranged in a 2 × 2 matrix. For the DPC-3200-22-44 dSiPM type each pixel consists of 3200 microcells.

and disable the individual microcells that have a high dark count rate. All dies on the dSiPM tile have the same breakdown voltage, thus only a single bias voltage supply is needed per tile, which simplifies their operation. On the back of the tile there is also a temperature sensor, which can be used to adjust the bias voltage during operation.

3.4.5.3 Acquisition sequence

The dSiPM operates with an event based configurable acquisition sequence, which is shown in figure 3.16. Each die operates independently from the other dies, thus only dies that detect sufficient photons to reach the configured threshold (set up by selected trigger level) will start the acquisition sequence. Due to the common system clock all dies share the same timing reference.

Ready State

First the dSiPM die is in the “ready state”, where the microcells are charged, and the die is waiting for the detection of the photon event. The die will stay in this state until a trigger occurs. There is no recharge of the microcells

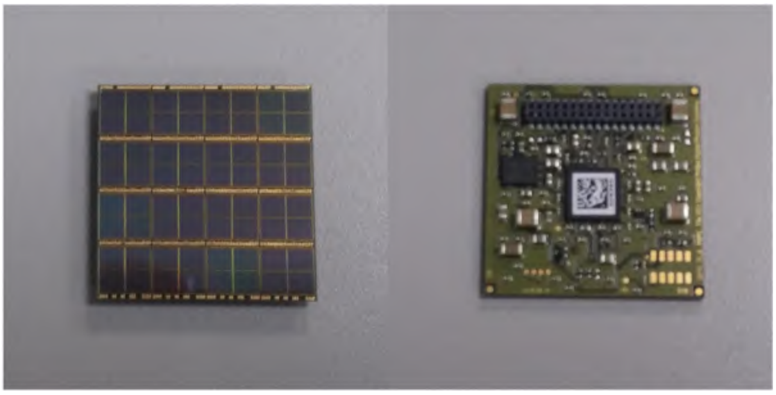

Figure 3.15: Top side (left) and bottom side (right) of the dSiPM tile. Top side is the active area of the dSiPM consisting of G-APDS microcells grouped in pixels. In the centre of the bottom side there is the FPGA, which is responsible for the configuration and synchronization of the individual dies.

in this state, unless the RTL refresh option is enabled (see section 3.4.5.5). This means that the dark counts can accumulate over time until the trigger condition is reached even when no optical photons arrived. Such an event is referred to as a dark count event and is undesirable as it provides no useful data and keeps the dSiPM die busy, preventing it from detecting true photon events, thus effectively extending the dead time of the dies.

Trigger

The trigger defines the moment, when the start of the acquisition sequence is initiated and the timestamp is generated. The die trigger is generated, when one of the pixels fulfils the configured trigger scheme i.e. a sufficient number of microcells is fired. The trigger scheme provides a stochastic threshold to suppress dark count events. Four different trigger schemes (called also trigger levels) are available for each die, which are based on different boolean interconnections of the four sub-pixels of a pixel (see table 3.2). Figure 3.17 plots the probabilities of die triggering as a function of the number of detected optical photons for different trigger schemes.

Validation time

The validation time gives a second threshold to separate true events from dark count events. After a trigger occurred, the die waits for a configurable

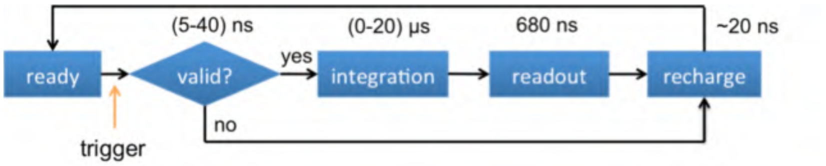

Figure 3.16: Acquisition sequence of the dSiPM die.

amount of time (between 5 and 40 ns) for more microcells discharges. At the end of the validation time it is checked if a configurable validation scheme is fulfilled. If yes, the event is validated as it is assumed that the amount of discharged microcell is sufficient to recognize the event as a true one. If not, the event will be invalidated and the die will go directly to the recharge phase (see figure 3.16).

Similar to the trigger logic, the validation logic checks for a geometrical distribution of microcell discharges on the pixel. The sub-pixel of the die is divided into 25 in row-trigger-lines (RTLs). These RTLs are combined in eight groups of three or four RTLs each, and connected to a configurable boolean network as shown in figure 3.18. Once an RTL within a group

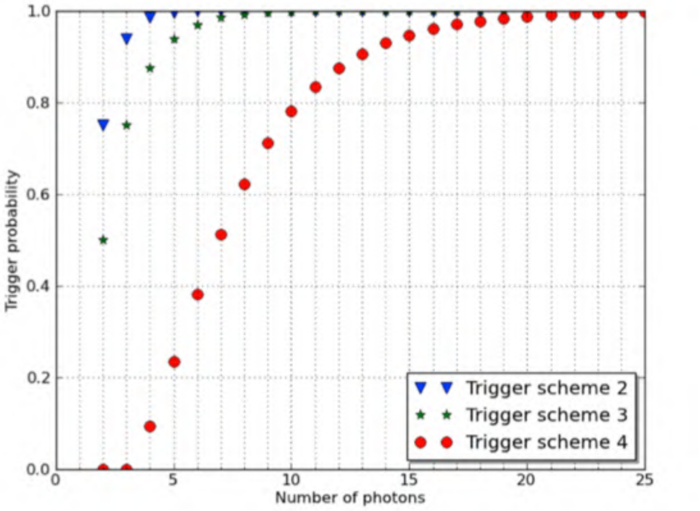

Figure 3.17: Trigger probabilities for the dSiPM die. Trigger scheme 1 is not plotted as a single photon is sufficient to trigger the die. Plot obtained from the PDPC MTEK Manual v0.31. [172]

Table 3.2: Different trigger schemes of dSiPM.

Trigger scheme	Sup-Pixel configuration
1	SP1 OR SP2 OR SP3 OR SP4
2	[(SP1 OR SP2) AND (SP3 OR SP4)] OR [(SP1 OR SP4) AND (SP2 OR SP3)]
3	(SP1 OR SP2) AND (SP3 OR SP4)
4	SP1 AND SP2 AND SP3 AND SP4

detects a cell-discharge within the validation time, the corresponding input of the connected logic gate is set to logic high. The valid-signals of all sub-pixels are then fed into the top-level pixel gate, which is configurable as well. If this pixel-level gate generates a valid-signal within the validation interval, the event is successfully validated. To configure the validation scheme, a 7 bit validation pattern defines if a specific gate acts as AND (0) or as OR (1) gate.

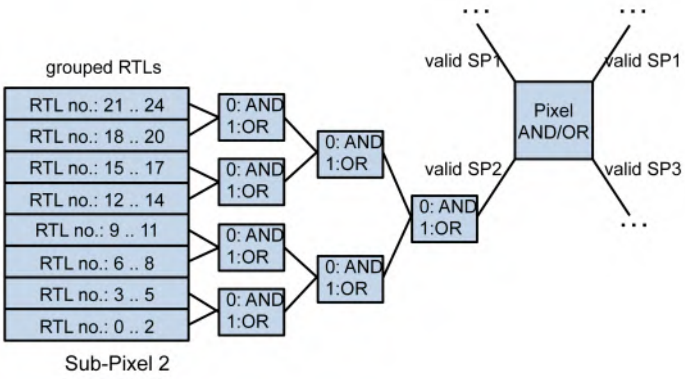
grouped RTLs
RTL no.: 21 .. 24
RTL no.: 18 .. 20
RTL no.: 15 .. 17
RTL no.: 12 .. 14
RTL no.: 9 .. 11
RTL no.: 6 .. 8
RTL no.: 3 .. 5
RTL no.: 0 .. 2
Sub-Pixel 2
0: AND
1:OR
Pixel
AND/OR
valid SP1
valid SP1
valid SP2
valid SP3
...

Figure 3.18: Validation logic network of the dSiPM.

Similar to the trigger schemes, the validation schemes do not define an exact threshold. The number of required photons depends on the distribution over the (sub-)pixel. This means that there is no difference for the validation network if one or more microcells within one RTL group are discharged. This leads to a stochastic validation threshold, with a minimum and average number of microcell discharges that are required to validate an event. Simulation results for minimum and average threshold of the pre-defined validation patterns are given in table 3.3.

Table 3.3: Validation schemes of the dSiPM die and the simulation results for average and minimum threshold of detected optical photons to successfully validate an event. Values obtained from the PDPC MTEK Manual v0.31.

Validation scheme	Threshold average # of fired microcells	Threshold minimum # of fired microcells
1	1	1
2	4.6 ± 2.1	2
4	16.9 ± 6.2	4
8	52.2 ± 15	11

Integration time

After successful validation the die enters the photon integration phase, which can be configured between 0 and 20 μs. During this phase the die waits for the arrival of more optical photons emitted by the gamma photon that initialized the currently registered event. The integration phase can be configured to match the decay time of a scintillation crystal.

Readout

After the integration interval is finished the die starts to readout the state of the microcells row by row. The processed rows are already recharged during this phase. The number of discharged microcells is summed up at the pixel level, giving one separate photon count value per pixel. At the end of the summation process these four photon count values and the trigger timestamp are sent out from the die for an external data processing.

Recharge

At the end of the acquisition sequence a die is recharged and is ready for the next event acquisition. The standard length of this recharge phase is 20 ns.

3.4.5.4 Neighbour Logic

As mentioned earlier, each die of the dSiPM works independently. However, there is an option called *Neighbour Logic* (NL) that allows to configure dies in such way, that a single die can force an event acquisition sequence on neighbouring dies, even when these dies did not detect enough photons to start their own acquisition sequence. This feature can be extremely useful if the expected light distribution covers multiple dies, with a high light intensity in the center and lower intensities in the surrounding regions, e.g. when large monolithic scintillation crystals are coupled to multiple dies.

In this NL mode, the trigger and validation schemes can be set to a relatively high value, thus reducing unwanted dark count events and dead time. As long as one die (called the *master die*) detects enough photons to fulfil the trigger and validation criteria, the neighbouring dies (called *slave dies*) will be also triggered to start their acquisition sequence. This neighbour trigger will override the configured trigger and validation settings on the slave dies. In this way, even the low light intensities in the outer event regions can be collected and added to the central photon count values during later analysis.

Slave dies, that are in the recharge phase will however ignore the trigger signal from the master die. This can lead to events where not all of the expected dies are present. The master trigger signal, due to signal propagation delays, may need up to 20 ns to arrive at slave dies. This can cause a situation, where a die is triggered and then invalidated by its own acquisition sequence before the trigger signal form the master die arrives. In such situation, the invalidated die enters the recharge phase and ignores the delayed master trigger signal.

3.4.5.5 RTL refresh

In a dSiPM, the pixel is prone to generate a false trigger caused by dark counts. In the case of trigger scheme 1 (see table 3.2), a single dark count is enough while in higher trigger schemes the trigger is caused by accumulated dark counts over a long period of time. Therefore, dSiPMs offer a fast recharge mode, called *RTL refresh*. It allows to recharge all microcells grouped in a single row-trigger-line of a sub-pixel after a short period of time if none of the four pixels generated a trigger. Consequently, this option is available only for trigger schemes above 1, where more than a single discharged microcell is necessary to trigger a die. The RTL refresh checks all row trigger lines once each 10 ns and compares them against the global die trigger. In case an RTL has triggered, but no die trigger was generated after 20 ns, the respective RTL is immediately recharged.

3.4.5.6 Inhibit memory

The dSiPM has the possibility to physically disable individual microcells, by writing to so called 'inhibit memory'. This feature is used to control the dark count rate of the sensor. Due to the manufacturing process of dSiPM, the different microcells within a single device have different dark count rate (DCR). The biggest contribution to the overall DCR of a dSiPM die is caused by only a small percentage of the cells. It is typical that about 10% of the microcells are responsible for 70% to 80% of the DCR. By disabling these high DCR microcells, the overall DCR of a die is significantly reduced, with a relatively small reduction of the active area.

This inhibit memory allows also to measure the individual DCR of each single microcell (so called dark-count map), by only enabling a single microcell on a pixel and measuring its event rate in complete darkness. By repeating this measurement for all microcells, the complete DCR distribution of a die can be measured. This can be used to disable the high DCR microcells with an inhibit map.

3.5 Small animal PET detectors

Due to the small size of rodents, a small animal PET system requires high-resolution detectors to clearly visualize and accurately quantify the distribution of a radio-tracer. However, the benefits of high spatial resolution cannot be achieved without significantly improving the detector sensitivity. To take advantage of high resolution, the image data must be reconstructed into smaller voxels. However, smaller voxels result in a smaller amount of counts per voxel and therefore a lower SNR. Thus, the simultaneous achievement of high sensitivity and resolution is mandatory to obtain a sufficient SNR in the reconstructed images.

Currently, nearly all small animal PET systems are based on detectors that consist of individual scintillator crystals optically separated by a reflective material introduced between them and assembled into a single scintillator matrix. The pixelated scintillator matrix is coupled to a number of photosensors (e.g., PMTs), and the pixel in which the gamma photon interacts is identified using light sharing between the photosensors.

The resolution of such a pixelated PET detector is primarily defined by the cross-section of scintillator pixels. The smaller the pixels are, the more precisely the position of gamma interaction can be defined, and thus, the better the spatial resolution is. In clinical PET scanners, the typical cross-section of a pixel is between 4 and 6 mm [192], [200]. In small animal PET systems, due to the need for higher resolution, the pixel cross-section varies between 1 and 2 mm [77]. Recently, some designs use pixels with a pixel cross-section of only 0.5 mm [187].

3.5.1 Disadvantage of pixelated detectors

The pixelated detector design has a number of drawbacks.

First, despite the fact that finely pixelated crystals improve resolution by limiting the spread of light, the performance of such detectors is still limited by inter-crystal scattering of the gamma photons, which is more prevalent in smaller crystals.

Furthermore, as the cross-section of the pixels decreases, more reflective material separating individual crystals must be introduced. In some designs, particularly in those that use finely pixelated crystals, the reflective material can account for a considerable fraction of the detector volume, thus reducing its sensitivity.

To increase sensitivity, one could use thicker scintillator crystals to improve their stopping power. However, the long but narrow aspect ratio of individual pixels compromises the efficiency of scintillation light collection [43], [114]. The longer and narrower pixels are, the less light that is collected from the small face of the crystals. Therefore, the majority of current small animal PET systems uses crystals that are only approximately 1 cm long. This relatively short length leads to a low intrinsic detection efficiency, which significantly contributes to the relatively low overall detector sensitivity achieved in currently available high-resolution PET systems.

Another solution to improve the overall sensitivity of PET systems is to improve the geometric efficiency (i.e., the solid angle coverage). One approach to improve the geometric efficiency is to reduce the system diameter, which essentially brings the detectors closer to the imaged object. However, bringing detectors close to each other results in more photons entering the detector crystals at large oblique angles. This causes substantial parallax positioning errors and associated spatial resolution loss resulting from the gamma photon penetration of scintillator crystals.

Moreover, the effect of parallax error is stronger in long pixels with a small cross-section. DOI correction can be applied to solve this problem but pixelated detectors do not intrinsically provide this. In pixelated detector designs with DOI correction, the DOI is often gained at the expense of other performance parameters, such as energy resolution and/or detection efficiency.

Finally, producing finely pixelated scintillation crystals is complex and expensive. This leads to a high cost per detector module and significantly increases the cost of the entire PET scanner, thus limiting its use in clinical practice.

Therefore, in pixelated detectors, a trade-off has to be made between detector resolution (many pixels with a small cross-section) and sensitivity (large dead area). To overcome the sensitivity limitation of the high spatial resolution detectors for small animal PET, novel detector designs, new scintillators with higher stopping power and/or new geometrical designs are required.

3.5.2 Monolithic detectors

An alternative for the pixelated detector designs are detectors based on monolithic (continuous) crystals coupled to one or more multi-pixel photosensors.

In a monolithic crystal, the scintillation light produced by gamma photon interaction spreads freely within the entire volume of the scintillator. Depending on the exact interaction position (e.g., crystal's center, corner or edge) and interaction depth (far or close to the photosensor surface), the scintillation light measured by the multi-pixel photosensor produces a different light intensity pattern. A strongly simplified example of such a distribution is presented in figure 3.19. By analysing these measured light distributions, one can estimate the position of the gamma photon interaction.

The monolithic detectors, due to the absence of any dead space within the scintillator, allow higher sensitivity to be achieved compared to pixelated detectors. Monolithic detectors also allow for both good energy resolution and good spatial resolution. Moreover, they intrinsically provide DOI correction without any additional modifications in the detector design. Furthermore, monolithic scinitllator crystals are easier to manufacture, require less crystal surface treatment, are cheaper to produce than pixelated ones and assembly of the detector module is easier.

3.5.2.1 Event positioning

In practice, estimating the position of the gamma photon interaction in monolithic scintillators is not a trivial task, and many different methods

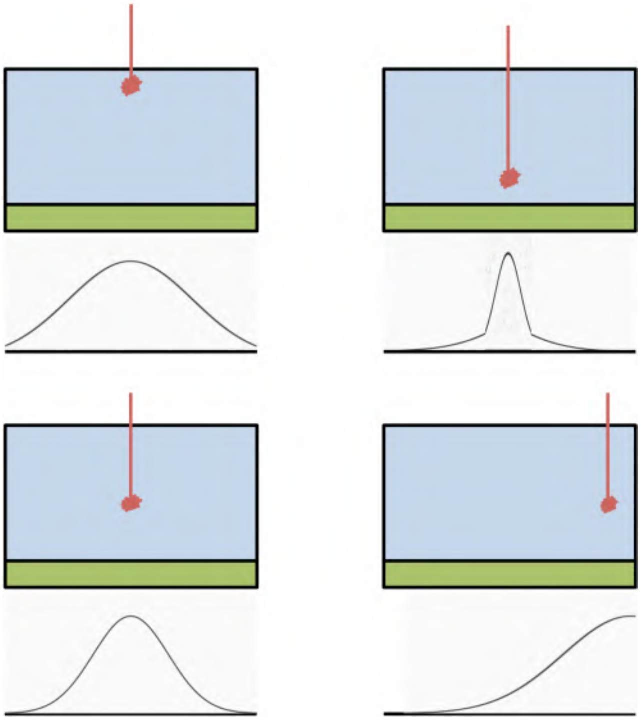

Figure 3.19: Simplified representations of a scintillation light distribution in a monolithic detector for different positions of gamma photon interactions.

have been proposed for this purpose [205], [122], [28], [211], [197], [120], [123], [128]. Using the measured light distribution based on Anger logic appears to be insufficient for precisely estimating the position and achieving good spatial resolution. Methods that use models of light propagation can be employed for estimating the interaction position from the measured distribution. Another solution is the use of statistical methods based on a calibration in which multiple light distributions are measured at known interaction positions. These statistical methods include nearest neighbour [205], maximum likelihood estimation [122] or neural networks [28].

3.5.2.2 Challenges

Successful implementation of monolithic detectors in PET systems faces a number of technical challenges that need to be overcome. The main challenge is the determination of the interaction position of a gamma photon, which is far more complex than in pixelated detectors. In pixelated detectors, the position of the gamma photon interaction can be simply determined by the position of the pixel in which the interaction occurred. In monolithic detectors, the position is estimated from the scintillation light distribution across the photosensor pixels.

Note that due to various physical phenomena (e.g., Compton scattering), the gamma photon may interact in multiple points within a monolithic crystal, which complicates the estimation of the interaction position. Moreover, the light distribution is strongly influenced by reflections on the sides and the top of the crystals, which depend on the type of crystal surface treatment and the type of reflector material applied on the crystal's sides.

Monolithic-based detectors may also require advanced electronics and readout methods. This requirement arises from the fact that scintillation photons are spread over multiple pixels and a smaller number of photons is detected per pixel. Consequently, the influence of the statistical fluctuations and the electronic noise on the number of detected photons per pixel is stronger.

Finally, the correct positioning of gamma photons in monolithic crystals may require to collect a large amount of calibration data and sophisticated, time-consuming algorithms. The calibration may be required in order to measure the differences in detector response to gamma interactions at different positions. These differences arise from effects such as inhomogeneity of the gains of a photosensor or imperfect coupling of a scintillator crystal to a photosensor. In turn, this leads to very large data sets and increased calculation times, which would require high-bandwidth and high-speed processing units.

Chapter 4

Optimized light sharing for high-resolution TOF PET detector based on Digital Silicon Photomultiplier

This chapter has been published as: R. Marcinkowski, S. España, R. Van Holen and S. Vandenberghe, "Optimized light sharing for high-resolution TOF PET detector based on Digital Silicon Photomultiplier", Phys. Med. Biol., 2014, vol. 59(23): 7125-39

4.1 Introduction

The last three decades have seen a significant improvement in the image quality of clinical PET systems [146]. The current generation of whole-body PET scanners has the axial field of view (FOV) ranging from 15 to 22 cm and typically a ring of 90 cm diameter. The majority of scanners nowadays employ detectors based on pixelated LYSO arrays with 4 mm pixel pitch and a thickness of 20-30 mm coupled to photomultipliers tubes (PMTs). The combination of fast response LYSO scintillators and fast photosensors with high-speed electronics allowed for introduction of time-of-flight (TOF) in PET clinical systems. TOF information used in whole body PET imaging results in faster convergence, better contrast and lower noise of the reconstructed images [124], [97].

Recently, combined PET/MR scanners have captured the attention of the research community. In comparison with PET/CT scanners, PET/MR benefits from the very high soft-tissue contrast of MR and lack of extra radiation dose delivered to the patient. Furthermore, the MR scanner offers many additional advantages: sequence specific contrast, functional MRI, spectroscopy and the ability to acquire simultaneous PET/MR images [155]. The first simultaneous whole body PET/MR scanner has recently been released by Siemens [58]. However, early PET/MR systems were using avalanche photodiodes (APDs), which do not allow an accurate measurement of arrival time due to their low gain and slow response [184].

A new type of photosensor known as silicon photomultiplier (SiPM) was introduced relatively recently [62],[160] as an alternative for PMTs. This new photosensors made of arrays of Geiger-mode APDs (cells) achieve high gain, fast response and are insensitivity to magnetic fields. Single SiPM devices of the recent generation are capable of achieving very good results for TOF-PET applications [69]. This makes them suitable for combined TOF-PET and MR scanners. However, readout of signals from arrays of SiPMs requires the development of high-performance and low noise application specific integrated circuits (ASICs) in order to fully exploit the intrinsic performance of SiPM photosensors. This imposes a scalability challenge for use in PET scanners, where hundreds of SiPMs arrays need to be read out by hundred of ASICs, each needed to display a low noise and a high stability.

Philips Digital Photon Counting (PDPC) has recently introduced a novel type of SiPM – a digital silicon photomultiplier called Digital Photon Counter (DPC) [74], [54]. These devices employ early digitalization of the APD signals by integrating CMOS circuitry into the SiPM chip. Thanks to this approach, noise free, gain-independent photon counting is achieved. DPC also allows to precisely measure time of photon arrival. In addition, DPC are not affect by afterpulses. Furthermore, the readout of these devices can be easily scalable in systems. A TOF-PET demonstrator was built based on DPC devices coupled to LYSO arrays with a one-to-one coupling scheme (crystal size 4×4×22 mm^3) obtaining a coincidence resolving time (CRT) of 266 ps [53], which outperforms the results obtained with current TOF-PET scanners (585 ps, [192]). Another advantage is that the timing performance was independent of the count rate, contrary to what is obtained in TOF-PET scanners based on photomultiplier tubes (PMTs) [190]. Based on this technology, just recently Philips Healthcare released Vereos PET/CT scanner (Veroes), which is the world's first whole-body PET scanner base on DPC detectors from PDPC.

Like the Vereos, most of the whole body PET scanners are based on crystal arrays with a transverse pixel size of 4 mm and a thickness varying from 20 to 30 mm. However, recent studies using Monte Carlo simulations have shown that a significant improvement in image spatial resolution can be obtained when decreasing the pixel size from 4 to 2 mm (see table 4.1) [201], [193].

Table 4.1: Spatial resolution FWHM at the centre of the field of view obtained with Monte Carlo simulation for whole body PET scanners with different LYSO pixel sizes [201]

Pixel size (mm^3)	Radial (mm)	Tangential (mm)	Axial (mm)
2×2×22	2.2	2.2	2.4
4×4×22	3.3	3.4	3.5

Here we present the evaluation of a high-resolution, TOF-PET detector based on the DPC coupled to pixelated LYSO array with 2 mm transversal pixel size intended for a whole body scanners. The optimal detector configuration and arrangement was explored in order to provide a feasible detector design. First, we provide a brief description of the working principle of the DPC arrays and study their performance in a typical crystal arrangement (white reflector and light guide) with crystal pitch of 2 mm. Based on these results we then propose an optimized detector design using a special reflector arrangement in order to overcome count rate and sensitivity limitations while further improving the CRT results.

4.2 Materials and Methods

4.2.1 Working principle of DPC arrays

The DPC3200-44-22 array from PDPC was used in this work. The Philips Digital Photon Counter Technology Evaluation Kit (PDPC-TEK) was used to perform data acquisition. A single DPC has a size of 3.2 × 3.2 cm^2, with a fill-factor of 78%, and consists of 4 × 4 independent units called dies. Each die is further divided into 4 DPC pixels arranged in a 2×2 matrix with a 4 mm pitch. Each pixel consists of 3200 cells of 59 × 64 μm^2. Furthermore, each pixel is divided into 4 quadratic logic units called sub-pixels. Each of these sub-pixels is even further divided into 8 logic sub-units called RTL rows (row-trigger-lines). An overview of the building blocks of a DPC is shown in figure 4.1.

Each die can work independently providing an individual time stamp and the number of fired cells in each pixel. Compared to analogue devices that

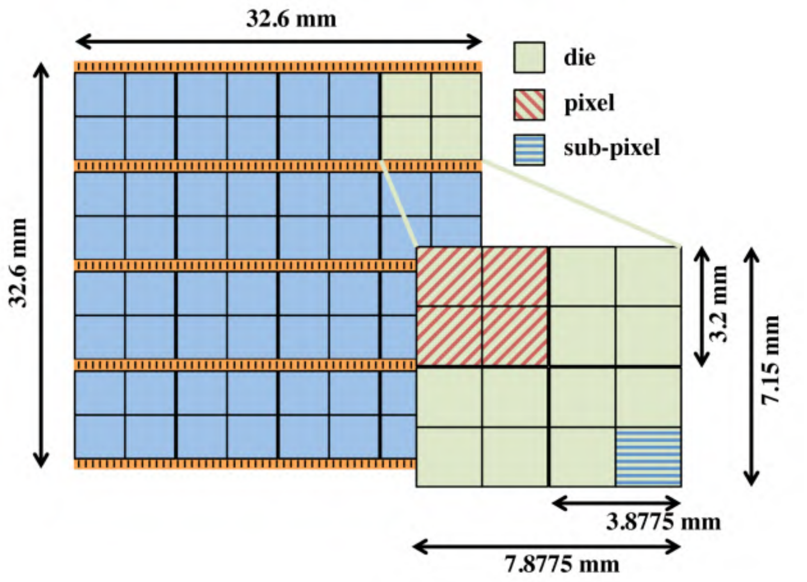

Figure 4.1: Overview of the DPC. The array consists of 4 × 4 dies, each cnsisting of 4 × 4 pixles that further splits into 4 × 4 sub-pixels.

rely on the comparison of the output signal with reference thresholds in order to produce trigger and validation signals, DPCs are based on the Boolean interconnection of sub-pixels to generate a trigger signal and the Boolean interconnection of RTL rows to generate a validation signal for each die. Trigger signal indicates a start of DPC acquisition sequence and defines a moment of generating a corresponding timestamp. Validation signal is a second, higher-level photon count threshold, which indicates that a number of detected photons across a surface of the pixel is high enough to consider event as a valid one and not a noise event. A die is triggered only when a Boolean expression set by a chosen trigger level of a DPC tile is fulfilled. Respectively, the validation signal is generated only when the Boolean expression between RTL rows set by a chosen validation level of a DPC tile is fulfilled. Sub-pixel and RTL row logic units achieve Boolean state of 1 when at least one cell in this unit has been fired. The Boolean interconnections corresponding to particular trigger and validation levels of DPC are presented in table 4.2 and 4.3 respectively.

The acquisition sequence of a single DPC die is shown in figure 4.2. When the trigger is generated, a die is saving a timestamp. Immediately after the trigger, there is a limited and configurable amount of time, called the

Table 4.2: The four different Boolean interconnections between sub-pixels corresponding to different trigger levels of DPC.

Trigger level	Logic connection of sub-pixels (sp)
1	sp1 $\vee$ sp2 $\vee$ sp3 $\vee$ sp4
2	[(sp1 $\vee$ sp2) $\wedge$ (sp3 $\vee$ sp4)] $\vee$ [(sp1 $\vee$ sp4) $\wedge$ (sp2 $\vee$ sp3)]
3	(sp1 $\vee$ sp2) $\wedge$ (sp3 $\vee$ sp4)
4	sp1 $\wedge$ sp2 $\wedge$ sp3 $\wedge$ sp4

validation time (5-40 ns), during which the validation level, i.e. a threshold of detected optical photons across a pixel, needs to be fulfilled to recognize the occurred trigger as a valid event. If the trigger is not validated during this time, the event is discarded and all the cells of the die are recharged (20 ns). During recharge the die is unable to detect arriving events. In case the trigger is validated, an integration time can be set (0-20 μs) to accumulate additional incoming light photons. After this, the readout of the number of fired cells in each pixel takes exactly 680 ns and recharge of the die takes place.

The DPCs generate dark signal due to thermal excitation. Thermally generated carriers can start the avalanche process, which causes cells to fire even in the absence of light. Such firing of a cell is called a dark count. In normal acquisition mode of DPC, the cells are recharged only at the end of acquisition chain as explained before. Therefore, even when no optical photons arrive, a DPC is accumulating fired cells produced by dark counts until the trigger level is reached. Depending on the dark count rate (DCR) and the chosen trigger level, the DPC generates dark count triggers at different rate. Furthermore, depending on the validation level and validation time, such trigger can be validated resulting in the registration of an event not related to gamma detection (called a dark count event). If the validation is not fulfilled the recharge of the die will be invoked after the validation time.

Table 4.3: The four different Boolean interconnections between RTL rows corresponding to different validation levels of DPC.

Validation level	RTL rows logic gates connection							Sub-pixels connection
	0	1	2	3	4	5	6	
1	OR	OR	OR	OR	OR	OR	OR	OR
2	OR	OR	OR	AND	OR	OR	OR	OR
4	OR	AND	OR	AND	OR	AND	OR	OR
8	AND	AND	AND	AND	AND	AND	AND	OR

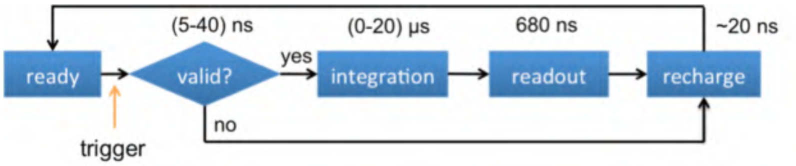

Figure 4.2: Acquisition sequence for a single die of the DPC.

During this recharge process a die is inactive. This can lead to a complete or partial loss of the light generated by gamma events that arrived during the recharge of the die. Furthermore, the increase in the number of recharge steps caused by dark counts leads to the extension of the overall dead time of the detector [132].

The DPC allows to measure the DCR of each cell and to enable or disable cells. It was shown by Frach [74] that 80% of the dark counts of the entire die are produced by only 10% of cells with the highest DCR. Therefore, those cells can be disabled to significantly reduce the DCR while the active area is reduced by 10%. We chose 10% as a good compromise between active area and DCR for TOF applications.

In addition to the independent operation mode each individual die, the DPC can work in Neighbour Logic (NL) mode. In the NL mode, the first die that triggers and validates successfully force all the other dies to start data acquisition cycle regardless of their own trigger and validation criteria. This is useful when the scintillation light is spread over several dies and all of them are needed to calculate the energy, position and arrival time of the event. In that way, even dies illuminated with a low light intensities, that normally would not be able to fulfill the trigger/validation criteria by their own, can record incoming optical photons.

4.2.2 Reference detector

In the following measurements we used a reference detector consisting of a DPC coupled to a single LYSO crystal with size of $2 \times 2 \times 22$ mm^3 wrapped with Teflon tape and placed at the centre of one of the DPC pixels. Silicone optical grease (BC-630, Saint-Gobain) was used for the optical coupling. The individual timing resolution of the reference detector (Δt_{ref}) was obtained using two identical reference detectors.

For all presented measurements we used some common configurations for all DPC devices, which are: validation level 8, validation time 40 ns, integration time 165 ns, coincidence window of 20 ns and 10% of deactivated

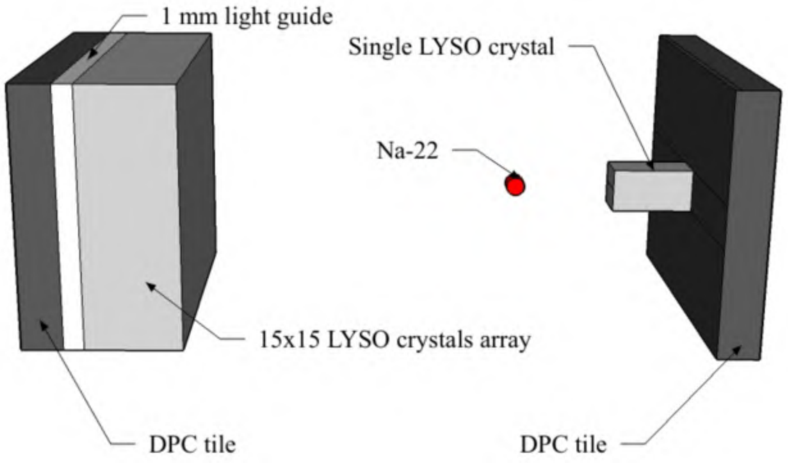

Figure 4.3: Schematic of the setup containing a reference detector (right) and an array detector (left).

cells. We used an energy window of ±10% the photopeak. The working temperature of all DPC devices was held within the range of 6 °C to 7.5 °C.

4.2.3 Pixelated array with a light guide

A DPC was optically coupled to an LYSO array with 15 × 15 crystals, each of size 2 × 2 × 22 mm^3 , all surfaces polished, separated by a 51 μm thick white diffuse reflector (Saint-Gobain). In order to achieve correct crystal identification the light needs to be spread to different pixels of the DPC. A 1 mm thick light guide made of borosilicate glass was placed between the scintillation crystal array and the DPC. This detector was placed at 16 cm opposite to the reference detector as shown in figure 4.3. The 10 μCi ^{22}Na source was placed at 1 cm from the reference detector and 15 cm from the detector. The NL option was enabled to read out all dies of the DPC, even those that recorded only a small fraction of optical photons, which could be insufficient for successful validation when each die would work independent. The use of the NL option allows to record all optical photons generated in a single event, thus allows to correct resolve all crystals in the array.

4.2.3.1 Coincidence resolving time, energy resolution and flood map

The CRT was measured for each of the trigger level configurations (1, 2, 3 and 4) of the DPC arrays acquiring 5 million coincidence events for each case. The energy resolution was also measured for one case (trigger level 1), as it is not expected to change with the trigger level. A flood map of the detector was obtained and a self-organizing map (SOM) algorithm ([87] was applied to it to automatically build the crystal look-up table.

4.2.3.2 Time calibration

For timing measurements, only events within the energy window were used. Due to the light spread among different dies that each one contains individual timestamp, it was necessary to perform a skew time calibration between dies. Setup shown in figure 4.3 was used for calibration. Both detectors were set to trigger level 1. The skew time value for each die was obtained as the mean time difference for the coincidence events recorded between the reference detector and the LYSO crystal closest to the center of that die in the other detector. As shown by Seifert [175], the earliest photons arriving at the photosensor contain the most precise information of the arrival time of the gamma photon on the detector. The earliest timestamp obtained after applying skew correction, was used as the arrival time of the detected photon.

4.2.3.3 Estimation of event loss due to dark counts

The presence of dark counts can lead to a loss of events as explained in section 4.2.1. We studied what was the fraction of recorded events that had at least one die missing due to the dark counts and had to be discarded due to missing data. The fraction of event loss was evaluated for different trigger levels and temperatures. In order to minimize the loss of events a special detector arrangement is proposed in the following section.

4.2.4 Special reflector arrangement without NL

Several strategies can be followed to reduce the loss of events when using DPC arrays for TOF-PET. One option is to decrease the dark count rate by reducing the working temperature [203] while increasing the complexity of the system. Another possibility is to reduce the dark count rate by disabling a higher fraction of cells although the active area gets reduced, resulting in a

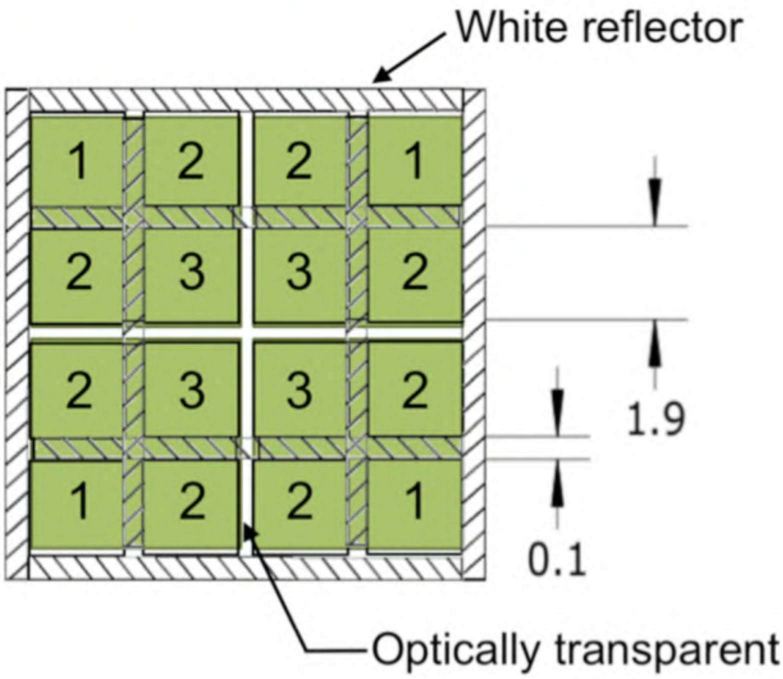

Figure 4.4: Schematic representation of the 4 × 4 LYSO crystal array and the special reflector arrangement proposed to focus the scintillation light onto single die of the DPC array. Each crystal has a size of 1.9 × 1.9 × 22 mm^3. Individual crystals are represented by black boxes. Four pixels of a single die of DPC are represented here by four green squares. The dashed area represents white reflector and the remaining inter-crystal area represents an optically transparent foil.

loss of energy resolution. To solve the issue of event loss we propose to build a scalable array of 4 × 4 crystals that focuses all the light on a single die while allowing for crystal separation by using a special reflector arrangement. The arrangement splits crystals into subgroups with different light sharing pattern among them as presented in figure 4.4. This allows each die to work independently as in 1:1 coupling scheme with 4 mm crystal pitch (shown by Degenhardt [53]) and still use crystals with 2 mm pitch for achieving higher spatial resolution. In order to better adjust the crystal array to the active area of the DPC die (7.15 × 7.85 mm^2) we chose a crystal size of 1.9 × 1.9 × 22 mm^3. We built one of the proposed arrays and coupled it to one die of a DPC. The flood map, energy resolution and CRT were measured using trigger level 1.

4.3 Results

4.3.1 Reference detector

A CRT of 253 ps was obtained using two reference detectors leading to an individual timing resolution of the reference detector (Δt_{ref}) of 178 ps.

4.3.2 Pixelated array with light guide

4.3.2.1 Coincidence time, energy resolution and flood map

The CRT obtained for trigger level 1 for each individual crystal of the array is shown in figure 4.5(a). An average time resolution of 376 ps was obtained for this particular trigger level. It can be noticed that three rows of crystals provided worse CRT. This is caused by the reduced amount of detected photons as these crystals are located over the dead area of the DPC array that contains the wiring (see figure 1). Figure 4.5(b) presents the histograms of the CRT obtained for each crystal of the array using different trigger levels. There is a significant degradation of the CRTs when the trigger level is increased obtaining average CRT values of 376, 558, 758 and 1483 ps for trigger levels 1 to 4 respectively. The CRT_{array} for two equal array detectors would be equal to 468, 747, 1042 and 2082 ps respectively.

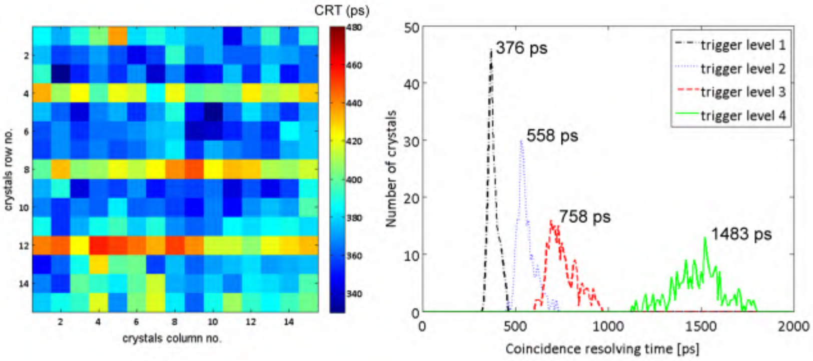

(a) (b)

Figure 4.5: (a) CRT for all the crystals of a 15 × 15 LYSO array obtained using the trigger level 1 option. (b) Histogram of the CRT for all crystals in the array using different trigger levels.

The number of optical photons and the energy resolution at the photopeak position for each crystal of the array are shown in figure 4.6(a) and 4.6(b)

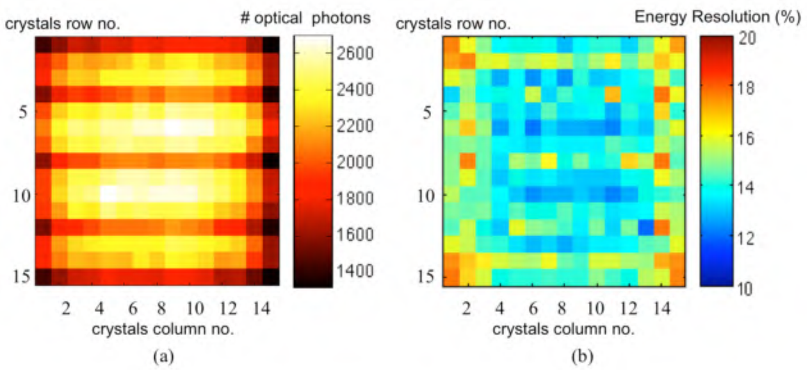

Figure 4.6: (a) 511 keV photopeak position and (b) energy resolution FWHM across the detector array.

respectively. The photopeak position shift by 30 % down when moving from the central region to the edges of the detector. This can be explained in part by the fact that we did not use reflector on the lateral sides of the light guide. The three rows of crystals with a lower photopeak position in the central region are located over the dead area of the DPC array that contains the wiring.

An average energy resolution of 14.5 % FWHM was obtained with a sigma equal to 1.3 %. Cross talk and saturation corrections [204] were not included. The flood histogram of the detector consisting of 15 × 15 LYSO crystals coupled to a DPC array obtained at trigger level 1 is shown in figure 4.7(a). All of the individual crystals in the crystal array can be clearly resolved. Figure 4.7(b) shows a line profile across one of the crystal rows in the flood histogram. An average peak to valley ratio of 12:1 was obtained. In the presented flood histogram the edge crystals contain more counts than the central crystals due to higher number of events accepted after applying the event filter described in section 4.2.3.3. As the light of the crystal in the edges spreads over a smaller number of dies, there is a lower probability to lose one of the dies containing relevant information of the event.

4.3.2.2 Skew time calibration

In order to proceed with the time skew calibration we selected for each die the crystal that deposits the highest fraction of light in that particular die. The die with the shortest delay was then used as a reference in order to obtain only positive values of relative skew time (see figure 4.8). Time skews up to 858

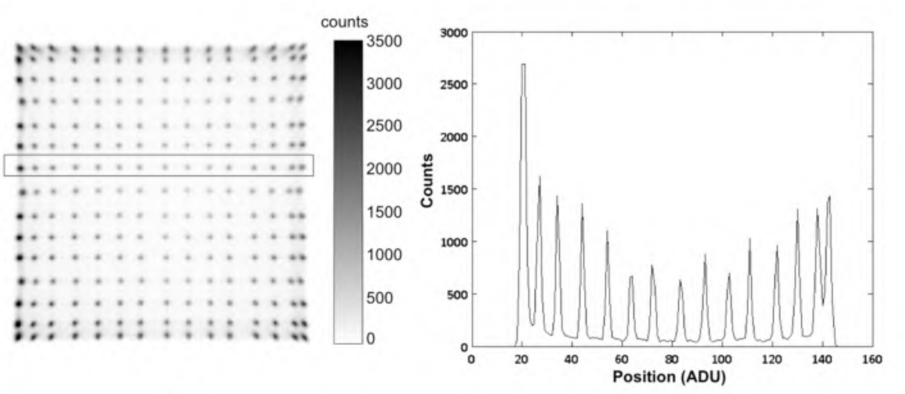

(a) (b)

Figure 4.7: (a) Flood histogram of the array of 15 × 15 LYSO crystals coupled to a DPC array and (b) line profile across the row of crystals inside the box shown in the flood histogram.

ps were obtained, which is much larger than the timing resolution obtained for the reference detector. Therefore, taking these skews into account is of crucial importance for DPC-based TOF-PET detectors where the scintillation light is spread among different dies and an individual time stamp for each die is obtained.

4.3.2.3 Valid events

As explained in section 4.2.3.3, incomplete events with missing dies can be obtained due to the triggers produced by dark counts. Figure 4.9(a) shows

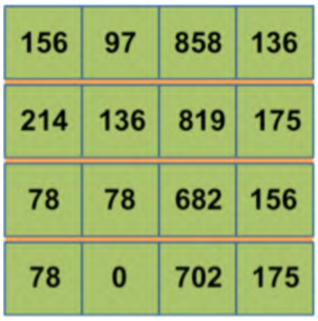

156	97	858	136
214	136	819	175
78	78	682	156
78	0	702	175

Figure 4.8: Map of electronic time skews the dies in DPC using the one labelled with a 0 as a reference. The values are in units of picoseconds.

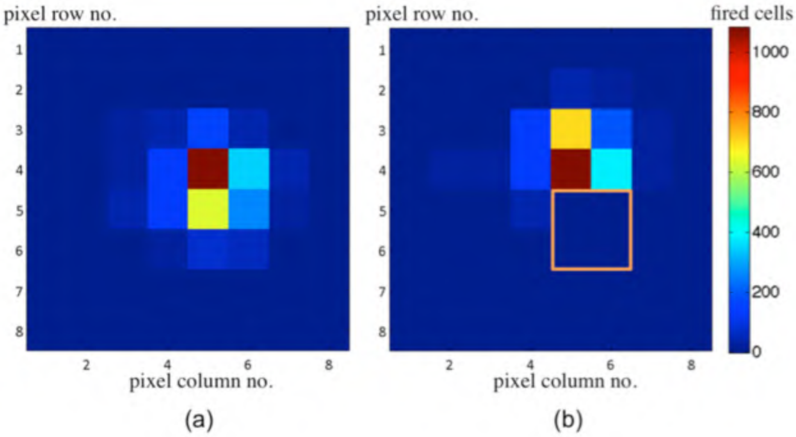

Figure 4.9: Examples of recorded events (a) where all dies were available during photon detection and (b) where one die (marked by the orange box) adjacent to the position of gamma interaction was lost. Colour scale represents number of recorded optical photons in DPC's pixels (8 × 8)

an example of the light distribution obtained for one event where all the dies with relevant information were recorded. Figure 4.9(b) shows an example where one die containing relevant information was lost. As described in section 4.2.3, incomplete events are discarded in order to avoid detector performance degradation in terms of crystal identification, energy resolution and CRT.

For used trigger level 1, 2, 3 and 4 the fraction of accepted singles events out of the total number of recorded singles was 39, 66, 69 and 80 % respectively. The average cumulated dark count rate per die was 3.2 Mcps for all conducted measurements. The higher event loss for lower trigger levels is caused by the fact that less accumulated dark counts are needed to trigger a die. Thus, for the lower trigger levels there is a higher probability that one or more dies are recharging when the gamma event is being recorded. Cumulated dark count rate in the DPC depends on the temperature of the device. Thus, at higher working temperature the dark counts trigger rate is higher causing a higher percentage of events with missing dies. We measured a tile at room temperature (22-23 °C): with the same setup and detector configuration, only 11, 37, 39 and 68 % of recorded events could be accepted for trigger level 1 to 4, respectively.

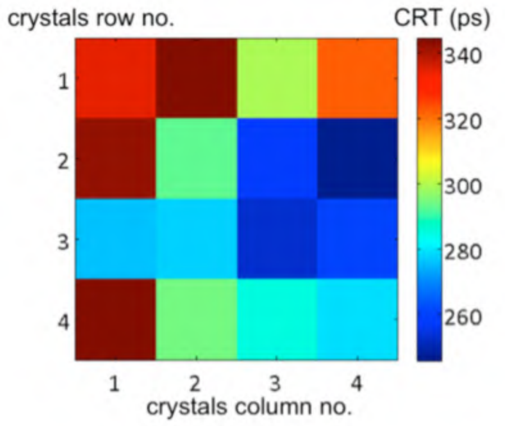

Figure 4.10: CRT for all crystals in the array with special reflector arrangement. Values obtained for trigger level 1

4.3.3 Special reflector arrangement

Figure 4.10 shows the CRTs obtained for all crystals in the array with reflector arrangement for trigger level 1. The average CRT achieved in this case was 295 ps, what for two equal detector arrays would give CRT_{array} of 332 ps. Worse CRT values can be observed in corner crystals. This is related to the reduced number of optical photons detected for these crystals as the first photons arriving at the photosensor can be lost in the inactive areas of the die over which these crystals are located.

Figure 4.11(a) shows the 511 keV photopeak position across all individual crystal elements in the array. A non-uniformity of the photopeak position can be observed across the array. The average photopeak position is 2130, 1720 and 1230 optical photons for central, edge and corner crystals respectively. This is caused by the different light sharing pattern between different crystals groups described in section 2.4. Furthermore, crystals located along die edges, especially crystals in the corners, are not fully placed over the active area of a die (7.15×7.85 mm^2) as the array is slightly too large. This causes a loss of a small fraction of light for these crystals. These factors also cause the position dependent energy resolution at 511 keV across all crystals in the array as shown in figure 4.11(b). Average energy resolution yields a FWHM of 11% and 17% for the crystals located in the center and at the corners respectively.

The flood histogram of the scalable 4×4 crystal array with the proposed reflector arrangement coupled to one of the dies of the DPC is shown in

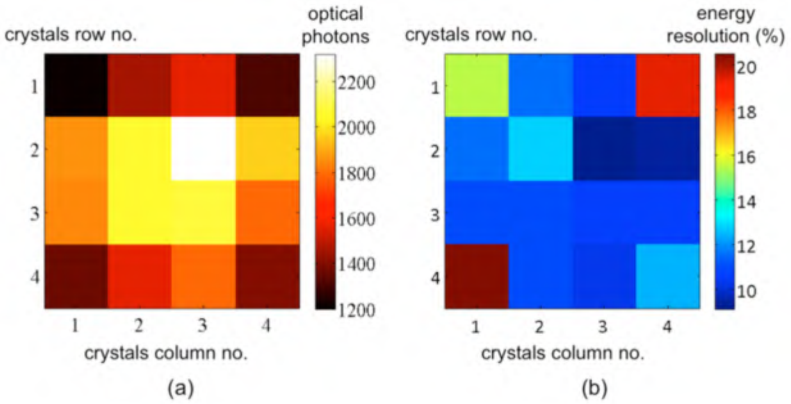

Figure 4.11: (a) 511 keV photopeak position and (b) energy resolution FWHM across all crystals of the array with special reflector arrangement.

figure 4.12(a). All crystals in the array can be clearly resolved obtaining an average peak to valley ratio of 20:1. Figure 4.12(b) shows a line profile along one column of crystals in the flood histogram. The dislocation of part of the crystals inside the array is caused by misalignments made during manual assembly of the array from single crystals and Teflon tape.

The most significant advantage of this crystal arrangement is the fact that only one die is necessary to correctly record incoming event as each of

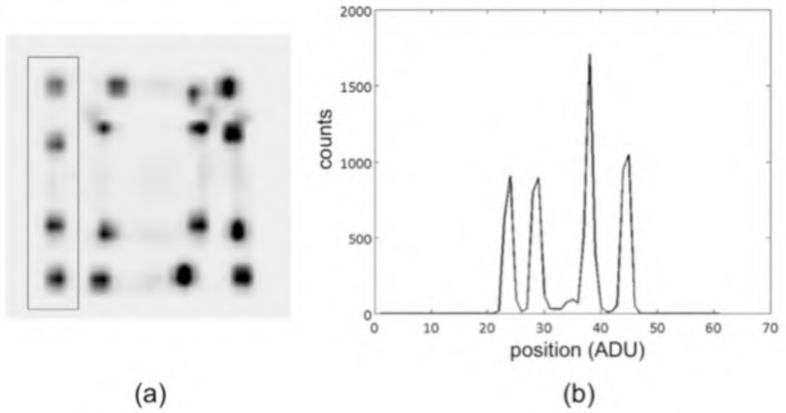

Figure 4.12: (a) Flood histogram of the array of 4 × 4 LYSO crystals coupled to a DPC array and (b) line profile across the column of crystals inside the box shown in the flood histogram.

sixteen dies works independently. This allows for a remarkable improvement in terms of detector's count rate in comparison to the use of NL and a light guide in light sharing approach where multiple dies are necessary to record a single gamma event. Using a pulse light emitting diode (LED) driven by a pulse generator as a source of known output in terms of events count rate it has been shown by Marcinkowski et al [132] that for the chosen configuration (trigger level 1, validation level 8, validation time 40 ns, 10% of cells deactivated) a single die is able to correctly record 86% of generated LED events. LED pulses were generated at rate of 10 kHz and the amplitude of generated pulses was set to match LED light output with the number of optical photons registered by a DPC for a 511 keV gamma interaction in LYSO.

4.4 Discussion

The use of a light guide and NL allows to correctly resolve crystals with 2 mm pixel pitch coupled to a DPC despite the lack of one-to-one coupling. All pixels in the 15×15 LYSO array can be clearly identified with a good peak to valley ratio, 12:1. Using such an approach it is possible to achieve reasonable energy resolution, 14.5% on average.

A CRT of 376 ps is obtained for 15 × 15 LYSO array which is substantially worse than that obtained by Degenhardt [53]. Differences can be explained by the contribution of different factors. The size of the crystals used in this study was $2 \times 2 \times 22$ mm^3 compared to $4 \times 4 \times 20$ mm^3 pixels employed by Degenhardt [53]. As shown by Levin [114], using thinner and longer crystals produces a decrease of the light reaching the photosensor due to the increase of light absorption along its propagation in such crystals. Furthermore, the use of one-to-one coupling scheme by Degenhardt [53] results in a smaller transit time spread contribution ([145], [45], [110]), which results in better CRT. In addition, the light guide further increases transit time spread, thus worsening the CRT. Finally, the accuracy of the time skew calibration can also contribute to a decrease of the timing resolution. The calibration could be improved by using a picolaser and a DPC without scintillator as shown by van Dam [203].

The reduced amount of valid events, i.e. those where all dies with relevant information were recorded (see section 4.3.2), prevents to use a standard configuration of scintillator crystal array with light guide proposed in the first place. Van Dam [203] showed that reducing the temperature to -25 °C could significantly reduce the DCR in the DPC facilitating the use of a light sharing configuration with optimal timing performance. However, a complete PET scanner working under such low and uniform temperature would need a very complex cooling system.

Therefore, we proposed an alternative solution (section 4.3.3) that allows to focus all light of the crystal array onto a single die, obtaining an equivalent situation in terms of dark counts effect as the one-to-one coupling scheme used by Degenhardt [53]. Moreover our design allows the use of crystals with half transverse size, which can greatly improve the image quality of human PET scanners as shown by Thoen [201] and Surti [193]. With the proposed approach it was possible to correctly resolve crystals with 1.9 mm transverse pitch while achieving an average CRT of 295 ps. Two such array detectors in coincidence would result in CRT equal to 332 ps, which is only 19% worse compared to the results obtained in [53]. The improvement in timing resolution compared to the 15 × 15 LYSO array are caused by reduced transit time spread of light in the detector due to the absence of a light guide and the focus of the light on a smaller area of photosensor.

To achieve such good timing resolution the DPC needs to operate at trigger level 1. In order to reduce the fraction of time during which individual dies are recharging, it is important to reduce the DCR as much as possible when using this trigger level. As DCR depends on the temperature of the DPC it is necessary to cool down the device below room temperature. In terms of detector's dead time, operating a DPC at trigger level 1 and at room temperature is not feasible. As was shown here and by Degenhardt [53], operating the device at 5-10°C is possible. Achieving such level of cooling in the system can be possible with water-cooling or with Peltier cooling. This amount of cooling is far more reasonable to achieve at system level than -25°C [203].

Another approach, which can be employed to reduce DCR, is to turn off a larger fraction of the device's cells that contribute most to the DCR (here, we deactivated 10% of the cells). However, this can lead to a degradation of the energy and timing resolution of the detector.

4.5 Conclusion

The performance of a detector based on DPCs and pixelated LYSO crystal arrays with 2 mm and 1.9 mm transverse pixel size intended for high-resolution whole body TOF-PET has been investigated. We found that the DPC is a suitable photosensor to build a high-resolution detector for whole body TOF-PET scanners that employ crystals with transverse pitch below 4 mm, which are typically used in state-of-the art systems. With a LYSO array of 2 × 2 × 22 mm^3 crystals and use of the light guide and NL we achieved the average CRT of 376 ps and the average energy resolution of 14.5 %. However, this configuration has the disadvantage of count loss due to dark counts. We solved this issue by developing a detector based on LYSO array with 1.9 × 1.9 × 22 mm^3 crystal size with special reflector arrangement between crystals. With this approach the average CRT of 295 ps was achieved and the average energy resolution yielded 11 %. To achieve such CRT, which outperforms state-of-the art TOF-PET scanners, trigger level 1 was used in both cases. In order to work at trigger level 1 (and do not compromise detector's overall count rate performance), DCR needed to be reduced by cooling the detector and deactivating DPC's cells with the highest DCR.

4.6 Acknowledgements

S. España is funded by the BOF (Special Research Fund) of Ghent University. Roel Van Holen is funded by the Research Foundation - Flanders (FWO, Belgium) and Ghent University. This work was supported in part by EU FP7 project SUBLIMA, grant agreement no 241711, see also www.sublima-pet-mr.eu and by iMinds - Future Health Department.

Currently S. España is with Advanced Imaging Unit, Centro Nacional de Investigaciones Cardiovasculares (CNIC), Madrid, Spain.

Chapter 5

Effects of dark counts on digital silicon photomultipliers performance

This chapter has been published as: R. Marcinkowski, S. España, R. Van Holen and S. Vandenberghe, "Effects of dark counts on digital silicon photomultipliers performance", Nuclear Science Symposium and Medical Imaging Conference (NSS/MIC), 2013 IEEE. IEEE, 2013, p. 1-6

5.1 Introduction

5.1.1 Digital Silicon Photomultipliers

Digital Silicon Photomultipliers (dSiPM) are solid-state single-photon sensitive devices made of arrays of Geiger-mode avalanche photodiodes. In contrast to analogue SiPM, these devices integrate CMOS electronics into a silicon photomultiplier chip for early digitization of Geiger-cell output resulting in fully digital readout. As a result, they achieve gain-independent photon counting with accurate photon arrival time information. This makes them very promising devices for the next generation of detectors for medical imaging applications [1]. Due to the novel architecture, the dSiPM contains a set of configurable parameters that must be well understood for the optimal use of this device as a gamma photon detector. The optimal configuration parameters for each application vary depending on the energy of the gamma, the light output, time response of the scintillator and the spread of the scintillation light over the sensor. In particular, dark counts can lead to partial or complete loss of gamma events or give rise to noise events, uncorrelated with gamma events.

Since dSiPMs are solid-state devices, they generate dark signal due to thermal excitation. Thermally generated carriers can fire the avalanche process, what leads to the firing cells of the device even in the absence of light. These noise events are referred as dark counts. The amount of dark events generated per second is referred as dark count rate and depends on the temperature of the device. The higher the temperature, the higher the dark count rate.

To explain loss of gamma events due to dark counts we will first give a brief introduction to the operation principles of the dSiPM. The dSiPM device consists of 16 independent units, called dies. Each die contains 4 SiPM pixels (active area: 3.2×3.8 mm^2) with each pixel further split into four sub-pixels. Each die contains individual trigger and validation logics, which are based on different Boolean interconnection of pixels and sub-pixels. A trigger is produced when the configured trigger level is met [2]. At that moment a configurable time (validation time) is started during which a certain validation level (i.e. a certain number of light photons) must be reached in order to start recording the event. The die is reset if the validation level is not reached. During this reset, the cells are recharged and are therefore not able to detect any arriving light photons. According to specification, the recharge time is 20 ns. The acquisition sequence of the dSiPM is presented in figure 5.1.

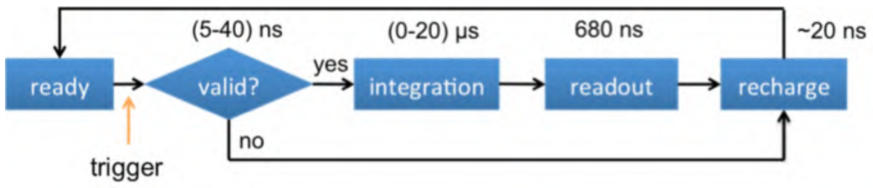

Figure 5.1: Acquisition sequence of dSiPM sensor.

5.1.2 The influence of dark counts on the dead time and the spectrum of dSiPM

With the lowest trigger level (1) only one fired cell is needed to trigger the die. When combined with a high validation level, the trigger caused by the dark count fired cell will probably not be validated and recharging will start after the validation time. Therefore, the higher the dark count rate, the longer the fraction of time during which the die will be inactive. This inevitably will lead to longer dead time and to the higher loss of real gamma events. This is illustrated in figure 5.2.

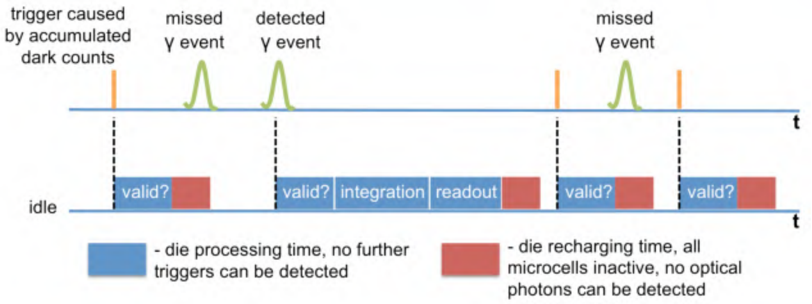
trigger caused
by accumulated
dark counts
missed
γ event
detected
γ event
missed
γ event
t
idle
valid?
valid?
integration
readout
valid?
valid?
t
- die processing time, no further triggers can be detected
- die recharging time, all microcells inactive, no optical photons can be detected

Figure 5.2: Illustration how dark counts can lead to the loss of gamma events in dSiPM.

At a higher trigger level, cells fired due to dark counts accumulate until the trigger level is met. In that way, at the same dark count rate, the dark count trigger rate is reduced but will still have a significant influence. On the other hand, when we use a higher trigger level it will be more likely that the trigger produced by dark counts will also meet the validation level. This would then result in events in the energy spectrum formed by a combination of dark counts; these will be called dark count events. To prevent this effect there is an option, called RTL refresh, that allows for fast reset of full cell rows of sub-pixels (row-trigger-lines; RTL), where one or more cells have been fired but no die trigger has been generated after a predefined time (20 ns). Thus, this feature avoids the dark counts to accumulate. During this RTL reset, only cells in one particular RTL line are recharged while all other cells are kept active. This allows the entire die to remain in an active state and detect incoming gamma events. This feature can obviously not be used for trigger level 1 as each fired cell already generates a trigger.

For several configurations it is necessary to have light spreading over different dies. Typical examples are detectors employing monolithic crystals [167], [174] or pixelated crystal arrays with pixel size not matching the light sensor pixelization [130], [169]. In these cases it is required to simultaneously read out several dies in order to process the event. As the light is spread onto several dies there is a higher probability that one or more dies, which are supposed to collect light from an incoming gamma photon, are in the recharge phase after being triggered by dark counts. Such situation is presented in figure 5.3.

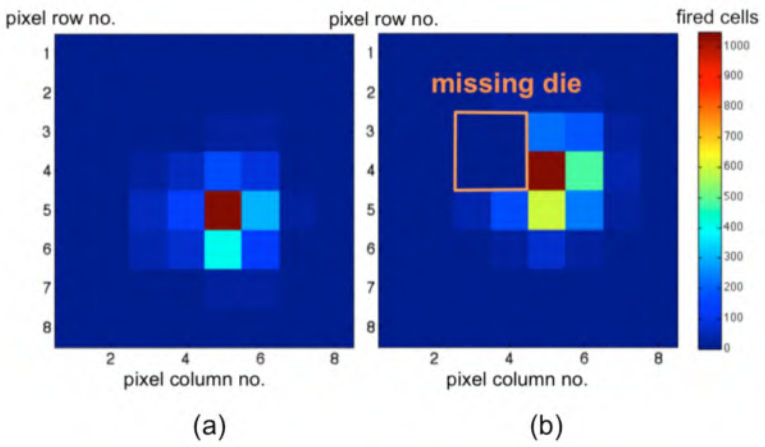

Figure 5.3: Example of recorded light distribution of 511 keV interaction where all dies of dSiPM array were available (a) and where one die was missing (marked by the orange box) due to undergoing recharge (b). Color scale represents number of recorded optical photons in dSiPM's pixels.

In dSiPM devices there are two ways to detect light spread over several dies. The first approach is to set the validation level to a low value such that all dies measuring a significant amount of light will independently start their readout. The second approach is to force the readout of all the dies in the devices by using the Neighbor Logic (NL) option. NL is a feature of dSiPM that allows a first successfully triggered and validated die to become a 'master die', forcing all other dies to start acquiring data.

In this work we studied different DPC configurations in order to quantify events loss of the dSiPM device due to dark counts and to provide guidelines on the optimal configuration for different detector designs and applications.

5.2 Materials and methods

In this study a single dSiPM array DPC3200-22-44 (Philips Digital Photon Counting) was used. In order to control the expected output in terms of events count rate and number of detected optical photons per event a pulse light emitting diode (LED) was used as a source of optical photons. The LED was placed 7 cm from the detector so that the whole surface of dSiPM was illuminated by light produced by the LED. The LED was driven by Agilent Function/Arbitrary Waveform Generator, type 33220A-ABA, which was set to output pulses 100 ns width, 5 ns both rising and falling edge at a frequency of 10 kHz. Since the main scintillator of interest to use with the detector is LYSO, the amplitude of generated pulses was set to match LED light output with the number of optical photons registered by a DPC for a 511 keV gamma interaction in LYSO (3000 registered photons per die). The whole setup was placed in a temperature chamber where the working temperature of dSiPM during measurements was kept within 3.5 °C to 5 °C. The overview of measurement setup is shown in figure 5.4.

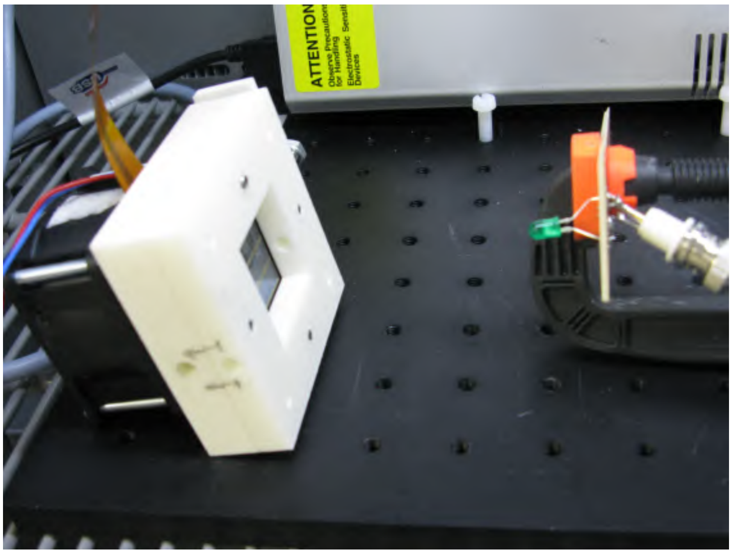

Figure 5.4: Overview of the measurement setup.

For all measurements a fixed integration time length of 165 ns (similar to setting used for LYSO) was used for dSiPM device. Furthermore, 10% of the most active cells were disabled in order to reduce dark count rate (DCR) in the detector. At the given working temperature, this resulted in a cumulated DCR of about 3.1 MHz per die. Figure 5.5 shows the measured cumulated DCR of a single die (active area: 7.15 × 7.87 mm^2) at 4 °C as a function of the percentage of active cells.

To quantify the event loss for different dSiPM configurations and to de-

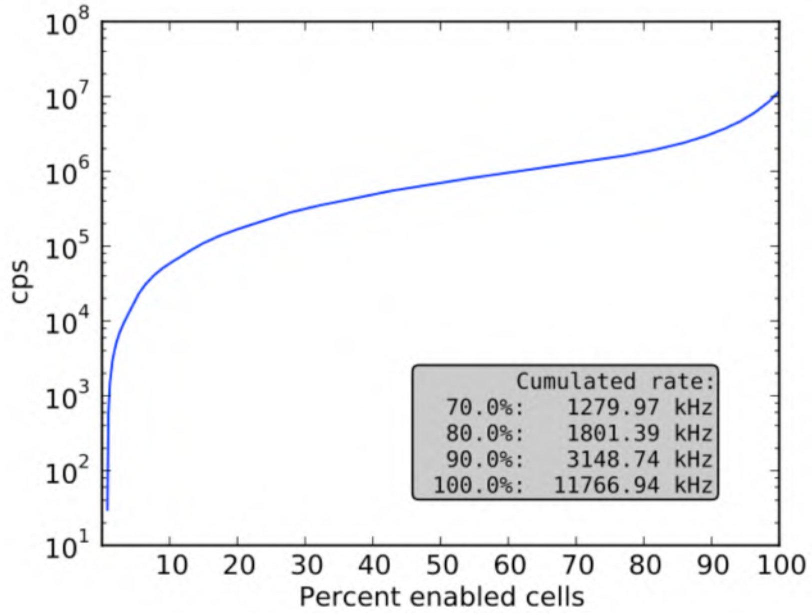

Figure 5.5: Cumulated dark counts rate (DCR) of a single die at 4°C. Values in the box show cumulated DCR for 100%, 90%, 80% and 70% of active cells.

terminate which configuration provides the highest sensitivity of the device a fixed number of light pulses was generated with the LED. In order to filter LED events from other types of events (dark counts or false events) a histogram of the number of fired cells per event was obtained and only the events contained in the photopeak were selected for further processing (see figure 5.6 in the next paragraph). Subsequently the number of recorded LED events by the DPC was compared to the number of generated light pulses and the fraction of lost events was calculated.

For the first results only one of the central dies of dSiPM tile was activated. First the fraction of recorded LED events was measured for different validation time length (validation level set to 8 and trigger level was set to 4 for this measurement). Second, the fraction of recorded events was determined for varying validation level (validation time set to 40 ns and trigger level was set to 4 for this measurement). Finally, the percentage of recorded events was measured for different trigger levels (1, 2, 3 and 4). Validation time and level for this study was chosen based on the previous measurements to provide the highest fraction of correctly recorded LED events. These three measurements were performed both with RTL refresh option switched on and off to evaluate its efficiency to reduce the influence of dark counts on dSiPM.

Next, different combinations of RTL refresh and NL options were studied for cases where the simultaneous readout of multiple dies is required to process a single event. For this study trigger level 4, validation level 8 and validation time of 40 ns were used. All dies were active and all four combinations of RTL refresh and NL were studied (on/off). An event with one or more missing dies was considered as an invalid event.

Finally, the event loss of the dSiPM was quantified for situations where multiple dies were required to record a single event. For this purpose a different number of dies (1, 2, 4 and 16) was activated per acquisition and the fraction of recorded LED events was measured in each case. As in the previous studies, measurements were performed for RTL refresh turned on and off and events with at least one die missing were considered as invalid. The NL option was turned off. Trigger level 4, validation level 8 and a validation time of 40 ns were used.

Furthermore the actual length of recharge time of dSiPM was verified. For this, the fraction of recorded events for different trigger rates of dSiPM was measured. Different trigger rates were acquired by deactivating a different fraction of dSiPM's cells for each acquisition. Monte Carlo simulations of the dSiPM acquisition chain were performed with different dead times (non-paralyzable model). The results obtained with simulations were fit to the measured data. From a comparison of the simulated and the measured data, the real dead time of the device was obtained. For this study only one die was activated and trigger level 1, validation level 8 and validation time of 40 ns were used.

5.3 Results

5.3.1 Quantification of event loss

Table 5.1 shows the percentage of recorded LED events for different validation time lengths for both RTL refresh turned on and off. It can be clearly seen the percentage of recorded events increases with the validation time.

Table 5.2 shows the percentage of recorded LED events for different validation levels for both RTL refresh turned on and off. In case of RTL refresh turned on the percentage is constant for all validation levels while with RTL refresh off the percentage reduces at lower validation levels.

The percentage of recorded LED events for different trigger levels is pre-

Table 5.1: Percentage of recorded LED events for different validation time (settings used: trigger level 4, validation level 8)

Validation time	RTL	
	ON	OFF
5 ns	12.01%	8.58%
10 ns	58.85%	46.35%
20 ns	99.29%	98.09%
40 ns	99.31%	98.48%

sented in Table 5.3. For RTL refresh on, the percentage is almost constant with the slight reduction at trigger level 2. For RTL refresh turned off a slight decrease of recorded events can be observed for lower trigger levels with a significant drop for trigger level 1.

Table 5.4 shows the percentage of LED events recorded by all 16 dies for different combinations of RTL refresh and NL options. The highest percentage of recorded events was observed for RTL refresh turned on and NL turned off while the highest loss of events was observed when both options were enabled.

Table 5.5 shows the percentage of recorded LED events in the situation where multiple dies are needed for event detection. For RTL refresh enabled, the fraction of recorded events was constant irrespective of number of dies required. For RTL refresh disabled, the fraction of recorded events decreases as the number of required dies increased.

5.3.2 False events caused by the RTL refresh option

In the histograms of the number of recorded optical photons per event, for both cases of RTL refresh (on/off), peaks at low values were observed (figure 5.6). It was observed that with RTL enabled, this low energy peak contained more counts than in case of RTL refresh turned off. Also the number of optical photons recorded per event for this peak was much higher in case of RTL refresh. All recorded events forming this peak at low values for RTL refresh turned on had a repeating pattern of fired cells in a die. In each event one pixel of a die had very high number of fired cells (even few hundreds) while rest of die's pixels had just a few fired cells.

This is depicted in figure 5.6. The peaks at higher values correspond to correctly recorded LED events for RTL refresh turned on (blue) and turned off (red). In case of disabled RTL refresh, the low energy peak obtained at

Table 5.2: Percentage of recorded LED events for different validation levels (settings used: trigger level 4, validation time 40 ns)

Validation level	RTL	
	ON	OFF
2	99.46%	53.62%
4	99.15%	97.61%
8	99.31%	98.48%

Table 5.3: Percentage of recorded LED events for different trigger levels (settings used: validation level 8, validation time 40 ns)

Trigger level	RTL	
	ON	OFF
1	-	86.29%
2	98.88%	96.84%
3	99.41%	97.66%
4	99.31%	98.48%

Table 5.4: Percentage of recorded LED events for different RTL & NL configurations (settings used: trigger level 4, validation level 8, validation time 40 ns)

Neighbor Logic	RTL	
	ON	OFF
ON	37.83%	65.78%
OFF	99.00%	89.83%

Table 5.5: Percentage of recorded LED events for different number of dies needed to record a single event (settings used: trigger level 4, validation level 8, validation time 40 ns)

Number of dies	RTL	
	ON	OFF
1	99.31%	98.48%
2	99.64%	97.69%
4	99.57%	98.36%
16	99.00%	89.83%

lower values corresponds to events caused by accumulated dark counts that managed to fulfil the validation level. For RTL refresh turned on the low values peak corresponds to previously described events with repeating pattern of fired cells. As the RTL refresh prevents accumulation of dark counts and the pattern of fired cells indicates that, these events were considered as an undesirable side effect of using RTL refresh option.

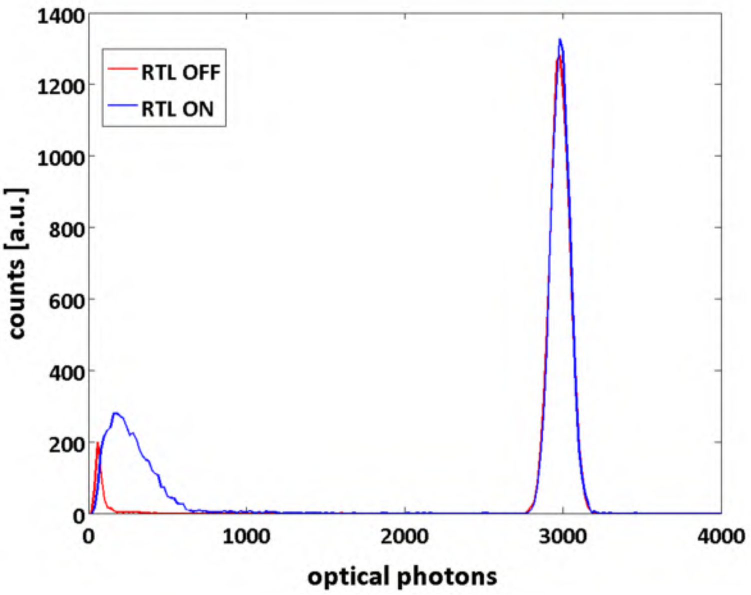

Figure 5.6: Spectrum of recorded LED pulse by dSiPM for RTL refresh turned on (blue) and RTL refresh turned off (red).

5.3.3 Verification of the dead time of the dSiPM

Figure 5.7 shows the percentage of recorded LED events for different trigger rates (blue plot) fitted with the results of Monte Carlo simulations of dSiPM acquisition chain for different lengths of dead time according to a non-paralyzable model (red plots). The percentage of recorded events increases with the decrease of trigger rate caused by dark counts. The drop in the fraction of recorded events for very low trigger rates is caused by the fact that in these cases, a very limited number of cells was left active to acquire such low trigger rates. It can be observed that the best match between the measured data and the outcome of simulation is achieved for the case when dead time was assumed to be equal to 50 ns.

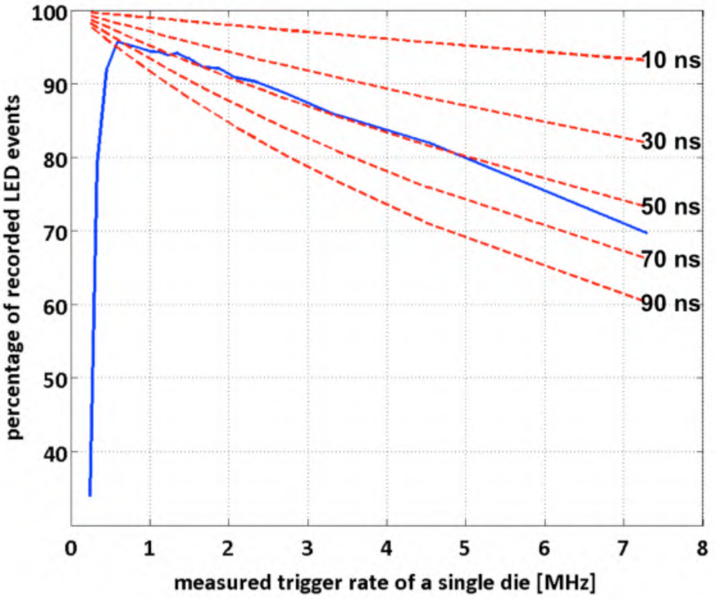

Figure 5.7: Fraction of recorded LED events as a function of dark counts trigger rates (blue) with fit of simulated number of recorded events according to non-paralyzable dead time model for different dead time lengths (red).

5.4 Discussion

We observed that the RTL refresh option allows recording almost 100% of the events while completely removing the accumulated dark count events for trigger level 2, 3 and 4. RTL refresh also allows achieving maximum sensitivity in terms of correctly recorded events regardless of used validation level as presented in table 5.2. This allows the dSiPM sensor to correctly validate events with a low number of optical photons. In table 5.5 it is shown that RTL refresh can be efficiently used to achieve maximum sensitivity with any number of dies needed to record a single event. We also observed that using the RTL refresh option causes appearance of false events (see figure 5.6). These events have a repeating pattern with one pixels of the dSiPM die containing a very high value of fired cells (even a few hundred) while other pixels have just a few fired cells. The cause of these events is RTL's fast recharge of cells. During this fast recharge there is a probability that photon avalanche are generated in the pixel of dSiPM. This is why one pixel, in which such avalanche was generated, has so high number of fired cells while other not. Due to the pattern of these events they can be efficiently filtered out from the data however for the detection of low energy gamma photons the filtering might be more challenging. For efficient filtering, the light distribution of low energy gamma photons in the detector should be carefully studied in order to distinguish them from false RTL events. Also at the high dark count rates the false RTL events can cause a slight drop in detector sensitivity as each acquisition of these false events is finished by die recharge phase, which contributes to the dead time of the detector.

RTL refresh should not be combined with NL as shown in table 5.4. The loss in the sensitivity in case of using NL is due to two factors. First, the dies that are recharging due to their own unsuccessful validation are still ignoring the master trigger signal, which needs up to 20 ns to propagate from the master die to other dies. Therefore, a die, that is already in the recharge phase before the master trigger reaches, will not record incoming photons and will be missing. Second, due to internal processing in the current version of the dSiPM, it can happen occasionally, that the valid master signal is generated although the master die invalidated the event and it is recharging. In this case the master die will be missing and other dies will be recording an invalidated event. These two factors combined with the appearance of false RTL events cause a significant drop in dSiPM sensitivity when both RTL and NL options are combined.

When comparing the fraction of recorded events for RTL refresh enabled and disabled for some cases the difference might appear to be insignificant. However one should remember, that this study was based on a very simplified scenario (LED light) when each event contains a high number of optical photons recorded by each die of the sensor. In real applications this is not the case and events with a lower number of optical photons are more probable. In the case of light spreading, some dies are illuminated by a much lower number of optical photons than the other dies. In this situation RTL refresh combined with lower validation level will give a much better result than the use of NL and higher validation level.

When using trigger level 1 and a single die active, we found the fraction of recorded events to be 86.29%. The loss of events was caused by the dark counts triggers, which measured rate was 3.3 MHz, and the expected recharge time of a die 20 ns. From Monte Carlo simulation of the dSiPM acquisition chain we expected this value to be 93.6%. To verify the recharge time of dSiPM, which is the dead time of the sensor, we measured the fraction of recorded events as a function of the trigger rate (see figure 5.7). Then we repeated the Monte Carlo simulations for different lengths of recharge time for acquired trigger rates and fitted the results to measured data. From the fit, based on non-paralyzable dead time model, we concluded that the actual dead time of dSiPM is around 50 ns instead of just 20 ns stated in the device's specification. Repetition of the simulations with dead time of 50 ns resulted in a fraction of recorded events equal to 86.7%. This difference of dead time length might be caused by internal excess delays in the device between switching from recharge state to active state in the acquisition chain. This effect should be taken into account when evaluating the sensitivity of detector based on dSiPM working at a given dark count rate.

5.5 Conclusion

We have found that RTL refresh is an effective option to reduce dark counts and to ensure maximum sensitivity of the detector regardless of trigger level, validation level and number of dies needed to record an event. Therefore, in cases when the scintillation light is spread onto several dies, the use of RTL refresh option should be employed and combined with a low validation level in order to guarantee the individual validation of all required dies. This approach ensures higher sensitivity of the detector than employing NL.

When trigger level 1 is required for accurate timing measurements [5] the following strategies can be followed to reduce the loss of events. First, the dark count rate can be reduced by lowering the working temperature of dSiPM and by deactivating a larger fraction of the most active cells of the device. Second, the light can be focused in a small area of the dSiPM tile so less dies are needed to process the incoming event.

Furthermore we found that the dead time of dSiPM is longer than just recharge time of this device and is around 50 ns instead of 20 ns.

Chapter 6

DigiPET: Sub-millimetre spatial resolution small animal PET imaging using thin monolithic scintillators

This chapter has been published as: S. España, R. Marcinkowski, V. Keerman, S. Vandenberghe and R. Van Holen, "DigiPET: Sub-millimetre spatial resolution small animal PET imaging using thin monolithic scintillators", Phys. Med. Biol., 2014, vol. 59(13): 3405-20

6.1 Introduction

Preclinical imaging has been used in life sciences not only to facilitate discovery, design and evaluation of drugs, but also to refine our understanding of the molecular pathways of disease and therapy. Together with structural imaging (using CT, MRI and HF-US), molecular imaging (using optical imaging, PET and SPECT) has been applied in the study of neurological aging disorders, brain functioning, oncology, cardiology, and several other fields [39]. Cherry [39] reviews the large range of applications of in vivo preclinical imaging and emphasizes that the detection of lower levels of proteins and gene expression is only possible through further improvement in imaging technology.

After optical imaging, micro PET/CT is the second most important preclinical imaging modality, representing 26.1 % of the preclinical imaging market (in revenues in Europe, Frost & Sullivan). The main reason for this is the unrivalled sensitivity of PET that enables the detection of picomolar concentrations of tracer in vivo [134].

Besides the technical challenges associated to the integration of different modalities [41], researchers have been continuously investigating ways to improve system performance. In the design of a PET scanner, the first goal is to optimize spatial resolution and sensitivity. These parameters are influenced by the detectors and by geometry of the scanner. The geometry influences system resolution through annihilation photon acolinearity and through parallax. The larger the system radius, the larger the effect of acolinearity and the lower the effect of parallax [115]. The detector technology used defines the detector intrinsic resolution in 2D and, if depth-of-interaction (DOI) capability is present, in 3D. The smaller the diameter of the system, the larger the solid angle covered by the detectors and the higher the sensitivity. The stopping power of the detectors is the second factor influencing system sensitivity. Next to sensitivity and spatial resolution, noise equivalent count rate (NECR) and of course cost are important design parameters.

The need for scaling down large human or primate systems was already recognized early on (e.g. [109], [27], [44], [37]). The early approach was to combine fine pixelated scintillation crystals with either Avalanche Photodiodes (APDs) [153], wire chambers [29] or PS-PMTs [82]. By downsizing large systems, the solid angle coverage improves tremendously and a sensitivity of around 0.5 % was reported [37]. The combination of the small ring geometry with pixelated LSO detectors of 1.6 mm intrinsic resolution detectors resulted in 1.8 mm spatial resolution in the reconstructed images [37]. By the year 2006, five commercial systems were available on the market, some of them based on the above research efforts, some of them developed as a joint effort between research institutes and world leading manufacturers. By that time, spatial resolutions down to 1.3 mm and sensitivities up to 6.5 % were feasible [107], [196], [191]. By 2012, additional systems made it to the market (Inveon (McFarland [138], Vista [212], LabPET [72], VrPET [105]) and the previous generation was upgraded. An objective performance characterization of 11 commercially available systems is given by [77]. Remarkably, these efforts have not focused on better spatial resolution. Improvements were merely made with respect to increasing the field of view, sensitivity and NECR of the previous generation. Moehrs et al. proposed the use of stacks of monolithic crystals combined with SiPM devices but is has not been experimentally demonstrated yet [144].

Finally, two remarkable recent efforts are worth mentioning: the development of PETBox4 [81] and the use of 0.5 mm pixelated crystals at UC Davis [187]. The first system reaches a sensitivity of 18 % while hot rods down to 0.6 mm can be resolved with the latter system based on the 0.5 mm crystal detectors.

All the above designs use pixelated scintillation crystals. There have been a limited number of studies using continuous scintillation crystals, motivated by the high cost of pixelated crystals ([181], [95], [18]). Spatial resolution of around 1 mm has been reported in combination with 1 % sensitivity. The use of monolithic crystals allows reducing the cost and increases the sensitivity along with the energy and timing resolution of the detector [203]. However, as the continuous crystal technology has been used in only a limited number of cases, there is still a large potential for system optimization.

Here, we present the proof of concept of a dedicated mouse/rat-brain PET system which is based on a combination of a large solid angle (small diameter) and thin monolithic crystals for low parallax and high intrinsic resolution while maintaining cost at a fraction of current preclinical PET scanners. In addition, the use of thin crystals significantly reduces the inter-crystal scatter and the transit time spread of the scintillation photons. This will further improve the intrinsic spatial resolution and the coincidence resolving time.

In the next sections we give a description of the technology used to build the system and explain the procedure for detector calibration. Furthermore, we evaluate the system in terms of coincidence resolving time, sensitivity and spatial resolution. The image quality is further evaluated by acquiring a hot-rod phantom and a rat head.

6.2 Materials and methods

6.2.1 System description

6.2.1.1 Description of the PET system

The DigiPET scanner consists of four 32 × 32 mm^2 detectors placed in a square arrangement with 34.5 mm distance between opposite detectors, as depicted in figure 6.1. This yields a field-of-view (FOV) of 32 × 32 × 32 mm^3 with the possibility of placing the source very close to the detector surface. Each detector consists of a thin monolithic LYSO crystal (Hilger Crystals, Margate, United Kingdom) with a size of 32 × 32 × 2 mm^3 optically coupled with silicone optical grease BC-630 (Saint-Gobain, refractive index 1.465) to a DPC-3200-22-44 digital silicon photomultiplier array (dSiPM, Philips

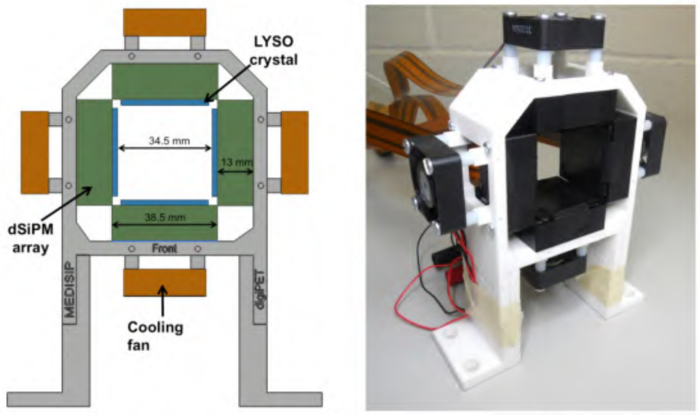

(a) (b)

Figure 6.1: Schematics (a) and picture (b) of the PET system prototype developed in this study.

Digital Photon Counting, Eindhoven, The Netherlands) [54], [74]. White reflectors were used to cover the top of the crystals to avoid scintillation light loss at the top side of the detector. Black paint was used on the sides in order to extend the useful detector area and to reduce the spatial resolution degradation on the edges. The system is extremely compact: the external dimensions of the system were 115 × 150 × 38 mm^3. The dark count rate in the dSiPMs was reduced by operating the scanner in a temperature chamber at 5-6 °C.

6.2.1.2 dSiPM description

Data acquisition was performed using the Philips Digital Photon Counter Technology Evaluation Kit (PDPC-TEK). A single dSiPM array consists in 4 × 4 independent units called dies. Each die is further divided into 4 dSiPM pixels arranged in a 2 × 2 matrix with 4 mm pitch. The active area of the dSiPM array is 32 × 32 mm^2 with a fill-factor of 78 %. Compared to analogue devices that rely on the comparison of the summed output signal from all cells with reference thresholds in order to produce trigger and validation signals, dSiPM are based on the interconnection of different logical units. The trigger level defines the amount of signal required to start the acquisition chain. However, the event is not fully processed unless a second validation level is reached in a time shorter than a defined validation time. The trigger is used to generate a time stamp for the event while the validation process is used to reject noise and events with low energy deposition. The higher the trigger and validation levels the higher the amount of photons (on average) that are needed to produce a trigger and validation signal respectively. Once an event is validated the optical photons are further accumulated during a parameter defined as integration time in the dSiPM configuration. However, this terminology can be confusing as the accumulation of photons has already started in after the trigger signal. Further details of the working principles of the dSiPMs can be found in the literature [203], [74], [176].

6.2.2 Acquisition configuration

Table 6.1 summarizes the configuration of the dSiPM arrays used to perform all acquisitions. The scintillation light produced in one interaction event is typically detected by more than one die of the dSiPM array. Each die has an independent trigger and validation procedure, and therefore a very low validation level of 2 was chosen to record all the dies that detected a significant amount of light. The trigger level was set to 2 to yield optimal timing resolution. Trigger level 1 (trigger with the first photon) cannot be used, as a large amount of true events are lost in that situation due to dark counts keeping the detector busy [132]. An integration time of 45 ns was chosen, as we found that higher values did not lead to a higher signal. The integration time can be chosen that short due to the fact that integration also occurs during the validation time and approximately half of the readout time (680 ns / 2 = 340 ns). The last contribution is produced because the cells are read sequentially in rows and they can still fire before they are read [203]. All the single events are processed on each detector and sent to a base processing unit were only coincidence events within the coincidence window are sorted and sent to the PC. A wide coincidence time window of 20 ns was used to ensure that all the dies contributing to a gamma detection are considered to belong to the same event as the time stamp of each individual die is used to sort the coincidence events. However, a narrower coincidence window could be applied during the post-processing step. Each detector is able to acquire single events up to 120 kcps and send them to the base unit were the coincidence events are sorted. The coincidence events are sent to the PC through a USB port. The current bottleneck of this system is in receiving and recording those events on the PC side. Therefore, long acquisition times were used in this study in order to compensate this limitation.

Table 6.1: dSiPM parameter settings used in all the acquisitions performed in this study

Parameter	Values
Validation level	2
Validation time	40 ns
Trigger level	2
Integration time	45 ns
Inhibit map	20% cells with the highest dark count rate disabled
Coincidence window	±20 ns
Energy window	400-650 keV
Temperature	3-5 °C

6.2.2.1 System calibration

Positioning of the gamma interactions within the monolithic scintillation crystals was performed using the maximum likelihood estimation (MLE) positioning algorithm [89], which requires calibration with sources with known incident position. Only transverse positioning calibration was performed, assuming that depth of interaction (DOI) uncertainty produces a negligible effect due to the limited thickness (2 mm) of the monolithic crystals used in the DigiPET scanner. For transverse calibration, the complete detector area was scanned using a beam of 511 keV gamma rays (see figure 6.2). The beam was obtained by placing a 22Na point source with 7.4 MBq activity and 250 µm diameter on the center of one of the bases of a tungsten cylinder with 7 cm length and 4 cm diameter. A hole with 1 mm diameter was drilled along the central axis of the tungsten cylinder except for the last 1.2 cm opposite to the source location where the hole has a diameter of 0.4 mm. On the other side of the source, a lead cylinder with 10 cm length, 6 cm diameter and a hole with 6 mm diameter along the central axis was placed with its axis aligned with the axis of the tungsten cylinder. Calibration measurements were performed in coincidence mode using a reference detector in order to reject the LYSO self-activity and to perform timing calibration alignment. The reference detector consisted of a dSiPM array optically coupled to a single LYSO crystal with 6 × 6 × 22 mm^3 dimensions wrapped with Teflon tape. The beam scan for each monolithic detector was obtained by attaching it to a 3-axis linear robot stage, as shown in figure 6.2 and a grid of 32 × 32 positions with 1 mm pitch was acquired. At each position coincidences were recorded during 160 seconds. Each detector was calibrated separately and later assembled in the system. An energy spectrum

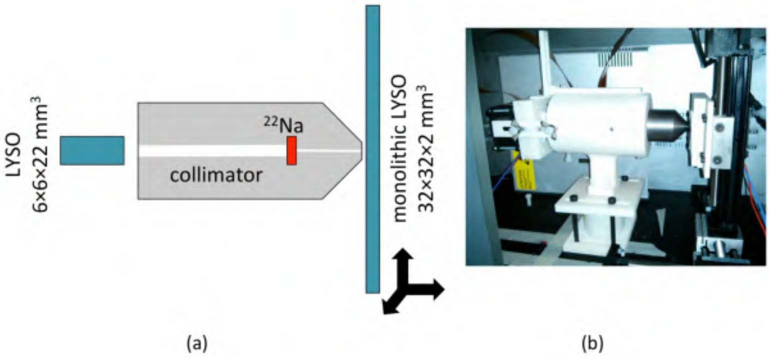

Figure 6.2: Schematics (a) and picture (b) of the PET system prototype developed in this study.

was generated for each position measurement. Only events within the energy window (400-650 keV) were used to obtain the probability density functions (PDFs). The PDFs were fitted to Gaussian functions and the mean and standard deviation values were stored. The two-dimensional (2D) maps of mean and standard deviation values were interpolated into a finer grid with 0.25 mm pitch leading to a grid of 125 × 125 bins. As described in the literature [61], the positioning of detected events is then accomplished by determining which of the stored positions has the maximum likelihood with the recorded event.

6.2.3 Performance

6.2.3.1 Detector performance

Energy spectra were obtained for each beam position used for the calibration of one of the detectors. The energy resolution at 511 keV was determined for a few cases (center, edges and corner of the detector) by fitting a Gaussian function to the photopeak and determining the full width at half maximum (FWHM) of the fit. The intrinsic resolution of one detector was obtained by applying the MLE positioning procedure to each of the beams used for calibration. For each fixed beam used for calibration a 2D histogram of the position was generated. The histogram bins with a value below 20 % of the maximum were set to zero in order to remove scattered and random events. The intrinsic spatial resolution was obtained for each beam position in X and Y directions by projecting the 2D histogram into each of the directions and fitting the obtained profile to a Gaussian function. The obtained FWHM results on each beam position are reported. These values were not corrected for the size of the beam. In addition, the mean position bias was determined as the distance from the actual beam position to the average estimated position.

6.2.3.2 System performance

The spatial resolution of the system was measured using a calibrated ^{22}Na point source with an activity of 234 kBq and a diameter of 250 μm. The source was embedded in an acrylic cube of 10 mm extent on all sides. The source was placed at different radial positions in the center of the axial field of view from 0 to 10 mm in 1 mm steps. $5{*}10^5$ coincidences were recorded at each position. The images were reconstructed using the list-mode maximum likelihood expectation maximization (ML-EM) algorithm [177] with Siddon ray-tracing [180] using 10 iterations and a voxel size of $0.25 \times 0.25 \times 0.25$ mm^3. The radial, tangential and axial resolutions were measured from the reconstructed images following the NEMA NU4-2008 protocol (National Electrical Manufacturers Association 2008). Contrary to the NEMA protocol we did not use the filtered backprojection method to reconstruct the images. However no resolution recovery methods were included during the ML-EM reconstruction.

The sensitivity of the system was determined using the same ^{22}Na point source used to measure the spatial resolution. The activity of the source is known within 10 % accuracy. The source was shifted in 1 mm steps along the central axis of the scanner, and at each position an acquisition of 200 seconds was performed. The source activity was low enough to neglect the influence of random events. The axial sensitivity profile was measured for 250-650 keV and 400-650 keV energy windows. The branching ratio of the radionuclide for positron emission (0.9033 in the case of ^{22}Na) was included in the calculation of the sensitivity.

The coincidence resolving time (CRT) was determined from an acquisition performed with the ^{22}Na point source at the center of the field of view (CFOV). A coincidence time spectrum was created with the time differences of the arrival of the gammas to the detectors with a bin size of 120 ps. Only events within an energy window of 400-650 keV were included. The CRT is reported as the FWHM obtained from the coincidence time spectrum.

6.3 Imaging

6.3.0.1 Phantom imaging

A hot-rod phantom was used to evaluate the image quality obtained with the system. The phantom contained 6 sectors with rods of different diameters (0.7, 0.8, 0.9, 1.0, 1.2 and 1.5 mm respectively). The distance between the centers of the rods was two times the rod diameter. The phantom was filled with 5.5 MBq of ^{18}F-FDG and placed in the FOV of the scanner. Data were collected during 8 hours. Image reconstruction was performed using the list-mode 3D-OSEM algorithm with Siddon ray tracing using 10 iterations and 10 subsets. The reconstructed matrix was 127 × 127 × 127 with a voxel size of $0.25 \times 0.25 \times 0.25$ mm^3. A post-smoothing Gaussian filter with 0.5 mm FWHM was applied. Corrections for random and scatter coincidences, attenuation and normalization were not included in the reconstruction. The same hot-rod phantom was also acquired during 20 minutes using the LabPET-8TM scanner after filling it with 20 MBq of ^{18}F-FDG. In this case the 2D-OSEM algorithm implemented in the scanner was used with 100 iterations. A post-smoothing Gaussian filter with 0.5 mm FWHM was also applied in this case.

6.3.0.2 Rat-brain imaging

An injection of 222 MBq ^{18}F-FDG was administered to an awake healthy adult Sprague-Dawley rat (male, 250 g). This high dose was used in order to show the potential image quality than can be achieved with the system. The animal was sacrificed and decapitated 45 minutes after the injection. The head of the rat was first scanned in the LabPET-8^{TM} scanner during 20 minutes collecting 150 million coincidences in the 375-650 keV energy window. Subsequently it was placed in the DigiPET scanner for 8 hours collecting 20 million coincidences within the 400-650 keV energy window. The images were reconstructed using the same configuration employed for the hot-rod phantom for both scanners. In order to correlate the different brain structures, an MRI scan was acquired of the rat head on a Pharmascan 7T system (Bruker, Ettlingen, Germany). The images were acquired with a turbo spin echo sequence (TR=6345.5ms, TE=37.1 ms, turbo factor 8, 4 averages). The acquisition matrix was 320 × 320× 49 with 109 μm in-plane resolution and 600 μm slice thickness. The PET images were manually coregistered with the MR image using anatomical landmarks. The rat was treated according to guidelines approved by the European Ethics Committee (decree 86/609/EEC). The experimental procedure was approved by the Animal Experimental Ethical Committee of Ghent University Hospital (ECD 13/14) with appreciation of the principles to avoid any unnecessary discomfort for the animals.

6.4 Results

6.4.1 Detector performance

The coincidence rate obtained during the calibration of the detectors was around 10 cps. Therefore, about 1500 coincidences were recorded with approximately one third of them within the 400-650 keV energy window. Figure 6.3(a) shows some sample energy spectra obtained for different beam positions in one of the detectors. The energy resolution at the photopeak for each case is also shown. An average energy resolution of 18 % FWHM was obtained. Figure 6.3(b) shows the map of photopeak positions across of the detector surface obtained for each of the 32 × 32 recorded beam positions. The dark areas observed in the map correspond to regions of the crystal that are on top of dead areas of the photosensor and therefore, part of the scintillation light is lost in these regions.

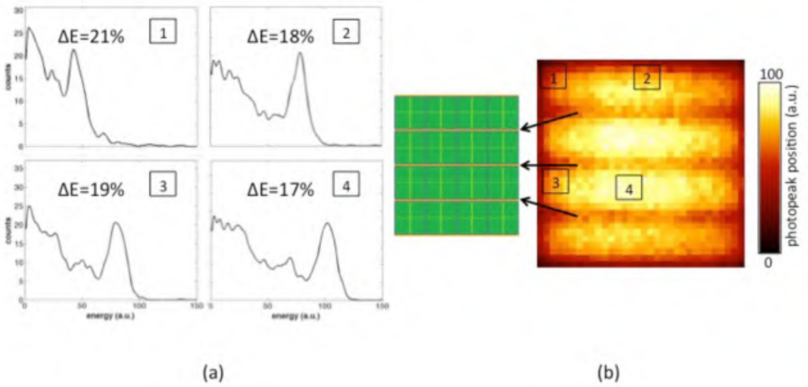

Figure 6.3: Energy spectrum obtained for some beam positions (a) and map of photopeak positions across one of the detectors (b). A schematic of the dSiPM array is shown to explain the reason of the three dark lines in the map.

Figure 6.4(a) and 6.4(b) show the map of intrinsic spatial resolution in X and Y directions respectively for one of the detectors when the MLE positioning method was applied. A mean value of 0.54 mm FWHM was obtained. However, the resolution at the edges of the detector might be

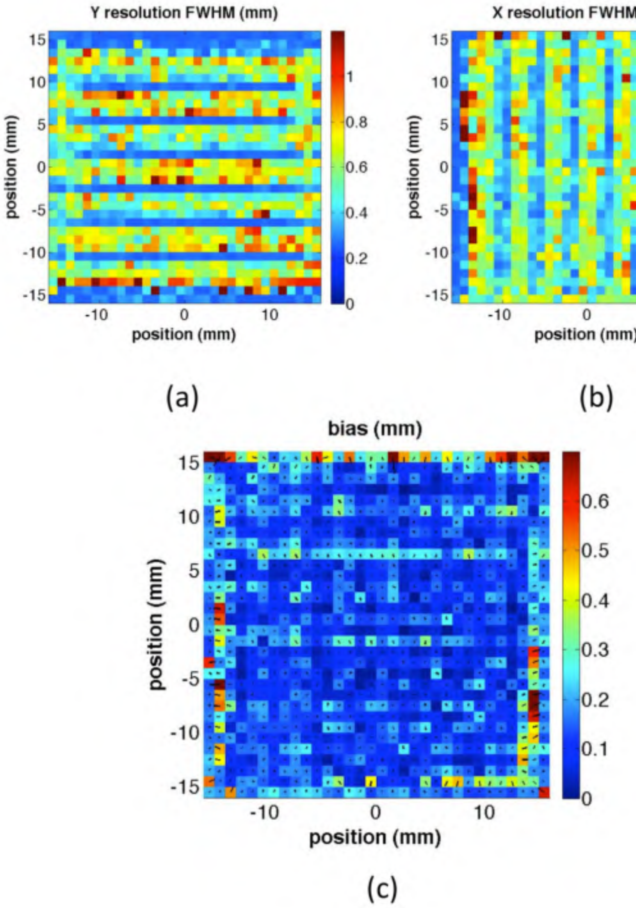

(a) (b)

(c)

Figure 6.4: Maps of intrinsic spatial resolution in X (a) and Y (b) directions and bias (c) obtained for one of the detectors of the system. The black lines on the bias map show the translation from the true beam positions to the measured one.

underestimated as the image of the source gets compressed as it can not be extended beyond the edges. Furthermore, figure 6.4(a) and 6.4(b) show horizontal and vertical lines where the resolution is significantly better than in the rest of the detector. We found that those regions correspond with the center of the dSiPM pixels where larger changes in light distribution are obtained leading to a better spatial resolution. Figure 6.4(c) shows the map of mean position bias obtained for the same detector. The black lines show the translation from the true beam positions to the measured one. The average of the absolute value of the mean position bias was 0.15 mm.

6.4.2 System performance

6.4.2.1 Spatial resolution

Radial, tangential, and axial resolutions (FWHM and FWTM) are plotted in figure 6.5 as a function of radial position in the central transverse slice of digiPET. The average obtained FWHM and FWTM were 0.7 and 1.7 mm respectively. The spatial resolution shows a very uniform behavior across the FOV and in all directions (radial, tangential and axial).

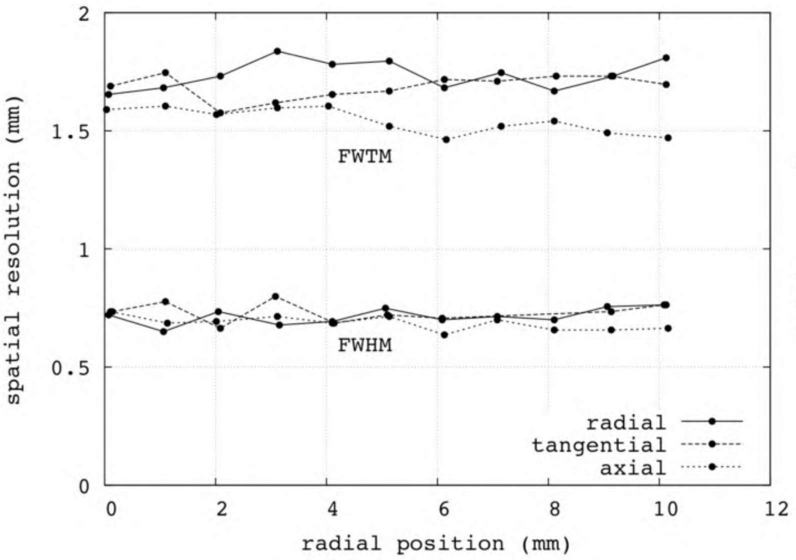

Figure 6.5: Radial (solid), tangential (dashed) and axial (dotted) spatial resolution (FWHM and FWTM) obtained for the DigiPET scanner as a function of the radial position.

6.4.2.2 Axial sensitivity profile

Absolute sensitivity, plotted along the central axis of the scanner is shown in figure 6.6. The sensitivity obtained at CFOV was 0.3 % and 0.6 % for an energy window of 400-600 keV and 250-650 keV respectively

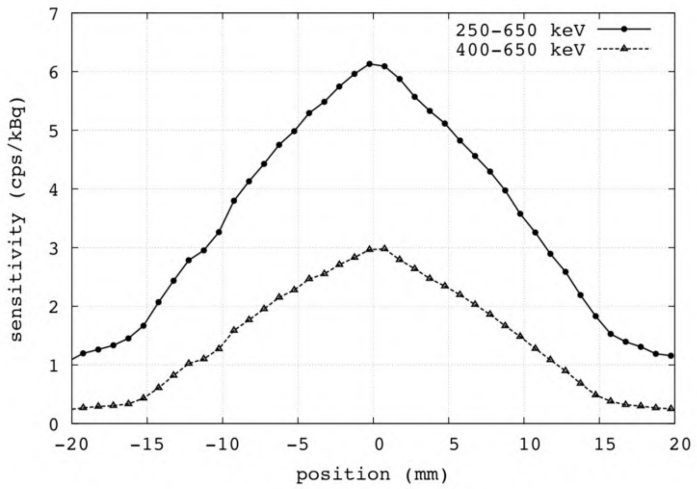

Figure 6.6: Absolute sensitivity profiles along the central axis of the DigiPET scanner for 250-650 keV (solid) and 400-650 keV (dashed) energy windows.

6.4.2.3 Coincidence resolving time

The coincidence time spectrum (see figure 6.7) was obtained with DigiPET scanner yielding a CRT of 680 ps FHWM.

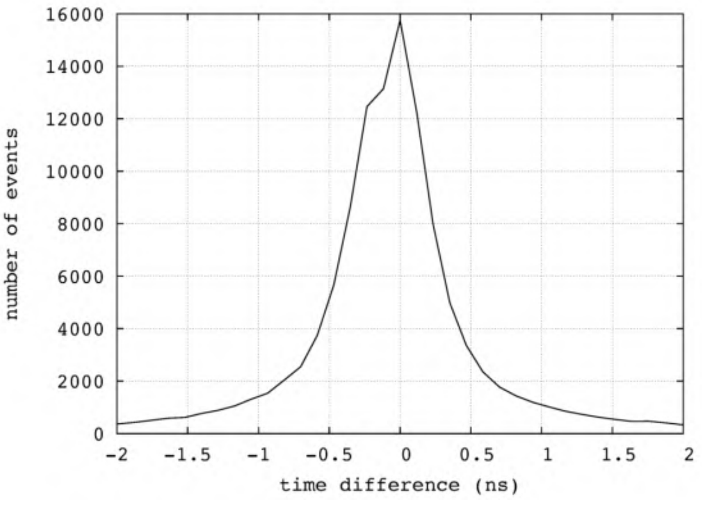

Figure 6.7: Time difference spectrum obtained with DigiPET scanner for a ^{22}Na point source located at CFOV.

6.4.3 Phantom imaging

Figure 6.8 shows the reconstructed images of the hot-rod phantom acquired with the DigiPET scanner (figure 6.8(a)) and the LabPET-8^{TM} scanner (figure 6.8(b)). Profiles through a row of 1.0 mm diameter hot rods in both images are shown on figure 6.9. Peak to valley ratios of 2.5 and 1.5 are obtained in 1.0 mm hot rods for DigiPET and LabPET-8^{TM} respectively. 15 million coincidences were acquired and used with the DigiPET system (400-650 keV) while 160 million coincidences were used for the LabPET-8^{TM} system (375-650 keV). All the rods down to 0.7 mm diameter are visible with the DigiPET scanner while the LabPET-8^{TM} system only shows rods down to 1 mm diameter.

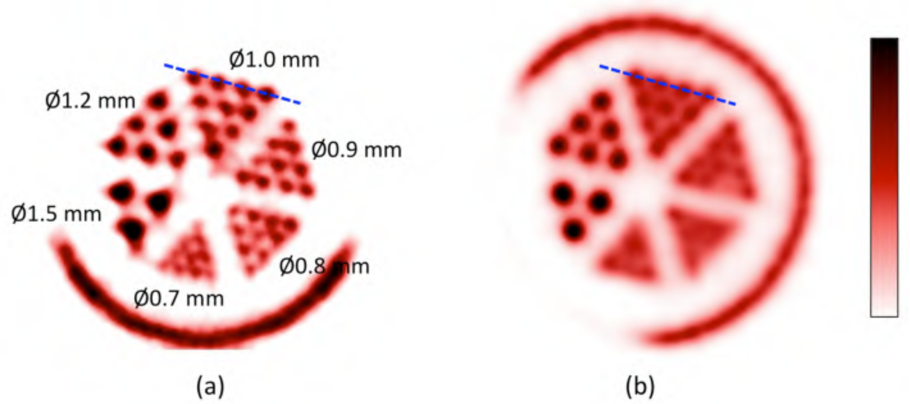

(a) (b)

Figure 6.8: Reconstructed images of the hot-rod phantom acquired using the DigiPET scanner (a) and the LabPET-8^{TM} scanner (b).

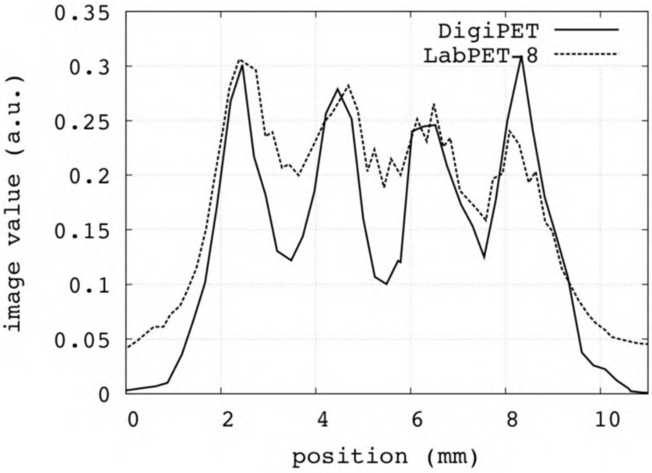

Figure 6.9: Profiles through a row of 1.0 mm diameter hot rods (blue dashed lines in 6.8) in both images.

6.4.4 Rat-brain imaging

Figure 6.10 shows the MRI and the ^{18}F-FDG rat-brain images obtained with the DigiPET scanner (figure 6.10(b)) and the one obtained with the LabPET-8^{TM} scanner (figure 6.10(c)). 20 million coincidences were collected within the 400-650 keV energy window in the DigiPET scanner while 150 million coincidences were collected in the LabPET-8^{TM} scanner within the 375-650 keV energy window.

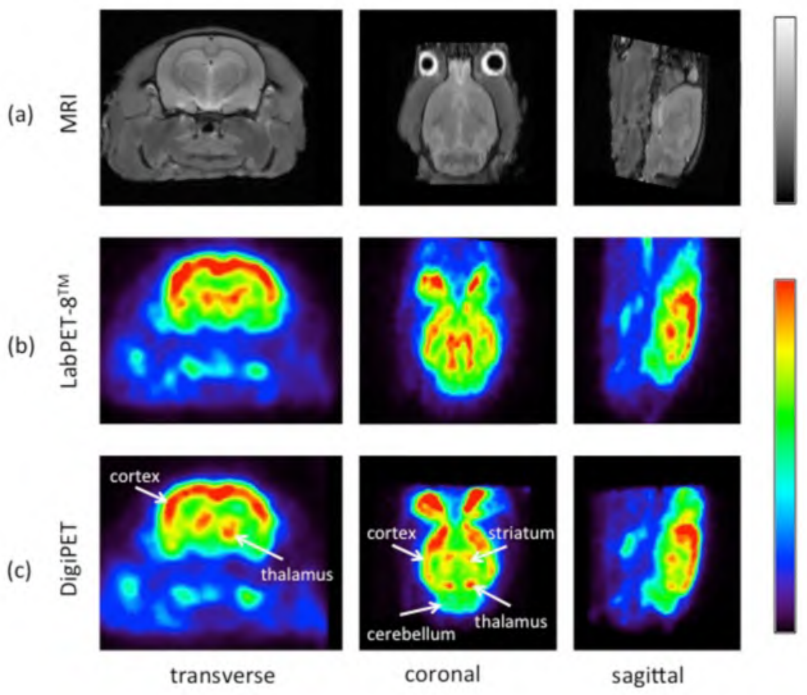

Figure 6.10: Image of the ^{18}F-FDG rat brain study obtained with the MRI (a), the LabPET-8^{TM} scanner (b) and the DigiPET scanner (c).

6.5 Discussion

The 0.7 mm FWHM spatial resolution obtained with the presented prototype system is, to our knowledge, the highest spatial resolution ever demonstrated for a full-ring PET system. This is substantially better than current commercially available small animal imaging systems, which obtain spatial resolutions of 1.1 mm when evaluated using standard protocols [187]. A comparable result was obtained by Stickel [187] using an LSO crystal array with 0.5 mm pixels. However, those results were obtained using two detectors only. Our result is attributable to the excellent intrinsic resolution of the detector (0.54 mm). This is due to the combination of thin monolithic crystals and the MLE position algorithm, which makes excellent use of the light output generated by these crystals. However other positioning algorithms have been proposed in the literature that might lead to similar results like artificial neural networks (ANN) [28] or k-nearest neighbors (KNN) [127].

However, the intrinsic resolution of the detector was not uniform as shown in figure 6.4(a) and 6.4(b) which might be solved by using a light guide or decreasing the SiPM pixel size. It is also clear from the uniformity of the spatial resolution throughout the FOV (see figure 6.5) that there is no relevant DOI effect inside the 2 mm thick monolithic crystal. The ability to image with such high resolution in the entire FOV yields a clear advantage over current small animal PET systems, especially for imaging small lesions in rats and mice.

The presented coincidence resolving time of 680 ps FWHM, attributable to the use of LYSO combined with the dSiPMs, may also prove to be an advantage of the system. It will allow using a short coincidence window in the order of 1–1.5 ns, thereby limiting the random coincidence rate. However, the reflector employed to wrap the scintillation crystals was not optimal and an improvement in energy and timing resolution is expected once this aspect is improved. As pointed out by Deprez [60], the escape of X-rays characteristic of lutetium (54 keV) due to the reduced thickness of the scintillation crystal can also contribute to the degradation of the energy resolution. Currently, the count rate capabilities of the system are limited by the transfer rate of sorted coincidence events from the PDPC TEK to the PC, which will be solved in a future version of the readout hardware. As an example, at the beginning of the acquisition of the hot-rod phantom the rate of events processed by the electronics was 135 kcps while only 22 kcps were transferred to the PC representing only 16 % of the processed events. The limited collection count rate and the absence of normalization correction explain the high noise level shown on figure 6.8(a). However, it has been proven that the finest rods can be resolved. This also lies at the basis of the very long acquisition time for the hot-rod phantom and the rat head. However, the dSiPM detectors should also allow for imaging at high count rates. In cases where there is no objection to high doses from a biological point of view, this will allow the administration of higher radiotracer doses to obtain better image quality.

The development cost of the presented prototype is low compared to other small animal imaging systems. This can be attributed to several factors. First of all the cost per detector is low, as thin and unpixelated crystals are used. As dSiPMs have all electronics on board to perform signal digitization and time stamping, there was no extra cost for the development of dedicated readout electronics. Furthermore the system only uses 4 detectors, thereby reducing total system cost. Due to the small bore of the system and the compact detectors, a low-cost gantry fabricated with rapid prototyping could be used. The outside dimensions of the prototype are also small, also yielding a cost advantage over most current small animal PET systems, which have a considerable footprint and require a dedicated room in the lab. Its size will also be an asset when considering integration into an existing MR system to perform simultaneous PET-MR imaging. By introducing sufficient shielding it should be possible to integrate this system is a small-bore MR system. As none of the components used in the prototype are intrinsically incompatible with MR, it is one of the goals to eventually use the system as a PET insert in a preclinical MR scanner.

Some limitations of the presented prototype should also be mentioned. First of all it is presented here as a prototype system, to demonstrate the capabilities of a small animal PET scanner based on dSiPMs and thin monolithic scintillators. A number of developments are still needed before it can function as a standalone system. Most importantly the operation inside a temperature chamber is not compatible with in-vivo imaging as the animals could not withstand long exposure to such low temperatures under anesthesia. We are currently developing a cooling system that will allow operating the scanner outside the temperature chamber. Apart from the cooling, other system parts such as an animal bed are also required but these are easily fabricated. In addition, the collection rate of the electronics must be improved in order to work at reasonable count rates.

Furthermore, the sensitivity of the system is also approximately between 4 and 10 times lower compared to the sensitivity of most currently available small animal PET scanners. This is an intrinsic limitation of the system, as it is mainly due to the use of thin monolithic crystals, which yield a limited stopping power. However, improvement is possible by using slightly thicker crystals, e.g. up to 5 mm. It is expected that this will only slightly reduce intrinsic detector resolution according to the transverse spatial resolution that has been reported with a 10 mm thick crystal [176]. More importantly, the small bore size of the scanner may then lead to the necessity of including DOI correction. With the MLE positioning algorithm and additional calibration, it may be possible to obtain an adequate DOI resolution to compensate for this. Sensitivity could also be gained by extending the system in the axial direction and thereby further improving solid angle coverage and axial FOV. We performed several Monte Carlo simulations using PeneloPET code [67] comparing the sensitivity obtained at CFOV for different scanner configurations (see figure 9). We compared the sensitivity obtained with crystal with thickness between 2 and 5 mm and with 1 and 2 rings of detectors in the axial direction for both 250-650 keV and 400-650 keV energy windows. A peak sensitivity of 3 % is possible by using 5 mm thick crystals and 2 axial detector rings. Future research includes the investigation of the effect of

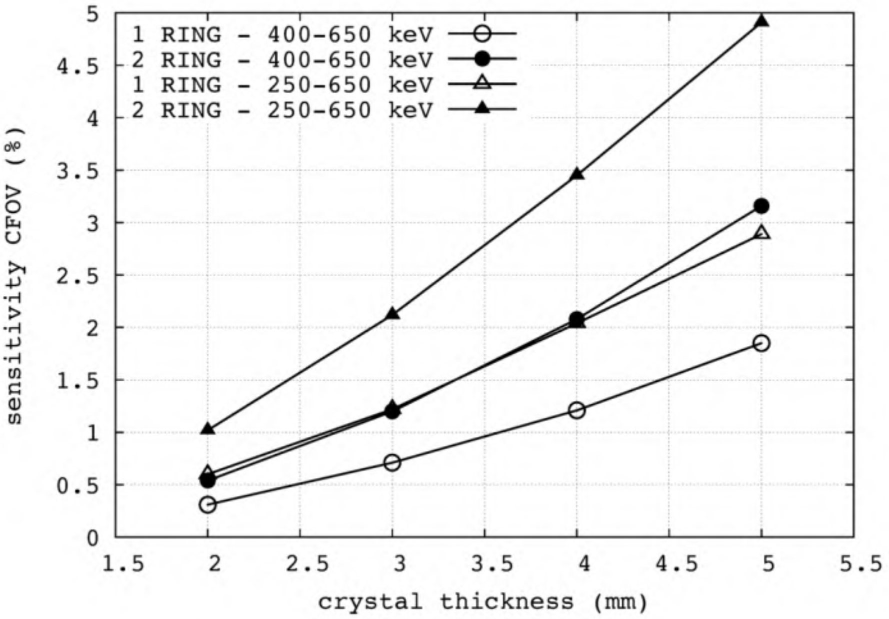

Figure 6.11: Sensitivity at CFOV obtained with Monte Carlo simulation for different variation of the DigiPET system in terms of crystal thickness (from 2 to 5 mm), number of detector rings (1 and 2 rings) and energy window (250-650 keV and 400-650 keV).

such a design on spatial resolution.

6.6 Conclusion

We have developed and evaluated the performance of a compact and low cost small animal PET scanner prototype dedicated to mouse and rat brain imaging based on thin monolithic LYSO crystals and dSiPMs. The obtained performance in terms of spatial (0.7 mm) and timing (680 ps) resolution outperforms currently available preclinical PET systems. Ex-vivo rat brain imaging was also performed, demonstrating the feasibility of imaging realistic objects. However, a number of developments are still required before the prototype can function as a standalone scanner.

6.7 Acknowledgements

S. España is funded by the BOF (Special Research Fund) of Ghent University. Roel Van Holen is funded by the Research Foundation-Flanders (FWO, Belgium) and Ghent University. This work was carried out using the STEVIN Supercomputer Infrastructure at Ghent University, funded by Ghent University, the Flemish Supercomputer Center (VSC), the Hercules Foundation and the Flemish Government – department EWI. This work was supported in part by EU FP7 project SUBLIMA, grant agreement no 241711, see also www.sublima-pet-mr.eu and by iMinds - Future Health Department. We would like to thank Christian Vanhove for performing the acquisitions and image reconstruction with the LabPET-8^{TM} system, and to Benedicte Descamps, Scharon Bruneel and Nathalie Van Den Berge for helping with the rat head experiment.

Chapter 7

Sub-millimetre DOI detector based on monolithic LYSO and digital SiPM for a dedicated small-animal PET system

This chapter has been published as: R. Marcinkowski, P. Mollet, R. Van Holen and S. Vandenberghe, "Sub-millimetre DOI detector based on monolithic LYSO and digital SiPM for a dedicated small-animal PET system", Phys. Med. Biol., 2016, vol. 61(5): 2196-2212

7.1 Introduction

With the increased use of mouse models for biomedical research, small-animal PET became a well-established tool in preclinical pharmacology, genetics and pathology investigation. This was possible thanks to the capability of PET to detect and quantify biological processes in vivo at the molecular level. Due to the need to visualize and quantify radiopharmaceuticals in anatomical structures of a millimetre or less, good spatial resolution and sensitivity are the most important considerations for small-animal imaging systems. As the range of potential preclinical PET application increase with the resolution and sensitivity of the PET system, there has been a significant effort to develop dedicated small-animal PET imaging systems [196], [191], [107], [77].

Most of the developed [49], [215], [81] and all commercially available high-resolution small-animal PET scanners [212], [138], [105], [72] were based on detectors employing pixelated scintillators. Spatial resolution achievable by these systems, down to 1.2 mm, was directly related to the size of employed crystal pixel size. In order to achieve even better resolution, detectors based on a smaller pixel size, even down to 0.5 mm [187], were proposed. However, the complexity and high cost of fabricating finely pixelated scintillators limit their adoption and use in commercial small-animal PET scanners. Moreover, finer discretization of the scintillator crystals causes a decrease in sensitivity due to the introduction of larger inter-pixel dead space.

Due to the limitations of pixelated detectors, the use of monolithic scintillator crystals for high-resolution small-animal PET systems has been proposed [26], [128], [143], [34]. Detectors based on monolithic scintillation crystals have shown to be a promising alternative for small-animal PET scanners with spatial resolution better than 2 mm reported [119], [32]. They show higher sensitivity due to lack of inter-pixel dead space and can provide both good energy and timing resolution [174]. Monolithic crystals are also cheaper and easier to fabricate than finely pixelated crystals, important for potential commercialization of small-animal PET systems. Moreover, in contrast to pixelated detectors, monolithic crystals provide depth of interaction (DOI) information without modification of crystals, which can be derived from the shape of the light distribution across the detector [112], [122], [206]. Most important, monolithic scintillators are capable of providing all of these benefits simultaneously, without trade-offs typical for pixelated detector designs.

Recently, we presented a prototype of a dedicated high-resolution small-animal PET scanner called DigiPET [68]. The scanner was based on detectors built from monolithic 32×32×2 mm^3 LYSO crystal and a digital silicon photomultiplier (dSiPM), also called Digital Photon Counter (DPC), from Philips Digital Photon Counting (PDPC). DigiPET achieved an excellent spatial resolution of 0.7 mm uniform in the entire field of view (FOV) and intrinsic spatial resolution of the individual detector modules was 0.54 mm full-width-at-half-maximum (FWHM). However, the limitation of the scanner was low sensitivity due to the low stopping power of the 2 mm thick LYSO crystals.

In this work we present an improved detector design intended for a new small-animal PET scanner currently being developed in our group. The new detector is based on the same dSiPM arrays and employs a thicker LYSO crystal with a thickness of 5 mm to overcome the sensitivity limitation of the previous design. Our goal is to build a detector that achieves higher sensitivity and simultaneously sustain a sub-millimetre spatial resolution. In the following sections, we describe the detector architecture and explain the calibration procedure of the detector and the positioning method used for the estimation of gamma photon interaction positions. Furthermore the performance in terms of energy resolution, coincidence resolving time (CRT), DOI decoding and spatial resolution is reported.

7.2 Materials and methods

7.2.1 Detector

7.2.1.1 Detector assembly

The detector consists of a monolithic LYSO scintillator (Hilger Crystals, UK) with a cross section of 32 mm × 32 mm and a thickness of 5 mm. All crystal surfaces are polished. A white reflector is applied on the top of the crystal, i.e. entrance surface proximal to the radiation source, and its lateral sides are painted black. The crystal is optically coupled to a Digital Photon Counter (DCP 3200-22-44, Philips Digital Photon Counting) photosensor [74]. For the optical coupling optical grease Saint-Gobain BC630 (refractive index 1.465) was used.

The dSiPM is a photosensor made of arrays of Geiger-mode single-photon avalanche photodiodes (SPAD), which each micro SPAD is integrated with CMOS logic circuitry. The CMOS logic provides trigger, timestamp, programmable control logic and digital readout for every micro SPAD. The entire dSiPM photosensor is called a tile and consists of 16 dies arranged in a 4 × 4 manner. Each die consists of 4 pixels arranged in 2 × 2 with each pixel containing 3200 cells. In addition each die has a time-to-digital converter (TDC). Furthermore, each pixel is further divided into four sub-pixels. Each die is independent and provides single timestamp and four values of the number of detected photons for each of the pixels. The active area of the dSiPM tile is 32 mm × 32 mm with a fill factor of 78%. The overview of the dSiPM tile structure is shown in figure 7.1.

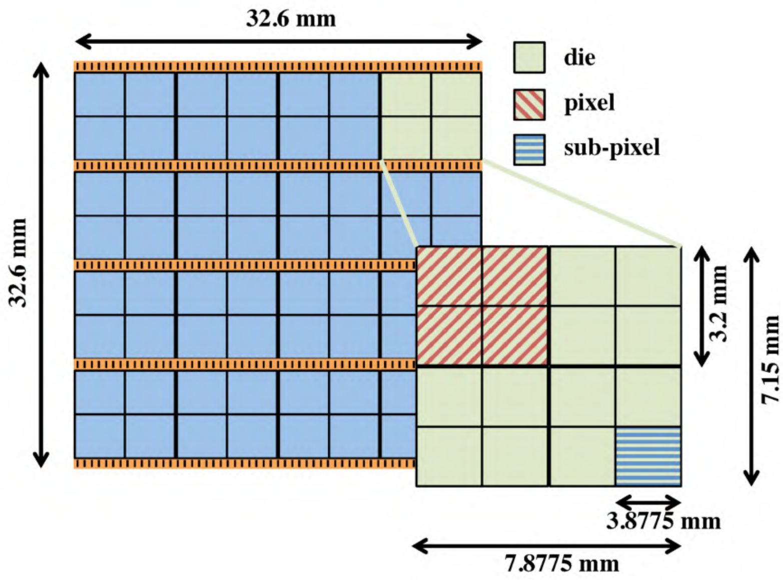

Figure 7.1: Schematic overview of the structure of the dSiPM tile. One die is enlarged to present in more detail the structure of the dSiPM die.

7.2.1.2 dSiPM tile configuration

Thanks to the CMOS circuitry inside the dSiPM chip, the device contains a set of configurable parameters that define its acquisition process such as a trigger level and integration time. Furthermore, the entire acquisition process of the dSiPM tile is controlled by several Boolean logic networks operating at the sub-pixels level. A detailed explanation of the acquisition process and these networks can be found elsewhere [74], [195].

In all measurements presented in this article the following configuration of the dSiPM tile has been used: trigger level 2, validation level 2, validation time 40 ns, integration time 45 ns, Neighbour Logic disabled, RTL refresh enabled. Furthermore, 20% of the cells with the highest dark count rate were switched off to reduce the influence of dark counts on detector's performance. This configuration has been found to be optimal in terms of sensitivity and performance of the detector based on monolithic crystals where a light from a single gamma interaction is spread over multiple dies [132]. This is the same configuration that has been used in our previous detector design [68].

7.2.1.3 Detector's cooling

The dSiPM, as every silicon-based detector, suffers from the occurrence of dark counts due to thermal excitation. This spontaneous, temperature dependent process, caused by the impurities in silicon material, leads to discharges of the cells of the dSiPM tile. Due to the acquisition process of the dSiPM the high dark count rate can lead to a significant decrease in the sensitivity of detectors based on this device [132], [131]. That is why the presented detector is operated at a lower temperature, to decrease the dark count rate.

For this purpose a dedicated cooling system was developed to cool the dSiPM tile and keep its temperature stable during measurement. The back of the detector is connected to a cooling stack consisting of a Peltier element, heat sink (aluminium) and a fan. A thin layer of thermo conductive paste is applied between each component to assure a better thermal conductivity between them. The Peltier element is controlled by a temperature controller 5R7-350 from Oven Industries. The temperature feedback to the controller is provided by a thermistor attached to the back of the dSiPM tile. With this cooling system the detector is cooled to a stable temperature of 6 °C ± 0.5 °C.

7.2.2 Measurement setup

An overview of the measurement setup used to perform the calibration of the detector is presented in figure 7.2. The setup consists of a tungsten-lead collimator for obtaining a 0.4 mm diameter gamma pencil beam for detector irradiation. The collimator is built from two parts, a 7 cm long and 4 cm diameter tungsten cylinder facing the detector under test and a 10 cm long, 6 cm in diameter lead cylinder facing a reference detector. The 511 keV photon beam is formed by placing a ^{22}Na point source (7.4 MBq) between two parts of the collimator: the diameter of the beam irradiating the detector under test is defined by the 0.4 mm aperture in the tungsten cylinder and the diameter of the beam irradiating the reference detector is defined by a 6 mm aperture in the lead cylinder. The central axes of both cylinders and the ^{22}Na source are aligned to maximize the coincidence count rate achievable with the collimator.

The reference detector consists of a 6 × 6 × 22 mm^3 LYSO crystal wrapped in Teflon optically coupled to a single die of dSiPM 3200-22-44 tile. Only a single die on top of which the crystal is located is activated for the reference detector. The reference detector is used to perform all data acquisition in the coincidence mode and to provide timestamps and energy for the identification of the 511 keV coincidence events.

The detector under test is mounted on an x, y, z translation stages (X-Slide, Velmex) which allow the detector to be moved in front of the 511 keV beam with a precision of 25 μm. The front face of each of detectors is located 1 mm away from the corresponding collimator face.

The entire setup was placed in a light tight cabinet. All data acquisitions were performed in coincidence mode to reject LYSO self-activity and to perform timing calibration using the Philips Digital Photon Counter Technology Evaluation Kit (PDPC-TEK).

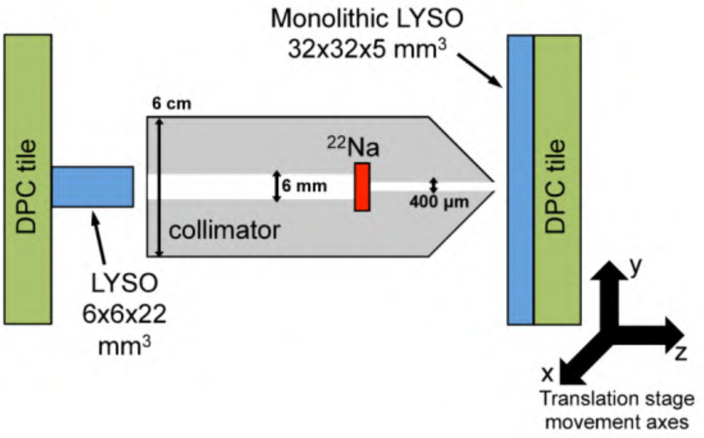

Figure 7.2: An overview of the calibration setup.

7.2.3 Calibration and data processing

7.2.3.1 Events processing and filtering

The detector under test was irradiated with a pencil beam of 511 keV gamma photons in a grid of 31 × 31 reference beam positions with a 1 mm step size and 1 mm spacing from the edges of the detector. At each grid position m a coincidence data acquisition was performed for duration of 200 s resulting in a separate set of data of ~2300 coincidence events for each grid position. For all recorded data a saturation correction of the total number of registered photons by each pixel of dSiPM was performed using the following formula:

$$\mathbf{N_{phot}} = -\mathbf{N_{tot}}\mathbf{ln}(\mathbf{1}-\frac{\mathbf{N_{fired}}}{\mathbf{N_{tot}}}) \tag{7.1}$$

where $\mathbf{N_{fired}}$ is the number of fired cells in the dSiPM pixel and $\mathbf{N_{tot}}$ is the total number of enabled cells of the dSiPM pixel. For each position an energy spectrum was generated and for further processing only scintillation events inside the 511 keV photopeak were accepted. For each accepted event a normalized value of recorded photons per pixel $\boldsymbol{k}$ ($\mathbf{N_{norm,k}}$) was calculated:

$$\mathbf{N_{norm,k}} = \frac{\mathbf{N_{phot,k}}}{\sum\limits_{\mathbf{k=1}}^{\mathbf{64}} \mathbf{N_{phot,k}}} \tag{7.2}$$

All recorded events are further sorted into separate groups depending on the index of the pixel ($\mathbf{Pixel_{m,k}}$) that recorded the highest fraction of detected photons per event. The group containing the highest number of assigned events per position $\boldsymbol{m}$ is labelled the $\mathbf{MainPixel_m}$. The events grouped in the $\mathbf{MainPixel_m}$ are considered the main detector response pattern for irradiation position m and are used for further processing. All other groups and their events are discarded unless the group contains at least 20% of the total number of recorded events at a given beam position m and the group's pixel is physically adjacent to the MainPixel. This step allows us to preserve events with a representative detector response pattern in a situation where a beam irradiation took place on the border of two or more pixels. In such situations, due to a propagation of optical photons and fluctuations of dSiPM response two or even more pixels can be competing for the position of the $\mathbf{MainPixel_m}$. Discarding all groups except the $\mathbf{MainPixel_m}$ in such scenario would cause a loss of a high fraction of representative events for given beam position m. On the other hand, the discarding procedure allows to reject events that are not main type of detector response for position m, such as multiple interactions, but ended up in the photopeak energy window (400-650 keV).

7.2.3.2 Mean maps creation

In the next step, the variance of normalized pixel values ($\mathbf{Var_i}$) for every event $\boldsymbol{i}$ in each accepted $\mathbf{Pixel_{m,k}}$ group is calculated:

$$\mathbf{Var_i} = \frac{\mathbf{1}}{\mathbf{64}} \sum_{\mathbf{k=1}}^{\mathbf{64}} (\mathbf{N_{norm,k}} - \boldsymbol{\mu}_\mathbf{i})^2 \tag{7.3}$$

where $\boldsymbol{\mu}_\mathbf{i}$ is a mean value of event $\boldsymbol{i}$ normalized pixel values. The calculated variance is a measure of scintillation light spread over the surface of the detector, which corresponds to the depth of interaction (DOI) of the scintillation event. For the gamma photons that interacted in the top layer of the scintillator crystal, far from the dSiPM face, the produced scintillation light is spread more uniformly across the detector surface and the variance of pixels' $\mathbf{N_{norm,k}}$ is smaller. On the other hand, the light produced from gamma photons that interacted in the bottom layer of the scintillator, close to the face of dSiPM sensor, will be concentrated on the small area of dSiPM tile resulting in a higher variance of pixels' $\mathbf{N_{norm,k}}$ values. Thus, sorting events on the basis of the variance of the light recorded per pixels allows us to obtain a profile of light spread within the crystal along the crystal's depth and allows us to determinate a depth at which the incoming event interacted within the crystal. This principle has been used to obtain the DOI information in the detector.

For each accepted $\mathbf{Pixel_{m,k}}$ group, variance of every event in that group is calculated and the resulting values are sorted in an ascending order. An example of such sorted variance values represented as a plot is shown in figure 7.3. After the plots of sorted events variance are obtained, events in each $\mathbf{Pixel_{m,k}}$ group are further split into separate groups corresponding to the defined DOI layers. Here three DOI layers were defined, each corresponding to 1/3 of the thickness of used LYSO crystal i.e. ~1.66 mm. The layers are labelled: top (the layer furthest from the dSiPM tile), middle (the layer equally distant from the dSiPM tile and the entrance face of gamma photons) and bottom (the layer closest to the dSiPM tile). For the remainder of this paper these labels will be used for describing DOI layers. Knowing the scintillator stopping power and the thickness of defined DOI layers, for each DOI layer we estimated a fraction of recorded gamma photons that should interact in that particular layer. Once the plot of sorted variance values is obtained, the values that demarcate the estimated fraction of interactions in each defined DOI layer are selected from the sorted variance values. These selected values, which estimate the boundaries of the DOI layers, are stored and used to determine the DOI of the detected gamma photons.

Events were then assigned to the particular DOI layer based on their variance of $\mathbf{N_{norm,k}}$ and the estimated boundaries that demarcated the defined DOI layers (i.e. number of events with the smallest variance, equal to the fraction of events that were assigned to the top layer and so on). A mean map of the normalized light distribution across the dSiPM array, **MeanMap**, is then calculated for each DOI layer of accepted $\mathbf{Pixel_{m,k}}$ group at each po-

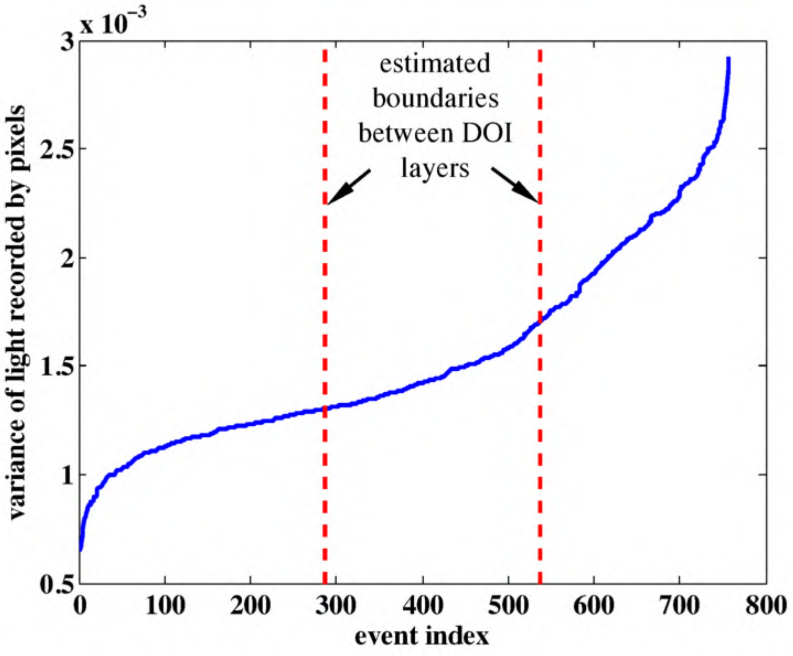

Figure 7.3: An example of the sorted variance values of normalized light fraction recorded by the dSiPM pixels per event. Dashed, vertical lines demarcate the estimated boundaries between defined DOI layers.

sition ***m***:

$$\mathbf{MeanMap_{l,m,k}} = \frac{\mathbf{1}}{\mathbf{M}} \sum_{\mathbf{m=1}}^{\mathbf{M}} \mathbf{N_{norm,k,m}} \ \forall \ \mathbf{m} \in \mathbf{Pixel_{m,k}} \tag{7.4}$$

where $\mathbf{MeanMap_{l,m,k}}$ is the value of pixel ***k*** of the calculated mean map, and ***M*** is the number of events assigned to DOI layer ***l*** $\in$ { top, middle, bottom }. An example of a normalized mean maps is shown in figure 7.4.

Once all mean maps are obtained, maps of normalized pixel values at each calibration position m for each DOI layer was created for each pixel ***k*** of the dSiPM array. A cubic spline interpolation method was then used to interpolate these maps to obtain normalized pixel values at a finer grid with 250 μm step size (see figure 7.5). Interpolated maps were then used to re-create mean maps of normalized light distribution across the dSiPM array with a finer irradiation grid with 250 μm step size. These interpolated maps were used as the reference data for the positioning algorithm.

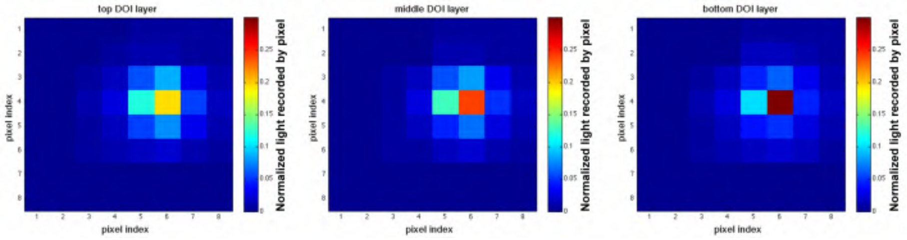

Figure 7.4: An example of normalized mean maps calculated for each DOI layer.

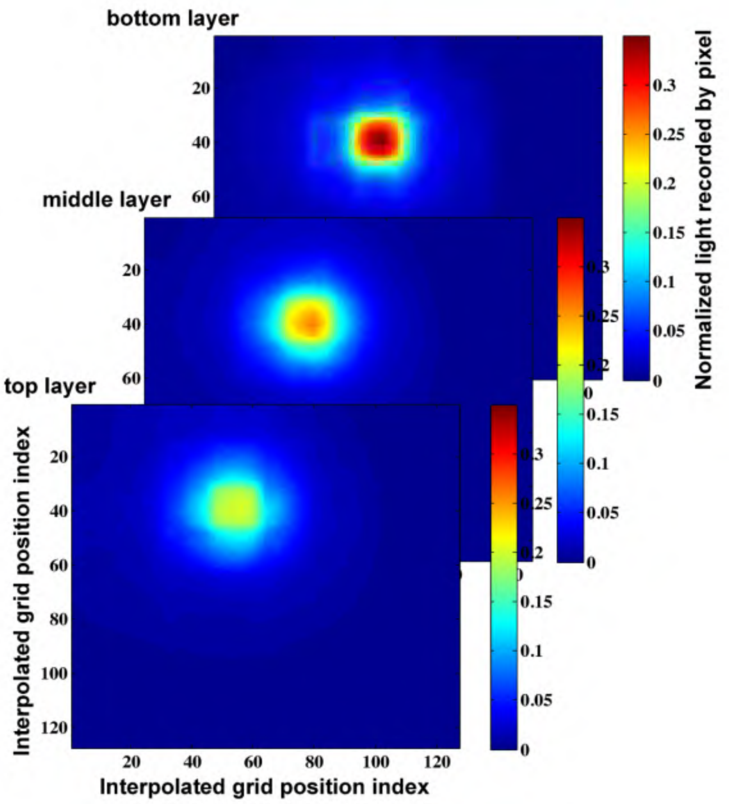

Figure 7.5: An example of maps of normalized value for a given pixel at each interpolated grid position for different DOI layers. The colour scale range is kept the same for all three displayed maps.

7.2.4 Events positioning

The Mean Nearest-Neighbour (MNN) algorithm [60] was used for event positioning. This method calculates the squared Euclidean distance of the light distribution of an event i to the mean light distribution at the calibration grid position $\boldsymbol{m}$:

$$\mathbf{Dist_{i,m}} = \sum_{\mathbf{k=1}}^{\mathbf{64}} (\mathbf{N_{norm,i,k}} - \mathbf{MeanMap_{m,k}})^2 \tag{7.5}$$

where $\mathbf{N_{norm,i,k}}$ is the normalized value of pixel k for event i.

The calculated distance is a measure of how similar the light distribution of event i is to the mean light distribution obtained at grid position m. The interaction position of event i is assigned to the grid position m for which the calculated squared distance is the smallest:

$$\mathbf{Pos_i} = \arg\min_{\mathbf{m}}(\mathbf{Dist_{i,m}}) \tag{7.6}$$

As each grid position $\boldsymbol{m}$ has three mean light distribution maps, each corresponding to the defined DOI layers, the MNN method determines event interaction position in x-, y- and z-dimension in a single step resulting in 3D positioning of events within the monolithic crystal.

7.2.5 Evaluation of detector performance

Energy spectra were obtained at each beam position. The energy resolution at 511 keV was determined at each position by fitting a Gaussian function to the 511 keV photopeak. The full width at half maximum (FWHM) of the fit is reported. An average energy resolution of the detector is given as a mean of the calculated FWHM obtained at each beam position.

The CRT was calculated at each beam position as the FWHM of the Gaussian fit to the timestamps difference histogram. Only events in 400-650 keV energy window were used. The timing resolution of the detector was obtained as the average value of the histogram of CRT values calculated for all beam position.

For the evaluation of detector's intrinsic spatial resolution an additional set of test data, independent from the calibration set used for mean map creation, was acquired. The same procedure, as for the acquisition of calibration data was used, i.e. pencil beam irradiation at the same 31 × 31 grid with 1 mm step, 200 s per position. The intrinsic spatial resolution of the detector was obtained by applying the MNN method to each test data beam position; only 511 keV photopeak events were selected. For each beam position a 2D histogram of the calculated position was created. FWHM and full width at tenth maximum (FWTM) of the cross-section of these 2D histograms along the x- and y- directions are reported as a measure of detector's intrinsic spatial resolution. The reported values are not corrected for the size of the pencil beam.

For each beam position the positioning bias was evaluated. The bias was calculated as the Euclidean distance from the actual beam position to the average estimated position:

$$\mathbf{Bias_i} = \sqrt{(\widehat{\mathbf{x_i}} - \mathbf{x_m})^2 + (\widehat{\mathbf{y_i}} - \mathbf{y_m})^2} \tag{7.7}$$

where $\widehat{\mathbf{x_i}}$ and $\widehat{\mathbf{x_i}}$ are estimated x and y coordinates of the test beam positioned at grid position x_m and y_m. Length and direction of the bias are reported.

The DOI capability of the detector was tested by irradiating one of the lateral sides of the crystal with the perpendicular 511 keV pencil beam. The irradiations were performed with 0.5 mm step size along the entire length of the crystal's lateral side (z axis). These lateral irradiations were performed in coincidence with the reference detector. At each z-position data were collected for 15 minutes. For each z-position, recorded events were positioned using the MNN method and for each positioned event the estimated DOI layer was compared with the true DOI layer corresponding to the z-coordinate of the beam irradiation. The mean absolute error (MAE) was then calculated for each z-position to represent the DOI resolution as a function of DOI.

7.3 Results

7.3.1 Energy resolution

An average energy resolution of the detector was 23±2% FWHM at 511 keV. The energy resolution was better in the centre region of the detector and worsened towards the detector's edges as presented in figure 7.6(a). Three lines of worse energy resolution across the detector correspond to the dead area regions of the dSiPM array that contain the wire bonding of the pixels' microcells. Therefore, the fraction of the scintillation light is lost in these regions. Detector energy resolution is correlated with the 511 keV photopeak position as shown in figure 7.6(b). The regions with the lower number of detected optical photons in the 511 keV photopeak corresponds to the regions with worse energy resolution.

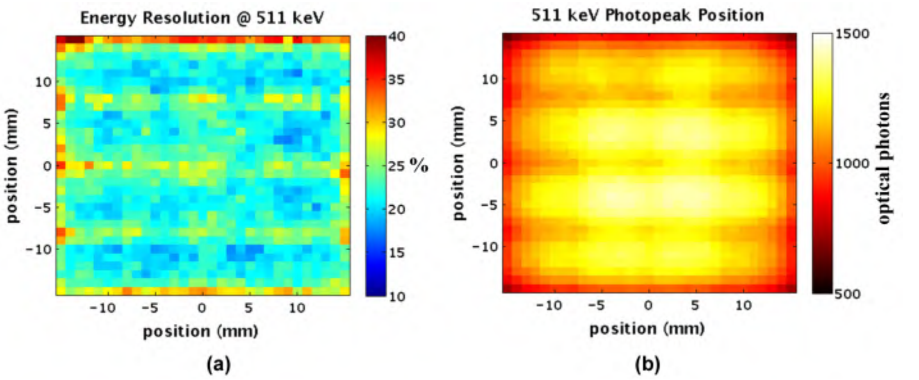

Figure 7.6: Map of detector energy resolution (a) and 511 keV photopeak position (b) obtained at each calibration position.

7.3.2 Timing resolution

The histogram of the detector CRT values obtained for all calibration position is presented in figure 7.7. Timing resolution of the detector, defined as the average of the CRT histogram, was 529±34 ps for the employed trigger level 2.

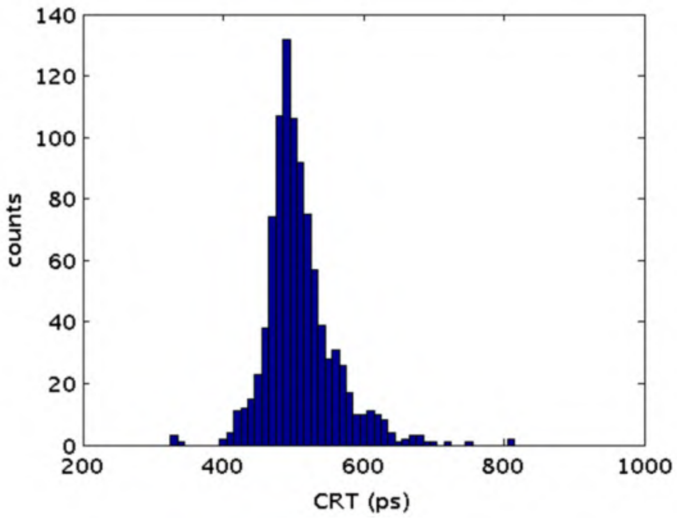

Figure 7.7: Histogram of the CRT values obtained at each calibration position.

7.3.3 Position estimation

7.3.3.1 Spatial resolution

Maps of the detector's intrinsic spatial resolution in the x and y directions are shown in figures 7.8(a) and (b) respectively. Using the MNN positioning method, an average resolution of 0.60 mm was achieved for the detector across its entire area. As the MNN method performs 3D positioning based on pre-defined DOI layers, maps of detector intrinsic spatial resolution obtained at each DOI layer are shown in figure 7.9. The average intrinsic spatial resolution in each independent layer was 0.43±0.19, 0.52±0.22 and 0.49±24 mm FWHM for top, middle and bottom layer respectively. Spatial resolution in terms of FWHM and FWTM for the entire detector and for each DOI layer is summarized in table 1.

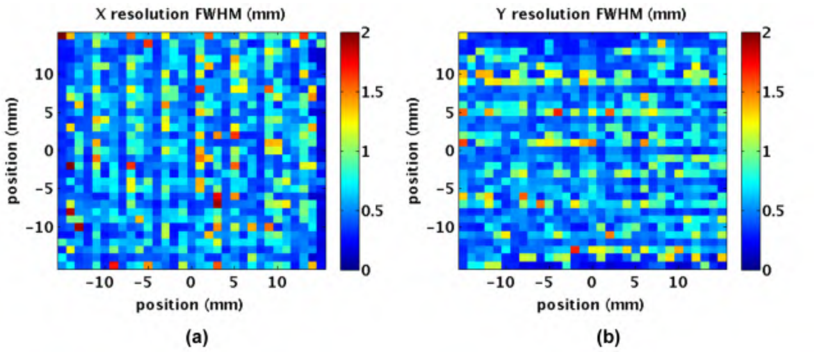

(a) (b)

Figure 7.8: Maps of detector's intrinsic spatial resolution in x (a) and y (b) directions.

The overall spatial resolution of the detector is slightly worsen than spatial resolution of each independent DOI layer. This is caused by an independent positioning bias in each DOI layer, that leads to a broader point spread function of the detector when the entire crystal volume is taken into account, and not only independent DOI layers. Slightly better spatial resolution along the y direction can be explained by the rectangular shape of the active area of the dSiPM pixel (3.2 mm × 3.88 mm). The orientation of the 3.2 mm pixel edge along the y-axis of the measurements resulted in a slightly better light sampling along the y direction. It is necessary to point out that the resolution along the edges might have been underestimated as the PSF got compressed and cannot be extended over the edges. Figure 7.10 shows the image that is the superposition of the positioned events acquired with the pencil beam scans performed at a grid with 3 mm step size. Positioning was

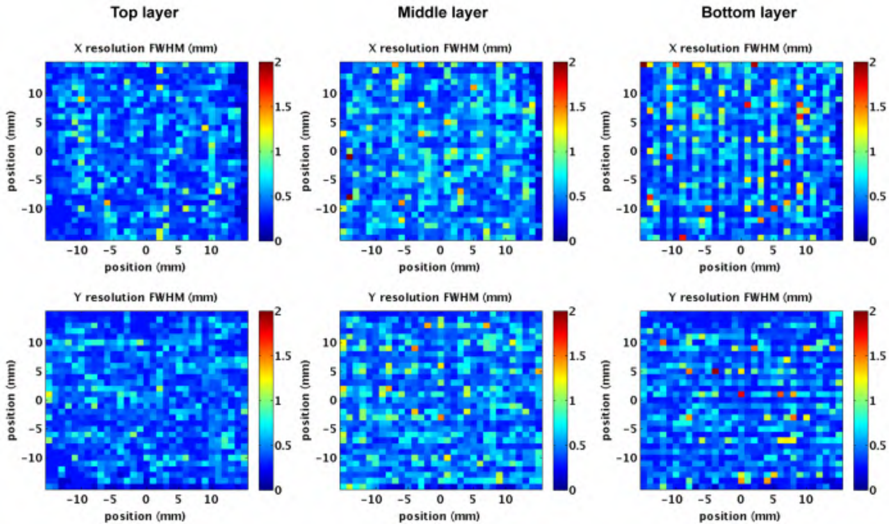

Figure 7.9: . Maps of intrinsic spatial resolution in x and y direction calculated for each of pre-defined DOI layer independently (the top layer is the layer furthest away from dSiPM array, the bottom one is the closest one, and the middle one is in between).

performed with the MNN method. The image size is 127 × 127 pixels with a pixel size of 0.25 mm × 0.25 mm. A post-smoothing Gaussian filter with 0.75 mm FWHM was applied.

Table 7.1: Intrinsic spatial resolution for the detector in each DOI layer and entire crystal volume

Selected plane	X-direction		Y-direction	
	FWHM (mm)	FWTM (mm)	FWHM (mm)	FWTM (mm)
top layer	0.43±0.19	1.65±0.68	0.42±0.16	1.59±0.57
middle layer	0.52±0.24	1.63±0.57	0.51±0.22	1.63±0.57
bottom layer	0.51±0.24	1.51±0.64	0.45±0.21	1.43±0.63
entire volume	0.60±0.27	1.66±0.56	0.58±0.26	1.64±0.57

7.3.3.2 Positioning bias

The map displaying the magnitude and direction of the bias calculated for the MNN positioning method is presented in figure 7.11. The colour scale decodes the magnitude of the bias and black arrows shows the translation

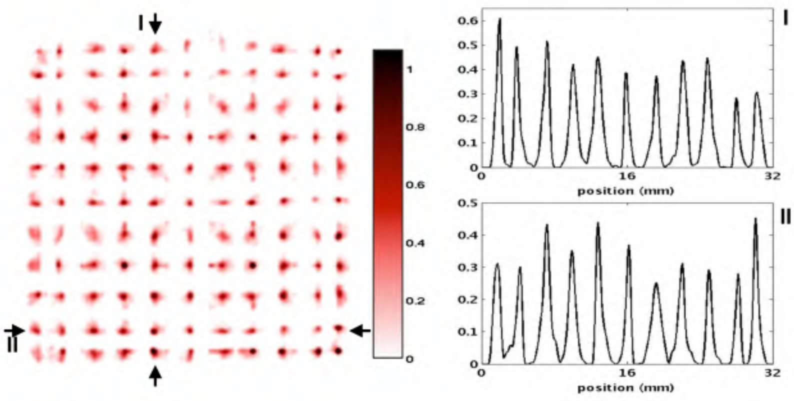

Figure 7.10: An image of positioned grid scan with line profiles through it. Arrows indicate the row and column selected for plotting the line profiles. Roman numbers associate the plotted profiles with the selected through-image lines.

from the true beam position to the measured one. The average value of the detector bias was 0.38±0.34 mm, with the bias magnitude higher along the crystal edges and in corners. Taking into account only the central region of the detector (26 × 26 mm^2) the bias was equal to 0.33±0.23 mm.

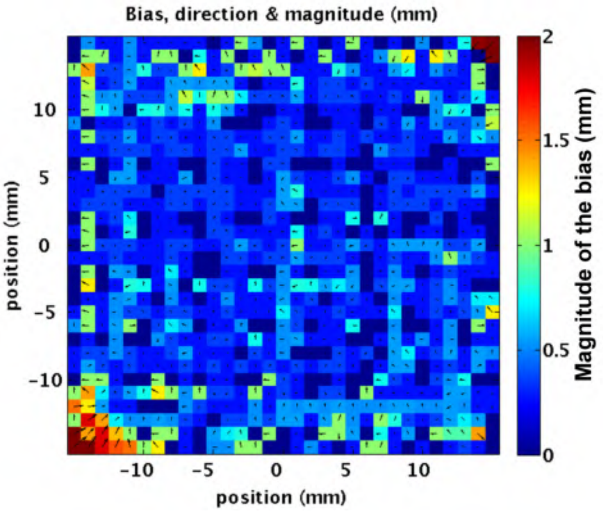

Figure 7.11: Map of detector's bias magnitude and direction. The colour scale decodes bias magnitude, black arrows show the translation from the true beam position to the measured one.

7.3.3.3 DOI resolution

The DOI resolution (mean absolute error) as a function of DOI is shown in figure 7.12. The DOI resolution is better closer to the surface of the dSiPM than close to the front face of the detector. This can be explained by the spread of scintillation light produced at the given DOI. The closer the gamma photon interacts to the surface of the dSiPM, the more focused is the recorded light and the higher calculated variance. This in turn is easier to resolve than for gamma photons that interacted at small DOI and produced more uniformly spread light which are more similar to each other. The peak of worse DOI resolution around the DOI of 3.5 mm is related to the fact that the border between the middle and the bottom DOI layer is located very close to this DOI. In that situation it is more difficult for the MNN algorithm to correctly resolve between these two DOI layers. However, the achieved DOI resolution is still comparable to the DOI resolution achieved close to the front face of the detector.

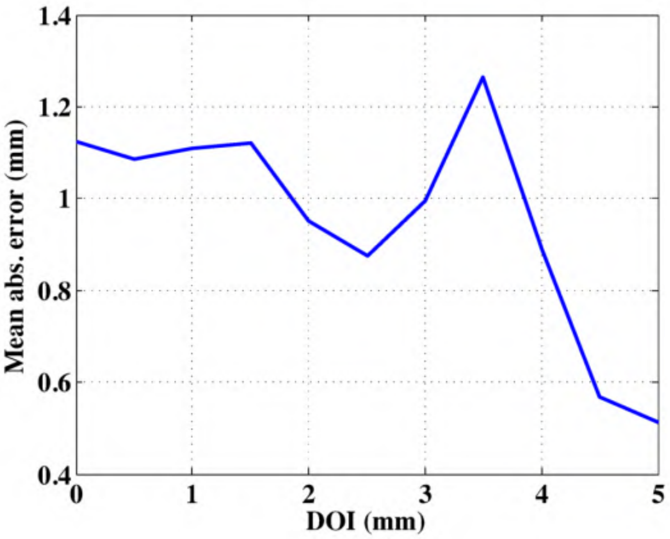

Figure 7.12: DOI resolution (mean absolute error) of the detector as a function of the DOI. DOI of 0 mm corresponds to the entrance face of the detector (proximal surface from the radiation beam).

7.4 Discussion

The use of 5 mm thick LYSO crystal increases the nominal sensitivity of the single detector ∼2.21 times in comparison to the 2 mm thick LYSO crystal used previously [68]. Still, the detector with a 5 mm crystal displays outstanding intrinsic spatial resolution of 0.60 mm. This can be attributed to DOI decoding based on the calculated variance of the light spread of detected events and the MNN positioning in each DOI layer. Each independent DOI layer displays internal spatial resolution of ∼0.5 mm that is consistent with the spatial resolution obtained with the previous crystal of 2 mm thickness. The achieved spatial resolution of 0.60 mm shows an improvement compared to previously published results obtained with monolithic scintillators. Cabello [32] reported spatial resolution of 0.69±0.08 mm FWHM and 1.89±0.22 mm FWTM obtained with the LYSO crystal of 12 × 12 × 5 mm^3 coupled to 8×8 pixels SiPM. A positioning method based on the analytical model using non-linear least squares data fitting [120] was used for the estimation of gamma photons interaction positions within the crystal. Similar results were reported by [123] also for the LYSO crystal of 12 × 12 mm^2 and the thickness of 5 mm coupled to a SiPM. The group reported the average spatial resolution of 0.77 mm FWHM using a non-linear least squares data fitting [120] for positioning. Improved results for our detector can be explained by the employed DOI decoding while Cabello [32] and Llosá [123] designs lacked the DOI decoding and reported positioning bias toward the crystal side coupled to the SiPM. Despite lack of the DOI, detectors showed very good spatial resolution which can be contributed to a good light sampling across the SiPM due to pixels small size of just 1.4 × 1.5 mm^2 and used positioning method. Both Cabello [32] and Llosá [123] also evaluated 10 mm thick crystals reporting spatial resolution of 0.73±0.11 mm FWHM and 0.81 mm FWHM, respectively. As expected, spatial resolution worsened for thicker monolithic scintillator blocks. Miyaoka [143] using 50 × 50 × 8 mm^3 monolithic LYSO block coupled to a 64-channel multi-anode PMT and the statistics based positioning method (SBP, [95]) achieved the average resolution in radial, transverse and axial direction equal to 1.05±0.08 mm, 0.99±0.07 mm and 1.24±0.31 mm FWHM respectively. This detector employed DOI decoding with 4 DOI bins and the average DOI resolution was ∼3.5 mm. Seifert [176] reported spatial resolution ranging between 0.95 mm and 1.28 mm FWHM depending on the irradiated region of the 24 × 24 ×× 10 mm^3 LSO:Ce,0.2%Ca crystal coupled to a dSiPM obtained with k-nearest neighbour algorithm [205].

Good DOI resolution allows us to achieve high spatial resolution in the entire FOV of the detectors while bringing them closer to the imaging object. This improves geometrical efficiency and hence increases system sensitivity. Comparing the intrinsic spatial resolution of the detector presented in this paper to the intrinsic spatial resolution of the previous detector design (0.54 mm) one can still expect spatial resolution below 1 mm for a system based on the improved detector. These factors allow us to increase sensitivity of the small animal PET scanner and sustain high spatial resolution of such system.

In the maps of detector's intrinsic spatial resolution (figure 7.8) lines of better resolution can be noticed. In maps of intrinsic spatial resolution for independent DOI layers (figure 7.9) this line pattern is getting stronger the closer a particular DOI layer is located to the dSiPM array. We found that these lines correspond to centres of dSiPM pixels. Investigating this further, we found that this is an effect of limited light spread sampling due to the dSiPM pixel size of 3.2 mm × 3.88 mm. Due to the small beam size diameter (0.4 mm) and low thickness of the LYSO crystal and DOI layers, the changes in the light distribution across dSiPM pixels for beam positions located in the centre region of the pixels are smaller then in case of beam positions located closer to the edges of the pixels. The closer the beam is getting to the edge of the pixels, the larger the difference in normalized values of pixels. Thus, the calculated mean maps have larger difference between each other for cases when the test beam is located in the centre and at the edge of the same pixel than in cases for two test beam positions located in the centre region of the same pixel. This causes the MNN method to perform better in positioning events along the edges and in the strict centre of the pixel, while for events belonging to an intermediate region of the pixel located between centre and the edge of the pixel, MNN performs worse. For these events, due to limited light distribution sampling and thus smaller differences in the mean maps used as the reference, the MNN method has a tendency to position them toward the centre of the pixel, which results in the appearance of line pattern of better and worse spatial resolution. This effect gets stronger the closer a scintillation event took place to the dSiPM surface as the light will be less spread across the entire detector and more focus in a small region of the photosensor leading to worsen light sampling. This can be clearly seen in figure 7.9. For the top DOI layer the lines of better spatial resolution are barely visible, as the light of the events that interact in that layer is more spread across the dSiPM array. Similar trends are observed for the middle DOI layer, where line pattern is more easily visible but are not dominant. In contrast, in the bottom layer, the line pattern of better spatial resolution is significant as the scintillation light of events interacting in that layer is much more focused locally. It is also the reason why spatial resolution is better in the top layer; more spread scintillation light leads to better sampling and smaller tendency to position events toward the pixel centre. Improving the light sampling in the detector, by employing more pixels with smaller area in the photosensor, would limit this effect and simultaneously would lead to better spatial resolution of the detector in general as the changes in light distribution across the detector for different beam positions could be recorded and traced with higher precision.

The relatively poor energy resolution might be partially explained by deactivating 20% of cells with the highest DCR and use of the RTL refresh option. Turning off 20% of the cells effectively reduces the total number of dSiPM cells and allows a fraction of photons that reach deactivated cells to be irrevocably lost. The smaller fraction of cells can be deactivated to reduce this effect, however this requires cooling the detector to lower temperature in order to keep low DCR of the dSiPM. The RTL refresh option of the dSiPM array allows for fast recharge of the device's full cell rows, that contain fired cells but which did not cause triggering of the die for a longer period of time (20 ns), without recharging the entire die [171]. This prevents cells fired by the dark counts to accumulate and cause triggering of dies, which might cause missing dies in recorded true gamma events. However, continuous recharge of the number of cell rows causes temporal reduction of the number of active cells that are available to detect scintillator light of true gamma events. This can increase noise in collected energy spectra and thus cause worse energy resolution. Nonetheless, the reported energy resolution is still in comparable range to results obtained by other groups for similar crystal thickness. Llosá [123] reported energy resolution of 20% FWHM for white painted LYSO crystals and Miyaoka [143] reported 17.2% FWHM for LYSO crystal with roughened surfaces and white paint on the top face and black one on the lateral ones. However, it is necessary to state that some groups achieved significantly better energy resolution with monolithic scintillators e.g. [176] with 12.8% FWHM at 511 keV obtained for $24 \times 24 \times 10$ mm^3 LSO:Ce,0.2%Ca wrapped in Teflon.

The detector also achieves a good CRT of 529 ps, which allows us to narrow the coincidence window and thus limit the randoms coincidence rate.

7.5 Conclusion

We have developed and evaluated performance of the improved detector for a dedicated mouse and rat PET scanner based on 5 mm thick monolithic

LYSO crystals and dSiPM array. This new detector allows us to overcome the sensitivity limitations of the previous design and simultaneously sustain the sub-millimetre spatial resolution. The achieved performance in terms of spatial resolution (0.60 mm), timing resolution (529 ps) and DOI decoding (3 layers of 1.66 mm each) belongs to one of the finest presented to date for small animal PET [187], [81], [143], [123]. These results show the high potential of the detectors based on the continuous scintillator crystals for small-animal PET imaging systems. Introduction of these novel detectors in the next generation of preclinical PET systems could allow to outperform the currently available commercial preclinical PET scanners [77]. Our next goal will be to demonstrate the performance on the system level by implementing the presented detector in the small-animal PET scanner currently being developed in our research group.

7.6 Acknowledgements

This work was supported by EU FP7 project SUBLIMA, grant agreement 241711, see also www.sublima-pet-mr.eu and by iMinds Medical IT. Roel Van Holen is funded by the Research Foundation – Flanders (FWO, Belgium) and by Ghent University.

Chapter 8

Evaluation of DigiPET2, a dedicated high resolution small animal PET scanner

This chapter is going to be submitted for publication in Phys. Med. Biol. as: R. Marcinkowski, P. Mollet, R. Van Holen and S. Vandenberghe, "Evaluation of DigiPET2, a dedicated high resolution small animal PET scanner"

8.1 Introduction

In chapter 6 we developed a prototype of a dedicated, high-resolution small animal PET scanner based on thin monolithic LYSO crystals and digital silicon photomultipliers (dSiPM). Thanks to the combination of 2 mm thick LYSO crystals, multipixel dSiPM and statistical event positioning we achieved a very compact PET system with an excellent spatial resolution of 0.7 mm, which was uniform over the entire field of view (FOV).

Since the 1990s, significant efforts have been made by the scientific community to develop dedicated small animal PET with both exceptional spatial resolution and sensitivity. However, achieving simultaneously high spatial resolution and high sensitivity is not a trivial task. Therefore, various approaches have been proposed by different groups to push both the limits of spatial resolution and sensitivity of the dedicated small animal PET systems [196], [191], [107], [77], [81]. Main focus was put on the use of different crystals sizes, system geometries and detectors configurations. This resulted in a number of developed academic PET scanners [107], [196], [19], [164],

[81] as well as a number of commercial systems [138], [212], [72], [105], [33], [194]. Spatial resolution of the developed systems ranged between 1.3 mm to 2.4 mm FWHM while sensitivity ranged between 1.2 % and 6.7 % at the center of field of view. The majority of these scanners are based on finely pixelated scintillator crystals. A limited number of systems were based on monolithic crystals, which allows to reduce the cost and increase the sensitivity as well as the energy and timing resolution of the detector [26], [128], [143], [34], [119], [123], [32]. However, the most important disadvantage of monolithic crystals is the fact that the positioning of the events is much more challenging. Complex algorithms are required. Moreover, the event positioning algorithms often require time consuming calibration.

Despite the excellent spatial resolution, the DigiPET1 prototype had some limitations. Due to the low thickness of the LYSO crystals the system had low sensitivity. The DigiPET1 also consisted of only four detectors arranged in a square orientation providing a very limited FOV of 32 × 32 × 32 mm^3. In addition, our prototype needed to be operated in a temperature chamber in order to reduce dSiPM dark count rate, which prevented scanning of living animals.

In order to overcome the limitations of the DigiPET1 prototype, we developed an improved detector with thicker LYSO crystals of 5 mm (see chapter 7). This allowed to significantly improve the sensitivity and still achieve intrinsic spatial resolution of 0.6 mm and DOI resolution of ∼1.1 mm [133]. Energy resolution of 23 % FWHM at 511 keV and a CRT of 529ps were measured for the detector.

In this chapter we present the second version of our dedicated small animal DigiPET scanner based on the thicker crystals. The new DigiPET2 system has a larger FOV, which is sufficient for both mouse and rat imaging thanks to the increased number of detectors in the scanner. Good DOI resolution of the detectors allows us to place the detectors close to the object. This results in improved angular coverage of the DigiPET2 scanner in combination with a very compact system geometry. Furthermore, our new system contains a dedicated cooling system that allows the scanner to operate at room temperature. In the following sections, we describe the system architecture and evaluate its performance in terms of spatial resolution and image quality. Imaging capabilities of the scanner and its suitability for high-resolution imaging are evaluated by acquiring scans of a micro-Derenzo phantom and a mouse head.

8.2 Materials and methods

8.2.1 System description

The DigiPET2 scanner is a high-resolution preclinical PET system dedicated for mouse and rat imaging. The scanner consists of seven detector modules arranged in a ring. The front face length of the module is 34.6 mm and the inscribed circle radius of the scanner heptagonal ring is equal to 35.9 mm. Figure 8.1 shows the geometry of the DigiPET2 scanner. The heptagonal geometry of the system was selected over the more symmetrical one (e.g. hexagon or octagon) as a trade off between scanner field of view (FOV) and the angular coverage of the object. The hexagonal ring would result in a relatively small FOV which would be insufficient to scan larger rats, while the octagonal geometry would lead to a reduced angular coverage, thus lower scanner sensitivity. The scanner has a very compact geometry: the gantry has an external diameter of 22 cm and a total length of 15 cm.

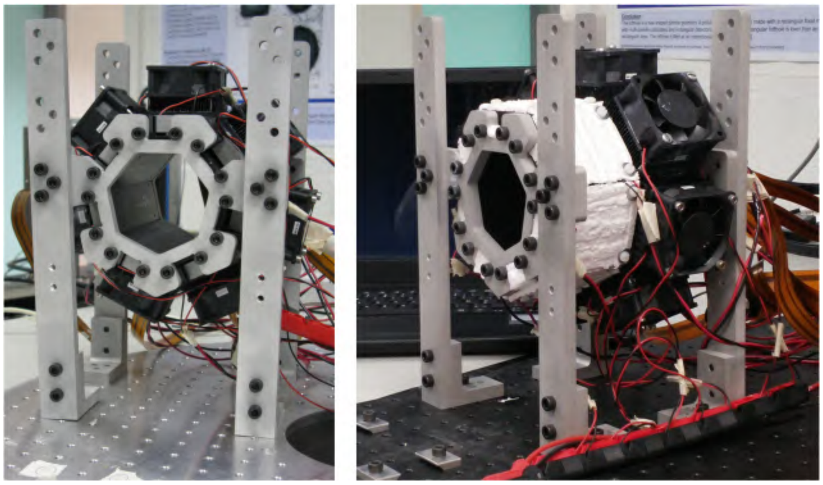

Figure 8.1: Front (left) and side (right) picture of the new DigiPET2 scanner.

Each module of the current system can house up to two detectors placed in axial direction. However, only one ring is populated with detectors giving the scanner an axial FOV of 32 mm.

Each detector [133] consists of a monolithic LYSO crystal (Hilger Crystal) with a surface of 32 mm x 32 mm and a thickness of 5 mm optically coupled to a DPC-3200-22-44 digital silicon photomultiplier (dSiPM, Philips Digital Photon Counting) [74]. The LYSO crystals have all faces polished. A white, diffusive reflector is applied on the top of the crystals and the lateral sides of the crystals are painted black to limit light reflections. For the optical coupling of the crystals to the dSiPMs a BC630 optical grease (Saint-Gobain) was used.

A detailed description of the dSiPM structure and operating principle can be found in chapter 3. However, to shortly characterize the DPC-3200-22-44, it consists of 4 × 4 individually operating dies with a pitch of 8 mm. Each die has four 3.2 × 3.8 mm pixels, each with 3200 microcells, arranged in a 2 × 2 matrix. In addition, every die has its own control logic and time-to-digital converter (TDC). Thus, for every recorded event each die provides four values of the number of photons recorded by the pixels and a single timestamp. A moment of timestamp generation is set by the programmable trigger network. The programmable validation network is then used to distinguish true events from dark counts.

In order to reduce the dark count rate (DCR) of the dSiPM, each detector has an individual cooling system that keeps the detector working temperature at 6°C± 0.5°C. The cooling system consists of a Peltier element, aluminium heat sink, cooling fan and a temperature controller (5R7-350, Owen Industries).

8.2.2 Data acquisition and processing

Data acquisition was performed using the Philips Digital Photon Counting Module Evaluation Kit (PDPC-MTEK) that allows to connect up to eight dSiPM tiles. Data are collected in a singles mode and sent to the controlling computer in list mode format. A custom Fast List-mode Iterative Reconstruction (FLIR) software developed in our group is used to identify coincidence events and to reconstruct tomographic images. The FLIR software uses Mean Nearest Neighbour (MNN) for 3D positioning of events within the monolithic crystal [60], [133] and 3D list-mode Ordered Subset Expectation Maximization (OSEM) for image reconstruction. To accelerate the image reconstruction the OSEM algorithm was implemented on a graphics processing unit (GPU) using the compute unified device architecture (CUDA) framework [50]. The MNN method calculates the squared Euclidean distance of the light distribution of an unknown event to the mean light distribution recorded at all known positions and all defined DOI layers during the calibration procedure. In this study, three DOI layers were defined per calibration point, each corresponding to 1/3 of the thickness of the LYSO crystal. The calculated distance is a measure of how similar the light distribution of the unknown event is to the mean light distribution recorded at the known position of the calibration grid and a given DOI layer. The interaction position of the unknown event is assigned to the calibration position (x and y coordinates) and DOI layer (z coordinate) for which the calculated squared distance is the smallest. A more detailed description of the used MNN algorithm and the process of defining DOI layers can be found in chapter 7.

All data measurements presented in this study were acquired with a coincidence time window of 5 ns, and with an energy window of 250-650 keV.

8.2.3 Spatial resolution

Spatial resolution of the system was measured with a 138 kBq ^{22}Na point source. The source had an active area of 0.25 mm diameter and is embedded in a 1 cm^3 acrylic cube (Eckert & Ziegler). The point source was placed in a source holder mounted on an x-, y-, z- translation stages (X-Slide, Velmex) which allow the source to be moved freely inside scanner's FOV. The ^{22}Na source was placed at two axial positions: one in the center of the axial FOV and one at a quarter of the axial FOV, i.e. 8 mm, from the center along the axial direction. At each of these two positions, the point source was moved towards the edge of the transverse FOV with a 1 mm step size across the central 7 mm. Across the remaining transverse FOV up to 25 mm a step size of 2 mm and 3 mm was used. At each source location more than 10^5 prompt counts were acquired.

Events were positioned using the MNN algorithm and the images were reconstructed using the OSEM with 10 subsets and 10 iterations. The reconstructed matrix was $100 \times 100 \times 100$. The voxel size of the reconstructed images was $0.2 \times 0.2 \times 0.2$ mm^2. No smoothing was employed on the reconstructed images. For both axial positions and for each source location the radial, tangential and axial resolution was determined. The spatial resolution was calculated as the full width at half maximum (FWHM) and the full width at tenth maximum (FWTM) of the response functions formed by summing one-dimensional profiles that were parallel to the radial, tangential and axial directions. FWHM and FWTM were determined by linear interpolation between adjacent pixels at half and one-tenth of the maximum value of the response function, respectively. The maximum value of the response function was determined by a parabolic fit of the peak point and its two nearest neighbours. The measured spatial resolutions were neither corrected for source size nor for positron range and photon acolinearity.

8.2.4 Sensitivity, scatter and count-rate performance

The current version of the DigiPET2 scanner is using a module technology evaluation kit (M-TEK) from PDPC to collect, pre-process and send acquired data to a reconstruction computer. The M-TEK was not designed to meet the requirements of the data transmission rate of a full-ring PET system. Therefore, the detectors in the scanner are capable of detecting events at higher rate than the M-TEK data baud rate. This inability to transmit data at sufficient speed resulted in a loss of a significant fraction of detected events. Because of this limitation a proper evaluation of sensitivity, count rate performance and scatter of the DigiPET2 scanner was not possible. Insufficient data transmission speed of the available electronics was also the reason for long acquisition times of all measurements presented in this paper.

8.2.5 Imaging studies

8.2.5.1 Phantom studies

A hot-rod micro-Derenzo phantom was used to evaluate the image quality obtained with the DigiPET2 system. The micro-Derenzo phantom consisted of six sectors with hollow rods of different diameter: 0.7, 0.8, 0.9 1.0, 1.2 and 1.5 mm, with a separation between rod centres equal to two times the diameter of the rods. The length of the rods was 12 mm. The phantom also consisted of a uniform region with length of 12 mm and a diameter of 26 mm. The external dimensions of the phantom were 55 mm in length and 28 mm in diameter.

The phantom was filled with 14.8 MBq of ^{18}F solution and placed in the center of the scanner's FOV. An acquisition of five hours was performed in order to obtain sufficient data. The PET image was reconstructed using 3D-OSEM with 100 iterations. The matrix size was 100 x 100 x 100 with a voxel size of 0.3 x 0.3 x 0.3 mm^3.

For comparison, the same micro-Derenzo phantom was also measured with the LabPET-8^{TM} scanner. The phantom was filled with 15 MBq of ^{18}F solution and data was acquired for 30 minutes. For image reconstruction the 2D-OSEM algorithm implemented in the scanner software was used with 100 iterations and voxel size of 0.25 x 0.25 x 0.25 mm^3.

8.2.5.2 Animal studies

A bone scan study (^{18}F-NaF Sodium Fluoride) was performed on an adult BALB/c mouse. The mouse was intravenously injected with 60 MBq of ^{18}F-NaF. The radio-tracer was administered though an intravenous tail injection under anaesthesia. One hour post injection the animal was sacrificed and placed in the DigiPET2 scanner and imaged for a duration of 5 hours. An energy window of 250-650 keV and a coincidence time window of 5 ns were used for the data acquisition. The PET images were reconstructed using Maximum-Likelihood Expectation Maximization (MLEM) with 200 iterations and with total variation noise reduction. The reconstructed matrix was 70 x 70 x 70 with a voxel size of 0.4 x 0.4 x 0.4 mm^3. A CT transmission scan of the mouse was obtained using the X-CUBE scanner (Molecubes, Belgium) to correlate PET images with the anatomical structures. The CT scan was performed with 6 bed positions with 512 projections per rotation and X-ray source was operated at 250 μA and 50 kVp. The CT image was reconstructed with the Image Space Reconstruction Algorithm (ISRA) iterative algorithm, using 5 iterations with 32 subsets and voxelsize of 0.1 mm. The PET images were manually co-registered with the CT scan using the bone structures as a reference.

8.3 Results

8.3.1 Spatial resolution

Figure 8.2 shows the radial, tangential and axial resolution (FWHM and FWTM) plotted as a function of the radial offset for both axial positions (center and one-fourth off the center of the axial FOV). For both axial positions, the spatial resolution was almost identical. The spatial resolution at one-fourth off the center was slightly better. The average tangential and axial resolution was 0.87 mm and 0.93 mm FWHM and 2.03 mm and 2.21 mm FWTM, respectively.

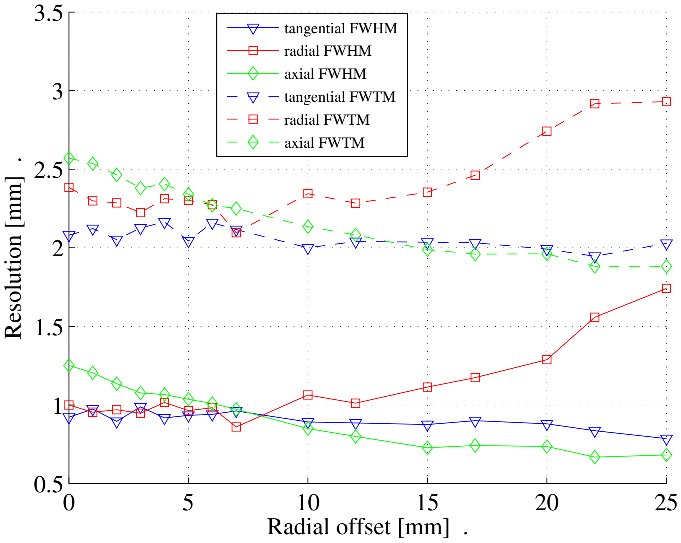

Figure 8.2: Radial (squares), tangential (triangles) and axial (diamonds) spatial resolution FWHM (solid) and FWTM (dashed) obtained for the DigiPET2 scanner as a function of the radial position.

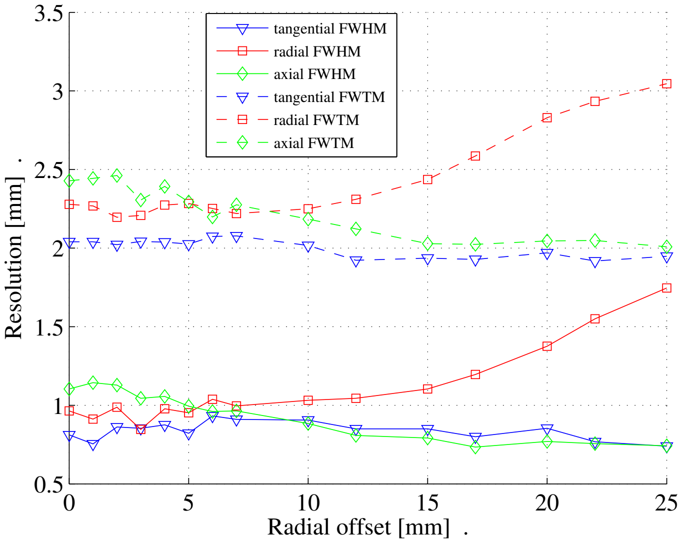

Figure 8.3: Radial (squares), tangential (triangles) and axial (diamonds) spatial resolution FWHM (solid) and FWTM (dashed) obtained for the DigiPET2 scanner as a function of the radial position for the point source located one-fourth off the center of the axial FOV.

Both tangential and axial resolution show good uniformity in the entire FOV. The radial resolution within a radius of 13 mm from the center of FOV had good uniformity with an average resolution equal to 0.98 mm FWHM and 2.23 mm FWTM. For the radial offsets larger than 13 mm from the center the radial resolution worsened systematically towards the edge of the FOV, remaining however, well below 1.8 mm FWHM and 3.0 mm FWTM.

8.3.2 Imaging studies

8.3.2.1 Phantom studies

Figure 8.4 shows the image of a transversal section through the micro-Derenzo phantom acquired with the DigiPET2 scanner. Rods down to 0.8 mm can be resolved. In addition, some of the 0.7 mm rods can be resolved. Figure 8.5 shows the cross-section profiles through the 0.8 mm rods region along the depicted lines in figure 8.4. Some artifacts, caused by the lack of attenuation and normalization corrections, can be noticed in the region with 1.0 mm rods of the reconstructed image.

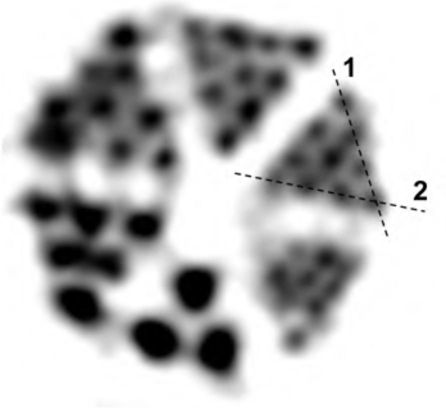

Figure 8.4: Reconstructed images of the micro-Derenzo phantom acquired with the DigiPET2 scanner.

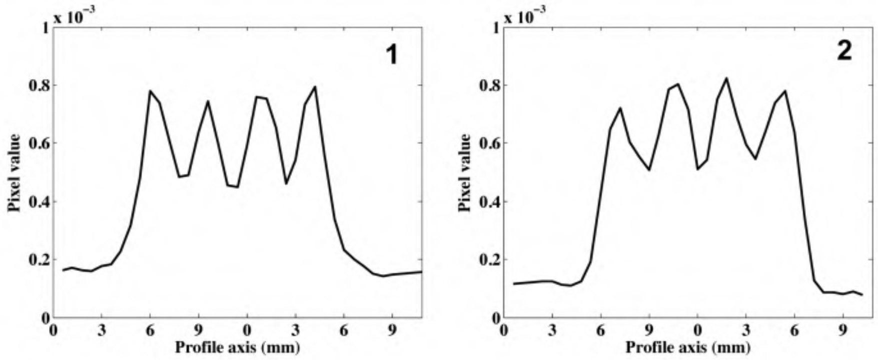

Figure 8.5: Profiles through the row of 0.8 mm diameter hot rods along the lines depicted in figure 8.4.

The image of the transverse section through the uniform region of the micro-Derenzo phantom and its cross section profile is shown in figure 8.6. A post-smoothing Gaussian filter with 0.5 mm FWHM was applied.

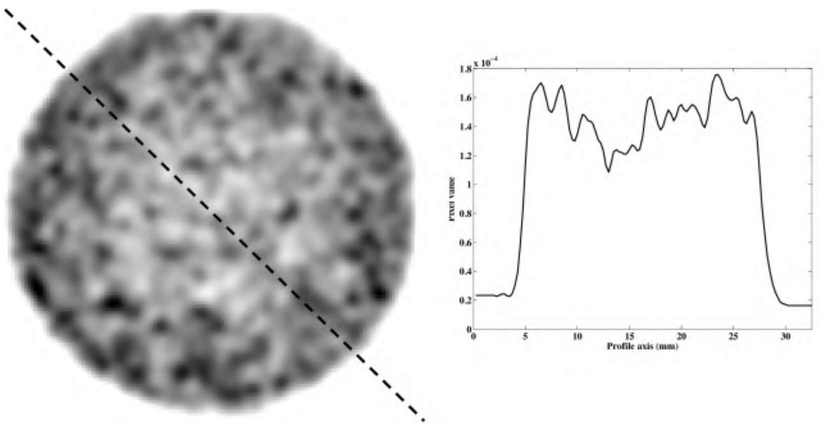

Figure 8.6: Transverse slice through the uniform region of the micro-Derenzo phantom and the profile through it (dashed line).

For image quality the comparison of the two scanners, the transverse planes of the reconstructed images of the same micro-Derenzo phantom obtained with the DigiPET2 scanner and the LabPET-8^{TM} are shown in figure 8.7. With the LabPET-8^{TM} rods down to 1.0 mm in diameter can be resolved.

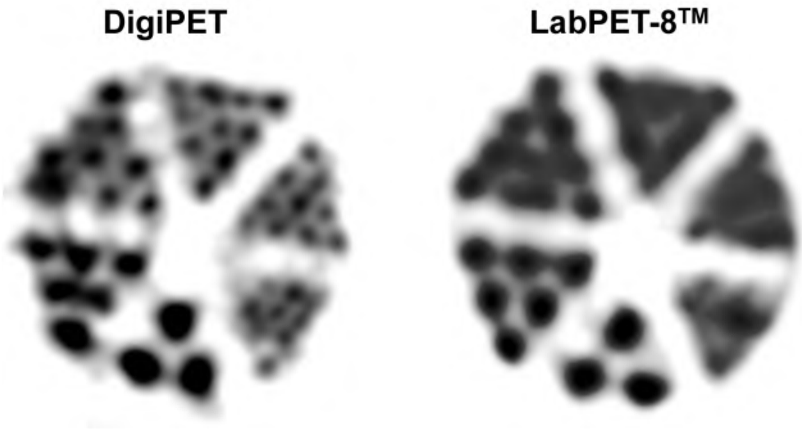

Figure 8.7: Comparison of the reconstructed images of the micro-Derenzo phantom acquired with the DigiPET2 scanner (left) and the LabPET-8^{TM} scanner (right).

8.3.2.2 Animal study

The bone images of the mouse head obtained with the DigiPET2 scanner are presented in figure 8.8. A total of 12 million coincidences were acquired.

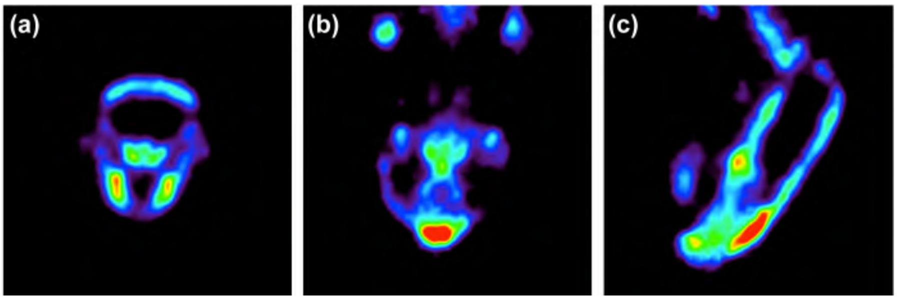

Figure 8.8: Transversal (a), coronal (b) and sagittal (c) images of the mouse head obtained with the ^{18}F-NaF.

Figure 8.9 shows the co-registered PET and CT images of the mouse head in the transverse plane. The co-registered PET/CT images of the head in the coronal and sagittal plane are shown in figure 8.10.

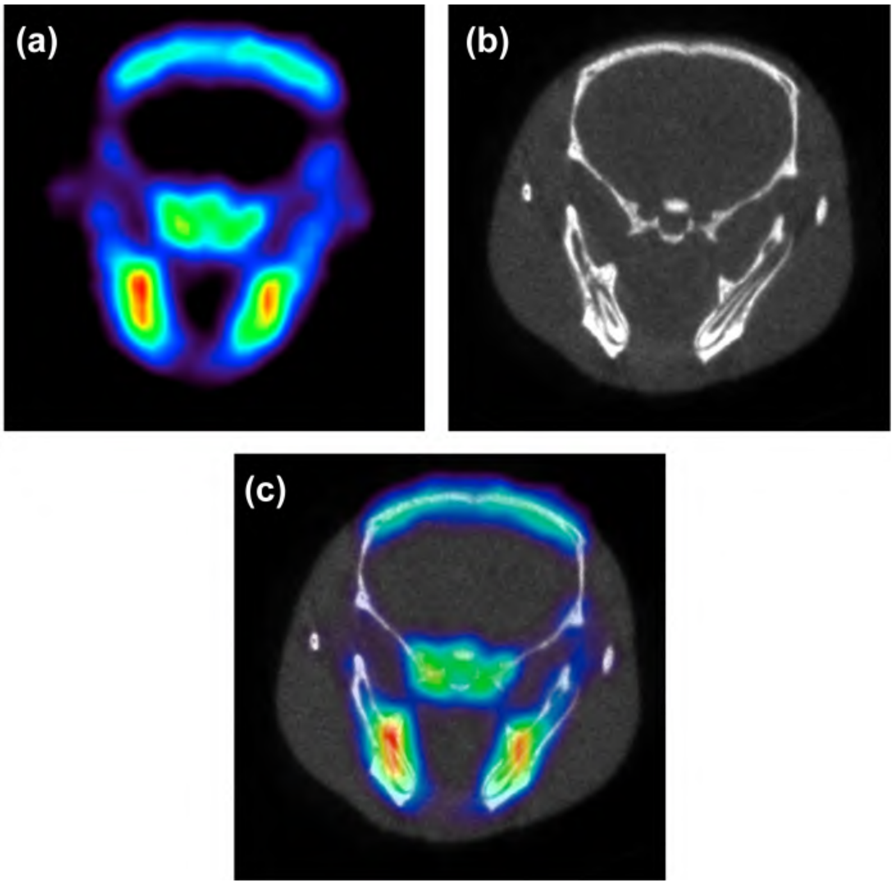

Figure 8.9: Transverse images of the mouse head obtained with (a) DigiPET2, (b) X-CUBE and (c) co-registered PET/CT image.

8.4 Discussion

The spatial resolution of the DigiPET2 scanner is worse compared to the first scanner with 2 mm thick crystals that achieved 0.7 mm spatial resolution uniform within entire FOV. Within the central 15 mm diameter FOV the spatial resolution of the new DigiPET2 scanner approaches 0.9 mm FWHM for both radial and tangential directions and 1.0-1.2 mm FWHM for the axial direction. For the radial offsets within 50 mm FOV the radial component remains well below 1.8 mm FWHM and below 0.9 mm FWHM for the tangential component. Spatial resolution for the axial component remains mostly below 1.0 mm FWHM and the resolution improves with increasing radial distance. The achieved spatial resolution allows to resolve

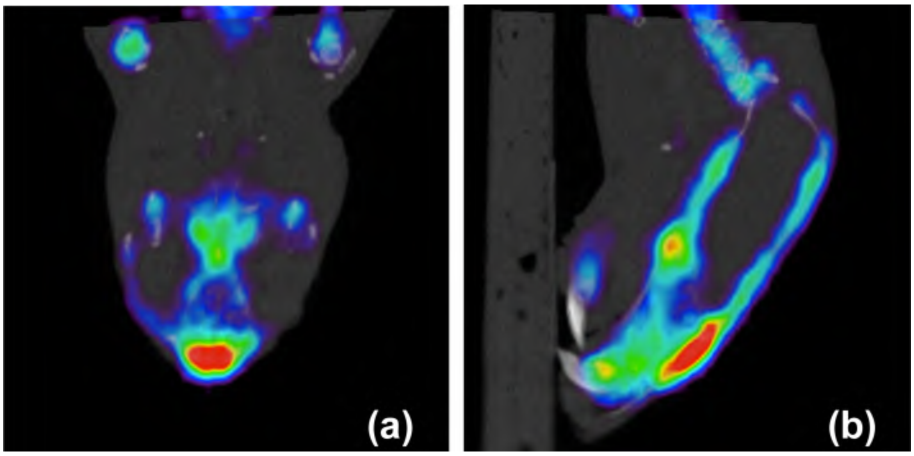

Figure 8.10: Coronal (a) and sagittal (b) images of the mouse head obtained with the DigiPET2 scanner and co-registered with the CT.

all 0.8 mm diameter hot rods in the micro-Derenzo phantom. Moreover, even some of the 0.7 mm diameter hot rods could be resolved. This submillimetre spatial resolution is one of the best spatial resolution presented up to date for a full-ring small animal PET imaging system [14], [194], [13], [196]. DigiPET2 outperforms the majority of current commercially available small-animal PET systems with average spatial resolution from 1.3 mm to 2.1 mm FWHM [77], [165]. For the same range of radial offsets the spatial resolution of the DigiPET2 ranges from 0.9 to 1.8 mm. Such improvement in terms of spatial resolution yields a clear advantage over current small-animal PET systems, especially for imaging small lesions in rodents. The achieved resolution is attributable to the excellent intrinsic resolution of the detector (0.6 mm) and its DOI resolution ($\sim$1.1 mm) [133], which were obtained through the combination of the MNN position algorithm and used calibration procedure.

Due to the use of 5 mm thick monolithic crystals the DOI effect was no longer negligible as it was in the previous scanner design [68]. For radial offsets within a 13 mm radius, the radial resolution remains uniform. For larger offsets, the radial component systematically worsen toward the edge of the FOV despite DOI correction. This can be caused by the combination of thicker crystals with the large maximum acceptance angle caused by the relatively small detector ring diameter (75.77 mm). This makes the DigiPET2 more prone to radial resolution degradation at large radial offsets from the gamma photons entering the detector at large oblique angles. Radial resolution might be improved by using smaller acceptance angles, however, at the cost of reduction in scanner's sensitivity.

The image uniformity measurement was influenced by the lack of attenuation correction in the reconstruction software. The limited count rate and the absence of normalization correction explains the high noise level shown in figure 8.6.

The enlarged FOV of the new DigiPET scanner allows to easily accommodate mice and rats in comparison to our previous prototype. The enlarged FOV also increases the number of available detectors, which improves count rate capabilities of the scanner. However, in the current scanner, the axial FOV length is limited only to 32 mm. This is caused by the fact that the M-TEK electronics, which was used to collect and process data, allows for connecting only up to eight dSiPM detectors. Therefore only one ring of detectors was used in the second version of the DigiPET scanner.

It is important to point out that one of the most significant limitations of our DigiPET2 prototype scanner is the data baud rate. As explained in section 8.2.4, the M-TEK electronics was not designed to provide the data transfer rate for a full, small-animal PET imaging system. Therefore, a proper evaluation of sensitivity, count rate and scatter of the DigiPET2 scanner was not possible.

In order to overcome the limitation of the current design the next step should be to develop dedicated electronics that allows to extend the scanner's axial FOV and ensures high data transfer rates sufficient to meet the requirements of the small-animal PET system. This would allow for a proper evaluation of the system performance in terms of sensitivity and count rate capabilities according to NEMA NU-4 standard.

The DigiPET2 scanner achieves an excellent spatial resolution that allows to clearly resolve 0.8 mm diameter hot rods. DigiPET2 demonstrates that the combination of the monolithic scintillator crystals with multipixel SiPM photosensors and statistical event positioning has great potential for developing compact, high resolution small-animal PET imaging systems. In addition, thanks to easier and cheaper manufacturing of the monolithic crystals these PET system can be developed at lower price than pixelated systems with comparable performance.

8.5 Conclusion

In this study, we have evaluated the performance of the DigiPET2 scanner based on a detector with 5 mm thick monolithic LYSO crystal. The use of thicker crystals allowed to overcome the sensitivity limitation of the first DigiPET prototype. The spatial resolution approached 0.9 mm, which is one of the best presented up to date for full-ring preclinical systems. This resolution is primarily attributable to the combination of monolithic scintillator crystals and used event positioning algorithm. Enlarged FOV allows to accommodate mouse and rat specimens without any space constrains. The *in vivo* mouse imaging experiments demonstrated the feasibility of high resolution imaging of realistic objects. However, the data transmission speed of the readout electronics remains a limitation of the current design, which does not allow to evaluate the count rate capabilities of the DigiPET2 scanner.

8.6 Acknowledgement

This work was supported in part by EU FP7 project SUBLIMA, grant agreement no 241711 (see also `http://www.sublima-pet-mr.eu`). The authors would like to thank the staff of Philips Digital Photon Counting for providing M-TEK electronic readout and their assistance in operating it.

Chapter 9

General conclusions

In this chapter we give a general overview of each chapter and summarize the most important results obtained in this work. We also discuss possible future research directions and end with a final conclusion.

9.1 Summary

In chapter 2 the basic concepts of the Positron Emission Tomography (PET) were introduced and the importance of PET in oncology, cardiology and neurology was outlined. First, the working principles of PET were described starting from the tracer principle through physics of β^+ decay and gamma photon emission to PET scanner architecture, gamma photons detection, coincidence detection and data acquisition. Further, the process of PET image reconstruction from the measured data was explained. Two different categories of image reconstruction algorithms were presented: analytical and iterative. Subsequently, the effects that cause degradation of the image quality were described. Next, the concept of Time of Flight (TOF) PET was introduced and its influence on PET image quality was explained. The following section described how PET imaging evolved into multi-modal imaging techniques such as combined PET/CT and PET/MRI. Finally, the use of PET for small animal imaging in preclinical research was discussed together with the challenges of high resolution and high sensitivity in small animal PET imaging.

In chapter 3 we discussed the PET detector in detail: its architecture, principles of operation and properties. First, the parameters characterizing the performance of PET detector were described and their influence on PET system performance was explained. Afterwards, the two main components of the PET detector, scintillators and photodetectors, were explained in detail. In the first part, the physics of the scintillation mechanism was explained and the properties of scintillator crystals were discussed. In the second part, different types of photodetectors used in PET detectors were presented. First we described the photomultiplier tube (PMT), which is the most mature and frequently used photodetector type for PET detectors. Afterwards, new types of semiconductor photodetectors were introduced as an alternative to the PMT technology. Photodetectors such as avalanche photodiodes (APD), Geiger mode APD and the most promising alternative to PMTs - silicon photomultipliers (SiPM) were described. Finally, the most recent type of the SiPMs, a digital silicon photomultiplier (dSiPM) from Philips Digital Photon Counting (PDPC) was discussed. The architecture and working principles of the dSiPM were explained in details. The use of this novel photodetector for PET detectors is the subject of this dissertation. The last sections of this chapter were focused on PET detectors dedicated for small animal imaging and their requirements to provide good quality PET images. The technical challenges of achieving simultaneously high spatial resolution and high sensitivity in such PET detectors were discussed. Lastly, the concept of PET detectors based on monolithic scintillator crystals was introduced as a promising alternative to the classical PET detector design based on a pixelated scintillator matrix. The potential benefits of such monolithic design and the technical challenges that need to be overcome to fully exploit the potential of the monolithic PET detector were discussed.

In chapter 4, a high-resolution TOF-PET detector with a 2 mm transversal pixel size for whole-body PET imaging was presented. Two different designs of the detector were proposed and investigated. In the first, classical design, the detector consisted of a scintillator matrix of 15 × 15 LYSO crystals, each of size 2 × 2 × 22 mm^3, and a 1 mm thick light guide made of borosilicate glass coupled to a dSiPM. This detector achieved the average energy resolution of 14.5% at 511 keV. Timing resolution of the detector depended on the used dSiPM trigger level. The best CRT of 376 ps was achieved for trigger level 1. A self-organizing map (SOM) algorithm was used to automatically build the crystal look-up table and all LYSO crystals could be clearly resolved. As there is light sharing due to the lack of 1:1 coupling, a single event needed to be recorded by multiple dies of the dSiPM. Therefore, the NL option was enabled to ensure the read out of all dSiPM dies, even those that recorded only a small fraction of optical photons. However, this setting resulted in poor count rate performance: a significant fraction of detected events suffered from a complete or partial loss of scintillation light due to the recharge process of the dSiPM dies. These events with missing scintillation light were discarded to prevent a degradation of the detector performance in terms of energy and timing resolution as well as event positioning. To solve this issue, the second, optimized detector design was developed and evaluated. The second design consisted of an array of 4 × 4 LYSO crystals of $1.9 \times 1.9 \times 22$ mm^3 with a special reflector arrangement between the crystals to ensure different light sharing patterns among them. The size of the LYSO crystals was slightly decreased in order to better fit the 4 × 4 LYSO array into an active area of a single dSiPM die. As the result of the 1:1 coupling between the dSiPM die and the 4 × 4 LYSO array, the second detector design with the special reflector arrangement allowed for a remarkable improvement in terms of count rate performance. Using the SOM algorithm all crystals could be clearly resolved. The second detector design achieved an average CRT of 295 ps and an average energy resolution of 11%. The improvement in terms of the CRT and the energy resolution was caused by reduced light sharing among different dies. We found that the dSiPM is a suitable photosensor to build a high resolution detector for whole body TOF-PET scanners based on crystals with transverse pitch below 4 mm (current standard in whole-body PET systems). However, to achieve the best CRT, which outperforms the state-of-the art TOF-PET scanners, trigger level 1 of the dSiPM needs to be used. In order to work at trigger level 1 and not compromise the detector's count rate performance, the DCR needed to be reduced by cooling the detector and deactivating DPC's microcells with the highest DCR.

In chapter 5 we investigated different configurations of the dSiPM to quantify the event loss in the dSiPM device due to dark counts. This was done to provide guidelines on the optimal configuration for different detector designs and applications. Configuration parameters such as trigger level, validation level, validation time, RTL refresh and NL and their different combinations were investigated. The main focus was on the light sharing scenario when multiple dies of dSiPM are required to record a single event. In the experiments a blue LED (connected to a pulse generator) was used as a source of optical photons. This allowed to control the expected output in terms of the event count rate and the number of detected optical photons per event. The RTL refresh was found as the most effective option to reduce the influence of dark counts on the count rate performance. It also resulted in the maximum sensitivity of the dSiPM detector regardless of the validation level and the number of dies needed to record an event. Moreover, it was shown that a combination of RTL refresh with a low validation level ensures better count rate performance than the NL option. However, the

RTL refresh can be used only for trigger levels above level 1. For trigger level 1, which provides the best timing resolution, the best strategy is to reduce the DCR as much as possible. This can be done by lowering the working temperature of the dSiPM and deactivating a large fraction of the microcells with the highest DCR. Additionally, the light sharing among dies should be avoided or at least limited and high validation levels need to be applied. Furthermore, we performed Monte Carlo simulation of dSiPM dead time based on a non-paralyzable dead time model. Comparing the results of our simulation with experimental data we found that actual total dead time of the dSiPM is larger than expected one, which was calculated based on the recharge time of dSiPM dies. In our case the total dead time was equal to 50 ns instead of expected 20 ns.

In chapter 6 we presented a prototype of a dedicated mouse/rat-brain PET imaging system called DigiPET. The system was based on a combination of a large solid angle (small diameter) and thin monolithic crystals for low parallax and high intrinsic resolution. The DigiPET scanner consisted of four detectors placed in a square arrangement with a field of view (FOV) of $32 \times 32 \times 32$ mm^3. Each detector consisted of a thin monolithic LYSO crystal with a size of $32 \times 32 \times 2$ mm^3 coupled to dSiPM. The system was evaluated in terms of the CRT, sensitivity and spatial resolution and the image quality was evaluated by acquiring a hot-rod phantom and a rat head scans. Thanks to the combination of thin monolithic crystals and the MLE position algorithm the DigiPET system achieved an excellent spatial resolution of 0.7 mm FWHM uniform throughout the entire FOV. These results were substantially better than spatial resolution of currently available commercial small-animal PET systems, which achieve spatial resolutions of $\sim$1.1 mm. The DigiPET system achieved timing resolution of 680 ps, which also outperformed current commercial preclinical PET systems. Such timing resolution allows to use a short coincidence window of $\sim$1–1.5 ns, which will reduce the random coincidence rate. The ex vivo rat brain imaging demonstrated the feasibility of imaging realistic objects with the presented prototype scanner. However, due to low thickness of employed LYSO crystals and limited axial extent the sensitivity of this prototype was limited. This system showed the feasibility of developing low cost, high resolution small animal PET imaging system based on thin monolithic scintillator crystals and multi-pixel dSiPM photosensor.

To overcome the sensitivity limitation of this design, in chapter 7 we introduced an improved detector design based on a 5 mm thick LYSO crystal coupled to the same dSiPM. Thanks to the use of a thicker crystal the nominal sensitivity of the detector for 511 keV singles improved $\sim$ 2.21

times and the coincidence sensitivity over 4 times. To reach sub-millimetre spatial resolution in the new detector with a thicker scintillator crystal, a number of modifications were introduced. The Depth of Interaction (DOI) decoding was introduced in the detector based on the light spread across the dSiPM surface. The calibration procedure was modified to incorporate the DOI capabilities and the Mean Nearest Neighbour (MNN) algorithm for 3D event positioning within the monolithic crystal was used. Thanks to the implemented modifications, the new detector achieved intrinsic spatial resolution of 0.6 mm FWHM comparing to 0.54 mm FWHM intrinsic spatial resolution achieved in the detector with 2 mm thick LYSO crystal. The DOI resolution achieved with the new detector was $\sim$ 1.1 mm on average. This design has good timing resolution of 529 ps, which allows to use narrow coincidence window to limit the randoms coincidence rate. Thus, the new detector overcame the sensitivity limitations of the previous design while still reaching the sub-millimetre spatial resolution.

Finally, in chapter 8 we presented the second version of the DigiPET system based on the improved detector design that was described in chapter 7. The new DigiPET2 scanner consisted of seven detector modules arranged in a heptagonal ring, which results in a FOV of 35.9 mm in radius and 32 mm in axial length. This enlarged FOV allows to easily accommodate mice and rats specimens. Furthermore, the larger number of detectors improved the count rate capability of the scanner. With the DOI information, the detectors could be positioned close to the imagined object, which led to a very compact system and large solid angle. This resulted in high sensitivity of the DigiPET2 scanner. This system was also equipped with a dedicated cooling system to decrease the DCR of the dSiPMs. This allowed the DigiPET2 scanner to be operated in room temperature without compromising the count rate capability. Performance of the new DigiPET2 scanner were evaluated in terms of spatial resolution and its imaging capabilities were evaluated by acquiring a micro-Derenzo phantom and a bone scan of mouse head.

Despite the use of detectors with thicker monolithic crystals, the DigiPET2 achieved sub-millimetre spatial resolution of $\sim$0.9 mm FWHM and all hot rods with a diameter of 0.8 mm in micro-Derenzo phantom could be clearly resolved in the reconstructed image. Furthermore, the *in-vivo* mouse imaging demonstrated the feasibility of high resolution imaging. The loss in spatial resolution in the new scanner can be explained by the lower intrinsic resolution of detectors with 5 mm thick crystals. Even with DOI information there was still some degradation of radial resolution at the edges of the axial FOV. In general however, the DigiPET2 scanner significantly outperformed current commercial small animal PET systems. The average spatial resolution of currently available commercial systems ranges from 1.2 mm to 2.1 mm FWHM, while for the same FOV radial offset the spatial resolution of the second DigiPET ranges from 0.9 to 1.8 mm. Therefore, the DigiPET2 scanner demonstrated that the combination of the monolithic scintillator crystals with multi-pixel SiPM photosensors and proper event positioning algorithm has a great potential for developing compact, high resolution small-animal PET imaging systems that also achieve high sensitivity.

9.2 Future research possibilities

Based on results presented in this dissertation, a number of possible topics can be investigated in future research.

One of the most interesting topics, would be to investigate the possibility of replacing the calibration measurements with simulations. The event positioning method in our monolithic detectors uses the measured detector response of the 511 keV pencil beam at a known interaction position to position an unknown event. In order to obtain a calibration grid with a sufficient number of calibration points and a sufficient number of recorded events per point, we have to perform the calibration measurements for almost 72 hours for a single detector. Thus, it would be desirable to replace this time-consuming calibration measurements with simulations. The development of a proper simulation tool to accurately predict detector response would be of great interest. With real measurements, a true response of each detector can be achieved, which includes the detector's individual performance characteristic. These individual performance characteristic are hard to simulate, thus it is expected that the intrinsic spatial resolution of a detector that uses simulated calibration data would be worse than in case of measured data. However, if only a slightly worse spatial resolution can be achieved using the simulated calibration data, it would be beneficial to use simulations instead of calibration measurements.

A well validated simulation tool could be also used to optimize scintillator-reflector arrangement. Different combinations of reflector materials and crystal surface treatment could provide a more optimal distribution of the scintillation light within monolithic crystal (for example in the regions along the crystal edges and in corners). This could allow to achieve better event positioning in these regions, improving spatial resolution of the detector.

Another interesting research topic would be to investigate if spatial resolution of monolithic detectors could be improved by using photosensors with smaller pixels. Smaller pixels of SiPM and individual read out of a number of fired microcells from such pixels would improve spatial sampling of the scintillation light distribution. As a consequence, smaller changes in the light distribution patterns could be detected. This could be used to better distinguish light distributions produced by gamma photons that interacted in different positions and lead to the improvement of intrinsic spatial resolution of detectors based on monolithic crystals.

For the DigiPET2 scanner presented in chapter 8 it would be desired to add a second and/or third ring of detectors to extend the scanner's axial FOV and to develop a dedicated, fast read-out electronics with sufficient data baud rate that could readout all detectors. This would allow to resolve the issue of the data transmission bottleneck from the scanner to the PC. This is a limitation in the current prototype, which uses only Module Technology Evaluation Kit (M-TEK) electronics. The M-TEK was not designed to provide data transmission rate suitable for a full imaging system. Resolving this limitation would enable to properly evaluate the count rate performance of the DigiPET2 scanner.

For DigiPET2 the radial resolution of the scanner systematically deteriorated for large radial offsets close to the edge of scanner's FOV. Therefore, in order to prevent this resolution degradation and ensure a uniform spatial resolution in the entire FOV regardless of the radial offset, different DOI estimation methods suitable for monolithic crystals should be investigated. The method used in this dissertation uses a calculated variance of light intensity recorded by detector's pixels as a figure of merit to estimate DOI. However, some other methods for DOI estimation may provide better results.

9.3 Final conclusion

In this dissertation we have developed several PET detectors based on the dSiPM for both clinical and pre-clinical application.

As it was demonstrated on the detectors presented in this dissertation, the dSiPM can be successfully used to build novel high-resolution PET detectors.

Thanks to the employed architecture, early digitalization and on-tile time to digital converters (TDC) the dSiPM achieve very good timing performance. When using low trigger level, dSiPM based detectors can easily achieve timing resolution in the range of 300-400 ps, while current PET detectors achieve timing resolution in the range of 500-600 ps. This makes the dSiPM a good choice for developing TOF PET detectors that can greatly improve quality of PET images. However, the limitation in terms of the count rate at low trigger levels remains a serious issue for dSiPM and needs to be carefully considered when designing PET detectors.

We have shown that dSiPM in combination with both pixelated and monolithic scintillator LYSO crystals can be used to built high resolution PET detectors for both clinical and pre-clinical applications.

In particular, we have demonstrated that multi-pixel dSiPM is a very promising photosensor in combination with monolithic scintillator crystals and statistical event positioning algorithms to develop dedicated small animal PET detectors of sub-millimetre spatial resolution.

Moreover, during the course of the research presented in this dissertation we have build two compact, high resolution preclinical PET scanners. Both scanners were based on the PET detectors consisting of dSiPM coupled with monolithic LYSO crystals. Both achieved an excellent sub-millimetre spatial resolution, one of the highest demonstrated up to date. In addition, thanks to the use of monolithic scintillators the cost per detector in our system was lower than alternative detector based on pixelated scintillator matrix with similar spatial resolution.

In this place, however, it would be worthy to mention that further development of the digital SiPM technology should lead to better performance. Smaller pixels, independent readout of number of detected photons from the smaller sensor's areas, lower DCR rate of microcells and different acquisition sequence, that would achieve better count rate, would be highly desirable in author's opinion. Thus, it would be beneficial if other photosensor manufacturers, not only Philips Digital Photon Counting, would develop their own digital versions of SiPMs.

Bibliography

[1] Hamamatsu photonics k.k. http://sales.hamamatsu.com.

[2] Sensl. http://www.sensl.com/.

[3] Hamamatsu technical data sheet r3292-02, 1998.

[4] Hamamatsu technical data sheet r2486-01, 2001.

[5] Nora Adonai, Khoi N Nguyen, Joseph Walsh, M Iyer, Tatsushi Toyokuni, Michael E Phelps, Timothy McCarthy, Deborah W McCarthy, and Sanjiv Sam Gambhir. Ex vivo cell labeling with 64cu–pyruvaldehyde-bis (n4-methylthiosemicarbazone) for imaging cell trafficking in mice with positron-emission tomography. *Proceedings of the National Academy of Sciences*, 99(5):3030–3035, 2002.

[6] Alex M Aisen, William Martel, Ethan M Braunstein, Kim I McMillin, William A Phillips, and TF Kling. Mri and ct evaluation of primary bone and soft-tissue tumors. *American journal of Roentgenology*, 146(4):749–756, 1986.

[7] Hal O Anger. Scintillation camera. *Review of scientific instruments*, 29(1):27–33, 1958.

[8] HO Anger. Survey of radioisotope cameras. Technical report, Univ. of California, Berkeley, 1966.

[9] National Electrical Manufacturers Association. Nema standards publication nu 2-2001: Performance measurements of positron emission tomographs, 2001.

[10] RD Badawi, PK Marsden, BF Cronin, JL Sutcliffe, and MN Maisey. Optimization of noise-equivalent count rates in 3d pet. *Physics in medicine and biology*, 41(9):1755, 1996.

[11] Chuanyong Bai, Ling Shao, Angela J Da Silva, and Zuo Zhao. A generalized model for the conversion from ct numbers to linear attenuation coefficients. *Nuclear Science, IEEE Transactions on*, 50(5):1510–1515, 2003.

[12] DL Bailey, T Jones, TJ Spinks, M-C Gilardi, and DW Townsend. Noise equivalent count measurements in a neuro-pet scanner with retractable septa. *Medical Imaging, IEEE Transactions on*, 10(3):256–260, 1991.

[13] Marcin Balcerzyk, George Kontaxakis, Mercedes Delgado, Luis Garcia-Garcia, Carlos Correcher, Antonio J Gonzalez, Aurora Gonzalez, Jose L Rubio, Jose M Benlloch, and Miguel A Pozo. Initial performance evaluation of a high resolution albira small animal positron emission tomography scanner with monolithic crystals and depth-of-interaction encoding from a user's perspective. *Measurement Science and Technology*, 20(10):104011, 2009.

[14] Qinan Bao, Danny Newport, Mu Chen, David B Stout, and Arion F Chatziioannou. Performance evaluation of the inveon dedicated pet preclinical tomograph based on the nema nu-4 standards. *Journal of Nuclear Medicine*, 50(3):401–408, 2009.

[15] Rachel Bar-Shalom, Nikolai Yefremov, Ludmila Guralnik, Diana Gaitini, Alex Frenkel, Abraham Kuten, Hernan Altman, Zohar Keidar, and Ora Israel. Clinical performance of pet/ct in evaluation of cancer: additional value for diagnostic imaging and patient management. *Journal of nuclear medicine*, 44(8):1200–1209, 2003.

[16] Harrison H Barrett and William Swindell. *Radiological imaging: the theory of image formation, detection, and processing*, volume 2. Academic Press, 1996.

[17] Jean-Mathieu Beauregard, Étienne Croteau, Naseem Ahmed, Johan E van Lier, and François Bénard. Assessment of human biodistribution and dosimetry of 4-fluoro-11β-methoxy-16α-18f-fluoroestradiol using serial whole-body pet/ct. *Journal of Nuclear Medicine*, 50(1):100–107, 2009.

[18] JM Benlloch, Vicente Carrilero, AJ González, J Catret, Ch W Lerche, Dori Abellán, F Garcia De Quiros, M Giménez, J Modia, F Sánchez, et al. Scanner calibration of a small animal pet camera based on continuous lso crystals and flat panel pspmts. *Nuclear Instruments and*

Methods in Physics Research Section A: Accelerators, Spectrometers, Detectors and Associated Equipment, 571(1):26–29, 2007.

[19] Mélanie Bergeron, Jules Cadorette, Jean-François Beaudoin, Martin D Lepage, Ghislain Robert, Vitali Selivanov, Marc-André Tétrault, Nicolas Viscogliosi, Jeffrey P Norenberg, Réjean Fontaine, et al. Performance evaluation of the labpet apd-based digital pet scanner. *Nuclear Science, IEEE Transactions on*, 56(1):10–16, 2009.

[20] Thomas Beyer, David W Townsend, Tony Brun, Paul E Kinahan, Martin Charron, Raymond Roddy, Jeff Jerin, John Young, Larry Byars, and Ronald Nutt. A combined pet/ct scanner for clinical oncology. *J Nucl Med*, 41:1369–1379, 2000.

[21] Chantal P Bleeker-Rovers, Ruud GL de Sévaux, Henk W van Hamersvelt, Frans HM Corstens, and Wim JG Oyen. Diagnosis of renal and hepatic cyst infections by 18-f-fluorodeoxyglucose positron emission tomography in autosomal dominant polycystic kidney disease. *American Journal of Kidney Diseases*, 41(6):e22–1, 2003.

[22] David J Brenner. Estimating cancer risks from pediatric ct: going from the qualitative to the quantitative. *Pediatric radiology*, 32(4):228–231, 2002.

[23] David J Brenner, Carl D Elliston, Eric J Hall, and Walter E Berdon. Estimated risks of radiation-induced fatal cancer from pediatric ct. *American journal of roentgenology*, 176(2):289–296, 2001.

[24] E Broussolle, C Dentresangle, P Landais, L Garcia-Larrea, P Pollak, B Croisile, O Hibert, F Bonnefoi, G Galy, JC Froment, et al. The relation of putamen and caudate nucleus 18 f-dopa uptake to motor and cognitive performances in parkinson's disease. *Journal of the neurological sciences*, 166(2):141–151, 1999.

[25] GL Brownell, CA Burnham, S Wilensky, S Aronow, H Kazemi, and D Strieder. New developments in positron scintigraphy and the application of cyclotron-produced positron emitters. In *Medical Radioisotope Scintigraphy. VI Proceedings of a Symposium on Medical Radioisotope Scintigraphy*, 1969.

[26] P Bruyndonckx, Christian Lemaitre, Sophie Leonard, Dennis R Schaart, DJ Van der Laan, Marnix C Maas, Olivier Devroede, Yibao Wu, Magalie Krieguer, and Stefaan Tavernier. Initial characterization

of a nonpixelated scintillator detector in a pet prototype demonstrator. *Nuclear Science, IEEE Transactions on*, 53(5):2543–2548, 2006.

[27] P Bruyndonckx, Liu Xuan, S Rajeswaran, W Smolik, S Tavernier, and Zhang Shuping. Design and physical characteristics of a small animal pet using baf 2 crystals and a photosensitive wire chamber. *Nuclear Instruments and Methods in Physics Research Section A: Accelerators, Spectrometers, Detectors and Associated Equipment*, 382(3):589–600, 1996.

[28] Peter Bruyndonckx, Sophie Léonard, Stefaan Tavernier, Cedric Lemaître, Olivier Devroede, Yibao Wu, and Magalie Krieguer. Neural network-based position estimators for pet detectors using monolithic lso blocks. *Nuclear Science, IEEE Transactions on*, 51(5):2520–2525, 2004.

[29] Peter Bruyndonckx, Xuan Liu, Stefaan Tavernier, and Shuping Zhang. Performance study of a 3d small animal pet scanner based on baf 2 crystals and a photo sensitive wire chamber. *Nuclear Instruments and Methods in Physics Research Section A: Accelerators, Spectrometers, Detectors and Associated Equipment*, 392(1):407–413, 1997.

[30] Thomas F Budinger. Instrumentation trends in nuclear medicine. In *Seminars in nuclear medicine*, volume 7, pages 285–297. Elsevier, 1977.

[31] P Buzhan, B Dolgoshein, L Filatov, A Ilyin, V Kaplin, A Karakash, S Klemin, R Mirzoyan, AN Otte, E Popova, et al. Large area silicon photomultipliers: Performance and applications. *Nuclear Instruments and Methods in Physics Research Section A: Accelerators, Spectrometers, Detectors and Associated Equipment*, 567(1):78–82, 2006.

[32] J Cabello, P Barrillon, J Barrio, MG Bisogni, A Del Guerra, C Lacasta, M Rafecas, H Saikouk, C Solaz, P Solevi, et al. High resolution detectors based on continuous crystals and sipms for small animal pet. *Nuclear Instruments and Methods in Physics Research Section A: Accelerators, Spectrometers, Detectors and Associated Equipment*, 718:148–150, 2013.

[33] Mario Cañadas, Miguel Embid, Eduardo Lage, Manuel Desco, Juan José Vaquero, and José Manuel Pérez. Nema nu 4-2008 performance measurements of two commercial small-animal pet scanners:

Clearpet and rpet-1. *Nuclear Science, IEEE Transactions on*, 58(1):58–65, 2011.

[34] M Carles, Ch W Lerche, F Sánchez, A Orero, L Moliner, A Soriano, and JM Benlloch. Performance of a doi-encoding small animal pet system with monolithic scintillators. *Nuclear Instruments and Methods in Physics Research Section A: Accelerators, Spectrometers, Detectors and Associated Equipment*, 695:317–321, 2012.

[35] Ciprian Catana, Thomas Benner, Andre van der Kouwe, Larry Byars, Michael Hamm, Daniel B Chonde, Christian J Michel, Georges El Fakhri, Matthias Schmand, and A Gregory Sorensen. Mri-assisted pet motion correction for neurologic studies in an integrated mr-pet scanner. *Journal of Nuclear Medicine*, 52(1):154–161, 2011.

[36] Ciprian Catana, Alexander R Guimaraes, and Bruce R Rosen. Pet and mr imaging: the odd couple or a match made in heaven? *Journal of Nuclear Medicine*, 54(5):815–824, 2013.

[37] Arion F Chatziioannou, Simon R Cherry, Yiping Shao, Robert W Silverman, Ken Meadors, Thomas H Farquhar, Marjan Pedarsani, and Michael E Phelps. Performance evaluation of micropet: a high-resolution lutetium oxyorthosilicate pet scanner for animal imaging. *Journal of Nuclear Medicine*, 40(7):1164, 1999.

[38] V Chepel, MI Lopes, A Kuchenkov, R Ferreira Marques, and AJPL Policarpo. Performance study of liquid xenon detector for pet. *Nuclear Instruments and Methods in Physics Research Section A: Accelerators, Spectrometers, Detectors and Associated Equipment*, 392(1):427–432, 1997.

[39] Simon R Cherry. In vivo molecular and genomic imaging: new challenges for imaging physics. *Physics in medicine and biology*, 49(3):R13, 2004.

[40] Simon R Cherry. The 2006 henry n. wagner lecture: of mice and men (and positrons)—advances in pet imaging technology. *Journal of Nuclear Medicine*, 47(11):1735–1745, 2006.

[41] Simon R Cherry. Multimodality in vivo imaging systems: twice the power or double the trouble? *Annu. Rev. Biomed. Eng.*, 8:35–62, 2006.

[42] Simon R Cherry, Magnus Dahlbom, and Edward J Hoffman. 3d pet using a conventional multislice tomograph without septa. *Journal of computer assisted tomography*, 15(4):655–668, 1991.

[43] Simon R Cherry, Yiping Shao, Martin P Tornai, Stefan Siegel, Anthony R Ricci, and Michael E Phelps. Collection of scintillation light from small bgo crystals. *Nuclear Science, IEEE Transactions on*, 42(4):1058–1063, 1995.

[44] SR Cherry, Y Shao, RW Silverman, K Meadors, S Siegel, A Chatziioannou, JW Young, WF Jones, JC Moyers, D Newport, et al. Micropet: a high resolution pet scanner for imaging small animals. *Nuclear Science, IEEE Transactions on*, 44(3):1161–1166, 1997.

[45] Woon-Seng Choong. The timing resolution of scintillation-detector systems: Monte carlo analysis. *Physics in medicine and biology*, 54(21):6495, 2009.

[46] Se Young Chun, Timothy G Reese, Jinsong Ouyang, Bastien Guerin, Ciprian Catana, Xuping Zhu, Nathaniel M Alpert, and Georges El Fakhri. Mri-based nonrigid motion correction in simultaneous pet/mri. *Journal of Nuclear Medicine*, 53(8):1284–1291, 2012.

[47] Neal H Clinthorne, W Leslie Rogers, Lingxiong Shao, and Kenneth F Koral. A hybrid maximum likelihood position computer for scintillation cameras. Technical report, Univ. of Michigan, Div. of Nuclear Medicine, 3480 Kresge III, Box 552, Ann Arbor, MI 48109-552, 1987.

[48] Maurizio Conti, Bernard Bendriem, Mike Casey, Mu Chen, Frank Kehren, Christian Michel, and Vladimir Panin. First experimental results of time-of-flight reconstruction on an lso pet scanner. *Physics in medicine and biology*, 50(19):4507, 2005.

[49] John A Correia, Charles A Burnham, David Kaufman, Anna-Liisa Brownell, and Alan J Fischman. Performance evaluation of mmp-ii: a second-generation small animal pet. *Nuclear Science, IEEE Transactions on*, 51(1):21–26, 2004.

[50] Jing-yu Cui, Guillem Pratx, Sven Prevrhal, and Craig S Levin. Fully 3d list-mode time-of-flight pet image reconstruction on gpus using cuda. *Medical physics*, 38(12):6775–6786, 2011.

[51] J Czernin. Clinical applications of fdg-pet in oncology. *Acta Medica Austriaca*, 29(5):162–170, 2002.

[52] Paul De Leyn, Sigrid Stroobants, Walter De Wever, Toni Lerut, Willy Coosemans, Georges Decker, Philippe Nafteux, Dirk Van Raemdonck, Luc Mortelmans, Kristiaan Nackaerts, et al. Prospective comparative study of integrated positron emission tomography-computed tomography scan compared with remediastinoscopy in the assessment of residual mediastinal lymph node disease after induction chemotherapy for mediastinoscopy-proven stage iiia-n2 non–small-cell lung cancer: a leuven lung cancer group study. *Journal of Clinical Oncology*, 24(21):3333–3339, 2006.

[53] Carsten Degenhardt, Pedro Rodrigues, Andreia Trindade, Ben Zwaans, Oliver Mulhens, Ralf Dorscheid, Andreas Thon, Antoine Salomon, and Thomas Frach. Performance evaluation of a prototype positron emission tomography scanner using digital photon counters (dpc). In *Nuclear Science Symposium and Medical Imaging Conference (NSS/MIC), 2012 IEEE*, pages 2820–2824. IEEE, 2012.

[54] Carsten Degenhardt, Ben Zwaans, Thomas Frach, and Rik De Gruyter. Arrays of digital silicon photomultipliers—intrinsic performance and application to scintillator readout. In *Nuclear Science Symposium Conference Record (NSS/MIC), 2010 IEEE*, pages 1954–1956. IEEE, 2010.

[55] Timothy R DeGrado, Timothy G Turkington, J Jay Williams, Charles W Stearns, John M Hoffman, R Edward Coleman, et al. Performance characteristics of a whole-body pet scanner. *Journal of Nuclear Medicine*, 35(8):1398, 1994.

[56] Farrokh Dehdashti, Andrea H McGuire, Henry F Van Brocklin, Barry A Siegel, Dorothy P Andriole, Landis K Griffeth, Martin G Pomper, John A Katzenellenbogen, and Michael J Welch. Assessment of 21-[18f] fluoro-16-ethyl-19-norprogesterone as a positron-emitting radiopharmaceutical for the detection of progestin receptors in human breast carcinomas. *J Nucl Med*, 32(8):1532–1537, 1991.

[57] Alberto Del Guerra, Antonietta Bartoli, Nicola Belcari, Deborah Herbert, Alfonso Motta, Angela Vaiano, Giovanni Di Domenico, Nicola Sabba, Elena Moretti, Guido Zavattini, et al. Performance evaluation of the fully engineered yap-(s) pet scanner for small animal imaging. *Nuclear Science, IEEE Transactions on*, 53(3):1078–1083, 2006.

[58] Gaspar Delso, Sebastian Fürst, Björn Jakoby, Ralf Ladebeck, Carl Ganter, Stephan G Nekolla, Markus Schwaiger, and Sibylle I Ziegler.

Performance measurements of the siemens mmr integrated whole-body pet/mr scanner. *Journal of nuclear medicine*, 52(12):1914–1922, 2011.

[59] Arthur P Dempster, Nan M Laird, and Donald B Rubin. Maximum likelihood from incomplete data via the em algorithm. *Journal of the royal statistical society. Series B (methodological)*, pages 1–38, 1977.

[60] Karel Deprez, Roel Van Holen, and Stefaan Vandenberghe. A high resolution spect detector based on thin continuous lyso. *Physics in medicine and biology*, 59(1):153, 2013.

[61] Karel Deprez, Stefaan Vandenberghe, Bert Vandeghinste, and Roel Van Holen. Flexispect: a spect system consisting of a compact high-resolution scintillation detector (spectatress) and a lofthole collimator. *Nuclear Science, IEEE Transactions on*, 60(1):53–64, 2013.

[62] B Dolgoshein, V Balagura, P Buzhan, M Danilov, L Filatov, E Garutti, M Groll, A Ilyin, V Kantserov, V Kaplin, et al. Status report on silicon photomultiplier development and its applications. *Nuclear Instruments and Methods in Physics Research Section A: Accelerators, Spectrometers, Detectors and Associated Equipment*, 563(2):368–376, 2006.

[63] Arnaud Drezet, Olivier Monnet, Françoise Mathy, Guillaume Montemont, and Loïck Verger. Cdznte detectors for small field of view positron emission tomographic imaging. *Nuclear Instruments and Methods in Physics Research Section A: Accelerators, Spectrometers, Detectors and Associated Equipment*, 571(1):465–470, 2007.

[64] Thomas Eckert, Anna Barnes, Vijay Dhawan, Steve Frucht, Mark F Gordon, Andrew S Feigin, and D Eidelberg. Fdg pet in the differential diagnosis of parkinsonian disorders. *Neuroimage*, 26(3):912–921, 2005.

[65] Georges El Fakhri, Suleman Surti, Cathryn M Trott, Joshua Scheuermann, and Joel S Karp. Improvement in lesion detection with whole-body oncologic time-of-flight pet. *Journal of Nuclear Medicine*, 52(3):347–353, 2011.

[66] Samuel España, LM Fraile, JL Herraiz, José Manuel Udías, Manuel Desco, and Juan José Vaquero. Performance evaluation of sipm photodetectors for pet imaging in the presence of magnetic fields. *Nuclear Instruments and Methods in Physics Research Section A: Accelerators,*

Spectrometers, Detectors and Associated Equipment, 613(2):308–316, 2010.

[67] Samuel España, JL Herraiz, Esther Vicente, Juan José Vaquero, Manuel Desco, and José Manuel Udías. Penelopet, a monte carlo pet simulation tool based on penelope: features and validation. *Physics in medicine and biology*, 54(6):1723, 2009.

[68] Samuel España, Radoslaw Marcinkowski, Vincent Keereman, Stefaan Vandenberghe, and Roel Van Holen. Digipet: sub-millimeter spatial resolution small-animal pet imaging using thin monolithic scintillators. *Physics in medicine and biology*, 59(13):3405, 2014.

[69] Alessandro Ferri, Alberto Gola, Nicola Serra, Alessandro Tarolli, Nicola Zorzi, and Claudio Piemonte. Performance of fbk high-density sipm technology coupled to ce: Lyso and ce: Gagg for tof-pet. *Physics in medicine and biology*, 59(4):869, 2014.

[70] Jeffrey A Fessler, Neal H Clinthorne, and W Leslie Rogers. Regularized emission image reconstruction using imperfect side information. *Nuclear Science, IEEE Transactions on*, 39(5):1464–1471, 1992.

[71] Paolo Finocchiaro, Alfio Pappalardo, Luigi Cosentino, Massimiliano Belluso, Sergio Billotta, Giovanni Bonanno, Beatrice Carbone, Giovanni Condorelli, Salvatore Di Mauro, Giorgio Fallica, et al. Characterization of a novel 100-channel silicon photomultiplier—part ii: charge and time. *Electron Devices, IEEE Transactions on*, 55(10):2765–2773, 2008.

[72] Réjean Fontaine, François Bélanger, Nicolas Viscogliosi, Hicham Semmaoui, Marc-André Tétrault, Jean-Baptiste Michaud, Catherine Pepin, Jules Cadorette, and Roger Lecomte. The hardware and signal processing architecture of labpet™, a small animal apd-based digital pet scanner. *Nuclear Science, IEEE Transactions on*, 56(1):3–9, 2009.

[73] James G Fox, Stephen Barthold, Muriel Davisson, Christian E Newcomer, Fred W Quimby, and Abigail Smith. *The Mouse in biomedical research: diseases*, volume 2. Academic Press, 2006.

[74] Thomas Frach, Gordian Prescher, Carsten Degenhardt, Rik De Gruyter, Anja Schmitz, and Rob Ballizany. The digital silicon photomultiplier—principle of operation and intrinsic detector performance. In *Nuclear Science Symposium Conference Record (NSS/MIC), 2009 IEEE*, pages 1959–1965. IEEE, 2009.

[75] Sanjiv Sam Gambhir. Molecular imaging of cancer with positron emission tomography. *Nature Reviews Cancer*, 2(9):683–693, 2002.

[76] R Gariod, R Allemand, E Cormoreche, M Laval, and M Moszynski. The leti positron tomograph architecture and time of flight improvements. In *Proceedings of The Workshop on Time of Flight Tomography*, pages 25–29, 1982.

[77] Andrew L Goertzen, Qinan Bao, Mélanie Bergeron, Eric Blankemeyer, Stephan Blinder, Mario Cañadas, Arion F Chatziioannou, Katherine Dinelle, Esmat Elhami, Hans-Sonke Jans, et al. Nema nu 4-2008 comparison of preclinical pet imaging systems. *Journal of Nuclear Medicine*, 53(8):1300–1309, 2012.

[78] Robert M Gray and Albert Macovski. Maximum a posteriori estimation of position in scintillation cameras. *Nuclear Science, IEEE Transactions on*, 23(1):849–852, 1976.

[79] Ronald Grazioso, Nan Zhang, James Corbeil, Matthias Schmand, Ralf Ladebeck, Markus Vester, Günter Schnur, Wolfgang Renz, and Hubertus Fischer. Apd-based pet detector for simultaneous pet/mr imaging. *Nuclear Instruments and Methods in Physics Research Section A: Accelerators, Spectrometers, Detectors and Associated Equipment*, 569(2):301–305, 2006.

[80] John R Grierson and Anthony F Shields. Radiosynthesis of 3'-deoxy-3'-[18 f] fluorothymidine:[18 f] flt for imaging of cellular proliferation in vivo. *Nuclear medicine and biology*, 27(2):143–156, 2000.

[81] Z Gu, R Taschereau, NT Vu, H Wang, DL Prout, RW Silverman, B Bai, DB Stout, ME Phelps, and AF Chatziioannou. Nema nu-4 performance evaluation of petbox4, a high sensitivity dedicated pet preclinical tomograph. *Physics in medicine and biology*, 58(11):3791, 2013.

[82] A Del Guerra, F De Notaristefani, G Di Domenico, M Giganti, R Pani, A Piffanelli, A Turra, and G Zavattini. Use of a yap: Ce matrix coupled to a position-sensitive photomultiplier for high resolution positron emission tomography. *Nuclear Science, IEEE Transactions on*, 43(3):1958–1962, 1996.

[83] Roland Haubner, Wolfgang A Weber, Ambros J Beer, Eugenija Vabuliene, Daniel Reim, Mario Sarbia, Karl-Friedrich Becker, Michael

Goebel, Rüdiger Hein, Hans-Jürgen Wester, et al. Noninvasive visualization of the activated αvβ3 integrin in cancer patients by positron emission tomography and [18 f] galacto-rgd. *PLoS Med*, 2(3):e70, 2005.

[84] MR Hayden, WRW Martin, AJ Stoessl, C Clark, S Hollenberg, MJ Adam, W Ammann, R Harrop, J Rogers, T Ruth, et al. Positron emission tomography in the early diagnosis of huntington's disease. *Neurology*, 36(7):888–888, 1986.

[85] Ken Herrmann, Magnus Dahlbom, David Nathanson, Liu Wei, Caius Radu, Arion Chatziioannou, and Johannes Czernin. Evaluation of the genisys4, a bench-top preclinical pet scanner. *Journal of Nuclear Medicine*, 54(7):1162–1167, 2013.

[86] Carl K Hoh, Randall A Hawkins, Magnus Dahlbom, John A Glaspy, Leanne L Seeger, Yong Choi, Christiaan W Schiepers, Sung-cheng Huang, Nagichettiar Satyamurthy, Jorge R Barrio, et al. Whole body skeletal imaging with [18f] fluoride ion and pet. *Journal of computer assisted tomography*, 17(1):34–41, 1993.

[87] Dongming Hu, Blake E Atkins, Mark W Lenox, Bryan Castleberry, and Stefan B Siegel. A neural network based algorithm for building crystal look-up table of pet block detector. In *Nuclear Science Symposium Conference Record, 2006. IEEE*, volume 4, pages 2458–2461. IEEE, 2006.

[88] H Malcolm Hudson and Richard S Larkin. Accelerated image reconstruction using ordered subsets of projection data. *Medical Imaging, IEEE Transactions on*, 13(4):601–609, 1994.

[89] William CJ Hunter, Harrison H Barrett, and Lars R Furenlid. Calibration method for ml estimation of 3d interaction position in a thick gamma-ray detector. *Nuclear Science, IEEE Transactions on*, 56(1):189–196, 2009.

[90] T Ido, C-N Wan, V Casella, JS Fowler, AP Wolf, M Reivich, and DE Kuhl. Labeled 2-deoxy-d-glucose analogs. 18f-labeled 2-deoxy-2-fluoro-d-glucose, 2-deoxy-2-fluoro-d-mannose and 14c-2-deoxy-2-fluoro-d-glucose. *Journal of Labelled Compounds and Radiopharmaceuticals*, 14(2):175–183, 1978.

[91] Masayuki Inubushi, Joseph C Wu, Sanjiv S Gambhir, Gobalakrishnan Sundaresan, Nagichettiar Satyamurthy, Mohammad Namavari,

Simon Yee, Jorge R Barrio, David Stout, Arion F Chatziioannou, et al. Positron-emission tomography reporter gene expression imaging in rat myocardium. *Circulation*, 107(2):326–332, 2003.

[92] J Carl Jackson, Don Phelan, Alan P Morrison, R Michael Redfern, and Alan Mathewson. Toward integrated single-photon-counting microarrays. *Optical Engineering*, 42(1):112–118, 2003.

[93] BW Jakoby, Y Bercier, M Conti, M Casey, T Gremillion, C Hayden, B Bendriem, and DW Townsend. Performance investigation of a time-of-flight pet/ct scanner. In *Nuclear Science Symposium Conference Record, 2008. NSS'08. IEEE*, pages 3738–3743. IEEE, 2008.

[94] AP Jeavons, RA Chandler, and CAR Dettmar. A 3d hidac-pet camera with sub-millimetre resolution for imaging small animals. *Nuclear Science, IEEE Transactions on*, 46(3):468–473, 1999.

[95] Jinhun Joung, Robert S Miyaoka, and Thomas K Lewellen. cmice: a high resolution animal pet using continuous lso with a statistics based positioning scheme. *Nuclear Instruments and Methods in Physics Research Section A: Accelerators, Spectrometers, Detectors and Associated Equipment*, 489(1):584–598, 2002.

[96] Martin S Judenhofer, Ciprian Catana, Brian K Swann, Stefan B Siegel, Wulf-Ingo Jung, Robert E Nutt, Simon R Cherry, Claus D Claussen, and Bernd J Pichler. Pet/mr images acquired with a compact mr-compatible pet detector in a 7-t magnet 1. *Radiology*, 244(3):807–814, 2007.

[97] Joel S Karp, Suleman Surti, Margaret E Daube-Witherspoon, and Gerd Muehllehner. Benefit of time-of-flight in pet: experimental and clinical results. *Journal of Nuclear Medicine*, 49(3):462–470, 2008.

[98] Vincent Keereman, Yves Fierens, Tom Broux, Yves De Deene, Max Lonneux, and Stefaan Vandenberghe. Mri-based attenuation correction for pet/mri using ultrashort echo time sequences. *Journal of nuclear medicine*, 51(5):812–818, 2010.

[99] FYJ Keng. Clinical applications of positron emission tomography in cardiology: a review. *Annals-Academy of Medicine Singapore*, 33(2):175–182, 2004.

[100] Chang Lyong Kim, Gin-Chung Wang, and Sergei Dolinsky. Multi-pixel photon counters for tof pet detector and its challenges. *Nuclear Science, IEEE Transactions on*, 56(5):2580–2585, 2009.

[101] PE Kinahan, M Defrise, and R Clackdoyle. Emission tomography: the fundamentals of pet and spect, chapitre analytic image reconstruction methods, 2004.

[102] PE Kinahan, DW Townsend, T Beyer, and D Sashin. Attenuation correction for a combined 3d pet/ct scanner. *Medical physics*, 25(10):2046–2053, 1998.

[103] Sean L Kitson, Vincenzo Cuccurullo, Andrea Ciarmiello, Diana Salvo, and Luigi Mansi. Clinical applications of positron emission tomography (pet) imaging in medicine: oncology, brain diseases and cardiology. *Current Radiopharmaceuticals*, 2(4):224–253, 2009.

[104] Andrea L Lacaita, Franco Zappa, Stefano Bigliardi, and Manfredo Manfredi. On the bremsstrahlung origin of hot-carrier-induced photons in silicon devices. *Electron Devices, IEEE Transactions on*, 40(3):577–582, 1993.

[105] Eduardo Lage, Juan José Vaquero, Alejandro Sisniega, Samuel España, Gustavo Tapias, Mónica Abella, A Rodriguez-Ruano, Juan E Ortuño, A Udias, and Manuel Desco. Design and performance evaluation of a coplanar multimodality scanner for rodent imaging. *Physics in medicine and biology*, 54(18):5427, 2009.

[106] Kenneth Lange. Convergence of em image reconstruction algorithms with gibbs smoothing. *Medical Imaging, IEEE Transactions on*, 9(4):439–446, 1990.

[107] Michele Larobina, Arturo Brunetti, and Marco Salvatore. Small animal pet: a review of commercially available imaging systems. *Current medical imaging reviews*, 2(2):187–192, 2006.

[108] Carole Lartizien, Claude Comtat, Paul E Kinahan, Nuno Ferreira, Bernard Bendriem, and Régine Trébossen. Optimization of injected dose based on noise equivalent count rates for 2-and 3-dimensional whole-body pet. *Journal of Nuclear Medicine*, 43(9):1268–1278, 2002.

[109] R Lecomte, J Cadorette, S Rodrigue, D Lapointe, D Rouleau, M Bentourkia, R Yao, and P Msaki. Initial results from the sherbrooke

avalanche photodiode positron tomograph. *Nuclear Science, IEEE Transactions on*, 43(3):1952–1957, 1996.

[110] P Lecoq, E Auffray, S Brunner, H Hillemanns, P Jarron, A Knapitsch, T Meyer, and F Powolny. Factors influencing time resolution of scintillators and ways to improve them. *Nuclear Science, IEEE Transactions on*, 57(5):2411–2416, 2010.

[111] Chaehun Lee, Young Soo Kim, Woo Suk Sul, Hyoungtaek Kim, Seung Han Shin, and Gyuseong Cho. Feasibility study on tof-pet with fill factor improved sipms. *Nuclear Instruments and Methods in Physics Research Section A: Accelerators, Spectrometers, Detectors and Associated Equipment*, 633:S163–S165, 2011.

[112] Christoph Werner Lerche, JM Benlloch, F Sanchez, N Pavon, B Escat, EN Gimenez, M Fernandez, I Torres, M Gimenez, A Sebastia, et al. Depth of γ-ray interaction within continuous crystals from the width of its scintillation light-distribution. *Nuclear Science, IEEE Transactions on*, 52(3):560–572, 2005.

[113] Craig Levin, Gary Glover, Timothy Deller, David McDaniel, William Peterson, and Sri Harsha Maramraju. Prototype time-of-flight pet ring integrated with a 3t mri system for simultaneous whole-body pet/mr imaging. *Journal of Nuclear Medicine*, 54(supplement 2):148–148, 2013.

[114] Craig S Levin. Design of a high-resolution and high-sensitivity scintillation crystal array for pet with nearly complete light collection. *Nuclear Science, IEEE Transactions on*, 49(5):2236–2243, 2002.

[115] Craig S Levin and Habib Zaidi. Current trends in preclinical pet system design. *PET Clinics*, 2(2):125–160, 2007.

[116] Emanuel Levitan and Gabor T Herman. A maximum a posteriori probability expectation maximization algorithm for image reconstruction in emission tomography. *Medical Imaging, IEEE Transactions on*, 6(3):185–192, 1987.

[117] TK Lewellen, AN Bice, RL Harrison, MD Pencke, and JM Link. Performance measurements of the sp3000/uw time-of-flight positron emission tomograph. *IEEE Trans. Nucl. Sci.;(United States)*, 35(CONF-871006-), 1988.

[118] Robert M Lewitt. Multidimensional digital image representations using generalized kaiser–bessel window functions. *JOSA A*, 7(10):1834–1846, 1990.

[119] Xiaoli Li, William CJ Hunter, Tom K Lewellen, and Robert S Miyaoka. Use of cramer–rao lower bound for performance evaluation of different monolithic crystal pet detector designs. *Nuclear Science, IEEE Transactions on*, 59(1):3–12, 2012.

[120] Zhi Li, M Wedrowski, P Bruyndonckx, and G Vandersteen. Nonlinear least-squares modeling of 3d interaction position in a monolithic scintillator block. *Physics in medicine and biology*, 55(21):6515, 2010.

[121] Ruth Lim, Frederic H Fahey, Laura A Drubach, Leonard P Connolly, and S Ted Treves. Early experience with fluorine-18 sodium fluoride bone pet in young patients with back pain. *Journal of Pediatric Orthopaedics*, 27(3):277–282, 2007.

[122] T Ling, TH Burnett, TK Lewellen, and RS Miyaoka. Parametric positioning of a continuous crystal pet detector with depth of interaction decoding. *Physics in medicine and biology*, 53(7):1843, 2008.

[123] G Llosá, P Barrillon, J Barrio, MG Bisogni, J Cabello, A Del Guerra, A Etxebeste, JE Gillam, C Lacasta, JF Oliver, et al. High performance detector head for pet and pet/mr with continuous crystals and sipms. *Nuclear Instruments and Methods in Physics Research Section A: Accelerators, Spectrometers, Detectors and Associated Equipment*, 702:3–5, 2013.

[124] Cristina Lois, Bjoern W Jakoby, Misty J Long, Karl F Hubner, David W Barker, Michael E Casey, Maurizio Conti, Vladimir Y Panin, Dan J Kadrmas, and David W Townsend. An assessment of the impact of incorporating time-of-flight information into clinical pet/ct imaging. *Journal of Nuclear Medicine*, 51(2):237–245, 2010.

[125] Gary D Luker, Vijay Sharma, Christina M Pica, Julie L Dahlheimer, Wei Li, Joseph Ochesky, Christine E Ryan, Helen Piwnica-Worms, and David Piwnica-Worms. Noninvasive imaging of protein–protein interactions in living animals. *Proceedings of the National Academy of Sciences*, 99(10):6961–6966, 2002.

[126] Scott K Lyons. Advances in imaging mouse tumour models in vivo. *The Journal of pathology*, 205(2):194–205, 2005.

[127] Marnix C Maas, Dennis R Schaart, DJ Jan van der Laan, Peter Bruyndonckx, Cedric Lemaître, Freek J Beekman, and Carel WE van Eijk. Monolithic scintillator pet detectors with intrinsic depth-of-interaction correction. *Physics in medicine and biology*, 54(7):1893, 2009.

[128] Marnix C Maas, DJ Van Der Laan, Dennis R Schaart, Jan Huizenga, JC Brouwer, Peter Bruyndonck, Sophie Léonard, Cedric Lemaître, and Carel WE Van Eijk. Experimental characterization of monolithic-crystal small animal pet detectors read out by apd arrays. *Nuclear Science, IEEE Transactions on*, 53(3):1071–1077, 2006.

[129] David Malakoff. The rise of the mouse, biomedicine's model mammal. *Science*, 288(5464):248–253, 2000.

[130] R Marcinkowski, Sergio Espana, Hendrik Thoen, and Stefaan Vandenberghe. Performance of digital silicon photomultipliers for time of flight pet scanners. In *Nuclear Science Symposium and Medical Imaging Conference (NSS/MIC), 2012 IEEE*, pages 2825–2829. IEEE, 2012.

[131] Radoslaw Marcinkowski, S España, Roel Van Holen, and Stefaan Vandenberghe. Optimized light sharing for high-resolution tof pet detector based on digital silicon photomultipliers. *Physics in medicine and biology*, 59(23):7125, 2014.

[132] Radosław Marcinkowski, Sergio Espana, Roel Van Holen, and Stefaan Vandenberghe. Effects of dark counts on digital silicon photomultipliers performance. In *Nuclear Science Symposium and Medical Imaging Conference (NSS/MIC), 2013 IEEE*, pages 1–6. IEEE, 2013.

[133] Radosław Marcinkowski, Pieter Mollet, Roel Van Holen, and Stefaan Vandenberghe. Sub-millimetre doi detector based on monolithic lyso and digital sipm for a dedicated small-animal pet system. *Physics in medicine and biology*, 61(5):2196, 2016.

[134] Tarik F Massoud and Sanjiv S Gambhir. Molecular imaging in living subjects: seeing fundamental biological processes in a new light. *Genes & development*, 17(5):545–580, 2003.

[135] B Mazoyer, R Trebossen, C Schoukroun, B Verrey, A Syrota, J Vacher, P Lemasson, O Monnet, A Bouvier, and JL Lecomte. Physical characteristics of ttv03, a new high spatial resolution time-of-flight positron tomograph. *Nuclear Science, IEEE Transactions on*, 37(2):778–782, 1990.

[136] Massimo Mazzillo, Giovanni Condorelli, Delfo Sanfilippo, Giuseppina Valvo, Beatrice Carbone, Giorgio Fallica, Sergio Billotta, Massimiliano Belluso, Giovanni Bonanno, Luigi Cosentino, et al. Silicon photomultiplier technology at stmicroelectronics. *Nuclear Science, IEEE Transactions on*, 56(4):2434–2442, 2009.

[137] Mickel McClish, Purushottam Dokhale, James Christian, E Johnson, C Stapels, R Robertson, and KS Shah. Characterization of cmos position sensitive solid-state photomultipliers. *Nuclear Instruments and Methods in Physics Research Section A: Accelerators, Spectrometers, Detectors and Associated Equipment*, 624(2):492–497, 2010.

[138] Aaron R McFarland, Stefan Siegel, Danny F Newport, Robert Mintzer, Blake Atkins, and Mark Lenox. Continuously sampled digital pulse processing for inveon small animal pet scanner. In *Nuclear Science Symposium Conference Record, 2007. NSS'07. IEEE*, volume 6, pages 4262–4265. IEEE, 2007.

[139] CL Melcher and JS Schweitzer. Cerium-doped lutetium oxyorthosilicate: a fast, efficient new scintillator. *Nuclear Science, IEEE Transactions on*, 39(4):502–505, 1992.

[140] Janet C. Miller. Pet/ct in oncology. *Radiology Rounds*, 10(8), 2012.

[141] Michael Miller, Jerome Griesmer, David Jordan, Thomas Laurence, Raymond Muzic, Manoj Narayanan, Deepa Natarajamani, Kuan-Hao Su, and Sharon Wang. Initial characterization of a prototype digital photon counting pet system. *Journal of Nuclear Medicine*, 55(supplement 1):658–658, 2014.

[142] Jamie C Mitchell, Frederick Grant, Amy R Evenson, JA Parker, Per-Olof Hasselgren, and Sareh Parangi. Preoperative evaluation of thyroid nodules with 18 fdg-pet/ct. *Surgery*, 138(6):1166–1175, 2005.

[143] Robert S Miyaoka, Xiaoli Li, William Hunter, Larry A Pierce, Wendy McDougald, Paul E Kinahan, Thomas K Lewellen, et al. Resolution properties of a prototype continuous miniature crystal element (cmice) scanner. *Nuclear Science, IEEE Transactions on*, 58(5):2244–2249, 2011.

[144] Sascha Moehrs, Alberto Del Guerra, Deborah J Herbert, and Mark A Mandelkern. A detector head design for small-animal pet with silicon photomultipliers (sipm). *Physics in medicine and biology*, 51(5):1113, 2006.

[145] William W Moses and SE Derenzo. Prospects for time-of-flight pet using lso scintillator. *Nuclear Science, IEEE Transactions on*, 46(3):474–478, 1999.

[146] Gerd Muehllehner and Joel S Karp. Positron emission tomography. *Physics in medicine and biology*, 51(13):R117, 2006.

[147] Yuri Musienko, Etiennette Auffray, Andrei Fedorov, Mikhail Korzhik, Paul Lecoq, Stephen Reucroft, and John Swain. Sspm readout of lso,(lu-y) ap: Ce and pwo-ii pixels for pet detector modules. *Nuclear Science, IEEE Transactions on*, 55(3):1352–1356, 2008.

[148] Roger Newman. Visible light from a silicon p- n junction. *Physical Review*, 100(2):700, 1955.

[149] Agneta Nordberg. Pet imaging of amyloid in alzheimer's disease. *The lancet neurology*, 3(9):519–527, 2004.

[150] R Pani, A Pergola, R Pellegrini, A Soluri, G De Vincentis, S Filippi, G Di Domenico, A Del Guerra, and F Scopinaro. New generation position-sensitive pmt for nuclear medicine imaging. *Nuclear Instruments and Methods in Physics Research Section A: Accelerators, Spectrometers, Detectors and Associated Equipment*, 392(1):319–323, 1997.

[151] Catherine Michelle Pepin, Philippe Bérard, Anne-Laure Perrot, Claude Pépin, Daniel Houde, Roger Lecomte, Charles L Melcher, and Henri Dautet. Properties of lyso and recent lso scintillators for phoswich pet detectors. *Nuclear Science, IEEE Transactions on*, 51(3):789–795, 2004.

[152] ME Phelps, EJ Hoffman, and N Mullani. Design and performance characteristics of a whole body transaxial tomograph (pett). In *IEEE Nucl. Sci*, volume 23, pages 516–522, 1976.

[153] B Pichler, G Böning, E Lorenz, R Mirzoyan, W Pimpl, M Schwaiger, and SI Ziegler. Studies with a prototype high resolution pet scanner based on lso-apd modules. *Nuclear Science, IEEE Transactions on*, 45(3):1298–1302, 1998.

[154] Bernd J Pichler, Martin S Judenhofer, Ciprian Catana, Jeffrey H Walton, Manfred Kneilling, Robert E Nutt, Stefan B Siegel, Claus D

Claussen, and Simon R Cherry. Performance test of an lso-apd detector in a 7-t mri scanner for simultaneous pet/mri. *Journal of Nuclear Medicine*, 47(4):639–647, 2006.

[155] Bernd J Pichler, Armin Kolb, Thomas Nägele, and Heinz-Peter Schlemmer. Pet/mri: paving the way for the next generation of clinical multimodality imaging applications. *Journal of Nuclear Medicine*, 51(3):333–336, 2010.

[156] C Piemonte, M Boscardin, G-F Dalla Betta, M Melchiorri, N Zorzi, R Battiston, A Del Guerra, and G Llosa. Recent developments on silicon photomultipliers produced at fbk-irst. In *Nuclear Science Symposium Conference Record, 2007. NSS'07. IEEE*, volume 3, pages 2089–2092. IEEE, 2007.

[157] Claudio Piemonte. A new silicon photomultiplier structure for blue light detection. *Nuclear Instruments and Methods in Physics Research Section A: Accelerators, Spectrometers, Detectors and Associated Equipment*, 568(1):224–232, 2006.

[158] Jinyi Qi and Richard M Leahy. Iterative reconstruction techniques in emission computed tomography. *Physics in medicine and biology*, 51(15):R541, 2006.

[159] JG Rajendran, DC Wilson, EU Conrad, LM Peterson, JD Bruckner, JS Rasey, LK Chin, PD Hofstrand, JR Grierson, JF Eary, et al. [18f] fmiso and [18f] fdg pet imaging in soft tissue sarcomas: correlation of hypoxia, metabolism and vegf expression. *European journal of nuclear medicine and molecular imaging*, 30(5):695–704, 2003.

[160] D Renker and E Lorenz. Advances in solid state photon detectors. *Journal of Instrumentation*, 4(04):P04004, 2009.

[161] Juha O Rinne, David J Brooks, Martin N Rossor, Nick C Fox, Roger Bullock, William E Klunk, Chester A Mathis, Kaj Blennow, Jerome Barakos, Aren A Okello, et al. 11 c-pib pet assessment of change in fibrillar amyloid-β load in patients with alzheimer's disease treated with bapineuzumab: a phase 2, double-blind, placebo-controlled, ascending-dose study. *The Lancet Neurology*, 9(4):363–372, 2010.

[162] Emilie Roncali and Simon R Cherry. Application of silicon photomultipliers to positron emission tomography. *Annals of Biomedical Engineering*, 39(4):1358–1377, 2011.

[163] MASSIMO Salvatori, LUCA Melis, PAOLA Castaldi, MARIA LODOVICA Maussier, VITTORIA Rufini, GERMANO Perotti, and D Rubello. Clinical significance of focal and diffuse thyroid diseases identified by 18 f-fluorodeoxyglucose positron emission tomography. *Biomedicine & Pharmacotherapy*, 61(8):488–493, 2007.

[164] F Sanchez, L Moliner, C Correcher, A Gonzalez, A Orero, M Carles, A Soriano, María José Rodriguez-Alvarez, LA Medina, F Mora, et al. Small animal pet scanner based on monolithic lyso crystals: performance evaluation. *Medical physics*, 39(2):643–653, 2012.

[165] F Sanchez, A Orero, A Soriano, C Correcher, P Conde, A González, L Hernández, L Moliner, MJ Rodríguez-Alvarez, LF Vidal, et al. Albira: a small animal pet/spect/ct imaging system. *Medical physics*, 40(5):051906, 2013.

[166] Dennis R Schaart, Stefan Seifert, Ruud Vinke, Herman T van Dam, Peter Dendooven, Herbert Löhner, and Freek J Beekman. Labr3: Ce and sipms for time-of-flight pet: achieving 100 ps coincidence resolving time. *Physics in medicine and biology*, 55(7):N179, 2010.

[167] Dennis R Schaart, Herman T van Dam, Stefan Seifert, Ruud Vinke, Peter Dendooven, Herbert Löhner, and Freek J Beekman. A novel, sipm-array-based, monolithic scintillator detector for pet. *Physics in medicine and biology*, 54(11):3501, 2009.

[168] Heiko Schöder, Steven M Larson, and Henry WD Yeung. Pet/ct in oncology: integration into clinical management of lymphoma, melanoma, and gastrointestinal malignancies. *Journal of Nuclear Medicine*, 45(1 suppl):72S–81S, 2004.

[169] David Schug, Peter Michael Duppenbecker, Patrik Gebhardt, Bjorn Weissler, Ben Zwaans, Fabian Kiessling, and Volkmar Schulz. First evaluations of the neighbor logic of the digital sipm tile. In *Nuclear Science Symposium and Medical Imaging Conference (NSS/MIC), 2012 IEEE*, pages 2817–2819. IEEE, 2012.

[170] Volkmar Schulz, Torsten Solf, Bjoern Weissler, Pierre Gebhardt, Peter Fischer, Michael Ritzert, Viacheslav Mlotok, Claudio Piemonte, Nicola Zorzi, Mirko Melchiorri, et al. A preclinical pet/mr insert for a human 3t mr scanner. In *Nuclear Science Symposium Conference Record (NSS/MIC), 2009 IEEE*, pages 2577–2579. IEEE, 2009.

[171] R Schulze et al. Pdpc tek user manual. *Philips Digital Photon Counting, v0*, 21, 2014.

[172] Ralf Schulze. *Module-TEK User Manual.* Philips Digital Photon Counting, Pauwelsstrasse 17 D-52075 Aachen, Germany, 031 edition, 3 2014. Koninklijke Philips N.V. 2014.

[173] Jürgen Seidel, Juan José Vaquero, and Michael V Green. Resolution uniformity and sensitivity of the nih atlas small animal pet scanner: comparison to simulated lso scanners without depth-of-interaction capability. *Nuclear Science, IEEE Transactions on*, 50(5):1347–1350, 2003.

[174] Stefan Seifert, Herman T van Dam, Jan Huizenga, Ruud Vinke, Peter Dendooven, Herbert Löhner, and Dennis R Schaart. Monolithic labr3: Ce crystals on silicon photomultiplier arrays for time-of-flight positron emission tomography. *Physics in medicine and biology*, 57(8):2219, 2012.

[175] Stefan Seifert, Herman T van Dam, and Dennis R Schaart. The lower bound on the timing resolution of scintillation detectors. *Physics in medicine and biology*, 57(7):1797, 2012.

[176] Stefan Seifert, Gerben Van der Lei, Herman T Van Dam, and Dennis R Schaart. First characterization of a digital sipm based time-of-flight pet detector with 1 mm spatial resolution. *Physics in medicine and biology*, 58(9):3061, 2013.

[177] Lawrence A Shepp and Yehuda Vardi. Maximum likelihood reconstruction for emission tomography. *Medical Imaging, IEEE Transactions on*, 1(2):113–122, 1982.

[178] Paul Shreve, Ping-Chun Chiao, H David Humes, Markus Schwaiger, and Milton D Gross. Carbon-11-acetate pet imaging in renal disease. *Journal of nuclear medicine: official publication, Society of Nuclear Medicine*, 36(9):1595–1601, 1995.

[179] Leonard D Shultz, Fumihiko Ishikawa, and Dale L Greiner. Humanized mice in translational biomedical research. *Nature Reviews Immunology*, 7(2):118–130, 2007.

[180] Robert L Siddon. Prism representation: a 3d ray-tracing algorithm for radiotherapy applications. *Physics in medicine and biology*, 30(8):817, 1985.

[181] Stefan Siegel, Simon R Cherry, Anthony R Ricci, Yiping Shao, and Michael E Phelps. Development of continuous detectors for a high resolution animal pet system. *Nuclear Science, IEEE Transactions on*, 42(4):1069–1074, 1995.

[182] Donald L Snyder, Michael I Miller, Lewis J Thomas Jr, and David G Politte. Noise and edge artifacts in maximum-likelihood reconstructions for emission tomography. *Medical Imaging, IEEE Transactions on*, 6(3):228–238, 1987.

[183] Benjamin Solomon, Grant A McArthur, Carleen Cullinane, John R Zalcberg, and Rodney J Hicks. Applications of positron emission tomography in the development of molecular targeted cancer therapeutics. *BioDrugs*, 17(5):339–354, 2003.

[184] Virginia Ch Spanoudaki and Craig S Levin. Photo-detectors for time of flight positron emission tomography (tof-pet). *Sensors*, 10(11):10484–10505, 2010.

[185] Merry A Spurrier, Piotr Szupryczynski, Kan Yang, A Andrew Carey, and Charles L Melcher. Effects of co-doping on the scintillation properties of lso: Ce. *Nuclear Science, IEEE Transactions on*, 55(3):1178–1182, 2008.

[186] AG Stewart, V Saveliev, SJ Bellis, DJ Herbert, PJ Hughes, and JC Jackson. Performance of 1-mm 2 silicon photomultiplier. *Quantum Electronics, IEEE Journal of*, 44(2):157–164, 2008.

[187] Jennifer R Stickel, Jinyi Qi, and Simon R Cherry. Fabrication and characterization of a 0.5-mm lutetium oxyorthosilicate detector array for high-resolution pet applications. *Journal of Nuclear Medicine*, 48(1):115–121, 2007.

[188] SC Strother, ME Casey, and EJ Hoffman. Measuring pet scanner sensitivity: relating countrates to image signal-to-noise ratios using noise equivalents counts. *Ieee transactions on nuclear science*, 37(2):783–788, 1990.

[189] S Surti and JS Karp. Experimental evaluation of a simple lesion detection task with time-of-flight pet. *Physics in medicine and biology*, 54(2):373, 2008.

[190] Suleman Surti, Georges El Fakhri, and Joel S Karp. Optimizing acquisition parameters in tof pet scanners. In *Nuclear Science Symposium*

Conference Record, 2006. IEEE, volume 4, pages 2354–2359. IEEE, 2006.

[191] Suleman Surti, Joel S Karp, Amy E Perkins, Chris A Cardi, Margaret E Daube-Witherspoon, Austin Kuhn, and Gerd Muehllehner. Imaging performance of a-pet: a small animal pet camera. *Medical Imaging, IEEE Transactions on*, 24(7):844–852, 2005.

[192] Suleman Surti, Austin Kuhn, Matthew E Werner, Amy E Perkins, Jeffrey Kolthammer, and Joel S Karp. Performance of philips gemini tf pet/ct scanner with special consideration for its time-of-flight imaging capabilities. *Journal of Nuclear Medicine*, 48(3):471–480, 2007.

[193] Suleman Surti, Adam R Shore, and Joel S Karp. Design study of a whole-body pet scanner with improved spatial and timing resolution. *Nuclear Science, IEEE Transactions on*, 60(5):3220–3226, 2013.

[194] Istvan Szanda, Jane Mackewn, Gergely Patay, Peter Major, Kavitha Sunassee, Gregory E Mullen, Gabor Nemeth, York Haemisch, Philip J Blower, and Paul K Marsden. National electrical manufacturers association nu-4 performance evaluation of the pet component of the nanopet/ct preclinical pet/ct scanner. *Journal of Nuclear Medicine*, 52(11):1741–1747, 2011.

[195] V Tabacchini, V Westerwoudt, G Borghi, S Seifert, and DR Schaart. Probabilities of triggering and validation in a digital silicon photomultiplier. *Journal of Instrumentation*, 9(06):P06016, 2014.

[196] Yuan-Chuan Tai, Ananya Ruangma, Douglas Rowland, Stefan Siegel, Danny F Newport, Patrick L Chow, and Richard Laforest. Performance evaluation of the micropet focus: a third-generation micropet scanner dedicated to animal imaging. *Journal of nuclear medicine*, 46(3):455–463, 2005.

[197] S Tavernier, P Bruyndonckx, S Leonard, and O Devroede. A high-resolution pet detector based on continuous scintillators. *Nuclear Instruments and Methods in Physics Research Section A: Accelerators, Spectrometers, Detectors and Associated Equipment*, 537(1):321–325, 2005.

[198] Michel M Ter-Pogossian, David C Ficke, John T Hood Sr, Mikio Yamamoto, and Nizar A Mullani. Pett vi: a positron emission tomograph utilizing cesium fluoride scintillation detectors. *Journal of computer assisted tomography*, 6(1):125–133, 1982.

[199] Michel M Ter-Pogossian, David C Ficke, Mikio Yamamoto, and John T Hood Sr. Super pett i: a positron emission tomograph utilizing photon time-of-flight information. *Medical Imaging, IEEE Transactions on*, 1(3):179–187, 1982.

[200] M Teräs, T Tolvanen, JJ Johansson, JJ Williams, and J Knuuti. Performance of the new generation of whole-body pet/ct scanners: Discovery ste and discovery vct. *European journal of nuclear medicine and molecular imaging*, 34(10):1683–1692, 2007.

[201] Hendrik Thoen, Vincent Keereman, Pieter Mollet, and Stefaan Vandenberghe. Impact of the crystal pixel size on spatial resolution and contrast recovery in whole-body pet scanners. *Journal of Nuclear Medicine*, 53(supplement 1):2351–2351, 2012.

[202] WG Totty, WA Murphy, and Joseph K Lee. Soft-tissue tumors: Mr imaging. *Radiology*, 160(1):135–141, 1986.

[203] Herman T Van Dam, Giacomo Borghi, Stefan Seifert, and Dennis R Schaart. Sub-200 ps crt in monolithic scintillator pet detectors using digital sipm arrays and maximum likelihood interaction time estimation. *Physics in medicine and biology*, 58(10):3243, 2013.

[204] Herman T Van Dam, Stefan Seifert, and Dennis R Schaart. The statistical distribution of the number of counted scintillation photons in digital silicon photomultipliers: model and validation. *Physics in medicine and biology*, 57(15):4885, 2012.

[205] Herman T Van Dam, Stefan Seifert, Ruud Vinke, Peter Dendooven, Herbert Löhner, Freek J Beekman, and Dennis R Schaart. Improved nearest neighbor methods for gamma photon interaction position determination in monolithic scintillator pet detectors. *Nuclear Science, IEEE Transactions on*, 58(5):2139–2147, 2011.

[206] Herman T van Dam, Stefan Seifert, Ruud Vinke, Peter Dendooven, Herbert Löhner, Freek J Beekman, and Dennis R Schaart. A practical method for depth of interaction determination in monolithic scintillator pet detectors. *Physics in medicine and biology*, 56(13):4135, 2011.

[207] Carel WE Van Eijk. Inorganic scintillators in medical imaging. *Physics in medicine and biology*, 47(8):R85, 2002.

[208] Stefaan Vandenberghe and Paul K Marsden. Pet-mri: a review of challenges and solutions in the development of integrated multimodality imaging. *Physics in medicine and biology*, 60(4):R115, 2015.

[209] Amy L Vavere and Michael J Welch. Preparation, biodistribution, and small animal pet of 45ti-transferrin. *Journal of Nuclear Medicine*, 46(4):683–690, 2005.

[210] Eugene Veklerov and Jorge Llacer. Stopping rule for the mle algorithm based on statistical hypothesis testing. *Medical Imaging, IEEE Transactions on*, 6(4):313–319, 1987.

[211] Y Wang, W Zhu, X Cheng, and D Li. 3d position estimation using an artificial neural network for a continuous scintillator pet detector. *Physics in medicine and biology*, 58(5):1375, 2013.

[212] Yuchuan Wang, Jurgen Seidel, Benjamin MW Tsui, Juan J Vaquero, and Martin G Pomper. Performance evaluation of the ge healthcare explore vista dual-ring small-animal pet scanner. *Journal of Nuclear Medicine*, 47(11):1891–1900, 2006.

[213] Miles N Wernick and John N Aarsvold. *Emission tomography: the fundamentals of PET and SPECT*. Academic Press, 2004.

[214] WH Wong, NA Mullani, EA Philippe, RK Hartz, D Bristow, K Yerian, JM Gaeta, and N Ketharnavaz. Performance characteristics of the university of texas tofpet-i pet camera. *J. Nucl. Med.;(United States)*, 25(5), 1986.

[215] Yongfeng Yang, Yuan-Chuan Tai, Stefan Siegel, Danny F Newport, Bing Bai, Quanzheng Li, Richard M Leahy, and Simon R Cherry. Optimization and performance evaluation of the micropet ii scanner for in vivo small-animal imaging. *Physics in medicine and biology*, 49(12):2527, 2004.

[216] Hai-Bing Zhou, Jae Hak Lee, Christopher G Mayne, Kathryn E Carlson, and John A Katzenellenbogen. Imaging progesterone receptor in breast tumors: synthesis and receptor binding affinity of fluoroalkyl-substituted analogues of tanaproget. *Journal of medicinal chemistry*, 53(8):3349–3360, 2010.

[217] Karl Ziemons, E Auffray, R Barbier, G Brandenburg, P Bruyndonckx, Y Choi, D Christ, N Costes, Y Declais, O Devroede, et al. The

clearpet™ project: development of a 2nd generation high-performance small animal pet scanner. *Nuclear Instruments and Methods in Physics Research Section A: Accelerators, Spectrometers, Detectors and Associated Equipment*, 537(1):307–311, 2005.